Development of a clinically relevant 3D in vitro spinal cord injury model using bioprinted GelMA hydrogels

by Maryam Alsadat Rad

Thesis submitted in fulfilment of the requirements for
the degree of

Doctor of Philosophy

under the supervision of Prof. Joanne Tipper, A/Prof. Irina
Kabakoba

University of Technology Sydney
Faculty of Engineering and Information Technology

05/2023

Certificate of Original Authorship

I, **Maryam Alsadat Rad**, declare that this thesis is submitted in fulfilment of the requirements for the award of **Doctor of Philosophy**, in the **School of Biomedical Engineering/ Faculty of Engineering and Information Technology** at the University of Technology Sydney.

This thesis is wholly my own work unless otherwise referenced or acknowledged. In addition, I certify that all information sources and literature used are indicated in the thesis.

This document has not been submitted for qualifications at any other academic institution.

This research was supported by the Faculty of Engineering and Information Technology (FEIT), UTS.

Signature of Student:
(Maryam Alsadat Rad)
Date: 16th May 2023

Acknowledgements

First and foremost, I would like to express my sincere appreciation to Prof. Joanne Tipper, my main supervisor, for all the knowledge she has imparted to me and her support throughout this thesis process. Joanne has been very patient and supportive throughout the entirety of my project. She provides exceptional support as a supervisor in all aspects of the role. Her professional skills and enthusiasm will prove invaluable to me throughout my life. I truly would not have been able to get through my PhD without her. Having been a student of hers was a great privilege for me.

I would like to also express my deep gratitude and respect to my co-supervisor, Associate professor Dr. Irina Kabakova, whose advice and insight was invaluable to me. I benefited a lot from her valuable guidance, not only in the direction of research but also in my method of research, which was often of greater importance for me.

I am also grateful to Dr. Javad Tavakoli for supporting me in the laboratory to utilize the Impacter system. My sincere thanks go to Dr. Martin Stewart, who provided me with invaluable advice during my first year of PhD studies. Additionally, I would like to Prof. Thomas R. Cox and Dr. Elysse C. Filipe for supporting me in using the Rheometer.

I am grateful for the financial support provided by the UTS PhD scholarship for supporting this work. I take this unique opportunity to thank the School of Biomedical Engineering for providing me with the necessary facilities and an excellent academic environment to complete my work successfully. I would also like to express my appreciation to the laboratory assistants in the BMT lab for their cooperation, technical assistance, and valuable contribution to my work. The assistance from the staff of the Life Science Laboratory is also acknowledged, particularly Sarah Osvath.

Most importantly, none of this could have happened without my family during this journey. I thank my husband for giving me his great love, endless support, and encouragement when needed. I wish to express my gratitude to my sweet mom, who I am forever indebted for her continuous support of my goals and dreams. Last but not least, I would like to extend my heartfelt gratitude to my father and brothers for their unwavering support and encouragement throughout the completion of this thesis.

I dedicate this thesis to my recently deceased uncle, Mojtaba Sadeghi, for his profound influence on my life.

Format of Thesis

This is a conventional thesis consisting of 7 chapters. This thesis aims to develop a clinically relevant 3D *in vitro* spinal cord injury model using bioprinted GelMA hydrogels.

Chapter 1 is an introduction chapter, including the research background, motivation, aim, objectives and scope.

Chapter 2 is a comprehensive literature review and discusses *in vivo* and *in vitro* spinal cord injury models.

Chapter 3 includes general materials and methods used in this research.

Chapter 4 summarises the optimisation process of bioprinting GelMA hydrogels to form the basis of a spinal cord injury model. This includes an assessment of the printability, biocompatibility and structural stability of GelMA hydrogels with and without encapsulated neural cells.

Chapter 5 investigates the mechanical properties of 3D bioprinted acellular and cellular GelMA hydrogels using rheology and novel Brillouin microspectroscopy as a non-contact and non-destructive method.

Chapter 6 presents the simulation of a clinically relevant 3D *in vitro* spinal cord injury model in terms of the mechanical forces and the biological responses using the TA Instruments Electroforce BioDynamic 5110 system.

Chapter 7 summarizes the main research outcomes of the PhD and proposes possible future research directions that may arise based on the advances made.

List of Publications

1. **Rad, M. A.**, Mahmodi, H., Filipe, E. C., Cox, T. R., Kabakova, I., & Tipper, J. L. (2022). Micromechanical characterisation of 3D bioprinted neural cell models using brillouin microspectroscopy. Bioprinting, 25, e00179.

2. Mathew, M., **M. A. Rad***, J. P. Mata, H. Mahmodi, I. V. Kabakova, C. L. Raston, Y. Tang, J. L. Tipper, and J. Tavakoli. Hyperbranched polymers tune the physicochemical, mechanical, and biomedical properties of alginate hydrogels. Materials Today Chemistry 23 (2022): 100656.

3. Tavakoli, J., Shrestha, J., Bazaz, S. R., **Rad, M. A.**, Warkiani, M. E., Raston, C. L., ... & Tang, Y. (2022). Developing novel fabrication and optimisation strategies on aggregation-induced emission nanoprobe/polyvinyl alcohol hydrogels for bio-applications. Molecules, 27(3), 1002.

4. Polonchuk, l., Surija, L., Lee, M.H., Sharma, P., Ming, C.L.C., Richter, F., Ben-sefer, E., **Rad, M.A.**, Mahmodi, H., Al shamery, W., & Tran, H.A., 2021. Towards engineering heart tissues from bioprinted cardiac spheroids. Biofabrication, 13(4), 045009.

5. Morshedi Rad, D., **Rad, M.A.***, Razavi Bazaz, S., Kashaninejad, N., Jin, D., & Ebrahimi Warkiani, M. (2021). A comprehensive review on intracellular delivery. Advanced materials, 33(13), 2005363.

Conference Presentations (Oral)

1. Viscoelasticity Investigation of 3D Printed Neural Cell Containing GelMA Hydrogels by Confocal Brillouin Microscopy. In Regional ABC Sydney conference, Sydney, Australia, December 2020.

2. Micromechanical characterisation of 3D Bioprinted neural cell models using Brillouin spectroscopy. In 5th Virtual BioBrillouin Meeting, Vienna, Austria, 16th July 2021.

3. Bioprinted GelMA hydrogel constructs for 3D in vitro spinal cord injury model. In Sydney Spinal Symposium (SSS), Sydney, Australia, 9th September 2021.

4. 3D Bioprinted neural constructs for in vitro spinal cord injury models. In 3rd (Virtual) Australian Bioprinting Workshop for Tissue Engineering and Regenerative Medicine, Sydney, Australia, OCT 4 - 5, 2021.

5. Investigation of cellular responses to mechanical loading in a 3D in vitro spinal cord contusion injury model. In 13th Australasian Biomechanics Conference (ABC13) will be held in Brisbane from 27th to 29th November 2022. (Abstract accepted)

List of Abbreviations

2D	Two-dimensional
3D	Three-dimensional
ANOVA	Analysis of variance
ATP	Adenosine triphosphate
BFS	Brillouin frequency shift
BM	Brillouin microspectroscopy
CNS	Central nervous system
DMEM	Dulbecco's Modified Eagle Medium
ECM	Extracellular matrix
FBS	Foetal bovine serum
FIJI	FIJI is a module of ImageJ
GelMA	Gelatin Methacryloyl
GFAP	Glial fibrillary acidic protein
MMP	Matrix metalloproteinase
PBS	Phosphate buffered saline
PFA	Paraformaldehyde
PNS	Peripheral nervous system
RGD	Arginine-glycine-aspartic acid
SCI	Spinal cord injury
SD	Standard deviation
v/v	Volume per volume
w/v	Weight per volume

Table of Contents

ABSTRACT

Traumatic spinal cord injury (SCI) occurs primarily in young males and the elderly due to transport accidents, acts of violence, falls, and sporting activity, which usually involves very rapid mechanical injury. Due to the devastating effects of SCI, many researchers have been studying ways to regenerate neuronal cells and re-establish function in the spinal cord after injury. However, the complexity of the central nervous system (CNS) network makes it challenging to understand the reactions of different types of CNS cells, including neurons and glial cells, to mechanical injury *in vivo*. This study has concentrated on simulating a clinically relevant 3D *in vitro* SCI in terms of mechanical forces and biological responses. For this purpose, 3D Gelatin Methacryloyl (GelMA) hydrogels at various volume concentrations of 2.5, 5, 7.5, 10 and 15 % (w/v) embedded with NG108-15 neuronal and C6 astrocyte-like cells were bioprinted. The bioprinted GelMA hydrogels with 5% (w/v) concentration were the most appropriate matrix for a 3D *in vitro* SCI model due to optimal printability, structural stability, high cell viability, and optical transparency. To design a valid SCI model, the micromechanical properties of bioprinted GelMA hydrogels were assessed using Brillouin microspectroscopy (BM) as a non-invasive and label-free method. The results demonstrated that 5% (w/v) acellular GelMA hydrogel had similar mechanical properties to native neural tissue (~ 0.1-4.8 kPa). By assessing the mechanical properties of cellular GelMA hydrogels within and surrounding the NG 108-15 neuronal spheroids, it was demonstrated that the spheroid-type cells became stiffer over time, whereas the surrounding hydrogel matrix showed significant decreases in stiffness. Finally, the TA Instruments Electroforce BioDynamic Impaction system was utilised to simulate a spinal cord contusion injury using a 3D bioprinted GelMA hydrogel. The contusion injury was modelled at velocities of 1000 and 3000 mm.s^{-1} with displacement to 1, 2 and 4 mm to investigate cellular responses to displacement depth and injury velocity. Astrocytic expression of glial fibrillary acidic protein (GFAP) volume, ramification and metabolic activity of C6 astrocyte-like cells increased with increasing velocity and depth displacement over 10 days post impaction. However, neuronal cells showed the opposite behaviour, where βIII-tubulin (a neuronal marker) labelled cells exhibited significant neurite outgrowth in non-injured control samples than in post-injury samples over 10 days. In summary, a 3D SCI model was developed and presented in this thesis which was clinically relevant and mimicked the *in vivo* mechanical characteristics of an injury. In addition, the responses of both astrocytes and neuronal cells were similar to those observed *in vivo* after injury. The model developed within this study leaves scope for further development to increase the complexity of bioprinted structures with multiple cell types. This model possesses the potential for use in evaluating how injury biomechanics, such as displacement and velocity, affects the pathophysiological outcomes of cells and which biomechanical parameters are dominant in determining injury severity *in vivo*. The use of these preclinical models may aid in the preliminary testing of therapeutic interventions and the development of improved animal models of spinal cord injury.

List of Figures

List of Tables

CHAPTER 1 INTRODUCTION

1.1 Research background

The spinal cord serves as a crucial conduit, connecting the brain to nerve receptors and motor neurons responsible for muscle and end effector control through white and grey matter made up of various cell types, such as neurons and glial cells [1], while spinal cord injury (SCI) can lead to a wide range of dysfunctions, including pain, paralysis, and respiratory dependency [2]. In Australia, traumatic SCI is mainly caused by land transport crashes (46%) and falls (36%), with males accounting for 80% of new cases reported in 2017-2018 [3]. The prevalence of spinal cord injury in Australia exceeds 20,000 individuals, resulting in an annual cost of $3.75 billion to the economy and an estimated lifetime cost of $75 billion in 2020 [4]. Technology that may lead to successful regenerative therapies can, therefore, have an enormous economic and societal impact.

Many techniques have been developed to simulate human SCIs. The aim of *in vivo* models of SCI is to recapitulate features of human SCI as closely as possible [5]. However, *in vivo* SCI models can be time-consuming and expensive. Due to the ethical issues in the use of animal models (such as animal sacrifice), there is an increasing demand for accessible and valid (biologically relevant) *in vitro* neural tissue models which allow the user to track normal and aberrant cellular and molecular interactions, as well as whole system interconnectivity [6, 7]. The ideal *in vitro* models should mimic the native spinal cord tissues as closely as possible, biologically, mechanically, and organizationally. However, accurate mimicry of the complex nervous system in the *in vitro* environment is challenging via conventional techniques, especially when material and mechanical flexibility, control over cell placement, and precision in anatomical design are required [8].

Research at the University of Leeds has previously applied traumatic spinal cord injury insults to cast collagen hydrogel seeded with neural cells using the Infinite Horizon and TA instrument 5110 Electroforce apparatus [9-11]. In all these studies conducted at the University of Leeds, there was no control over the shape and dimensions of the hydrogel. In addition, the 3D constructs used in their study experienced problems such as batch-to-batch variability of collagen hydrogel and meniscus formation in cast hydrogels, which created a non-uniform surface and varying displacement depths. The meniscus also caused difficulty in cell seeding because most cells were placed in the gel centre, and the rest of the gel consists of a few cells. The increased tension experienced by cells at the top of the gel in the vicinity of the meniscus leads to cellular reactivity within 3D cast hydrogel before the injury has been delivered, particularly in astrocyte cells. Therefore, the design and precise control of the 3D mechanical environment is a significant challenge, and how cells remodel such environments over time remains an open question.

Recently, 3D bioprinting has emerged as a tool capable of producing cellular environments that are precise in shape and allow for the precise positioning of cells [12]. Unlike the traditional 3D *in vitro* models, which often involve cell seeding on top of cast hydrogels, 3D bioprinting allows the fabrication of complex neural models with many neural cells densely and uniformly distributed. The biomaterials used for 3D bioprinting are referred to as bioinks, which can be classified into natural and synthetic polymers. The advantages of the biocompatibility of natural hydrogels and the adjustable properties of synthetic hydrogels led to the hypothesis that the utilization of hybrid hydrogels would provide a robust platform for assessing neural cell physiology *in vitro*. However, the development of a robust hybrid hydrogel, which is suitable for both bioprinting and cell culturing of CNS cells, is still a challenge.

The following literature review will discuss spinal cord structures, cell types in CNS and the pathophysiology of SCI. The current *in vivo* and *in vitro* SCI models will also be discussed, highlighting their advantages and disadvantages and finally identifying where future research could be targeted. 3D *in vitro* hydrogel-based SCI models, which were fabricated by bioprinting, were also reviewed. Considering the currently available SCI models, it is proposed that a 3D bioprinted *in vitro* culture method could be used to study specific events associated with SCI. The effect of hydrogel composition and stiffness, two critical factors for designing a 3D *in vitro* SCI model, will also be discussed in this thesis chapter.

1.2 Research Motivation

The creation of SCI models *in vivo* is highly invasive and time-consuming. In addition, the complexity of CNS makes it challenging to understand the impact of mechanical injuries on the response of individual CNS cell types. On the other hand, current *in vitro* models have some challenges in the fabrication of 3D structures for forming a basis for spinal cord injury models as it is difficult to control the shape of the construct and position of the cells in the three-dimensional environment. Therefore, *in vitro* SCI models that mimic *in vivo* conditions and support cell growth and differentiation are essential to fully interrogate the biomechanical thresholds of various CNS cell types and the influence of cell-cell interactions on the secondary pathophysiology.

1.3 The Impact of Covid-19 and other issues on my project

During the years 2020 and 2021, the COVID-19 outbreak caused an unpredicted situation that influenced the design of this doctoral thesis. During the pandemic, HDR students could not freely access the Biomedical Engineering (BMT) and Science laboratories due to the lockdown. After returning to the campus, there was limited capacity in the BMT and Science laboratories due to the need to socially distance. The followings are all issues that occurred during my PhD:

1) Inability to access laboratories in FEIT and Faculty of Science during lockdowns (4 months)
2) Reduced access to laboratories during and after lockdown periods, maximum three days per week instead of 5 (6 months)
3) Significant delay for rheology measurements at Garvan institute, which was closed to visitors (9 months)
4) Failure of the interferometer controller unit of confocal Brillouin imaging (2 months),

   Delay in locating a missing part of TA Instruments Electroforce BioDynamic Impaction system (5 months)
5) Delay in accessing training on instruments, such as the Electroforce system and confocal microscopy during Covid-19 lockdown (2-3 months).

In addition, I also changed my research topic ten months after starting my PhD.

1.4 Research hypothesis and aim

Collagen hydrogels, a natural polymer often used to form a basis for a SCI model, have some drawbacks. Firstly, native crosslinks in collagen hydrogels could induce batch-to-batch variability, which makes it challenging to tune the mechanical properties of collagen. Secondly, cells incorporated into hydrogels fabricated using traditional methods, such as cast collagen hydrogels, cannot be uniformly distributed due to a lack of accuracy in casting the gels into wells. Therefore, the areas of the hydrogel with higher cell densities tend to cause faster contraction and a non-uniform surface. Another disadvantage of using a pipette to transfer hydrogels is the formation of a large number of bubbles. Thirdly, the cast hydrogels form a meniscus in a well plate and create tension in this area. Limiting the consistency and reproducibility of the final product can affect the cells in a 3D environment, leading to cellular reactivity within 3D cast hydrogel before the injury has been applied. This makes it difficult to differentiate cellular responses that result from the injury and those that result from artefacts caused by the experimental set up. 3D bioprinting allows a high level of precise control of the structure and shape of the construct, as well as precise positioning of multiple cell types. We hypothesize that the use of bioprinting will create a 3D environment that can be precisely controlled and is subject to fewer variations than a cast natural hydrogel allows. Therefore, in the case of presenting the injury scenario to the sample, a response to the injury will be truly recorded rather than the inherent variability of the system.

This research aims to investigate how CNS cells within a bioprinted 3D GelMA hydrogel respond to a contusion injury in a controlled environment.

1.5 Research objectives and scope

The following are the objectives of the project:

1. To optimise the 3D bioprinting process of GelMA hydrogels for use in a spinal cord injury model.

2. To perform mechanical assessment of 3D bioprinted GelMA hydrogels using rheology and Brillouin microspectroscopy.

3. To develop an *in vitro* 3D Spinal Cord Injury Model using bioprinted GelMA hydrogels and the TA Instruments 5110 Electroforce to apply a clinically relevant mechanical injury.

1.6 Research Significance

The innovation of this research is in creating a 3D environment that is more precise in shape and stiffness, which helps to maintain the astrocyte cells in a non-reactive state before the injury to form a basis of a spinal cord injury model. For this purpose, the combination of two techniques, 3D bioprinting and Brillouin microspectroscopy, was utilised. The former provides a technique for the fabrication of 3D *in vitro* models, which enables controlling the position of different types of CNS cells and the geometry of a scaffold. The latter allows non-contact, damage-free and label-free characterisation of the biomechanical properties of a scaffold. This combination approach is unique and has not been explored before in this context. The stiffness obtained via Brillouin microspectroscopy allowed us to understand the extracellular matrix changes in neural models over time. Thus, the proposed "fabrication + testing" approach will significantly improve the precision and reliability of the current *in vitro* SCI models. In addition, our 3D hydrogel model is clinically relevant to *in vivo* SCI in humans, as it simulates the biological cascade observed post-injury and the mechanical injury in terms of velocity and displacement depth.

1.7 Thesis structure

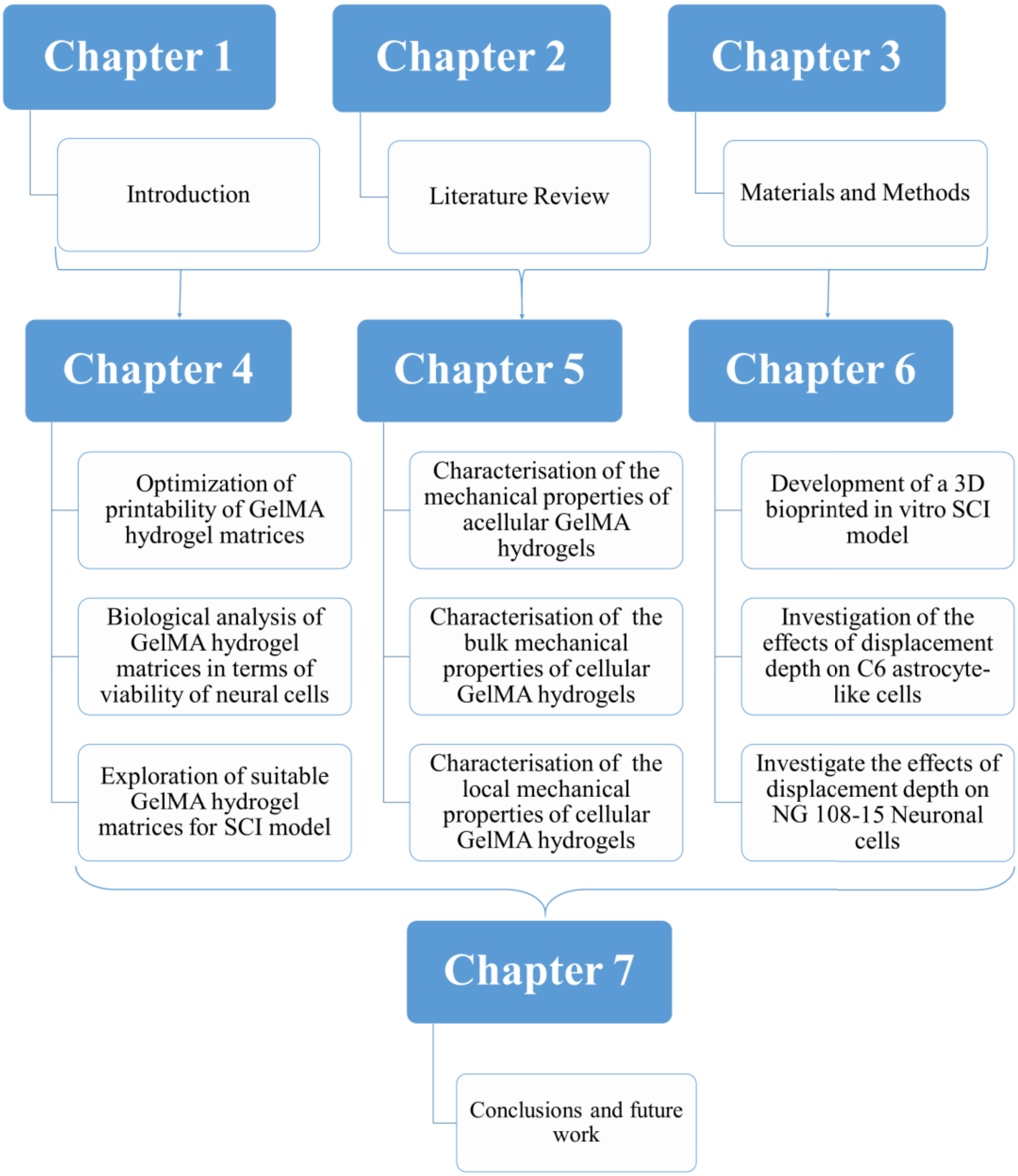

Figure 1.1. Flow diagram showing the outline of the thesis chapters.

CHAPTER 2 LITERATURE REVIEW

2.1 Central nervous system (CNS)

Our nervous system is categorised into central and peripheral parts, along with the separate autonomic system [13]. The central nervous system (CNS) is the processing centre for the nervous system, which has two main organs; the brain and spinal cord, while the peripheral nervous system (PNS) broadly consists of the nerves and ganglia (clusters of neurons) outside of the brain and spinal cord [14]. The principal function of the PNS is to connect the CNS to organs, practically serving as a relay between the spinal cord and brain and the rest of the body.

2.1.1 Spinal cord structure

The spinal cord is made up of several types of nerve cells [1]. Spinal nerves carry the motor, sensory, and autonomic signals between the spinal cord and the rest of the body (Figure 2.1(a)). The spinal cord comprises both neurons with a myelin sheath, which forms white matter, and neurons without a myelin sheath, which form the grey matter in the spinal cord [15]. If the spinal cord is cut in half horizontally, the grey matter is observed in the middle, surrounded by the white matter (Figure 2.1(a)). The white matter contains axons and glial cells, which include astrocytes, oligodendrocytes, and microglia (immune cells), and the grey matter consists of the cell bodies of excitatory neurons as well as glial cells and blood vessels. Motor tracts from the brain descend into the white matter to enter the grey matter and synapse with the spinal cord motor neurons [16].

The spinal cord is well-protected and surrounded by vertebrae, which constitute the spinal column (Figure 2.1(b)). The spinal column is comprised of 33 vertebrae with cartilaginous discs between the vertebrae, which assist in the transfer of load in the spine and provide flexibility. The vertebrae are stacked on top of each other and are named and numbered from top to bottom according to their location (Figure 2.1(c)).

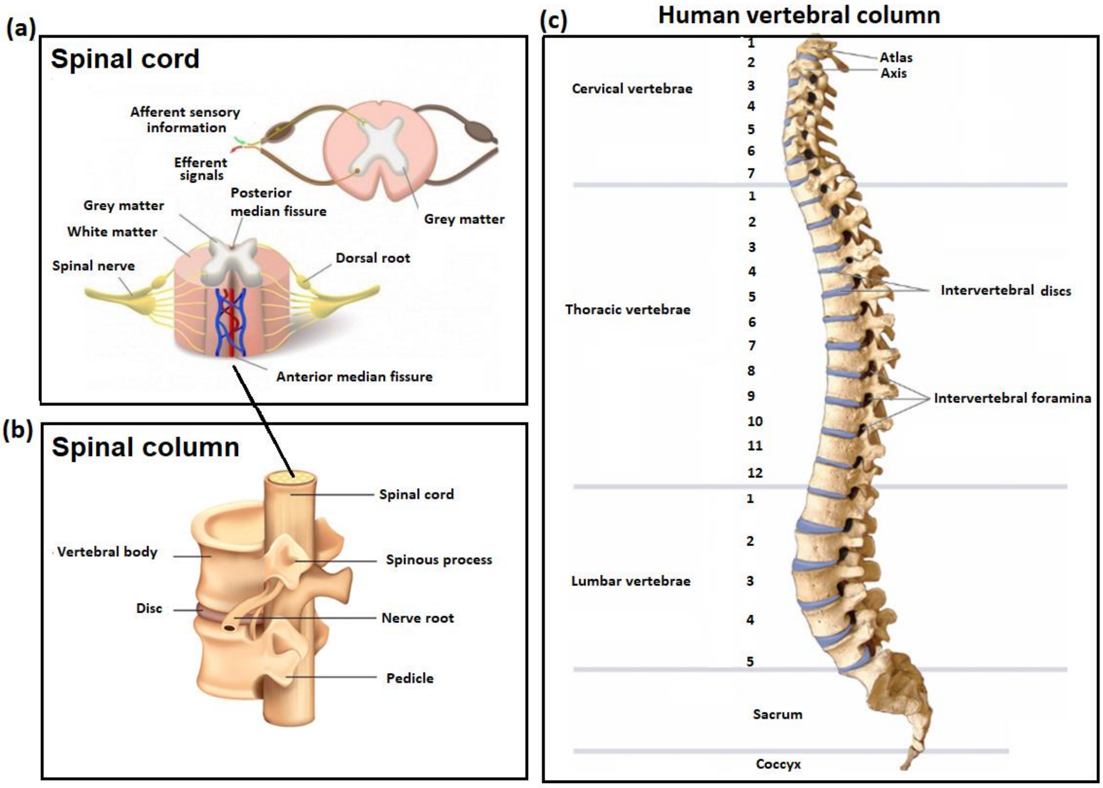

Figure 2.1. Spinal cord anatomy. (a) Spinal cord segments, (b) Spinal column and (c) Human vertebral column [17].

The spinal cord is divided into segments that correspond to specific parts of the body. Its white matter contains three types of tracts: ascending, descending, and commissural. Ascending tracts carry sensory information to the brain, including proprioception, touch, and pain. Descending tracts carry motor information from the brain to the body, controlling movement and posture. Commissural tracts connect the left and right sides of the spinal cord. Each spinal segment has a different combination of these tracts, depending on its location and function.

At C4, the spinal cord has tracts responsible for the voluntary control of the upper extremities, including the shoulder, elbow, wrist, and hand. The tracts present at this level include the corticospinal tract, spinothalamic tract, and dorsal columns. The corticospinal tract is the largest descending motor pathway in the spinal cord, while the spinothalamic tract and dorsal columns are ascending sensory pathways that carry information from the body to the brain.

At T10, the spinal cord has tracts that carry information from the lower limbs and trunk, including the abdomen and back muscles. The tracts present at this level include the spinothalamic tract and dorsal columns. The corticospinal tract does not extend down to this level, as its descending fibers terminate around the cervical and thoracic levels.

Therefore, the main difference between the tracts at C4 and T10 is their location and function. C4 has tracts that are responsible for the voluntary control of the upper extremities, while T10 has tracts that carry sensory information from the lower limbs and trunk.

2.1.2 Types of cells in the CNS

There are two major cell types in the CNS; conducting cells (neurons) and supporting cells (glia). The neurons create the circuitry within the brain and spinal cord. Their axons can range from just a few microns to almost 1 m in length [18]. Glial cells support, feed and protect the neural cells [15].

2.1.2.1 Neuron cells

Every neuron (also called neurones or nerve cells) has a basic structure consisting of three main parts: the cell body (soma), dendrites, and an axon [19] (Figure 2.2). The dendrites and axons are also known as nerve fibers. The cell body is the spherical part of the neuron that contains the nucleus, which plays an essential role in controlling all of the functions of the cell. The soma extends several branches (hair-like) called dendrites, which possess leaf-like structures known as spines. These structures conduct signals to the cell body from other neurons or the environment. Attached to the soma is another long structure known as the axon. The axon conducts the signals away from the cell body. The end-point of each axon branch is known as an axon terminal, which is separated from neighboring neurons by a small gap, a synapse. Axons are surrounded by an insulating myelin sheath, which are created by a wrapping of the cell membrane of oligodendrocytes (CNS) or Schwann cells (PNS) [16].

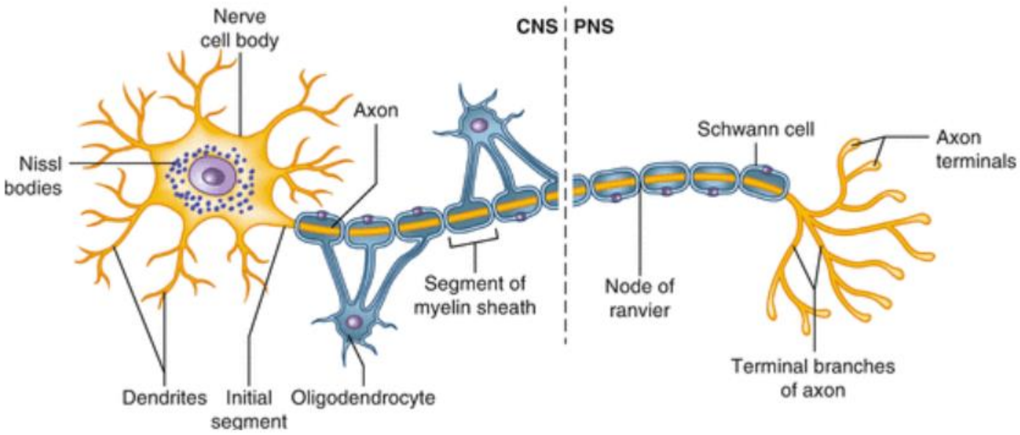

Figure 2.2. Anatomy of a typical neuron, with a myelinated axon, travelling through both the central part (CNS) and peripheral part (PNS) of the nervous system [20].

2.1.2.2 Glial cells

The different types of glial cells in CNS include astrocytes, oligodendrocytes, ependymal and microglial cells. Astrocytes ("star-like cells"), shown in Figure 2.3, make contact with both neurons in the CNS and capillaries [21]. They perform many functions, including the provision of nutrients and other substances to the nervous tissue, regulation of extracellular ion balance, biochemical support of CNS endothelial cells that create a blood-brain barrier, and play a role in the scarring process and recovery of the brain and spinal cord following injuries. An intermediate filament protein expressed in astrocytes cells is Glial fibrillary acidic protein (GFAP), expressed at low levels in the branches of the cytoskeleton. GFAP rapidly increases in response to SCI and is used as a standard marker for assessing astrocyte reactivity.

Astrocytes have been categorized into two general subgroups, protoplasmic and fibrous, which have similar functions but differ in morphology and distribution. Protoplasmic astrocytes are typically present in grey matter and have thick, short, and highly branched processes. Fibrous astrocytes more commonly exist in white matter and have thin, long and less branched processes. Both of these subgroups are in contact with blood vessels; while protoplasmic astrocytes are closely associated with synapses, fibrous astrocytes contact nodes of Ranvier (also known as myelin-sheath gaps) [22]. Oligodendrocytes cells are responsible for the production of the myelin sheath of axons in the CNS [18]. Ependymal (epithelial) support cells form thin sheets that line fluid-filled cavities in the CNS [23]. Some ependymal cells participate in producing cerebrospinal fluid (CSF) that fills these spaces, and other ependymal cells assist in CSF circulation. Microglial cells are the smallest of the glial cells and are located throughout the brain and spinal cord [24]. They are derived from phagocytes, white blood cells that migrate from the blood into the CNS and make up 5-10% of all CNS cells. The microglia enlarge and become phagocytic in regions of inflammation and cell destruction to remove cell debris, waste, and pathogens [25].

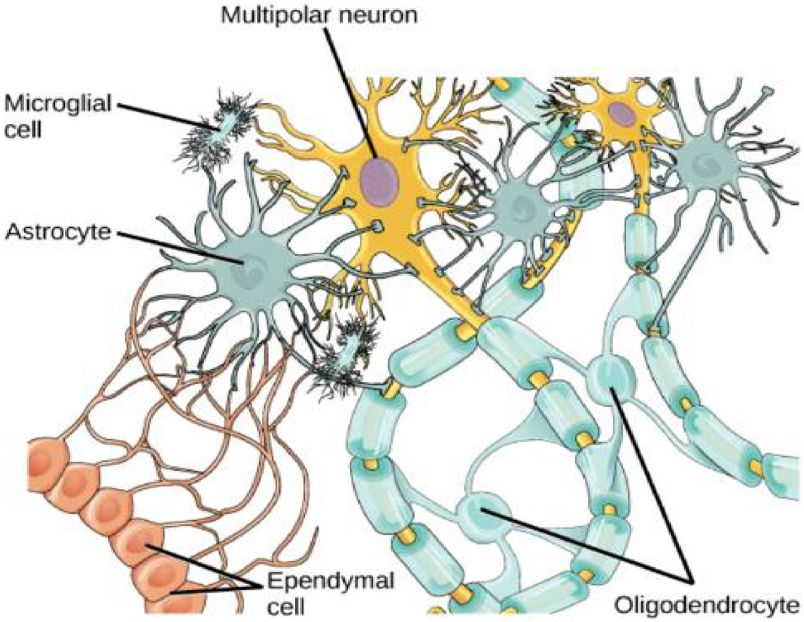

Figure 2.3. Types of glial cells in the CNS [21].

2.2 Spinal cord injury (SCI)

SCI can be divided into traumatic and non-traumatic aetiologies [26, 27]. An external physical impact (e.g. a fall or sports-related injury, etc.) causes traumatic SCIs that damage the spinal cord, whereas an acute or chronic disease process (e.g. a tumour or infection) causes non-traumatic SCI that generates the primary injury. After SCI, messages are blocked from below the point of injury, and the spinal cord can no longer transmit messages between the brain and parts of the body. The site of the injury determines what part of the body is impacted. The extent of the injury (level and type) is shown in Figure 2.4. For example, an injury at C4 causes complete paralysis below the neck, whereas an injury at L6 causes paralysis below the waist.

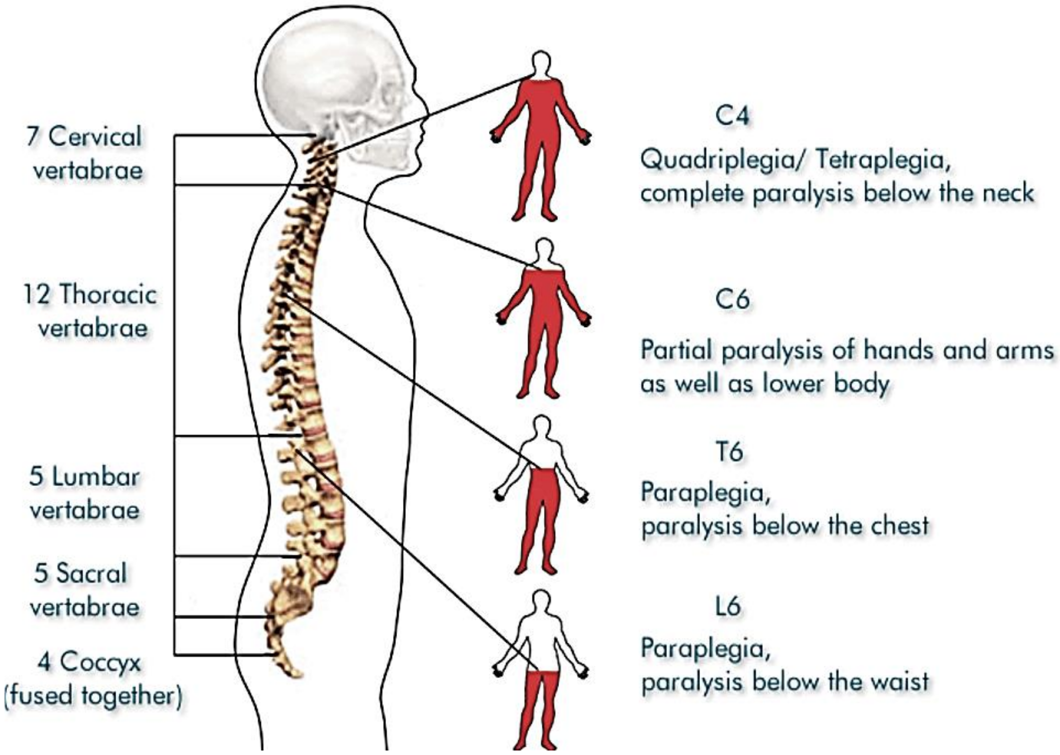

Figure 2.4. SCI according to level and type [28].

2.3 Mechanisms/ Pathophysiology of Traumatic SCI

Traumatic SCI is pathophysiologically classified into several phases; an acute phase (48 hours), a subacute phase (48 hours to 14 days), an intermediate phase (14 days to 6 months), and a chronic phase (more than 6 months) [29] (Figure 2.5). In the acute injury phase, primary injury occurs at the moment of the initial trauma and produces prompt mechanical disruption and/or dislocation of the vertebral column, which results in compression or transection of the spinal cord (Figure 2.5(a)) [29, 30]. The damage results in neuron and oligodendrocyte injury, vasculature disruption, and the compromising of the blood-spinal cord barrier. Consequently, all of these events trigger a sustained secondary injury cascade, causing further damage to the spinal cord and neurological dysfunction. Secondary injury leads to apoptosis and necrosis of neurons and oligodendrocytes, which can cause demyelination and the loss of neural circuits [31].

In the subacute injury phase (48 hours to 14 days after injury), blood supply problems may progress further, which began in the acute injury phase (Figure 2.5(b)) [29]. An interrupted blood supply may lead to glial and neuron cells death, an imbalance of cell homeostasis and inflammatory cellular responses, which cause further injury to the spinal cord. In fact, as glial and neuron cells within the spinal cord die, resulting in inflammation and excitotoxicity, cells release adenosine triphosphate (ATP), DNA and potassium, which can activate microglial cells. Activated microglia contribute to the ongoing apoptosis of neurons and oligodendrocytes cells, and they propagate the inflammatory response within the injury region. Therefore, throughout the acute and subacute phases of SCI multiple cell types die, and inflammation occurs, which produces significantly more damage than the primary injury.

By slowing the damage triggered by the acute and subacute phases, cystic cavities and glial scars are formed at the damaged site, during the intermediate-chronic injury phase (Figure 2.5(c)). Cystic cavities comprise extracellular fluid, connective tissue, and macrophages, and a glial scar forms around the cavity. The cystic cavities merge to become a formidable barrier to directed axonal regrowth and are a poor substrate for cell migration. All the spinal cord injury phases and the key pathological events are detailed in Table 2.1.

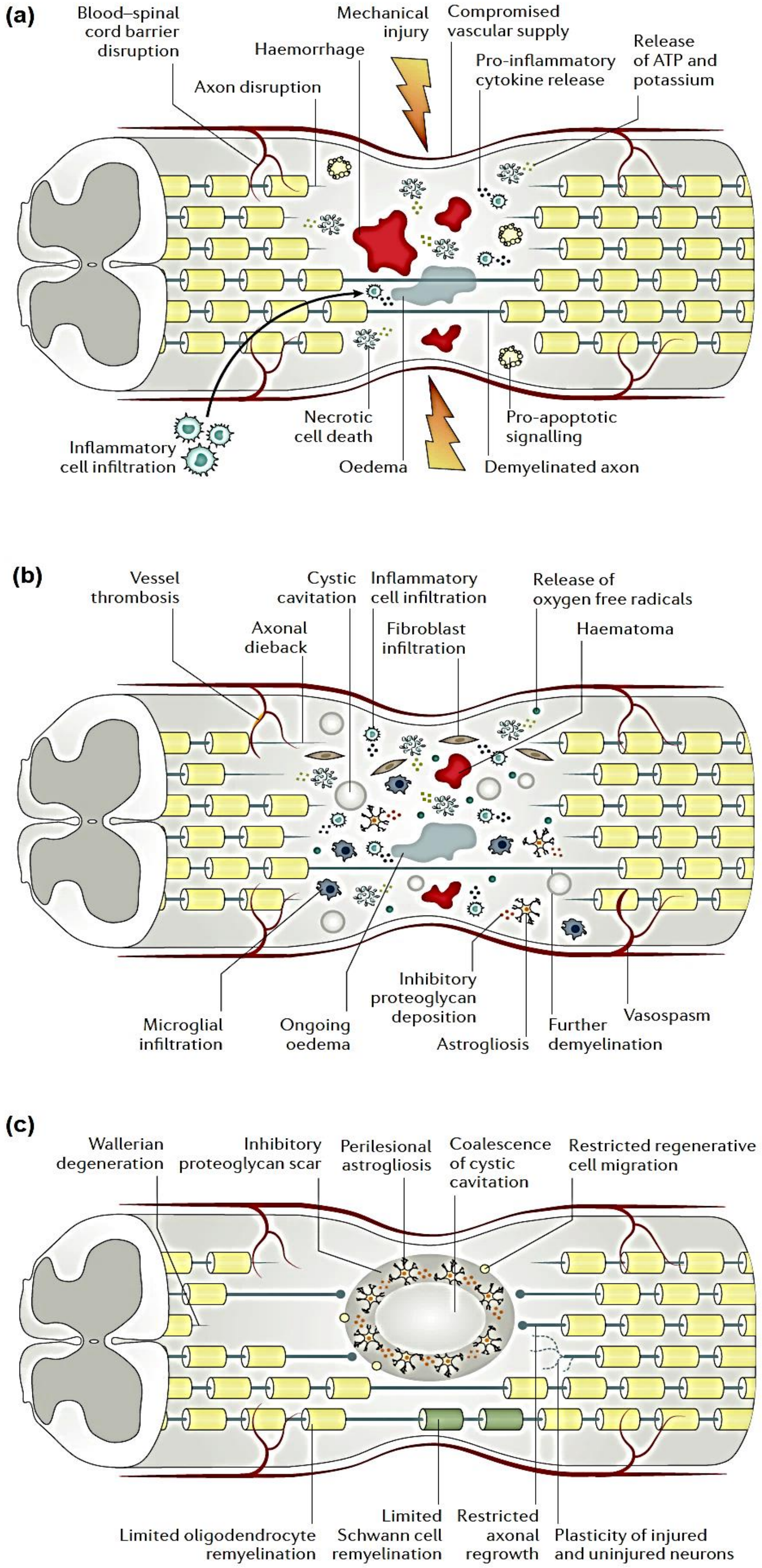

Figure 2.5. Pathophysiology of traumatic spinal cord injury. In (a) acute, (b) subacute and (c) intermediate and chronic phases [32].

Table 2.1. The major pathophysiological phases after spinal cord injuries [33].

Primary phase (within 2 hours)	**Acute phase (within 2 days)**	**Subacute phase (Days to weeks)**	**Intermediate/chronic phase (weeks to months)**
(1) Traumatic cell disability and death (2) Shearing, compression and stretch of axonal (3) Haemorrhage (4) Edema (5) Spinal shock and dysfunction	(1) Vascular disruption (inflammation, edema hemorrhage, BSCB and interruptions) (2) Ischaemia (3) Oxidative stress (4) Excitotoxicity caused by glutamate (5) loss of OLs and Demyelination (6) Inflammation and activation of microglia cells (7) Proliferation of astrocyte cells (8) Swelling of axonal and degeneration	(1) BSCB repair and resolution of haemorrhage and oedema (2) Increasing of activated microglial cells and inflammatory reactions (3) Macrophage infiltration (4) Activation of astrocyte cells and glial scar formation (5) ECM changes (CSPGs, collagen IV, and debris of axonal and myelin) (6) Axonal demyelination	(1) New blood vessel formation (Angiogenesis) (2) Glial scar and Cavity formation (5) Sprouting of uninjured axons (6) Axonal remyelination 4) Formation of syrinx and Cyst

BSCB: blood-spinal cord barrier; OLs: oligodendrocytes; ECM: extracellular matrix; CSPGs: chondroitin sulfate proteoglycans.

2.4 Review of models of spinal cord injury

Before developing new treatments for SCI, it is essential to understand the processes of nerve cell regeneration, neurogenesis, and gliogenesis. The purpose of models of injury is to simplify the cellular response to specific aspects and outcomes of spinal cord injury. These models can be categorized into *in vivo*, *ex-vivo,* and *in vitro* models.

2.4.1 *In vivo* models of SCI

An *in vivo* model of spinal cord injury aims to recapitulate as closely as possible the features of human spinal cord injury. These models differ with respect to the animal used, location of injury infliction and injury mechanism. According to the mechanism of injury, they are categorised into contusion [34], compression [35], distraction [36], dislocation, transection or chemical models. Summary of *in vivo* models and mechanisms of injury are given in Table 2.2. Contusion devices provide a transient, acute injury to the spinal cord. Four devices have been used regularly to generate controlled contusion SCIs in vivo; the Ohio State University (OSU) [37]; the Infinite Horizon (IH) impactor [38]; the Air gun impactor [39]; and the New York University (NYU)/Multicenter Animal Spinal Cord Injury Study (MASCIS) impactor [40]. In many studies, compression devices have been used to compress the cord at specific forces and durations [35, 41]. In some of these models, such as the contusion-compression model, the spinal cord is compressed after acute trauma. Procedures for causing compression-induced SCI include a clip [42], inflation of a balloon [43], a spinal cord strapper (SC strapper) [44] and the use of forceps to induce compression of the spinal cord [41]. In distraction injury models, the spinal cord is stretched by opposing traction forces, whereas it is injured by vertebral displacement during dislocation models. Several models have been used for creating distraction injuries in rats including the Harrington impactor [36], the University of British Columbia (UBC) multi mechanism device [45] and the University of Texas at Arlington (UTA) distractor [46]. Each of these devices attaches to the spine at two different vertebral locations, which are forced apart by an electromagnetic motor. Transection injury models can be complete, in which the entire spinal cord is cut, or partial, in which only a portion of the spinal cord is cut [47]. Complete transaction models provide well-controlled infliction and reproducible injuries; however, injuries of this type happen infrequently in humans, perhaps only as a result of a knife wound. Partial transection injuries provide the benefits of being more clinically relevant and allowing the comparison between damaged and undamaged parts of the spinal cord; however, these models are less reproducible [48]. In addition, chemicals are used in several models of secondary injury cascades that lead to traumatic spinal cord injuries [48, 49]. These chemical models are beneficial for investigating the effect of numerous therapies on specific pathways and molecular mechanisms involved in SCI. However, the accuracy of these models in estimating spinal cord injuries is less than that of other models.

Overall, each animal model has advantages and disadvantages, which are listed in Table 2.2. However, the major difficulty associated with the *in vivo* models is the utilization of large numbers of experimental animals [50]. Additionally, the formation of *in vivo* injury models needs many invasive interventions. There is often a high cost associated with such models and technical equipment for experimental purposes. All of these issues can be decreased by performing experiments *in vitro*. The advantages and disadvantages of the different tools used to create SCI injuries are given in Table 2.2.

Table 2.2. Summary of SCI in vivo models [48].

Model of injury	**Mechanism of injury**	**Advantages**	**Disadvantages**	**Animal model**
MASCIS [40]	Weight-drop contusion	Widely used, validated^1, reproducible,	Procedure learning curve, 'Weight-bounce', imprecise duration of impact	Rodents
Infinite horizon impactor [38]	Force-controlled contusion	Widely used, validated^1, reproducible	Procedure learning curve, clamping technique, No output data	Rodents
OSU [37]	Displacement contusion	Validated^1, reproducible	Procedure learning curve	Rodents
Air-gun impactor [39]	Air-pressure contusion	Less invasive	Not validated, inconsistent severity-based locomotor assessment	Rats
Clip [42]	Compression–contusion	Widely used, simple and easy procedure, limited resources necessary, inexpensive	Velocity of force, force delivered, extent of compression not recorded	Murine, rats
Forceps compression [41]	Compression	Simple, inexpensive, limited resources necessary	Lack of acute injury aspect, inability to record injury parameters	Pig, rat
Balloon compression [43]	Compression–contusion	Inexpensive	Less common, injury parameters not recorded, inconsistent injury	Dogs, rat, rabbit, primates
Spinal cord strapping [44]	Compression–contusion	Less-invasive, circumferential injury	Not validated, inconsistent, injury parameters not recorded	Rat
Harrington distractor [36]	Distraction	Clinical approximation	Not validated, inconsistent and variable injury, complex procedure	Rat
Clamps [51]	Dislocation	Control over the extent of injury, Similarity to human spinal cord injury, Cost-effectiveness	Limited ability to study chronic injuries, Lack of spontaneous recovery, Limited external validity	Rat
UBC device [45]	Contusion–distraction–dislocation	Clinical SCI approximation	Not validated, inconsistent and variable injury, complex procedure, no locomotor assessment	Rat
UTA distractor [46]	Distraction	Bidirectional distraction	Not validated, inconsistent and variable injury, complex procedure, no locomotor assessment	Rat
Complete transection [48]	Transection	Easy to perform, consistent, reliable, large animal models	Uncommon clinical SCI type	Rodents, cats, dogs, primates
Partial transection [48]	Transection	Large animal models, contralateral side comparison	Inconsistent reproducibility	Rodents, cats, dogs, primates

Chemical models [49]	Reagents	Inexpensive, simple procedure, mechanism specific	Inconsistent reproducibility	Rodents
Electromagnetic injury model [52]	Contusion	Consistency and reproducibility, Non-invasive, Control over injury location	Lack of similarity to human spinal cord injury, Limited external validity, Limited ability to study chronic injuries	Rats

Multicenter Animal Spinal Cord Injury Study (MASCIS) impactor; Ohio State University (OSU); University of British Columbia (UBC); University of Texas at Arlington (UTA).

1 "validated" means that impactor has been tested and confirmed to produce a consistent and accurate injury in animal models.

2.4.2 *Ex vivo* models of SCI

Ex vivo organotypic slice models of SCI require the extraction of the spinal cord from the animal. These models are beneficial due to the fact that they maintain the *in vivo* 3D structure of the tissue, the spatial orientation of heterogeneous cell types, tissue architecture and neuronal connections at a synaptic level. The results of these experiments are useful in analyzing extracellular matrix (ECM) molecules and cell-cell interactions, including neuronal networks, as well as in evaluating the efficacy of treatments [53]. For example, Ravikumar et al. utilized the organotypic method to study the mechanism of microglia-mediated neurotoxicity for neurodegeneration [54]. In addition, in another work, Sypecka et al. established a co-culture technique of longitudinal spinal cord slices with stem/progenitor cells for studying cell therapy with the aim of spinal cord regeneration [55].

However, the organotypic slice model has limitations, such as the absence of cerebrospinal fluid (CSF) and denticulate ligament support. In addition, some or all of the meningeal layers are often removed. These features affect the mechanical behavior of the tissue [56]. In Oakland et al., the tangent modulus of the spinal cord increased by 33 % following a time gap of 24 hours between mechanical testing and tissue dissection [57]. Both mechanical testing and cellular experiments must take into account the rapid degradation of CNS tissue post-mortem [58, 59]. In addition, the creation of the slice using a scalpel creates an injury response in the tissue, making these quite limited for investigating responses to injury.

2.4.3 *In vitro* two-dimensional (2D) models of SCI

In vitro SCI models can be classified into two-dimensional (2D) and three-dimensional (3D) CNS cell cultures. Models of the glial scar have been developed by mechanically scraping astrocyte cultures in 2D to produce a 'wound', which was first investigated in 1993 by Yu et al. [60]. These authors cultured primary rat astrocytes on culture dishes to confluency, then scratched a grid-like pattern across the cells using a sterile plastic pipette tip [60]. Despite the fact that this simple method uses an unrealistic injury mechanism, which has little clinical relevance, proliferation, migration, and activation of astrocytes was observed [60]. Polikov et al. [61] also demonstrated that primary glial cells were grown on a 2D substrate exhibit many hallmarks of glial scar formation following mechanical insult. It was observed that GFAP expression increased in astrocytes, and microglia were found near a microwire device located on top of the cell layer or a scrape wound. In another study, P_1 rat spinal cord cells grown in a monolayer were mechanically scratched with a pipette tip to imitate a SCI in an experimental model [62].

In other research [63], astrocytes were aligned through an electrical field in 2D cultures. In this study, electrically aligned astrocytic processes were permissive to neurite growth and guided the direction of neurite outgrowth. Although these 2D culture models have revealed vital information about the reactivity of astrocytes and their effects on neuronal growth (reviewed by [64]), there are restrictions to their effectiveness for investigating the process of reactive gliosis. The high reactivity of the astrocytes in 2D cultures makes it challenging to monitor additional activation caused by the introduction of an injury.

2.4.4 In *vitro* three-dimensional (3D) models of SCI

Three-dimensional *in vitro* SCI models have been developed in an effort to mimic conditions more closely *in vivo*. A 3D microenvironment allows cells to adopt 3D morphologies and receive biochemical and biomechanical cues. However, *in vitro* SCI models require using biomaterials with a high level of similarity to the ECM to enhance neural cellular functions. Biocompatibility, geometry, composition, and mechanical properties of biomaterials are the most critical factors for neuron regeneration in SCI models, which many researchers have investigated [65]. Hydrogels have recently been widely established as biomaterials with 3D topological structures to investigate the SCI models [66, 67]. Hydrogel-based biomaterials are typically soft and elastic due to their thermodynamic compatibility with water.

Fabricating 3D cell-laden hydrogels within a conventional multi-well plate is achievable [68]. However, this method requires a large amount of reagent volume to prevent evaporation during polymerization, which increases costs, makes drug penetration variable and complicates imaging [69]. The other limitation imposed by using a well plate is meniscus formation at the surface of the hydrogel [10], which makes imaging difficult as the cells are in many different focal planes. Also, the tension in the meniscus area leads to the cellular reactivity of astrocytes [70]. Other methods such as a fibre-based alignment of collagen gels is of particular interest since the microscale fibrillary structure of collagen deeply influences tissue mechanical properties and cell organization [71]. In addition, it has been shown that the alignment of collagen fibres directs neuronal growth, including in human stem cell-derived neurons [72]. Phillips *et al*. [73] demonstrated the use of 3D astrocyte-seeded collagen gel culture systems to investigate the effect of astrocyte alignment on neuronal growth. This system created tethered collagen gels within a collagen mould with mesh tethering bars at the ends, in which astrocytes were cultured in contracted aligned gels (Figure 2.6 (A-C)). Neurite growth in the aligned regions of the astrocyte-seeded gels was greater compared to the unaligned delta zones after three days of incubation (Figure 2.6 (D)). In general, in unaligned areas, an optimal direction does not exist and, accordingly, the neurite moves in random directions while continuously sampling the surrounding region. This constant sampling process involves the continuous assembly and disassembly of cytoskeletal proteins, which need both time and energy [63]. Although this is a gold standard model to study neuron survival and axon regeneration, it has some limitations such as using a very large volume of gel and a high number of cells, high cost and the inability to position cells.

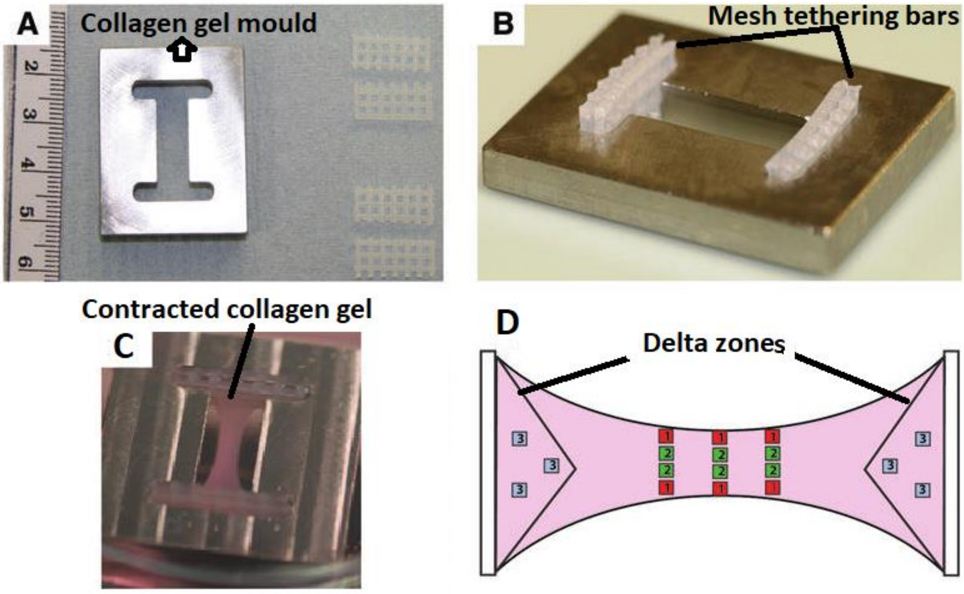

Figure 2.6. Three-dimensional aligned collagen gel preparation and data capture. (A) Collagen gel mould, (B) Collagen mould with tethering bars for collagen fibre alignment (C) Contracted collagen hydrogel after 72 h. (D) Data was collected from an aligned area (2) and a nonaligned area (3) [73].

2.5 Fabrication of 3D *in vitro* hydrogel-based SCI models by Bioprinting

3D bioprinting has gathered significant attention in tissue engineering to fabricate tunable 3D hydrogels. This technique has been utilized for printing cell-free [74] or cell-laden [75] hydrogels. Over the past decade, a variety of strategies for 3D bioprinting of the nervous system, such as stereolithography (SLA), inkjet bioprinting, laser-assisted bioprinting, extrusion-based bioprinting, electrospinning-based bioprinting (EBB) have been developed (Figure 2.7) [76]. Each of these techniques has unique advantages and limitations (Table 2.3) [76]. Lee et al. [77] used electrospinning combined with stereolithography for the fabrication of a 3D biomimetic neural scaffold. The researchers created a bioink using Polycaprolactone (PCL) and gelatin that demonstrated improved adhesion, proliferation, and survival of neural cells. PCL/gelatin fibres greatly increased neurite length of primary cortical neurons and directed neurite extension along their fibres, as shown by confocal microscopy. However, electrospinning has some limitations, including poor cell penetration, weak mechanical properties, high cost, and low throughput.

Among 3D fabrication methods, extrusion-based bioprinting has thus far been one of the most widely adopted forms of bioprinting, due to its relative simplicity in instrumentation. These systems can continuously extrude bioinks without interruptions by either air pressure, piston or screw systems. The air pressure system allows the depositing of bioinks of various types and viscosities by modulating the pressure and valve-gating time. The setup with piston-driven deposition provides extended control over the flow of the bioink, while screw-driven systems enable reasonable spatial control and help deposit highly viscous bioinks. However, bioprinter parameters such as extrusion pressure and printing speed can influence printability, which need to be optimized based on the desired construction. Chen et al. [78] developed collagen/heparin sulfate scaffolds with channels separated by ~ 400 μm using an extrusion bioprinter to simulate the linear structure of the spinal cord. Improvements in motor functions of neural stem cells (NSCs) loaded onto these biological scaffolds were observed after SCI.

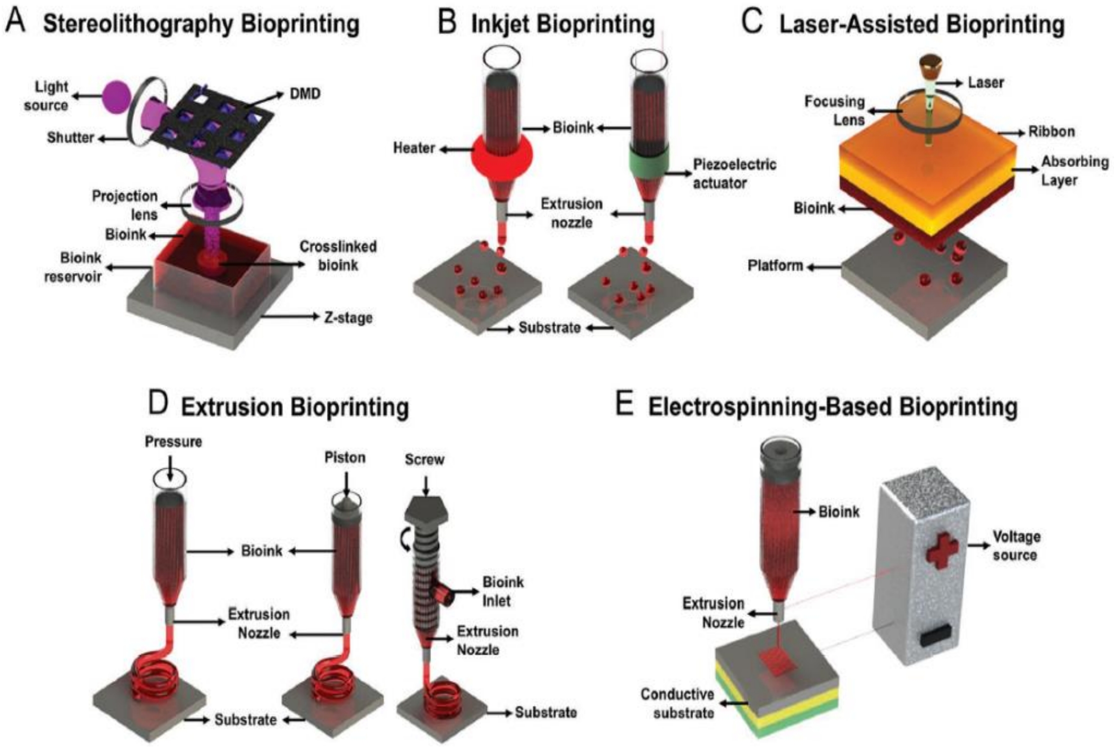

Figure 2.7. Schematic images of the different 3D bioprinting strategies. (A) Stereolithography-based bioprinting is based on a digital micromirror device (DMD). (B) Thermal (left) or piezoelectric (right) inkjet bioprinting. (C) Laser-assisted bioprinting. (D) Extrusion-based bioprinting systems. From left to right: pressure, piston, and screw-based. (E) Electrospinning-based bioprinting [76].

Table 2.3. Summary of advantages and disadvantages of different bioprinting techniques [76, 79].

3D Bioprinting Technique	Advantages	Disadvantages
Stereolithography	• Simultaneous crosslinking of the entire 2D layer avoids need for X-Y movement • High cell viability (>85%) • High variety of printable bioinks • High resolution of bioprinting (=1 µm) • No limit on the cell viscosity value • Possible to create highly complex geometrical features	• Crosslinking requires transparent and photosensitive bioinks, limiting choice of additives and cell density (10^8 cells mL^{-1}) • Comparatively complex system • Bioink must be photo-crosslinkable • Damage to cells during photo curing
Inkjet bioprinting	• Simple bioprinting method • Low cost • Applicability of multimaterial bioprinting, high resolution (=30 µm) • High cell viability (80-90%) • Fast printing speed	• Limited to low cell density ($<10^6$ cells mL^{-1}) • Limited to bioinks with viscosity of 3.5-12 mPa s
Laser-assisted bioprinting	• High cell viability (>95%) • Variety of printable bioinks with viscosity of 1-300 mPa s • Does not produce shear force at the nozzle-head.	• Limited to low cell density ($<10^6$ cells mL^{-1}) • Complex system • Comparatively high costs • Long print times
Extrusion-based bioprinting	• Printability of highly viscous bioinks ($30\text{-}6 \times 10^7$ mPa s) • Printability of high cell densities (including cell spheroids) • High cell viability (>90%) • Applicability of multimaterial bioprinting • Comparatively simple bioprinting process	• Relatively low printing speed • Low-to-medium resolution highly dependent on setup Moderate cell viability (40-80%) dependent on setup
Electrospinning-based bioprinting	• High resolution (<1 µm) • Optimal for the fabrication of scaffolds	• Not possible to directly bioprint cell-laden constructs • Complex system • High costs

2.6 The role of hydrogel composition in regulating CNS cell behaviour

Hydrogel biomaterials can be classified into natural, synthetic and semi-synthetic, depending on their polymer and chemical composition [80]. Natural polymers possess benefits compared to synthetic polymers, since these polymers contain the macromolecules that cells interact with *in vivo* (e.g. cell adhesion molecules). Natural hydrogel-based scaffolds applied in SCI research are shown in Table 2.4. The most appropriate are collagen, polysaccharides (agarose, alginate, cellulose, gellan gum, scleroglucan, and xyloglucan) and hyaluronic acid (HA). Studies have shown that hydrogels, such as alginate [81] or agarose [82], can support axonal regeneration. In addition, collagen is a primary protein found in the ECM of different tissues in mammals and comprises cell adhesion sites for cellular attachment and is used regularly.

Synthetic polymers have the potential to be designed based on their physical, chemical and mechanical properties to suit the favoured application [83]. Numerous synthetic hydrogels, such as poly (N-2-(hydroxypropyl) methacrylamide) (pHPMA), poly (hydroxyethyl methacrylate) (pHEMA), and polyethylene glycol (PEG), have been utilized widely in neural applications. Among them, PEG is a low-toxic polymer and biologically inert, which is reported to repair and protect cells following spinal cord injury [84]. Details of synthetic polymers used in SCI are presented in Table 2.5.

Table 2.4. Natural hydrogel-based scaffolds applied in SCI research [67].

Material	Description	Acronym	Application in SCI
Agarose	Polysaccharide		Cell growth matrix [85] Encapsulation and delivery of neurotrophic factors [86] Controlled chondroitinase delivery [87] Support for nanoparticle delivery [85, 86] Brain-derived neurotrophic factor (BDNF) controlled delivery [88, 89] Linear guidance (freeze-dried) [82, 90] Cell encapsulation for growth matrix [91]
	Co-methylcellulose	Agarose/MC	Nerve guidance [92]
Alginate	Polysaccharide		Anisotropic scaffold for axonal regrowth [81] Neural stem cell growth matrix [93-95] Embryonic stem cell growth matrix [96]
Cellulose	Polysaccharide		Mesenchymal stem cell growth matrix [97]
Chitosan	Polysaccharide		Scaffold for cell adhesion and growth with polylysine [98] Scaffold for neurite regrowth with hyaluronic acid [99]
Collagen	Polypeptide		Polymeric channels [100] Filament bridges as growth substances [101] Cell growth matrix [102, 103]
Fibrin	Linked proteins		Neural stem cell growth matrix [104]
Gelatin	Hydrolyzed collagen		Mesenchymal stem cell growth matrix [105]
Gellan gum	Polysaccharide		Tubular, porous scaffold for axonal regrowth [106]
Hyaluronic acid	Polysaccharide	HA	Controlled delivery of neurotrophic factors [107] Scaffold for neurite regrowth [99, 108] Controlled peptide delivery [109-111]
	Co-polylysine		Nogo 66 receptor antibody delivery system [112, 113]
	Co-methylcellulose	HAMC	Intrathecal drug and growth factor delivery [114-119] Neural stem cell carrier for cell therapies [120]
	Co-collagen		Cell growth matrix [121]
Matrigel	Laminin, collagen IV, heparin		Scaffold supporting cell adhesion and growth [122] Neural stem cell carrier for cell therapies [94]
Scleroglucan	Polysaccharide		Controlled drug delivery [123]
Xyloglucan	Polysaccharide		Scaffold supporting cell adhesion and growth [124, 125]

Methylcellulose (MC); Hyaluronic acid (HA); Hyaluronic acid methylcellulose (HAMC);

Table 2.5. Synthetic hydrogel-based scaffolds applied in SCI research [67].

Material	Description	Acronym	Application in SCI
Carbopol	Branched poly(acrylic acid)		Controlled drug delivery with cyclodextrin [126, 127]
Lysine-leucine polyacrylamide	co-polypeptide	DCH	Tunable vehicles for growth factor delivery [128] Scaffold for neurite outgrowth [129]
Polyalkylimide	acrylates		Scaffold supporting cell adhesion and growth [130]
Poly-ε-caprolactone	polyester	PCL	Nanofiber for axonal growth orientation [131]
Poly(ethylene glycol)	polyether	PEG	3D cell growth matrix [132-136] Microcapsules for cell growth [137] Controlled drug delivery with cyclodextrin [138] Microvascular networks for cell growth with PLGA [139-141] Controlled delivery of methylprednisolone [142]
		PLA-b-PEG-b-PLA	Delivery of neurotrophins [143-146]
		PNIPAA-PEG	Cell adhesion and neurotrophin release [147]
Polyethylene oxide		PEO	Injectable scaffold for drug delivery with cyclodextrin [148]
Poly(hydroxethyl methacrylate)	Polyester	PHEMA	Charged modified scaffold as bridges for axonal growth [149, 150] Guidance channels [150, 151] Fiber templated scaffold [152] Bone marrow stem cell carrier for cell therapies [153]
	Co-methylmetahcrylate	PHEMA-MMA	Reinforced guidance channels for nerve regrowth [154-156] Controlled drug delivery [157]
Poly(hydroxypropyl methacrylate)	Polyester	PHPMA	Mesenchymal stem cell growth matrix [158]
Poly(N-isopropylacrylamide)-copolyvinylpyrrolidone	Copolymer	PNIPAA-PVP	Scaffold for controlled drug delivery [159]
Pluronic	Polypropylene oxide + ethylene oxide	PF127	Scaffold supporting cell adhesion and growth [122, 160]
PuraMatrix	Oligopeptides		Scaffold supporting cell adhesion and growth [122]
Polyvynil alcohol	Acetate	PVA	Scaffold for controlled drug delivery [161]

Diblock copolypeptide hydrogels (DCH); poly(ε-caprolactone) (PCL); Poly(ethylene glycol) (PEG); Polyethylene oxide (PEO); poly(hydroxyethyl methacrylate) (PHEMA); Poly(N-isopropylacrylamide) (PNIPAA); methylmetahcrylate (MMA); Poly(hydroxypropyl methacrylate) (PHPMA); polyvinylpyrrolidone (PVP); Pluronic-F127 (PF127); Polyvynil alcohol (PVA).

The advantages of the biocompatibility of natural hydrogels and the adjustable properties of synthetic hydrogels led to the hypothesis that the utilization of hybrid hydrogels would provide a robust platform for assessing neural cell physiology *in vitro*. The development of hybrid hydrogels is an approach used for SCI repair since the exploration of the properties of different materials can be used to promote SCI recovery [106, 162]. Hybrid hydrogels could be the result of a block copolymerization between synthetic and natural macromers, or just an interpolymer complex bonded by physical interactions. The list of the composite hydrogels used in neural applications is presented in Table 2.6.

Gelatin methacryloyl (GelMA) hydrogels are semisynthetic polymers which extremely promising candidates for *in vitro* SCI models [163, 164]. GelMA hydrogel possesses a prolonged molecular chain through photocrosslinking, which enables the scaffold to hold a high water content and exhibit lower mechanical properties. In addition to arginine-glycine-aspartic acid (RGD) peptides, gelatin contains degradable motifs by matrix metalloproteinases (MMPs). The former is beneficial for cellular growth and attachment, and the latter controls cellular enzymatic degradation [165]. In addition, the mechanical properties of GelMA can be altered by adjusting the hydrogel concentration, degree of cross-linking, and gel time, thereby allowing simulation of the properties of the spinal cord [18]. Furthermore, the transparent nature of cross-linked GelMA allows for easy observation of cellular behaviour encapsulated within or seeded onto the hydrogel of various concentrations.

Table 2.6. Synthetic-Natural composite of hydrogel-based scaffolds applied in SCI research.

Material	Description	Acronym	Application in SCI
Carbopol + Agarose	Copolymer	AC	3D mesenchymal stem cell growth matrix [166], Scaffold for controlled drug delivery [167]
Carbopol + Chitosan	Interpolymer complex	IPC	Multiple drug delivery [168]
Methacrylamide + Chitosan	Cross-linked polymer	MC	Cell adhesion and neurite penetration [169, 170], Neural stem cell growth matrix [171]
Polyglycolic acid + Chitosan	Interpolymer complex	Chitosan/PGA	Bridge for neurite regrowth [172]
Poly(ethylene glycol) + hyaluronan	Interpolymer complex	HA-DTPH-PEGDA	3D growth matrix [173]
Poly(ethylene glycol)/Polyacrylic acid/agarose	Layer	PEG/PAA/agarose	Multilayer scaffold for BDNF controlled drug delivery [174]
Poly(ethylene glycol) + Polylysine	Copolymer	PEG/PLL	Cell growth matrix [175]
Poly(ethylene glycol) + Polypeptides	Copolymer	PEG/peptide	3D growth matrix [176]
Polylactide-co-glycolic acid + dex-lactate	Interpolymer complex	DP,DS	Controlled protein release [177]
Tetronic + lactide + heparin	Copolymer	TL	Bridge, with antiinflammatory agents, for axonal regeneration [178]
Gelatin+ methacrylate	photo-cross-linkable hydrogel	GelMA	3D matrix for neurite outgrowth [179], modified the reactive astrocyte responses [180]

Agarose Carbopol (AC); Carbopol interpolymer complex (IPC); Methacrylamide Chitosan (MC); poly(ethylene glycol) diacrylate (PEGDA); Polyglycolic acid (PGA); Poly(acrylic acid) (PAA); Poly-L-lysine (PLL); Tetronic-oligolactide (TL); Gelatinmethacrylate (GelMA)

Recently, several studies focusing on *in vitro* SCI models using 3D bioprinted GelMA hydrogels have been published [8, 179, 181]. *In vitro* models often use chemical injury or injury caused by a scalpel, rather than a mechanically applied injury. For example, researchers have constructed a polyethylene glycol–gelatin methacrylate (PEG–GelMA) hydrogel scaffold to create a complex CNS structure for regenerative medicine applications in the spinal cord [180]. However, the current models do not recapitulate the mechanical injury in humans very closely and therefore it is difficult to fully investigate and understand the complex cellular responses to injury that lead to the secondary biological injury cascade. A group of researchers has constructed a GelMA hydrogel scaffold for SCI scenarios [182] to assess the *in vivo* performance of the structure in rats impaired with hindlimb dysfunction as a result of spinal cord injury. Immunohistological evaluation revealed the long-term survival of neural stem cells, as they were observed in the GelMA scaffold 12 weeks after injury (Figure 2.8). Chitosan-methacrylamide, Gelatin-methacrylamide (GelMA) and PEG-polylysine hydrogels have been assessed with neural cells [169, 171, 183].

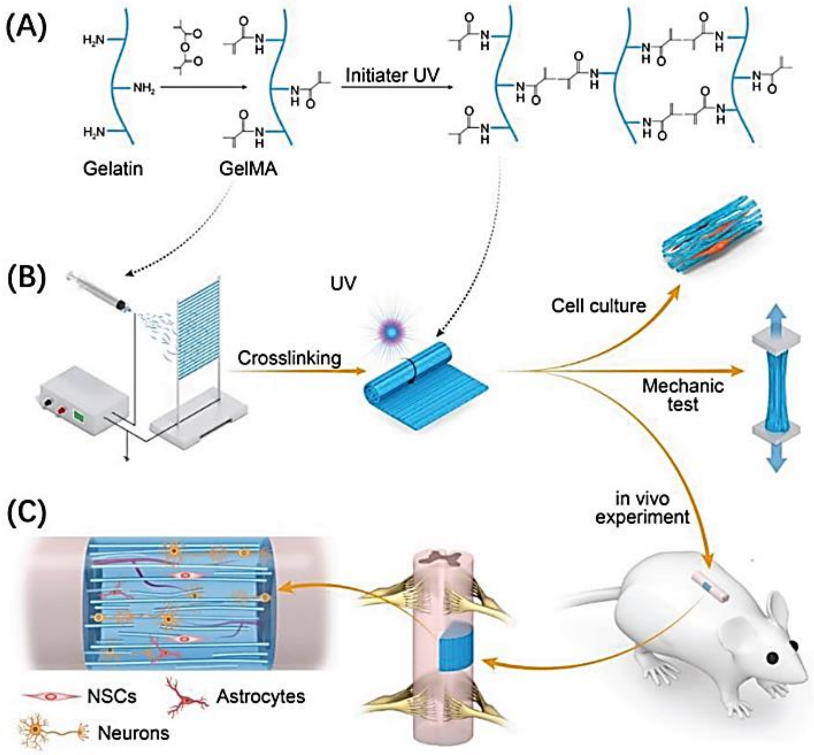

Figure 2.8. The fabricated process of GelMA hydrogel fibrous scaffold to repair SCI. (A) indicating chemical modification and crosslinking of GelMA hydrogels, (B) demonstrating the electrospinning process followed by characterization, and (C) showing the effect of *in vivo* neuron regenerative in a scaffold [182].

2.7 The role of hydrogel stiffness in regulating CNS cell behavior

Depending on the stiffness of the matrix, different types of CNS cells behave differently. It is difficult to establish what constitutes a 'stiff' or a 'soft' matrix stiffness in the literature. Here, we discuss the role of matrix stiffness in regulating the behavior of neurons and astrocytes cells in the CNS.

2.7.1 The role of hydrogel stiffness in regulating astrocyte cell behavior

Astrocytes respond to SCI in various ways through astrogliosis, a proliferation of the astrocytes as a result of trauma, infection, and neurodegenerative diseases [184, 185]. Matrix stiffness can have an effect on astrocyte reactivity [9], morphology [186], adhesion [187], traction forces [188], response to excitotoxicity [189] and intermediate filament expression in astrogliosis [186, 188]. Wilson *et al.* [186] isolated primary astrocytes from rat pups and cultured the cells on PLL coated Polydimethylsiloxane (PDMS) substrates to investigate if stiffness variations could create an astrogliosis-like cellular morphology. It was observed that after 72 h, primary astrocytes exhibited smaller and rounded morphology on 200 Pa (soft) substrates, while cells showed larger and elongated morphology on 8000 Pa (stiff) substrates. Primary human fetal-derived astrocytes that were cultured in hydrogels composed of collagen, hyaluronic acid (HA), and matrigel displayed the lowest levels of GFAP expression for gel stiffnesses of 1000 - 1500 Pa [188]. Also, it was demonstrated that the mechanical properties of scaffolds could significantly influence the differentiation of neural progenitor cells (NPCs). In [190], neurons and astrocytes cells were cultured in 3D hyaluronic acid hydrogels with tunable stiffness (1.5-7 kPa) coated with polylysine. The results showed differentiation of neural progenitor cells (NPCs) into astrocytes occurred at higher stiffnesses (7 kPa), and into neurons at lower stiffnesses (1.5 kPa) [190].

Stiffness of the matrix also affects the resistance of astrocytes to excitotoxic neuronal damage since one astrocyte function is to clear extracellular glutamate [189, 191]. Georges *et al.* [189] examined the survival of spinal cord neurons on polyacrylamide gels of different stiffnesses. The neurotoxic effect of glutamate (500 µM) on neurons cultured on stiff gels (27 kPa), where astrocytes were present, was strongly attenuated compared with that observed on soft gels (300 pa), where there was a relatively low number of astrocytes.

2.7.2 The role of hydrogel stiffness in regulating neuronal cell behavior

Recent studies have shown the importance of cell-substrate interactions on neuron outgrowth, where Young’s modulus of the matrix plays a crucial role in the neurite length, migration, proliferation, and morphology of neurons [192]. Researchers have examined the effects of matrix stiffness on neurite outgrowth using a variety of biomaterials. Regardless of the material, softer matrices result in longer neurite outgrowth across most studies. For example, cell proliferation and differentiation of neural stem cells (NSC) were modulated by the stiffness of a photocrosslinkable methacrylamide chitosan (MAC) hydrogel [171]. NSPCs proliferated on MAC substrates < 10 kPa and exhibited maximal proliferation on 3.5 kPa substrates. Here, neuronal differentiation was favored on the softest surfaces (<1 kPa) and oligodendrocyte differentiation was favored on stiffer scaffolds (>7 kPa). Also, Willits *et al.* [193] revealed how the stiffness of collagen gels modified neurite extension. Maximum neurite extension was observed in softer gels over a range of concentrations (0.6–0.8 mg/mL). In another study, mouse spinal cord primary neuronal cells were grown on protein laminated polyacrylamide gels with different elastic moduli ranging from 50 to 550 Pa for several weeks. It was observed that the neurons grown on softer substrates formed more than three times as many branches as those grown on stiffer gels [194].

Although many studies have shown that neurons grown on softer substrates formed more neurites or longer neurites than those grown on stiffer gels, the influence of substrate stiffness on the neurite length was found to be more complicated. In a recent study led by Wu et al. [195], to culture representative neurons on GelMA hydrogel substrates, PC12 cell lines were selected from a rat pheochromocytoma. Hydrogel substrates of various stiffnesses (3-180 kPa) were prepared by adjusting GelMA concentrations. According to their findings, GelMA hydrogel stiffness influences neuronal outgrowth, cell viability, adhesion, spreading, and average neurite length in neurons. Results showed that GelMA hydrogel with 5% (w/v) concentration exhibited the greatest cell attachment, while 10% (w/v) concentration GelMA hydrogel (34.9 kPa) exhibited the most extended neurite length of PC12 cells. Therefore, PC12 cells with intermediate substrate stiffness exhibited the longest neurite lengths. Previous studies also reported a similar tendency. Koch *et al.* [196] cultured dorsal root ganglion (DRG) neurons on polyacrylamide substrates with a stiffness range from 150 to 5000 Pa. DRG neurons displayed maximal neurite lengths on a substrate with 1000 Pa stiffness. The elongation of neurite length is effectively regulated by growth cones [197]. By sensing substrate stiffness, growth cones interact with myosin polymerized at their terminal to form retrograde fibrillar actin flow (F-Actin). Franze *et al.* [198] explained couplings between F-actin flow and substrate as focal adhesions (FA), and the substrate stiffness can influence FA by modifying stretch-activated ion channels, which eventually affects protrusion elongation. A summary of studies investigating the role of matrix stiffness on neural cell behaviour are given in Table 2.7.

Table 2.7: An overview of studies investigating the effects of matrix stiffness on neural cell behavior [10].

Hydrogel material	Soft Hydrogel (Pa)	Stiff Hydrogel (Pa)	Reference	The Influence of hydrogel stiffness on Neuronal Cells
Collagen	2.2	17	[193]	Dorsal root ganglia (DRG) neurite outgrowth was maximal at lower gel concentrations.
Collagen with fibronectin	1.13	28.27	[199]	Fibronectin inhibited neurite outgrowth in low concentration collagen gels and promoted growth in high concentration collagen gels.
Type I collagen (Col) and hyaluronic acid (HA)	1,000	10,000	[200]	Stiffness of 1 kPa promoted neuronal differentiation and a stiffness of 10 kPa promoted glial differentiation.
Fibrin (human)	2,500	80,000	[201]	When the stiffness of the gel was increased, the neurites of rat dorsal root ganglion (DRG) became longer and more branched.
Fibrin (salmon)	45	125	[202]	The DRG neurons grown in higher stiffness of salmon fibrin gels exhibited significantly longer neurite lengths than those grown in lower salmon fibrin gels.
Alginate	640	20,800	[203]	Soft hydrogels made of alginate were capable of promoting fast and plentiful growth of rat neuron neurites.
Agarose	5	130	[204]	The speed at which neurites extended was negatively associated with the stiffness of the agarose gels.
PEG with fibronectin (FN)	54	978	[199]	Higher concentrations of FN were found to promote greater neurite outgrowth, while increasing PEG stiffness hindered neurite growth.
PEGDA with RGD	75	400,000	[205]	Neurite growth was improved in PEGDA hydrogels incorporated with RGD, particularly in materials with lower stiffness.
PAM	500	5,500	[194]	On softer substrates, primary spinal cord neurones showed the greatest density of branching.
PAM	1,500	300,00	[206]	Soft substrates (1.5 kPa) led to elongated Schwann cells (SCs) with more process extensions, while rigid substrates (30 kPa) resulted in polygonal-shaped SCs.
PAM	300	47,000	[189]	On gels with a stiffness of 47 kPa, there was a significant decrease in the number of neurites compared to gels with a stiffness of 300 Pa.
PAM with DNA cross-links	6,600	29,800	[129]	The use of DNA in the PAM hydrogel was found to modulate neurite growth, where softer hydrogels promoted longer and more branched neurites, while stiffer

				hydrogels resulted in shorter and less branched neurites.
PAM conjugated to fibronectin	10	100,000	[207]	PC12 neurons displayed short and unbranched neurites on soft substrates, whereas longer and more branched neurites were observed on stiffer substrates.
Polydimethyl siloxane	200	8000	[186]	Soft substrates led to a subdued phenotype, while stiff substrates led to astrogliosis-like morphology.
Polydimethylsiloxane	5,000	500,000	[208]	Stiffer substrates promoted the formation of synaptic vesicles and enhanced the electrophysiological activity of neuronal networks

Polyacrylamide (PAM), Polyethylene gylcol (PEG), Polyethylene glycol diacrylate (PEGDA), Arginylglycylaspartic acid (RGD)

2.8 Techniques for mechanical characterization of cells and hydrogels

Accurate mechanical characterization of cells and their microenvironment is important for understanding the influence of mechanical properties on cells themselves. The most widely used techniques for biomechanical property measurements of cells include atomic force microscopy (AFM) [209, 210], micropipette aspiration [211], magnetic twisting cytometry [212], optical stretchers [213, 214], microfluidic deformability [215-217], and microrheology [218] (Figure 2.9). These techniques are used to measure global (such as AFM, microrheology and magnetic twisting cytometry) or local mechanical (such as micropipette aspiration, optical stretchers and microfluidic deformability) properties of cells.

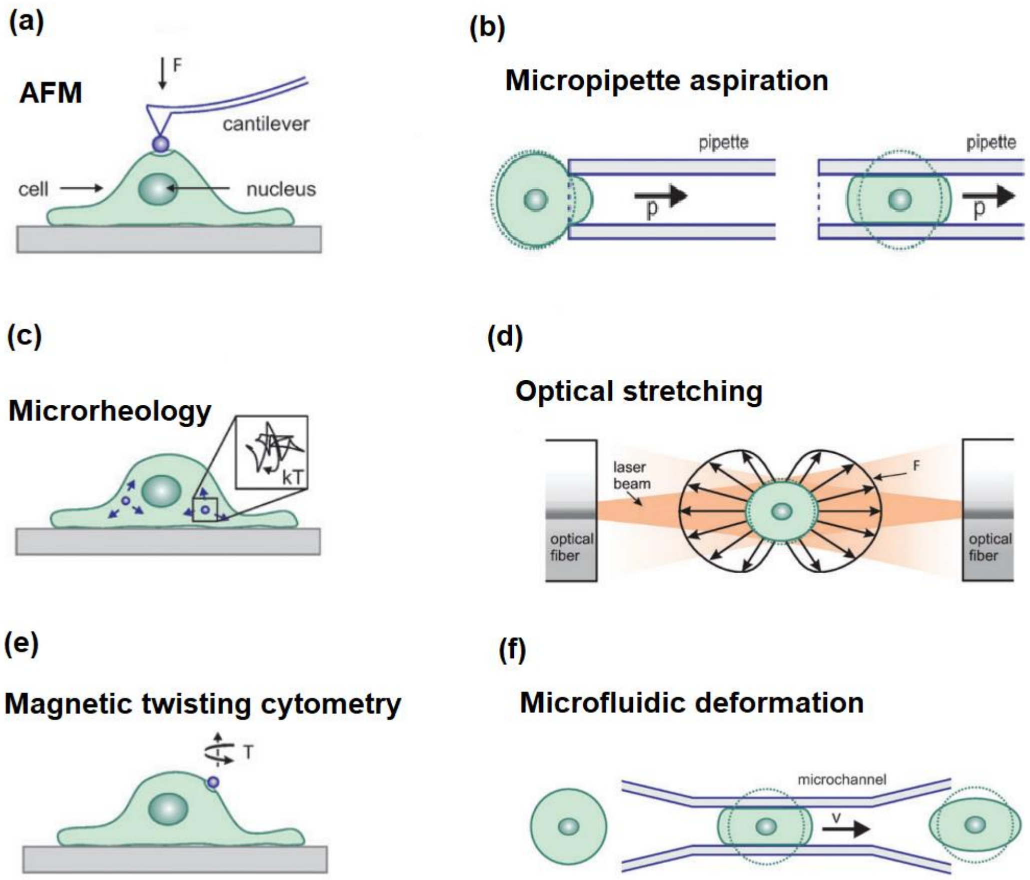

Figure 2.9. Measurement techniques for cell mechanical properties. (a) Atomic force microscopy (AFM), (b) Micropipette aspiration, (c) Microrheology, (d) Optical stretching, (e) Magnetic twisting cytometry, (f) Microfluidic deformation [219].

The mechanical properties of substrates such as hydrogels used in mechanotransduction studies are usually characterized globally by rheology, compression, and tensile testing (figure 2.10) [220]. However, the downside of conventional and gold standard mechanical tests, such as compression and shear rheology, is that it is necessary to exert mechanical forces directly on the surface of the biomaterial. The former measure Young’s modulus (E) and is generally obtained from the slope of the stress-strain curve. The latter allows characterisation of the average rheological properties in bulk materials, such as shear storage and loss moduli. These existing methods are difficult to extend to the measurement of cellular hydrogels because they can be considered 'destructive'; after the test is performed, the sample may be damaged or destroyed and cannot be used for further experiments. Therefore, these techniques are unsuitable for long-term and continuous monitoring of 3D cellular constructs.

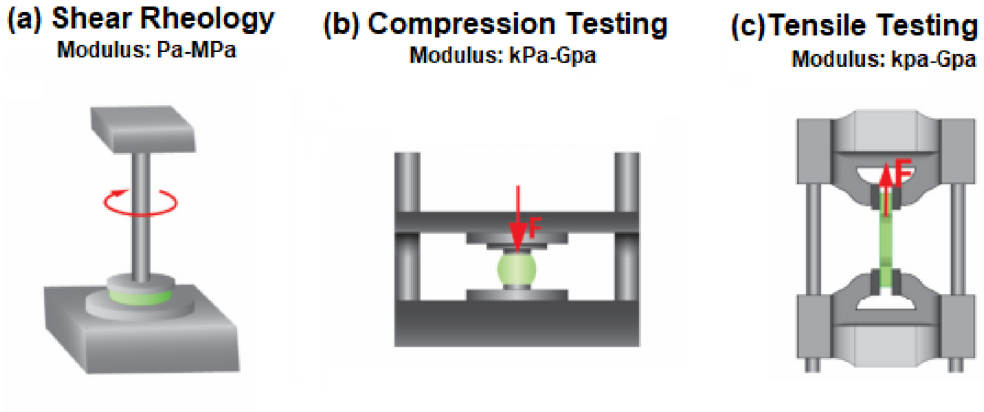

Figure 2.10. Techniques to measure mechanical properties of hydrogels. (a) Shear Rheology, (b) Compression testing, and (c) Tensile testing [220].

More recently, Brillouin microspectroscopy (BM), a non-contact, non-destructive and label-free technique, has been demonstrated to be helpful in characterising living organisms and artificial biomaterials, providing a unique insight into viscoelasticity at the micro-scale [221, 222]. This technique is based on Brillouin light scattering (BLS), which is an inelastic scattering process arising from the interaction of light (photons) with thermally driven acoustic vibration (phonons) in the material [223]. Unlike quasi-static techniques such as compression or shear rheology, BM provides information on the complex longitudinal elastic modulus of the material in a high-frequency regime (~1-10 GHz), which is emerging as a promising spectroscopic imaging technique with high resolution [224]. Brillouin microscopy probes the longitudinal modulus, which is the inverse compressibility. The measurement is equivalent to a confined compression at GHz frequencies, and the volume of the material is thus not kept constant during the deformation caused by pressure waves.

Mechanical mapping using BM is achieved by scanning the sample with a low-power focused laser beam, thus making this technology compatible with in situ and *in vivo* imaging in 3D. Until now, this technique has been applied *in vivo* to investigate the mechanical properties of the cornea [225], tumours [226], fibrous proteins of the extracellular matrix [227, 228], cellular mechanics [229, 230] and, more recently, the first mechanical images of a mouse embryo [231, 232]. In addition to the studies of living cells and tissues, BM has been employed to characterise the microscopic mechanical properties of various bio-compatible materials, including cast and bioprinted acellular hydrogels [233, 234]. For instance, covalently UV-cross-linked cast acellular GelMA hydrogels were assessed to determine the viscoelastic properties of the hydrogel network using the BM [221]. In another study, it was demonstrated that this technique is able to resolve variations between mechanical properties of the hydrogels with slightly different solid fractions [234]. The mechanical characterisation of 3D cellular models using BM is now being pursued intensively in order to better understand the interplay between cells and their microenvironment [235]. In addition, the non-contact and non-destructive nature of BM provides the time-dependant and reproducible measurements of the mechanical properties of 3D bioprinted hydrogel constructs and adds an extra channel of data to traditional methods.

2.9 Assessing the biological response to spinal cord injury

Assessing the biological response to injury is a critical component of understanding the impact of SCI on cells and tissues. There are various approaches to assess this response, including assays for cell viability, apoptosis, proliferation, and differentiation [236]. Additionally, biomarkers can be used to evaluate inflammation, oxidative stress, and other pathological responses to SCI [237].

One commonly used method to assess cell viability following injury is the MTT assay, which measures the metabolic activity of cells [238]. This assay can be used to quantify the number of viable cells in a sample and is often used to assess the cytotoxic effects of treatments or to evaluate the response of cells to injury. Similarly, assays for apoptosis, such as the Annexin V/propidium iodide assay, can be used to evaluate the level of cell death following injury [239]. Proliferation assays are also commonly used to assess the response of cells to injury. These assays measure the rate at which cells divide and can provide insights into the regenerative capacity of a tissue. One example of a proliferation assay is the BrdU assay, which measures the incorporation of BrdU into newly synthesized DNA during the S-phase of the cell cycle [240]. Bioluminescent ATP assays are another method that can be used to measure the metabolic activity of cells following injury and can provide insights into the overall cellular health and energy metabolism [241]. After injury, astrocytes can become activated and release various molecules, including ATP. This release of ATP can be increased compared to control samples, likely due to the increased metabolic demand and cellular stress associated with the injury.

Assessing differentiation is another important aspect of understanding the biological response to injury. In fact, in response to injury, astrocytes increase their expression of intermediate filaments such as GFAP, nestin and vimentin, and undergo hypertrophy [242]. Assays that measure the expression of specific markers or the production of certain proteins can be utilized for evaluation purposes. For instance, immunofluorescence staining is a method that can be employed to assess the expression of specific markers, while ELISA assays can be used to quantify the production of particular proteins. Apart from these approaches, biomarkers can also be employed to assess inflammation, oxidative stress, and other pathological responses associated with SCI. For example, cytokines such as interleukin-6 (IL-6) and tumor necrosis factor-alpha (TNF-α) are often used as indicators of inflammation [243]. Other markers, such as reactive oxygen species (ROS) and malondialdehyde (MDA), can be used to assess oxidative stress and lipid peroxidation, respectively [244].

Overall, there are numerous approaches that can be used to assess the biological response to injury. By using a combination of these methods, researchers can gain a comprehensive understanding of the impact of SCI on cells and tissues and develop strategies to promote regeneration and recovery.

CHAPTER 3 MATERIALS AND METHODS

3.1 Experimental approach

The following diagram (Figure 3.1) has been created to aid understanding of the relation of this chapter to other chapters.

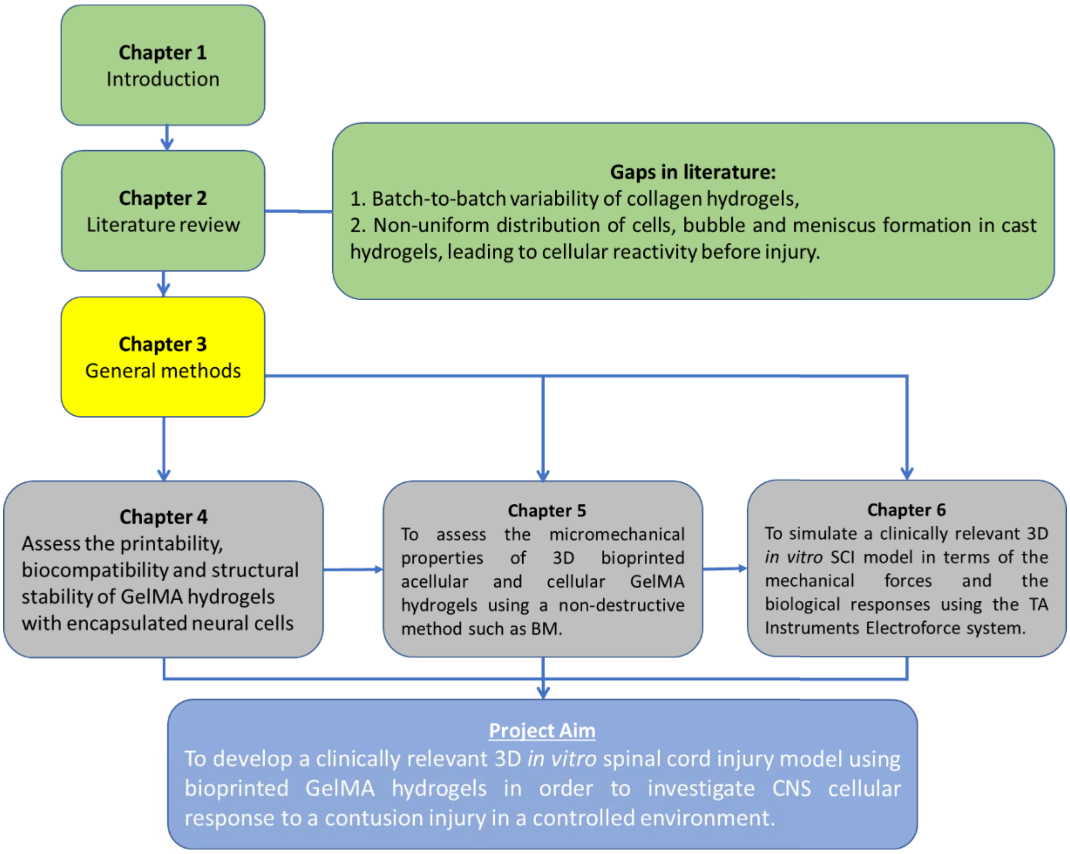

Figure 3.1. Flow diagram showing the work in this chapter in relation to other chapters, with the current chapter highlighted in yellow.

3.2 NG 108-15 neuronal cell culture

The NG 108-15 (mouse neuroblastoma × rat glioma hybrid, HPA Culture Collections) cell line was purchased from the European Collection of Cell Cultures (ECACC). This cell line was grown in DMEM containing 10% (v/v) FBS (Gibco), 1% (v/v) penicillin-streptomycin (10000 Units.mL^{-1} penicillin, 10000 µg.mL^{-1} streptomycin) (Gibco), and 2% (v/v) HAT (0.1 mM hypoxanthine, 400 nM aminopterin and 0.016 mM thymidine, Sigma Aldrich) at 37 °C in 5% (v/v) CO_2 in air. Cell culture was carried out in class II safety cabinets with the appropriate aseptic technique.

3.3 C6 Astrocyte-like line cell culture

A C6 rat glioma cell line was purchased from the American Tissue Culture Collection (ATCC, cell passage number 37). This cell line was grown in F-12K Medium (30-2004, ATCC), supplemented with penicillin-streptomycin (10000 Units.mL^{-1} penicillin, 10000 µg.mL^{-1} streptomycin) (Gibco) to a final concentration of 1% (v/v), fetal bovine serum (FBS, Gibco) to a final concentration of 2.5% (v/v) and horse serum (Sigma-Aldrich) to a final concentration of 15% (v/v) at 37 °C in 5% (v/v) CO_2 in air.

3.4 Qualitative analysis of neural cell viability in bioprinted GelMA hydrogels using a Live/dead assay

The viability of NG 108-15 neuronal and C6 astrocyte-like cells within the GelMA hydrogels was determined using the Live/Dead® Cell Viability assay. Briefly, cellular GelMA hydrogels were rinsed with PBS and stained with 2 µg.mL^{-1} Calcein AM (Sigma-Aldrich), 1 µg.mL^{-1} propidium iodide (Sigma-Aldrich), and 2 µg.mL^{-1} Hoechst (Thermo Fisher) for 30 min at 37 °C in 5% (v/v) CO_2 in air. The staining solution was discarded, and hydrogels were washed four times with PBS. Then, samples were kept in the dark until visualised using an inverted fluorescence microscope (Olympus IX 73 & CKX3). The cells were then visualized using immunofluorescence microscopy to count the number of cells staining positive.

3.5 Quantitative analysis of neural cell viability in bioprinted GelMA hydrogels using an ATP assay

The viability of NG108-15 neuronal and C6 astrocyte-like cells was measured via a Luminescent Cell Viability Assay on days 1, 3 and 7. In this research, Celltiter-Glo® reagent (Promega) was added to each cellular GelMA hydrogel sample according to the manufacturer's protocol. The cell culture medium was removed entirely and replaced with the ATP reagent at a volume that fully immersed the hydrogels. This process was followed by incubating cellular hydrogel samples covered by aluminium foil on a plate shaker at 100 rpm for 45 min [245]. The assay resulted in cell lysis and the generation of a luminescent signal proportional to the amount of ATP present. Luminescence was read by the Infinite M200 Pro Plate Reader (Tecan) using an Integration time of 1000 ms and a Settle time of 5 ms. The output data was expressed as Relative Light Unit (RLU).

3.6 Immunofluorescence Staining

The supernatant from each sample was aspirated and rinsed twice with DPBS. Then, hydrogels were fixed with 4% (w/v) paraformaldehyde (PFA) for 45 minutes on an orbital shaker at 110 rpm. After that, the hydrogels were rinsed three times with DPBS and permeabilised with 0.3% (v/v) Triton X-100 (diluted in DPBS) for 15 minutes at room temperature. Following 3 × 5 minute PBS washes, blocking of non-specific antibody binding sites was performed using 5% (v/v) goat serum solution for 45 minutes. Following 3 × 5 minute PBS washes, the hydrogels were incubated with primary antibody (C6 astrocyte-like, NG 108-15 Neuronal cells: Anti-GFAP, anti-βIII-tubulin) diluted in 5% goat serum solution (Table 3.1) overnight at 4 °C. Following rinse 3x 5 min with DPBS, the hydrogels incubated with a secondary antibody (C6 astrocyte-like, NG 108-15 Neuronal cells: Goat Anti-Rabbit, Donkey anti-Mouse) diluted in 5% goat serum solution (Table 3.1) for 1 h at room temperature on an orbital shaker, at 110 rpm. Hydrogels were rinsed with PBS (3 × 10 minutes) and then stained the cells with a DAPI solution (3 ng/mL) for 10 minutes prior to confocal imaging. At least three independent experiments were performed.

Table 3.1. Primary and secondary antibodies used throughout the study.

Antibody	Antigen	Type	Isotype	Dilution	Supplier
Primary	Glial Fibrillary Acidic Protein	Anti-GFAP antibody	Rabbit Anti-mouse	1:300	Abcam
	βIII-tubulin	anti-βIII-tubulin	Rabbit	1:500	Promega
Secondary	Rabbit IgG	Goat Anti-Rabbit	Alexa Fluor® 488	1:1000	Thermofisher
	Mouse IgG	Donkey anti-Mouse	Alexa Fluor™ Plus 594	1:1000	Abcam

3.7 Confocal microscopy

This study presents confocal images of cellular hydrogels at maximum intensity projections generated from their respective stacks. Images from fluorescent-stained cells were acquired using EVOS M5000 and Leica Stellaris confocal microscopies. The distance between adjacent images was precisely controlled in the z-stack. The z-stack of optical sections, 200 μm in total thickness, with 40 slices acquired at 5 μm intervals, was captured from cellular hydrogel samples. A total of three fields of view were obtained for each hydrogel sample (Figure 3.2) and was repeated three times. The starting point of the image acquisition was set by the z-position in which the cells first became apparent. Then, the acquired images were imported into Fiji software for analysis.

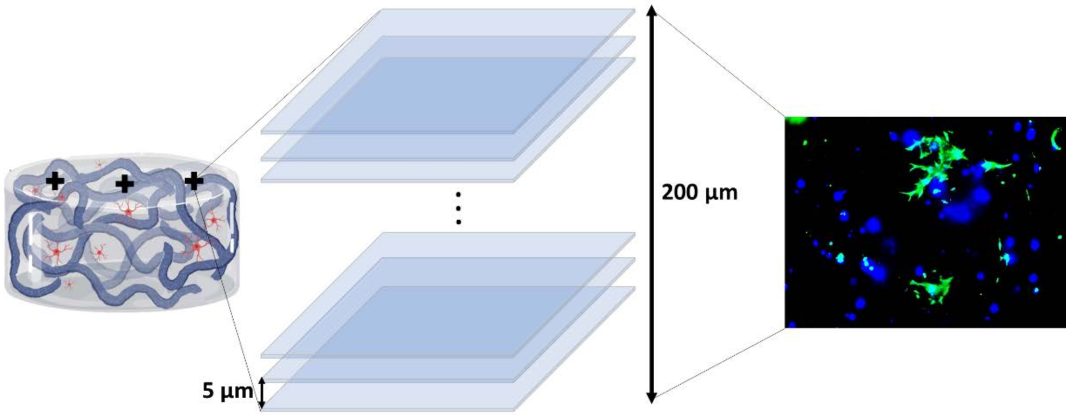

Figure 3.2. Confocal image acquisition of bioprinted GelMA hydrogel samples. Three fields of view were captured per sample, as denoted by the black cross. The z-stacks of those positions were 200 µm in total thickness, with 40 slices acquired at 5 µm intervals.

3.8 Quantitative analysis of cell viability staining using ImageJ

The cell viability percentage was measured using the ImageJ (FIJI) image analysis software. A fluorescence image was loaded into the ImageJ software (Figure 3.3 (a)) and then split into the separate channels of green and red (Image → Color → Split Channels → Select) (Figure 3.3 (b)). Afterwards, the threshold was adjusted using the default thresholding method (Image → Adjust → Threshold → Apply) (Figure 3.3 (c and d)). This was followed by selecting the process tab and processing it into a binary image (Process → Binary → Make a binary → Select). Therefore, the software could analyse and quantify the unlabelled pixels (white) from the labelled pixels (black). Then, 'Measure' option (Analysis → Measure) was used to measure the area in the image, shown in black. Finally, the total area in green and red was displayed in a summary table for analysis (Figure 3.3 (e)). The cell viability percentage was obtained by dividing the total area of green by the total area of green and red channels ($\frac{\text{Green}}{\text{Green+Red}} \times 100$) (Figure 3.3 (f)).

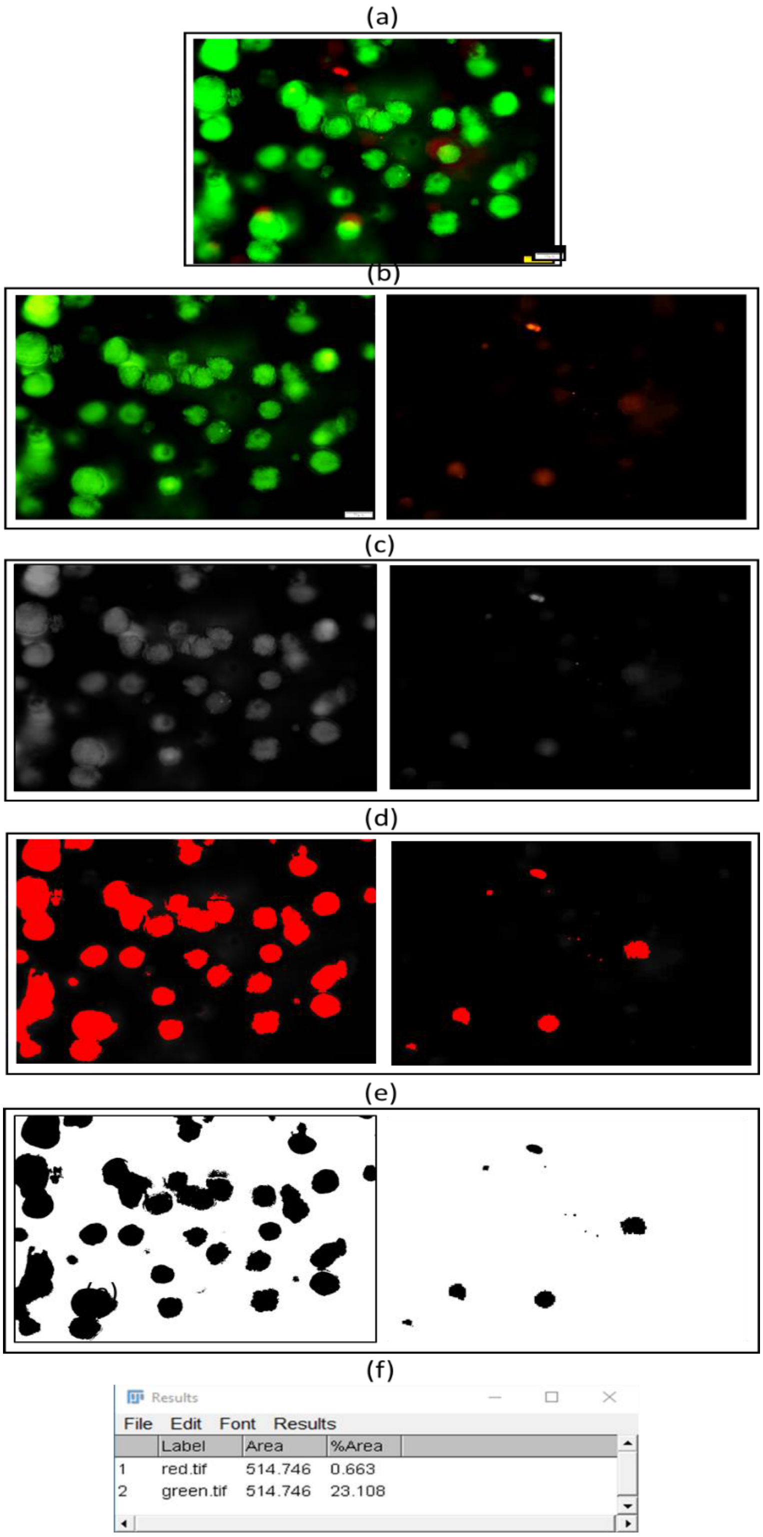

	Label	Area	%Area
1	red.tif	514.746	0.663
2	green.tif	514.746	23.108

Figure 3.3. Processing and analysing of fluorescent images using ImageJ software.

3.9 Quantitative analysis of GFAP expression by C6 astrocytes-like cells using ImageJ

The total area of GFAP expression was measured using the ImageJ (FIJI) image analysis software. After loading a fluorescence image into the ImageJ software (Figure 3.4 (a)), it was split into separate channels of green, red and blue (Image → Colour → Split Channels → Select) (Figure 3.4 (b)). Then, the colour threshold was adjusted using the default thresholding method (Image → Adjust → Colour Threshold → select), (Figure 3.4 (c)). This was followed by selecting the process tab and processing it into a binary image (Process → Binary → Make a binary → Select) (Figure 3.4 (d)). Therefore, the software was able to analyse and quantify the unlabelled pixels (white) from the labelled pixels (black). Subsequently, the 'Analyse Particles' option (Analysis → Analyse particles) was used to detect and measure objects in the image. In this step, the pixel units were set to 10-infinity to ensure the detection of a single cell to a large collection of cells. Finally, the measurement results were displayed in a summary table for analysis (Figure 3.4 (e)). The total area of the green channel was divided by the total of both the green and blue channels together ($\frac{\text{Green}}{\text{Green+Blue}} \times 100$). The results were investigated for statistical significance by performing a one-way ANOVA with Fisher LSD post hoc comparison (Significance level $P < 0.0001$).

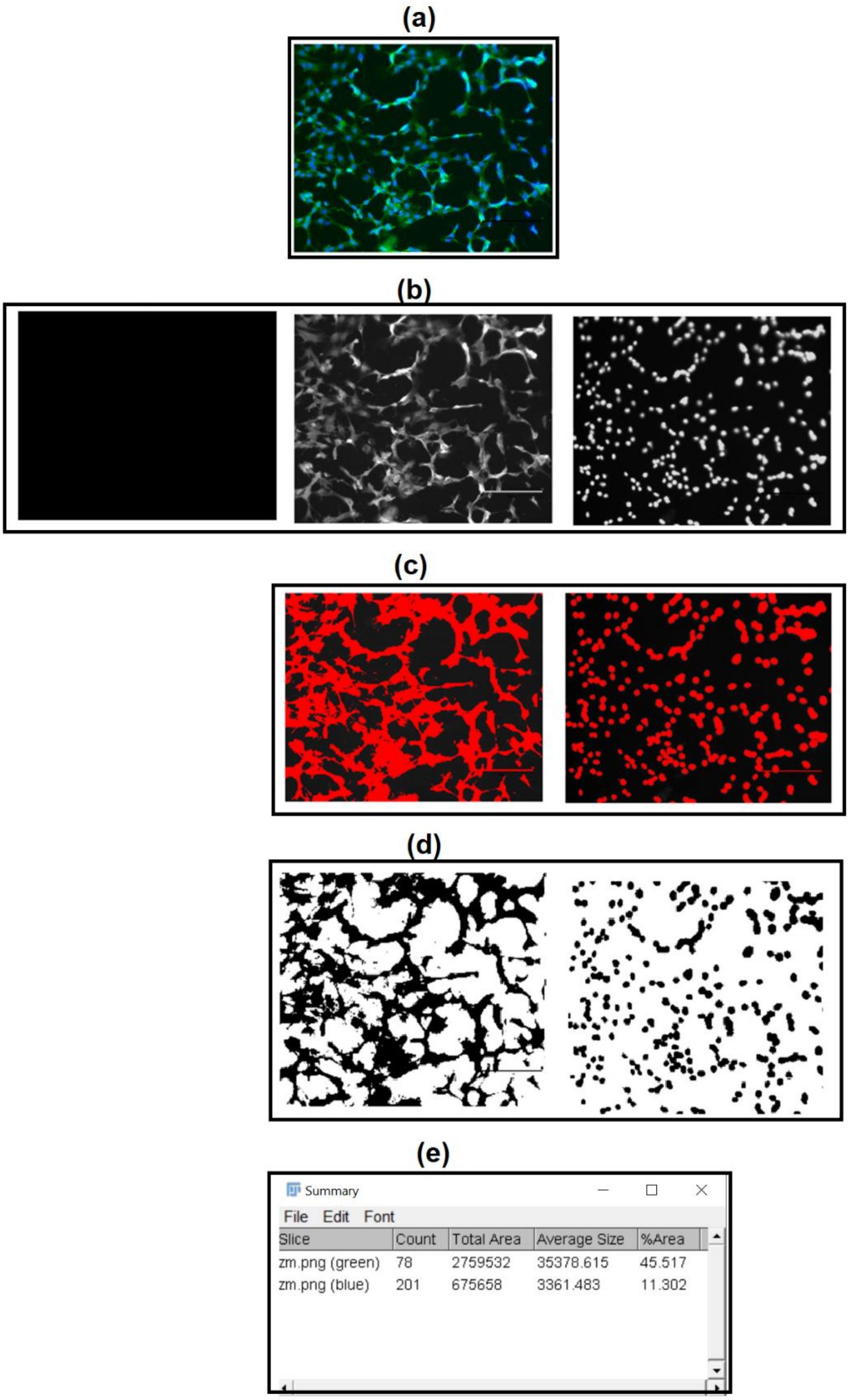

Slice	Count	Total Area	Average Size	%Area
zm.png (green)	78	2759532	35378.615	45.517
zm.png (blue)	201	675658	3361.483	11.302

Figure 3.4. Processing and analysing GFAP and DAPI fluorescent images using ImageJ software.

3.10 Statistical analysis

Calculated data points were presented as mean ± 95% confidence limits. Two-way ANOVA followed by Tukey post-hoc correction tests were performed where appropriate to measure statistical significance (GraphPad Prism 5.02 Software). $P<0.0001$ was chosen to represent statistical significance. All experiments were performed with at least three biological replicates. Despite employing 3 or 4 samples for every analysis, 3 separate locations within each sample were assessed, resulting in a minimum of 9 replicates per sample.

CHAPTER 4 OPTIMISATION OF 3D BIOPRINTING PROCESS OF GELMA HYDROGELS FOR USE IN A SPINAL CORD INJURY MODEL

4.1 Introduction

3D bioprinting techniques can produce 3D cellular environments with different orientations and geometries that can closely mimic the structure of CNS tissues. This technique allows a high level of precise control of the structure and shape of the construct, as well as precise positioning of multiple cell types and can create a 3D environment that can be precisely controlled and is subject to fewer variations than a cast natural hydrogel allows. However, the ideal bioink materials should satisfy specific criteria such as compatibility, printability, structural stability over incubation time and adjustable mechanical properties to use as a 3D environment for modelling a SCI.

As one of the most commonly used bioink types, hydrogels usually provide a highly hydrated environment that supports the growth of cells. However, in order to develop a 3D bioprinted neural tissue model for SCI, critical criteria of such a model include printability and neuronal biocompatibility. Printability refers to the capacity to form and maintain reproducible 3D hydrogel structures, and neuronal biocompatibility refers to allowing attachment and proliferation of neural cells within printed hydrogels. Natural polymers such as collagen or fibronectin are biocompatible and contain cell adhesion sites for cellular attachment [246]. Synthetic polymers have advantages over natural polymers in that their physical, chemical and mechanical properties can be designed to suit the application [246]. The benefits of the biocompatibility of natural hydrogels and the adjustable properties of synthetic hydrogels led to the hypothesis that hybrid (semisynthetic) hydrogels (like GelMA) would provide a robust platform for assessing neural cell physiology *in vitro*.

4.2 Aim and Objectives

4.2.1 Aim

This chapter aims to assess the printability, biocompatibility and structural stability of GelMA hydrogels with encapsulated living neural cells to form the basis of a spinal cord injury model. The hydrogel system which aligned most closely with the target criteria outlined in the objectives was chosen to simulate a clinically relevant mechanical injury mechanism.

4.2.2 Objectives

The specific objectives of this chapter are:

1. To determine the printability of acellular GelMA hydrogels with different volume concentrations using an extrusion-based 3D bioprinter. The printability of GelMA hydrogels in terms of print head temperature, printing pressure and printing speed were investigated.
2. To investigate the influence of volume concentration of GelMA hydrogels on the viability and proliferation of encapsulated cells within scaffolds (NG 108-15 neuronal and C6 astrocyte-like cells).
3. To investigate the stability of bioprinted GelMA hydrogels scaffolds incubated at 37 °C, 5% (v/v) CO_2 in air over 7 days.

The various volume concentrations of GelMA hydrogels were rated and compared against the following target criteria:

- There was a requirement for the GelMA hydrogels to be printable at various volume concentrations ranging from 2.5 to 15% (w/v) to fabricate a structure to form the basis of the SCI model.
- There was a requirement that the bioprinted GelMA hydrogels be suitable for 3D neural cell seeding and support the viability of cells over 7 days of cell culture, analysed qualitatively with Live/dead staining or quantitatively with the ATP cell viability assay.
- There was a requirement for the bioprinted GelMA hydrogels scaffolds to be stable over 7 days of incubation at 37 °C, 5% (v/v) CO_2 in the air to study cell behaviour after injury.

4.3 Specific Materials and Methods

4.3.1 Preparation of GelMA hydrogels with different volume concentrations

The CELLINK GelMA Kit (Cellink, Sweden) containing sterile freeze-dried Gelatin methacryloyl (GelMA) powder and Lithium acylphosphinate photoinitiator (LAP) was used in this study. The process of preparation of GelMA hydrogels is shown in Figure 4.1. Initially, LAP powder was mixed with phosphate-buffered saline (PBS; GIBCO, Thermo Fisher Scientific) (1X, pH 7.4) for 20 min at 50 °C to prepare a LAP solution with a concentration of 0.25% (w/v). After the mixture was entirely dissolved and became homogenous, the solution (PBS/LAP) was filter sterilised (0.22 µm) in a Class II biosafety cabinet and wrapped in aluminium foil to protect it from light. The desired volume of the sterilised photoinitiator was added to GelMA to achieve the desired hydrogel concentrations, which ranged from 2.5 to 15% (w/v), as shown in Table 4.1. For example, for making the 10 % (w/v) GelMA hydrogel with a LAP concentration of 0.25% (w/v), 5 mL of photoinitiator solution was added to 500 mg of GelMA powder with stirring and heating at 50˚C for 1 h until the GelMA powder wholly dissolved. Finally, the GelMA hydrogel was transferred into a 3 mL Luer-lock syringe (CELLINK) for bioprinting.

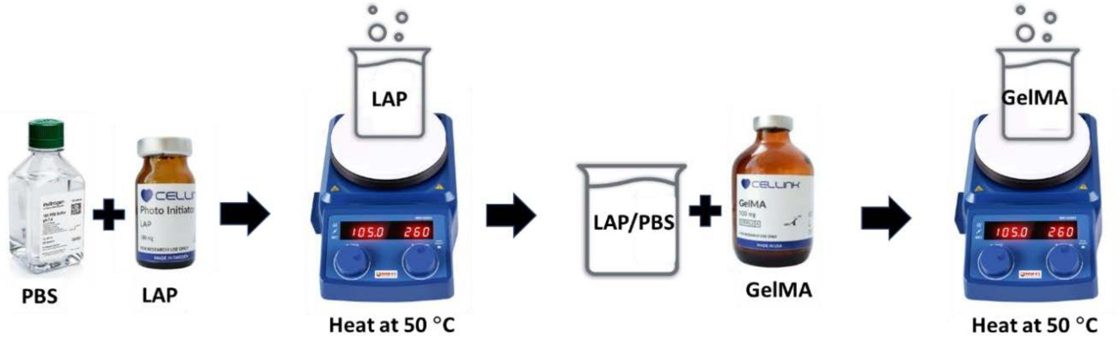

Figure 4.1. Process of preparation of GelMA hydrogels. Firstly, LAP was dissolved in PBS at 50 °C and mixed and sterilised using a 0.22 µm sterile filter to obtain the desired solution. The sterilised solution was added to the sterile freeze-dried GelMA powder (Cellink). The mixture was stirred for 1 h at 50 °C to ensure dissolution.

Table 4.1. Preparation of different GelMA hydrogel concentrations (for mixing with one bottle of 500 mg of GelMA).

Target GelMA (wt%)	Mass of GelMA (mg)	LAP solution (mL) (0.25%)
2.5	500	20
5.0	500	10
7.5	500	6.6
10	500	5.0
15	500	3.3

4.3.2 Preparation of Bioinks for bioprinting

The process of Bioink preparation for both NG 108-15 neuronal and C6 astrocyte-like cells was started by growing the cells in a T75 flask at 37 °C in 5% (v/v) CO_2 in air, as described in sections 3.2 and 3.3. When cells (NG 108-15 neuronal or C6 astrocyte-like cells) were approximately 80% confluent in a T75 flask at 37 °C in 5% (v/v) CO_2 in air, the culture medium was removed, and the cells were washed with 10 mL Dulbecco's phosphate-buffered saline (DPBS) (Gibco; without calcium and magnesium) to remove any remaining media. The DPBS was replaced with 2 mL of 0.25 % (v/v) trypsin/EDTA (Sigma-Aldrich), and the cells were incubated at 37° C for 5 min. After detaching cells, the cell suspension was transferred into a sterile universal tube containing 10 mL cell culture medium containing 10 % (v/v) FBS to neutralise the trypsin and centrifuged at 400 g for 5 minutes at room temperature. The waste media containing trypsin was removed, and the pellet of cells was collected.

Prior to printing, the GelMA hydrogel solution was warmed up to 37 °C in an incubator, and then 1 mL was transferred to a 3 mL syringe prior to mixing with cells at a ratio of 10:1. Then, a 100 µL volume of cell suspension, at a concentration of 4×10^6 cells/mL, was transferred to a 1 mL syringe by pulling out the piston. This was followed by mixing back and forth the GelMA solution and suspension of cells between the syringes to homogenise the cells in the bioink using a luer-lock coupler (Figure 4.2 (a)) and then placed in the bioprinter printhead with temperature control (Figure 4.2 (b)). After that, the GelMA hydrogels with different volume concentrations (2.5-15 % (w/v)) (section 4.3.1) were printed at desired temperature, pressure and speed, which were given in section 4.4.1. Then, the printed GelMA hydrogels were cross-linked by UV exposure (365 nm at an intensity of 19.42 $mW.cm^{-2}$) for a 120 s.

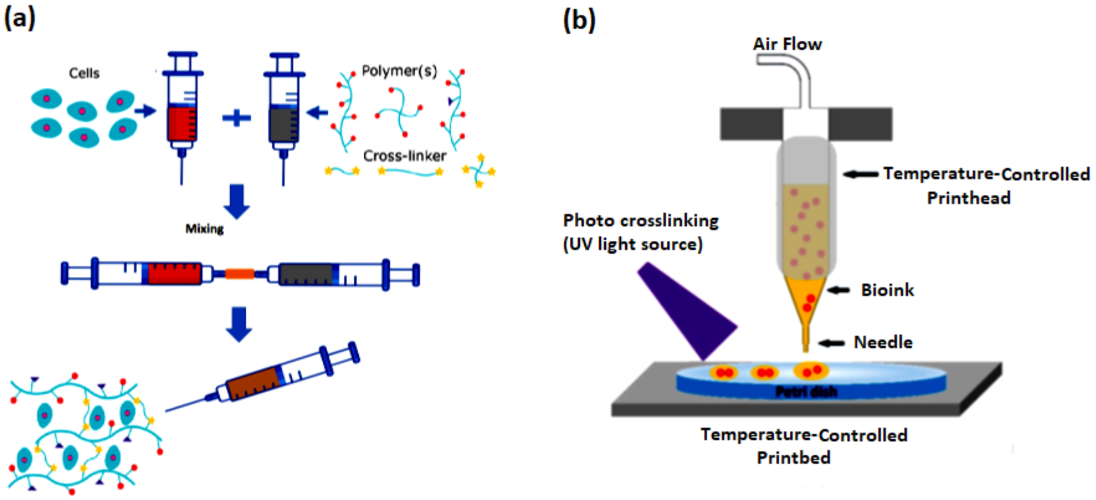

Figure 4.2. Schematic showing the loading GelMA solutions and cells into separate syringes. (a) The syringes were attached to a Luer-lock coupler, and the solutions were mixed by pushing back and forth until homogenous. (b) The cellular GelMA hydrogel was placed in the temperature control printhead before bioprinting 3D shapes.

4.3.3 Bioprinting System and Process

The CELLINK BIO X (CELLINK, Gothenburg, Sweden) is an extrusion-based bioprinter that was used to perform the experiments described in this thesis. It consists of a touchscreen LCD controller, print bed, three printhead bodies and piston-driven syringe heads. The CELLINK BIO X bioprinter system is shown in Figure 4.3.

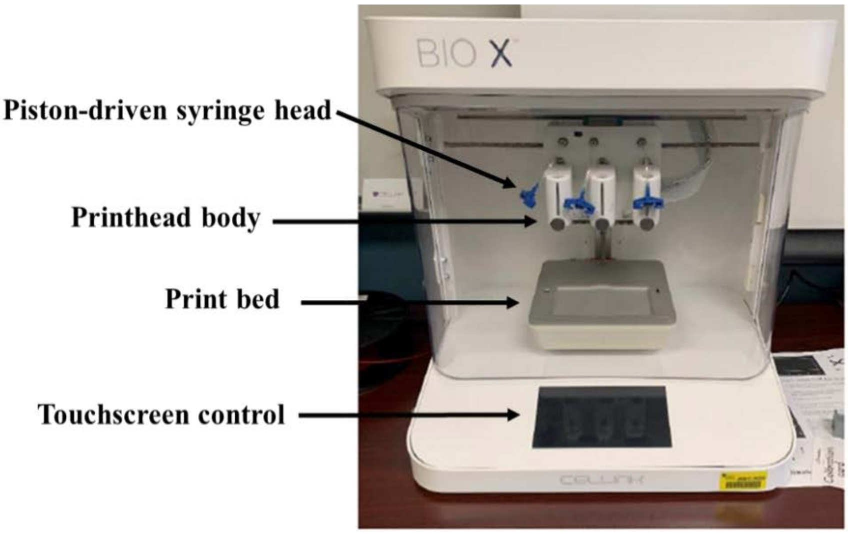

Figure 4.3. The CELLINK BIO X Bioprinter system.

A grid lattice was selected as an appropriate shape to print, as the pores facilitate the supply of the cells with media, nutrients and oxygen during cultivation. The bioprinting steps in BIO X bioprinter is detailed in Figures 4.4 and 4.5.

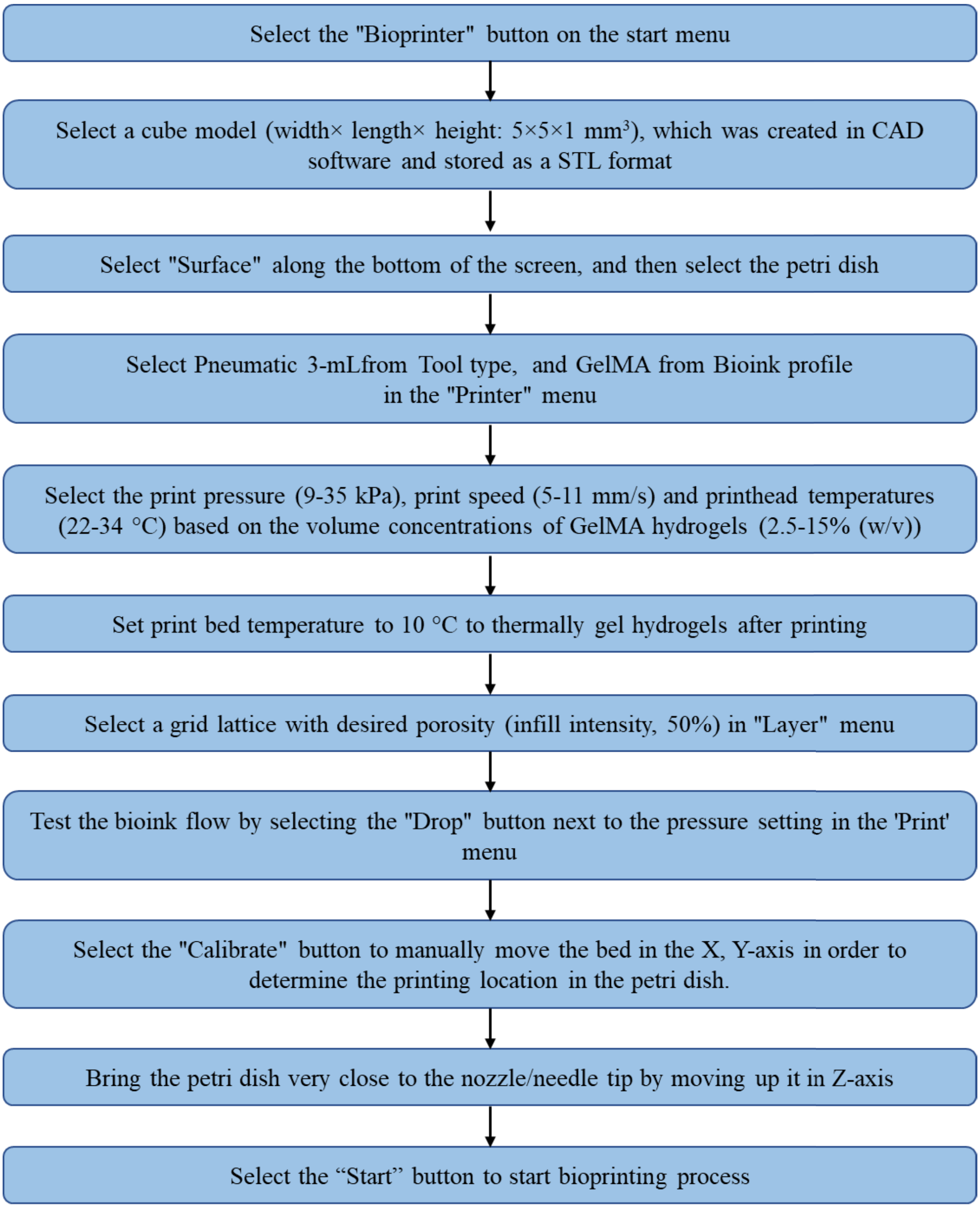

Select the "Bioprinter" button on the start menu

Select a cube model (width× length× height: 5×5×1 mm^3), which was created in CAD software and stored as a STL format

Select "Surface" along the bottom of the screen, and then select the petri dish

Select Pneumatic 3-mLfrom Tool type, and GelMA from Bioink profile in the "Printer" menu

Select the print pressure (9-35 kPa), print speed (5-11 mm/s) and printhead temperatures (22-34 °C) based on the volume concentrations of GelMA hydrogels (2.5-15% (w/v))

Set print bed temperature to 10 °C to thermally gel hydrogels after printing

Select a grid lattice with desired porosity (infill intensity, 50%) in "Layer" menu

Test the bioink flow by selecting the "Drop" button next to the pressure setting in the 'Print' menu

Select the "Calibrate" button to manually move the bed in the X, Y-axis in order to determine the printing location in the petri dish.

Bring the petri dish very close to the nozzle/needle tip by moving up it in Z-axis

Select the “Start” button to start bioprinting process

Figure 4.4. The flow diagram of a grid lattice printing steps in BIO X bioprinter.

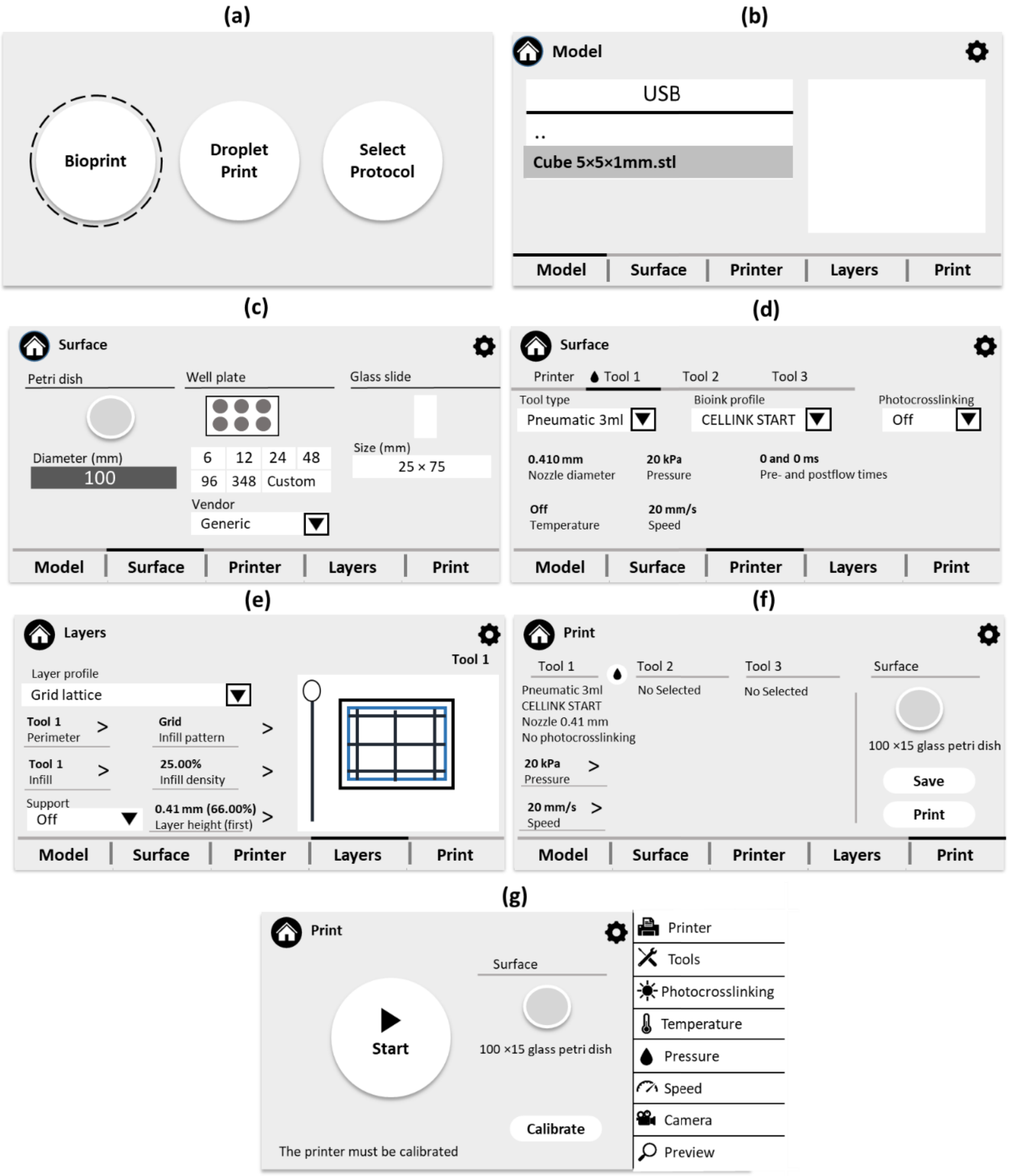

(c) Diameter (mm): 100
Size (mm): 25 × 75
Vendor: Generic

(d) Tool type: Pneumatic 3ml
Bioink profile: CELLINK START
Photocrosslinking: Off
0.410 mm Nozzle diameter
20 kPa Pressure
0 and 0 ms Pre- and postflow times
Off Temperature
20 mm/s Speed

(e) Layer profile: Grid lattice
Tool 1 Perimeter
Grid Infill pattern
Tool 1 Infill
25.00% Infill density
Support: Off
0.41 mm (66.00%) Layer height (first)

(f) Tool 1: Pneumatic 3ml, CELLINK START, Nozzle 0.41 mm, No photocrosslinking
Tool 2: No Selected
Tool 3: No Selected
20 kPa Pressure
20 mm/s Speed
100 ×15 glass petri dish

(g) 100 ×15 glass petri dish
The printer must be calibrated

Figure 4.5. The Bio X bioprinting processes: (a) Select Bioprint on the Start menu and proceeding to print setup. (b) Select an STL file from the Model menu. (c) Select a print substrate from the Surface menu. (d) Print parameters on the Printer menu. (e) Layer menu: Select the infill pattern and density and preview the layers. (f) Test bioink flow by using the "Drop" button next to the pressure setting. (g) Select Print to proceed to the calibration of the system and start the bioprinting process.

4.3.4 Morphological analysis of bioprinted structures

Morphological characterisation of the 3D printed hydrogels was carried out by observing constructs using an inverted fluorescence microscope (Olympus IX 73 & CKX3) at 4X and 10X magnifications. On each sample, four line width measurements were taken at random around the structure. The results were based on averaging 3 measurement repeats for each hydrogel sample, which define the line width. These were taken by imaging the bioprinted construct using a microscope and then importing the images into Fiji software for analysis.

4.4 Results

4.4.1 Determination of the printability of acellular GelMA hydrogels with different volume concentrations

This part of the study aimed to assess the printability of GelMA hydrogels with different volume concentrations (2.5-15 % (w/v)). Printability was defined as the geometrical difference between the designed and printed structures. The grid lattice (width × length × height: 5×5×1 mm^3) was selected as a 3D model and printed using a BIOX bioprinter, as previously explained in section 4.3.4. The printability was assessed by the parameters that controlled those two units, such as printhead temperature, extrusion pressure, and printing speed.

4.4.1.1 Determination of optimal print temperature for acellular GelMA hydrogels with various volume concentrations

The relationship between the concentration of GelMA hydrogels and cartridge/printhead temperature was initially examined as a critical parameter for printability. The printhead temperature was set from 20 to 34 °C for acellular GelMA hydrogels with volume concentrations from 2.5 to 15 % (w/v). Before printing, the GelMA hydrogel was incubated for 10 min in the printer to bring it to the desired temperature (20-34 °C).

Microscopy images of printed acellular GelMA hydrogels with a 10% (w/v) volume concentration at various printhead temperatures are shown in Figure 4.6. Three samples for each temperature were printed. The GelMA hydrogels gelled too quickly at temperatures below 28 °C and printed nonhomogeneously (Figure 4.6 (a-d)). Highly accurate printed grid patterns, with four empty squares between gridlines of bioink, were obtained at the optimised temperature of 28 °C, as shown in Figure 4.6 (e). Conversely, the GelMA hydrogels were liquid above this optimal print temperature (28 °C) and printed more droplet-like structures, resulting in poorly defined filaments of hydrogels, which tended to spread with filled pores (Figure 4.6 (f-h)).

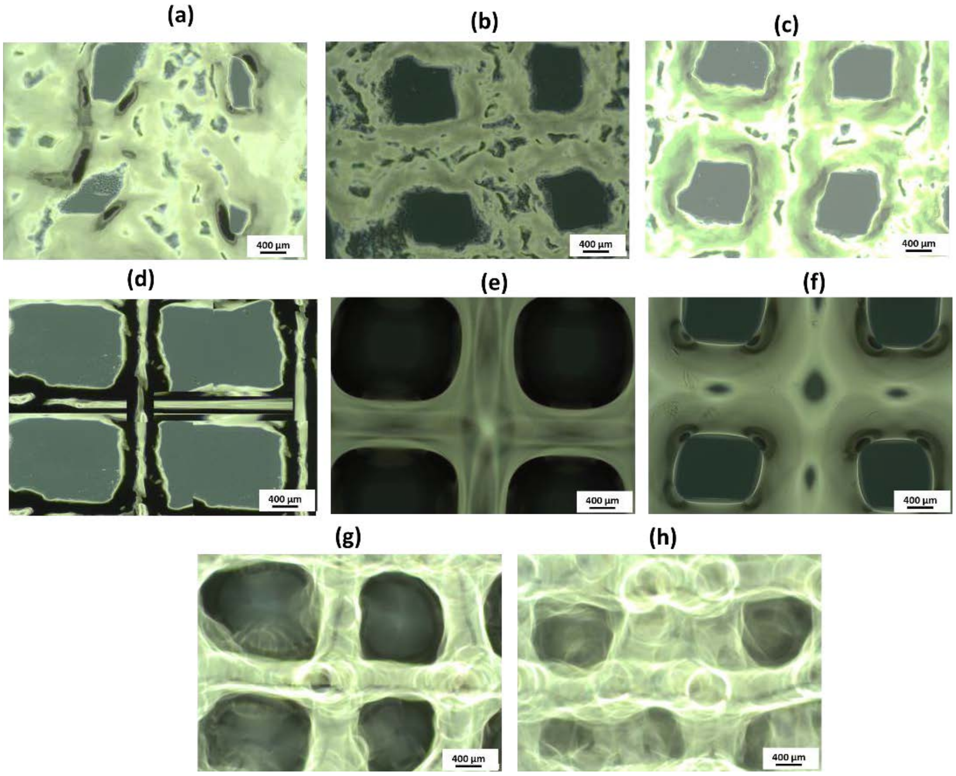

Figure 4.6. Light microscopy images of printed GelMA hydrogels with a volume concentration of 10 % (w/v). The printhead of the Bio X bioprinter was set at temperature of a (a) 20 °C, (b) 22 °C, (c) 24 °C, (d) 26 °C, (e) 28 °C, (f) 30 °C, (g) 32 °C, and (h) 34 °C.

A phase diagram of GelMA hydrogel printability at various volume concentrations from 2.5 % to 15% (w/v) at various temperatures from 20 °C to 34 °C is shown in Figure 4.7 (a). The GelMA hydrogels with low concentrations of 2.5 and 5% (w/v) were only printable at 22 and 24 °C, respectively. The optimal print temperature was increased to 26 and 28 °C at higher volume concentrations of 7.5 and 10% (w/v), respectively. Furthermore, the GelMA hydrogel with a very high concentration of 15% (w/v) was only printable at 32 °C. The bio-ink formed a liquid drop at the end of the nozzle when the temperature was higher than the optimal temperature (Figure 4.7 (b)). Conversely, the bio-ink was formed as a continuous filament upon extrusion but was too gelled when the temperature was lower than optimal (Figure 4.7 (c)). Generally, the bio-ink was produced as a continuous filament upon extrusion at optimal print temperatures and set for further experiments (Figure 4.7 (d)).

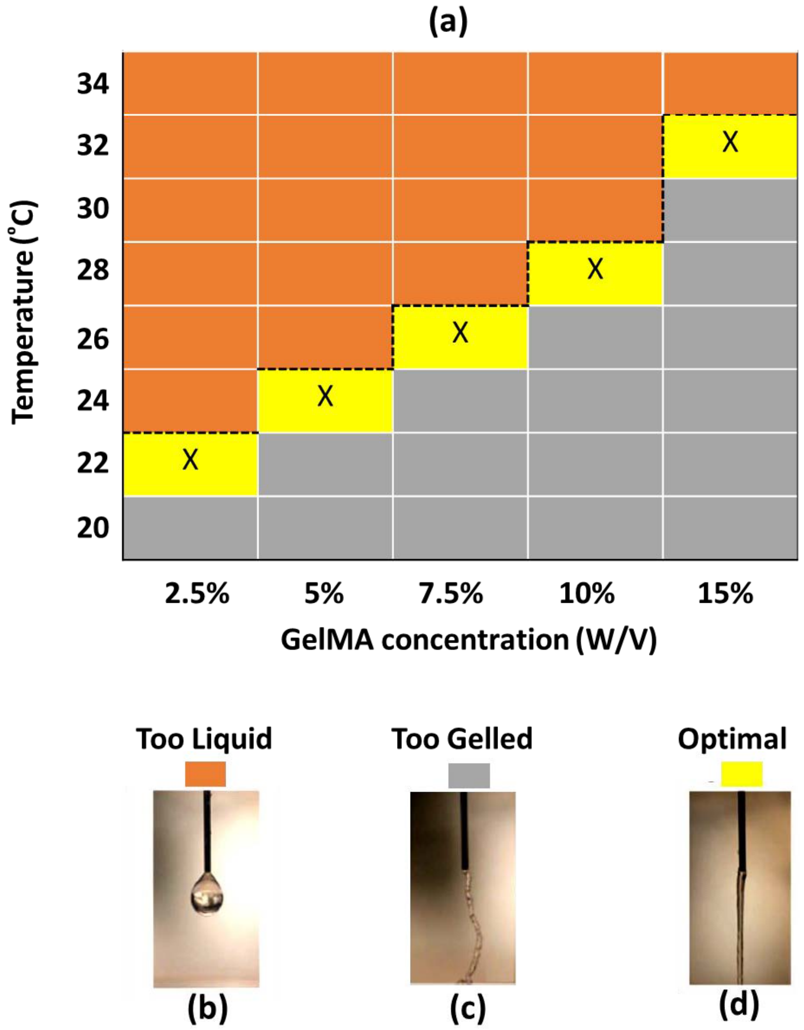

Figure 4.7. (a) Phase diagram of printability at various GelMA concentrations at temperatures ranges from 20 °C to 34 °C. The optimal temperatures for printing different GelMA hydrogels at 2.5, 5, 7.5, 10 and 15 (%w/v) are highlighted yellow. Representative images of (b) too liquid, (c) too gelled, and (d) optimal filament formations resulted from extrusion at different temperatures.

4.4.1.2 Determination of optimal print pressure and speed for acellular GelMA hydrogels with various volume concentrations

Bioprinting pressure and speed were optimised after determining the most suitable temperatures for the printing of GelMA hydrogels with various volume concentrations. For this purpose, the grid scaffold with the dimension of 5×5×1 mm^3 (Figure 4.8 (a)) was selected to print, as described in section 4.3.3. The GelMA hydrogels with a volume concentration of 10 % (w/v) were printed at a constant pressure of 10 kPa, and the speed was varied from 5, 7, 9, 11 to 13 mm/s. At printing speeds of 11 and 13 mm/s, the flow of the hydrogel was not continuous, resulting in a beaded construct and poor printability, as shown in Figures 4.8 (e) and (f). Whereas excessive outpour was observed at constructs with printing speeds of 5 mm/s, as shown in Figure 4.8 (b). The flow of the hydrogel was continuous, producing a more constant thickness of line at a printing speed of 7 mm/s, as shown in Figure 4.8 (c). Pores of the printed grid were filled at printing pressures of 18, 20 and 22 kPa, as shown in Figures 4.8 (i-k). The optimal printability for GelMA hydrogels with a volume concentration of 10 % (w/v) was obtained at a printing pressure and speed of 16 kPa and 7 mm/s, respectively, as shown in Figure 4.8 (h).

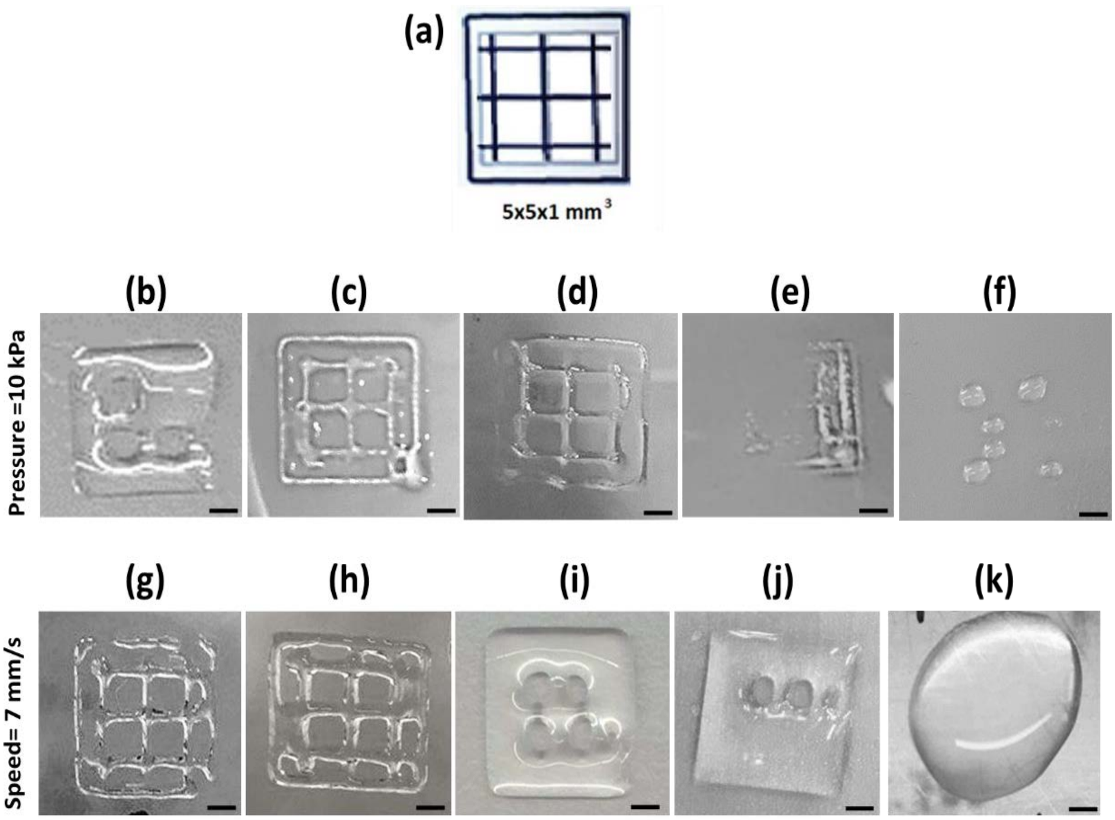

Figure 4.8. (a) 3D CAD grid structure for bioprinting optimization process. Microscopic images of printed lattice structures of GelMA hydrogels with 10 % (w/v) concentration using a BIO X 3D Bioprinter with constant pressure of 10 kPa at a print speed of (b) 5, (c) 7, (d) 9, (e) 11 and (f) 13 mm/s. The bioprinted structures were created using a constant speed of 7 mm/s and a print pressure of (g) 14, (h) 16, (i) 18, (j) 20, and (k) 22 kPa. Scale bar, 1 mm.

In order to better investigate the effects of pressure and speed on printing resolution, a simple square pattern (5×5 mm^2: width× length) was selected to print GelMA hydrogels with a concentration of 10 % (w/v). Each side of the bioprinted square structure was measured, as described in section 4.3.4. The linewidth was increased from 605 to 1069 µm by increasing the pressure from 14 to 20 kPa, as illustrated in Figure 4.9 (e). However, the linewidth was decreased from 1250 to 600 µm by increasing the speed from 5 to 11 mm/s, as shown in Figure 4.9 (f). Overall, the results demonstrated that printing pressure and speed could affect printability of scaffolds. The optimised bioprinting parameters of GelMA hydrogels with different volume concentrations of 2.5, 5, 7.5, 10 and 15 (w/v %) resulted in creating a pattern with the desired dimensions and geometries given in Table 4.2.

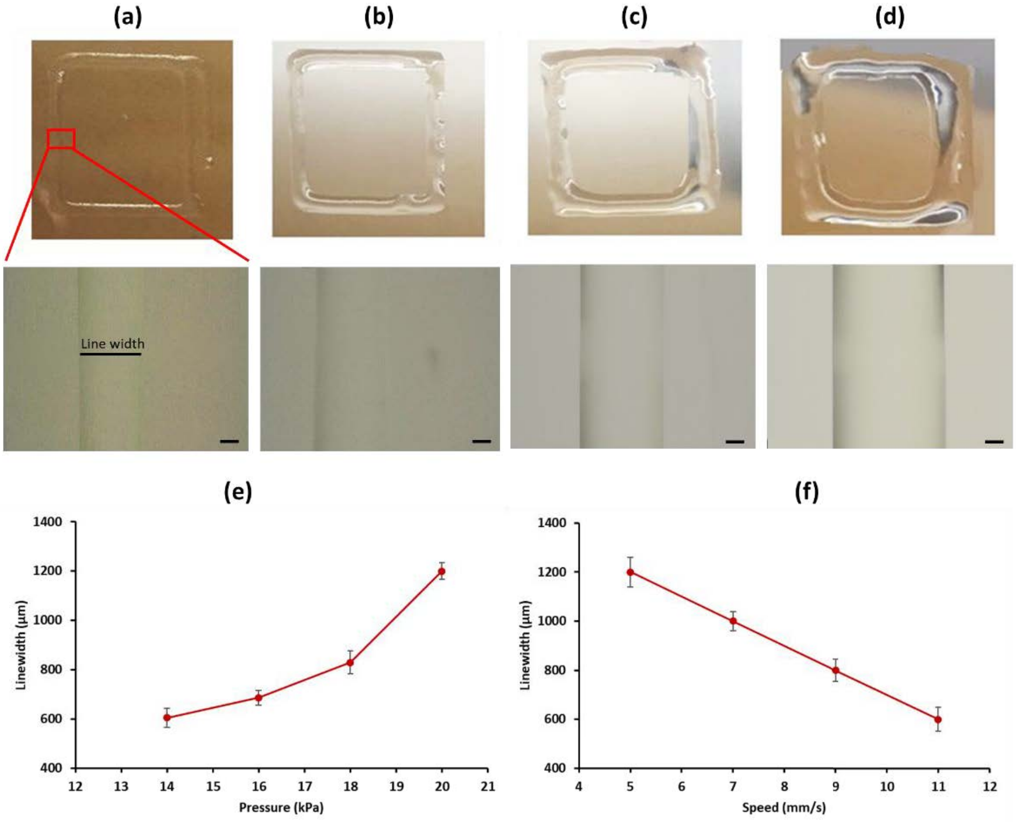

Figure 4.9. (a-d) Microscopy images of bioprinted GelMA hydrogels with a volume concentration of 10% (w/v) (Scale bar 200 µm). (b) Linewidth (µm) of the bioprinted lines (mean ± SD) for evaluation of the print accuracy and repeatability at different (e) printing pressures from 14 to 20 kPa, and (f) speeds from 5 to 11 mm/s.

Table 4.2. Optimised bioprinting parameters for different GelMA concentrations.

GelMA Concentration (w/v)	Bed temperature (°C)	Printhead temperature (°C)	Pressure (kPa)	Speed (mm/s)
2.5%	10	22	10	11
5%	10	24	12	11
7.5%	10	26	14	9
10%	10	28	16	7
15%	10	32	20	5

4.4.2 Determination of neural cell viability within bioprinted GelMA hydrogels with different volume concentrations

The aim of this part of the study was to investigate the biocompatibility of bioprinted GelMA hydrogels with volume concentrations of 2.5, 5, 7.5 and 10% (w/v)) embedded with C6 astrocyte-like and NG 108-15 neuronal cells at a concentration of 4 × 10^6 cells/mL. For this purpose, three samples for each volume concentration of GelMA hydrogels for each cell type were prepared and printed as explained in sections 4.3.2 and 4.3.3. All bioprinted GelMA hydrogels were cross-linked using UV light at a wavelength of 365 nm, a time of 120 s and intensity of 19.42 mW.cm^{-2}. Subsequently, the bioprinted GelMA hydrogel samples were immersed in the appropriate culture medium and evaluated over 7 days of incubation at 37 °C, with 5% (v/v) CO_2 in air. The viability of encapsulated astrocyte-like and NG 108-15 neuronal cells in bioprinted GelMA hydrogels were qualitatively and quantitatively assessed using live/dead staining and ATP assays, respectively, as described in sections 3.4 and 3.5. Live/dead staining was performed, where blue, green and red indicate nuclei, live and dead cells, respectively. In order to produce quantitative results from the live/dead images, four images were selected for each of the 2.5%, 5%, 7.5% and 10% (w/v) cellular bioprinted GelMA hydrogels, which had the highest cell attachment densities. These images were processed, and the results were assessed statistically as described in sections 3.8 and 3.10, respectively.

4.4.2.1 Determination of C6 Astrocyte-like cell viability within bioprinted GelMA hydrogels

The bright-field and fluorescence microscopy images of encapsulated C6 astrocyte-like cells grown in bioprinted GelMA hydrogels with a volume concentration of 2.5, 5, 7.5 and 10% (w/v) over 7 days at 37 °C, 5% (v/v) CO_2 in air are shown in Figures 4.10-4.13. Based on quantitative live/dead staining (Figure 4.14 (a)), the percentage of live C6 astrocyte-like cells within bioprinted GelMA hydrogels with concentrations 2.5 and 5% (w/v) wasn't changed significantly over one week of incubation at 37 °C, with 5% (v/v) CO_2 in air. However, the percentage of live cells in a 5 % (w/v) concentration (96%) was higher than 2.5 % concentration (82%) over one week of incubation. The fluorescent microscopy images of cellular gels also showed a large area of green labelled C6 astrocyte-like cells for both 2.5 and 5 % (w/v) GelMA concentrations, where the area of red labelled cells for 2.5 % (w/v) was higher than 5% (w/v) on day 7, as shown in Figures 4.10 and 4.11.

On the other hand, the quantitative live/dead staining (Figure 4.14 (a)) showed a significant reduction in live cells within the 7.5 and 10% (w/v) bioprinted GelMA hydrogels on day 7 compared to day 1. The cell viability percentage decreased from 89% to 42% and from 64% to 14.8% for GelMA hydrogels with 7.5 and 10% (w/v), respectively, over one week. In addition, the fluorescent microscopy images of cellular gels showed that C6 astrocyte-like cells did not grow well at 10 % (w/v) concentration, and all cells died from the third day onwards, as shown in Figures 4.12 (c) and (d). Overall, the bioprinted GelMA hydrogels with 5 and 10 % (w/v) concentrations encapsulating the C6 astrocyte-like cells showed the highest (96%) and lowest (14.8%) percentage of live cells over one week of incubation at 37 °C, with 5% (v/v) CO_2 in air.

The viability of encapsulated C6 astrocyte-like cells was also measured by quantifying the intracellular ATP activity on days 1, 3 and 7, as shown in Figure 4.14 (b). At GelMA hydrogel concentrations of 2.5 and 5% (w/v), C6 astrocyte-like viable cells significantly ($P<0.0001$) proliferated over 7 days. However, the cells failed to proliferate within GelMA hydrogels with 7.5 and 10 % (w/v) volume concentrations, as there were statistically ($P<0.0001$) fewer viable cells at day 7 compared to all other days (ANOVA, $p<0.0001$). Overall, the qualitative and quantitative cell viability data showed that C6 astrocyte-like cells had optimal proliferation rates and lower numbers of dead cells within the 5% (w/v) GelMA hydrogels compared to other GelMA volume concentrations (2.5, 7.5, and 10 % (w/v)).

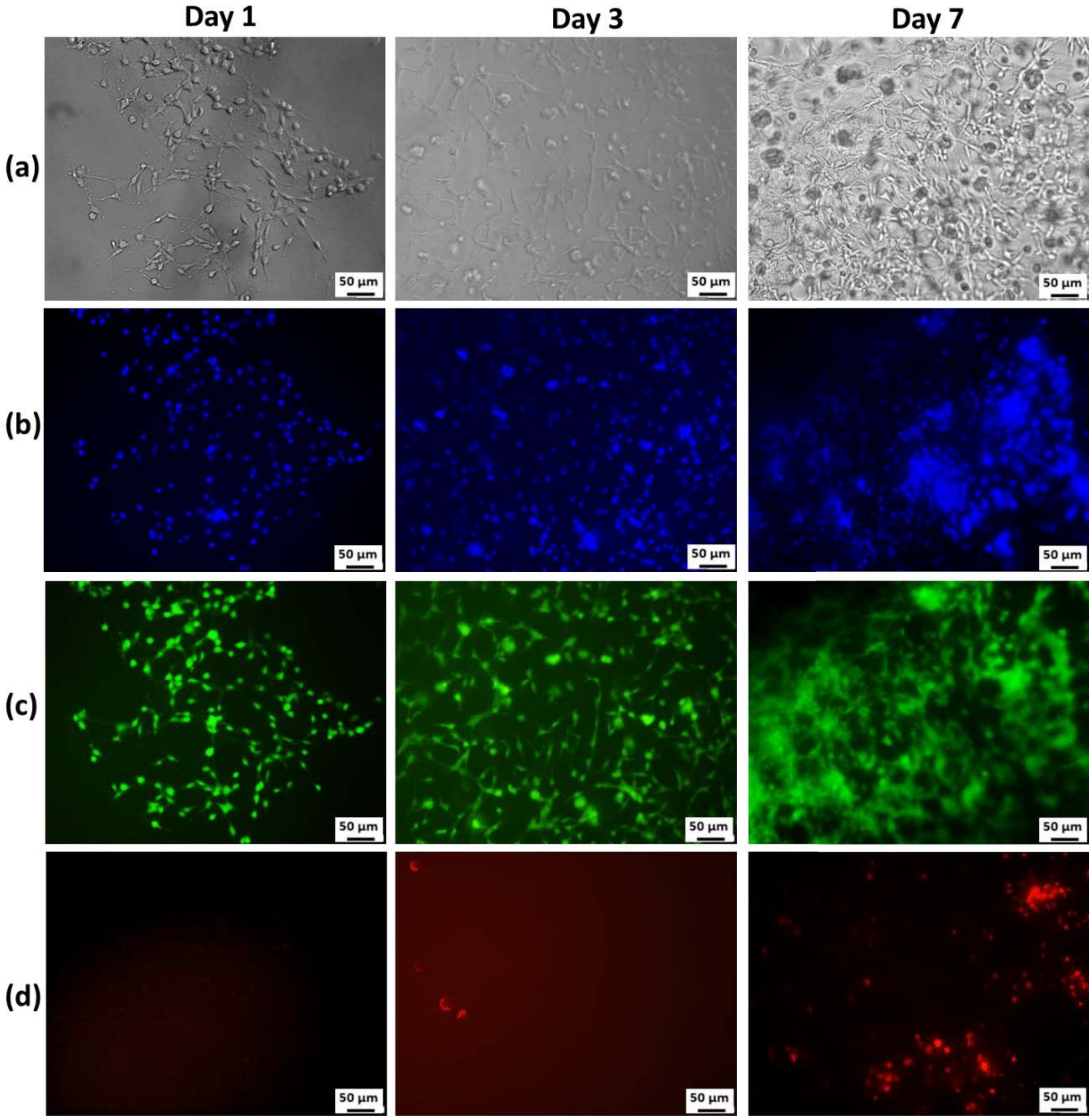

Figure 4.10. Representative bright-field (a) and fluorescence microscopy (b-d) images of C6 astrocyte-like cells at a concentration of 4 × 10^6 cells/mL embedded in a GelMA hydrogel with a concentration of 2.5% (w/v) at days 1, 3 and 7 at 37 °C, 5% (v/v) CO_2 in air. (b) The nuclei were stained with Hoechst and are shown in blue. (c) The cytoplasm of live cells was stained with Calcein AM and is shown in green. (d) Dead cells were stained with propidium iodide and are shown in red.

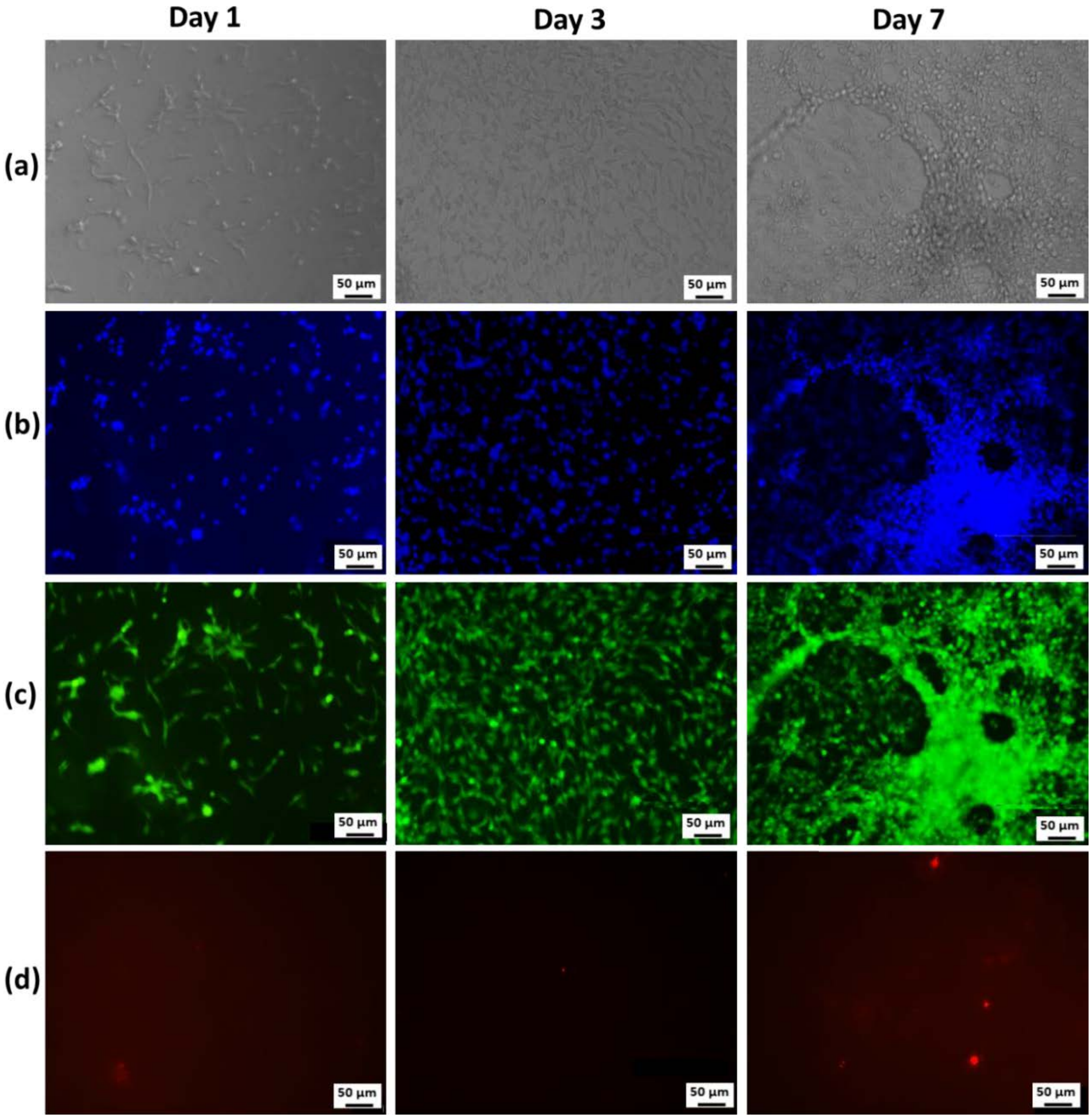

Figure 4.11. Representative bright-field (a) and fluorescence microscopy (b-d) images of C6 astrocyte-like cells at a concentration of 4 × 10^6 cells/mL embedded in a GelMA hydrogel with a concentration of 5% (w/v) at days 1, 3 and 7 at 37 °C, 5% (v/v) CO_2 in air. (b) The nuclei were stained with Hoechst and are shown in blue. (c) The cytoplasm of live cells was stained with Calcein AM and is shown in green. (d) Dead cells were stained with propidium iodide and are shown in red.

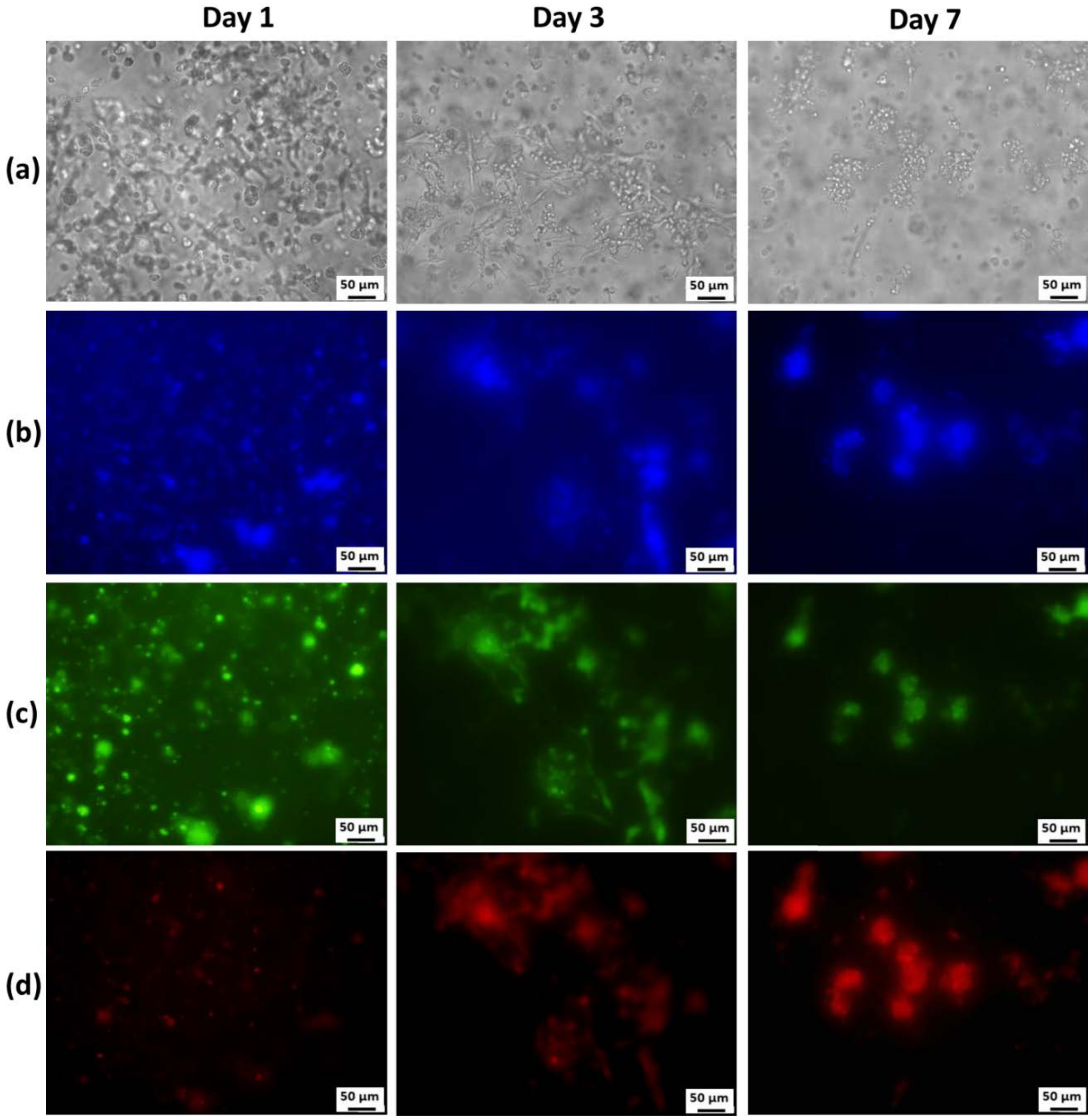

Figure 4.12. Representative bright-field (a) and fluorescence microscopy (b-d) images of C6 astrocyte-like cells at a concentration of 4 × 10^6 cells/mL embedded in a GelMA hydrogel with concentrations of 7.5% (w/v) at days 1, 3 and 7 at 37 °C, 5% (v/v) CO_2 in the air. (b) The nuclei were stained with Hoechst are shown in blue. (c) The cytoplasm of live cells was stained with Calcein AM and is shown in green. (d) Dead cells were stained with propidium iodide and are shown in red.

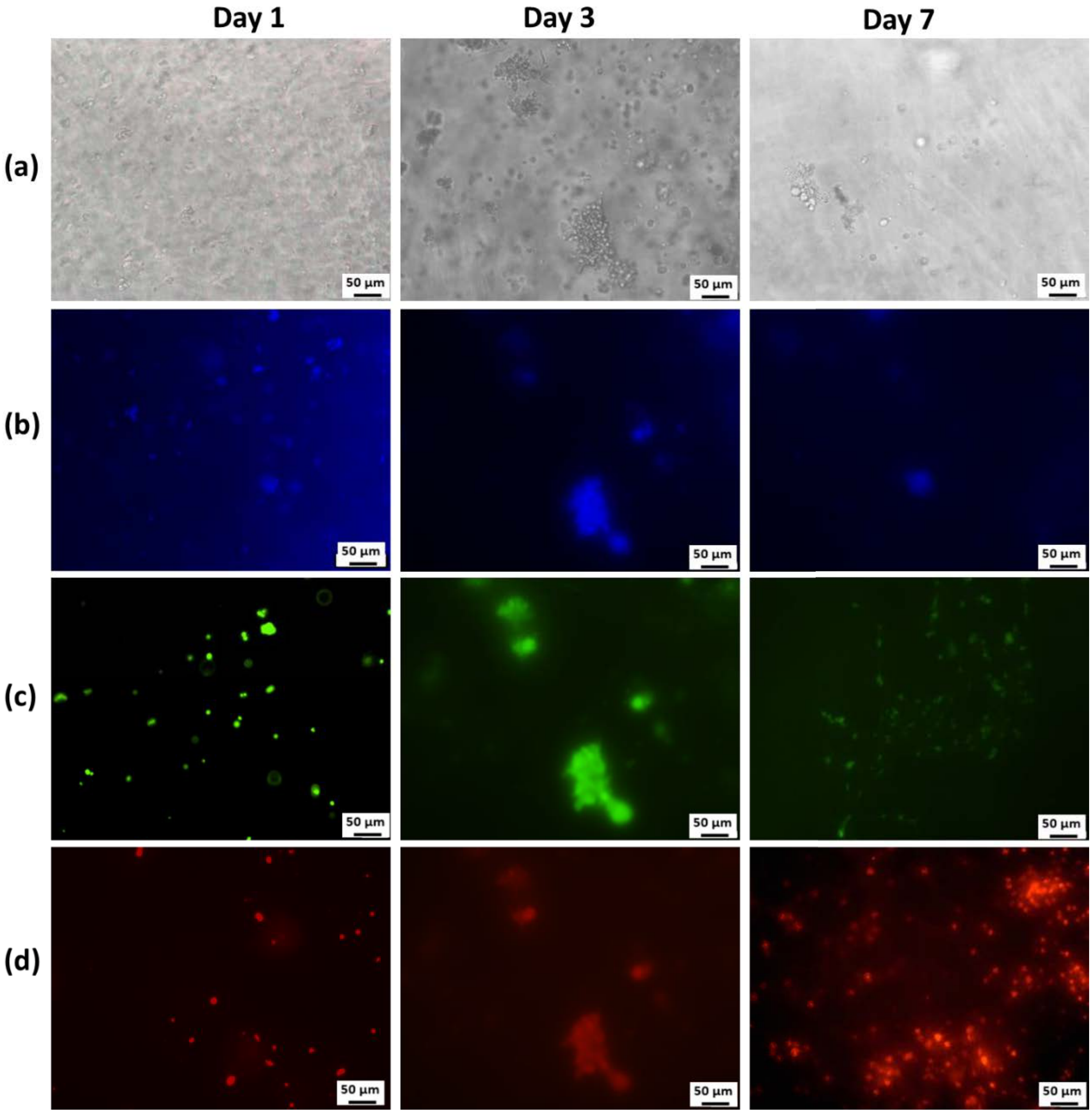

Figure 4.13. Representative bright-field (a) and fluorescence microscopy (b-d) images of C6 astrocyte-like cells at a concentration of 4 × 10^6 cells/mL embedded in a GelMA hydrogel with concentrations of 10% (w/v) at days 1, 3 and 7 at 37 °C, 5% (v/v) CO_2 in the air. (b) The nuclei were stained with Hoechst and are shown in blue. (c) The cytoplasm of live cells was stained with Calcein AM and is shown in green. (d) Dead cells were stained with propidium iodide and are shown in red.

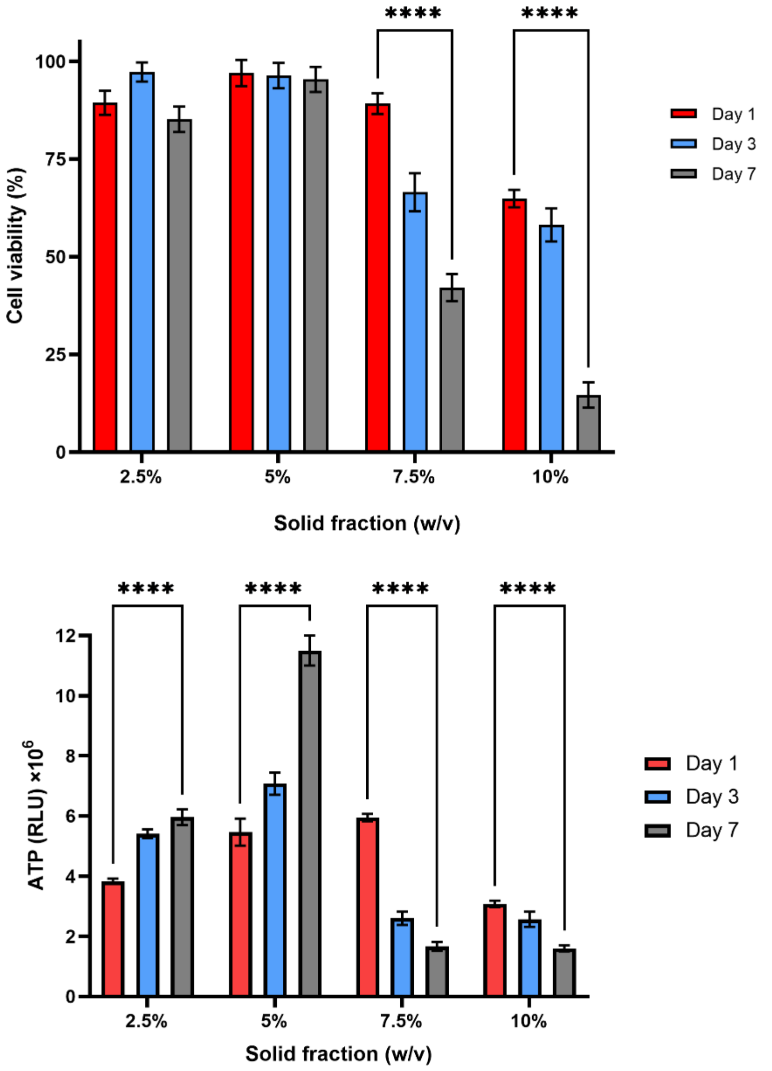

Figure 4.14. Quantification of (a) live/dead and (b) ATP cell viability assays results of C6 astrocyte-like cells embedded at a concentration of 4 × 10^6 cells/mL in bioprinted GelMA hydrogels with various volume concentrations of 2.5, 5, 7.5 and 10 % (w/v). The bioprinted GelMA hydrogel samples were immersed with appropriate culture medium and evaluated over 7 days of incubation at 37 °C in 5% (v/v) CO_2 in air. Error bars indicate 95% confidence intervals; lines indicate statistical differences determined by two-way ANOVA, N = 3. Significance level: ****P<0.0001.

4.4.2.2 Determination of NG 108-15 Neuronal cell viability within bioprinted GelMA hydrogels

The bright-field and fluorescent images of NG 108-15 neuronal cells grown in bioprinted GelMA hydrogels with concentrations of 2.5, 5, 7.5 and 10 % (w/v) on days 1, 3 and 7 at 37 °C, 5% (v/v) CO_2 in air are shown in Figures 4.15-4.18. Based on quantitative live/dead staining (Figure 4.19 (a)), the percentage of live NG 108-15 neuronal cells within bioprinted GelMA hydrogels with concentrations of 2.5 and 5% (w/v) wasn't changed significantly over one week of incubation at 37 °C, with 5% (v/v) CO_2 in air. The cell viability percentage was approximately 98% over one week for both 2.5 and 5 % (w/v) GelMA concentrations. In addition, the cells proliferated and organised into spheroid/aggregates in these concentrations of GelMA hydrogel, where an incremental increase in spheroid size from day 1 to day 7 was observed (Figures. 4.15 and 4.16).

In contrast, a significant reduction was observed in the cell viability percentage of NG 108-15 neuronal cells within bioprinted GelMA hydrogels with concentrations of 7.5 and 10% (w/v) over one week. The cell viability was decreased from which from 97% to 65% for 7.5 % concentration and from 79% to 24% for 10 % concentration. In addition, the NG108-15 neuronal cells within a 7.5% (w/v) GelMA concentration were presented in smaller sizes than 2.5 and 5% concentrations after 7 days of incubation, as shown in Figures 4.15-4.17. It's notable to mention that the cells didn't have uniform morphology within GelMA hydrogels with 10 % (w/v) concentration, as shown in Figure 4.18.

NG 108-15 cell viability was also determined by quantifying the ATP content of cells within bioprinted GelMA hydrogels on days 1, 3 and 7 (Figure 4.19 (b). The number of viable NG108-15 cells for GelMA hydrogels with a concentration of 2.5 % and 5% (w/v) was found to be significantly higher on day seven compared to day 1 (two way ANOVA, $P<0.0001$). However, no significant increase in cell viability in GelMA hydrogels with a concentration of 7.5 % (w/v) was observed between one and three days. Moreover, the ATP content decreased for cellular GelMA hydrogels with a concentration of 10% (w/v) over the seven day period. Overall, the qualitative and quantitative cell viability data showed that NG108-15 neuronal cells had optimal proliferation rates and lower numbers of dead cells in the 2.5% (w/v) GelMA hydrogels relative to ones with higher GelMA volume concentrations.

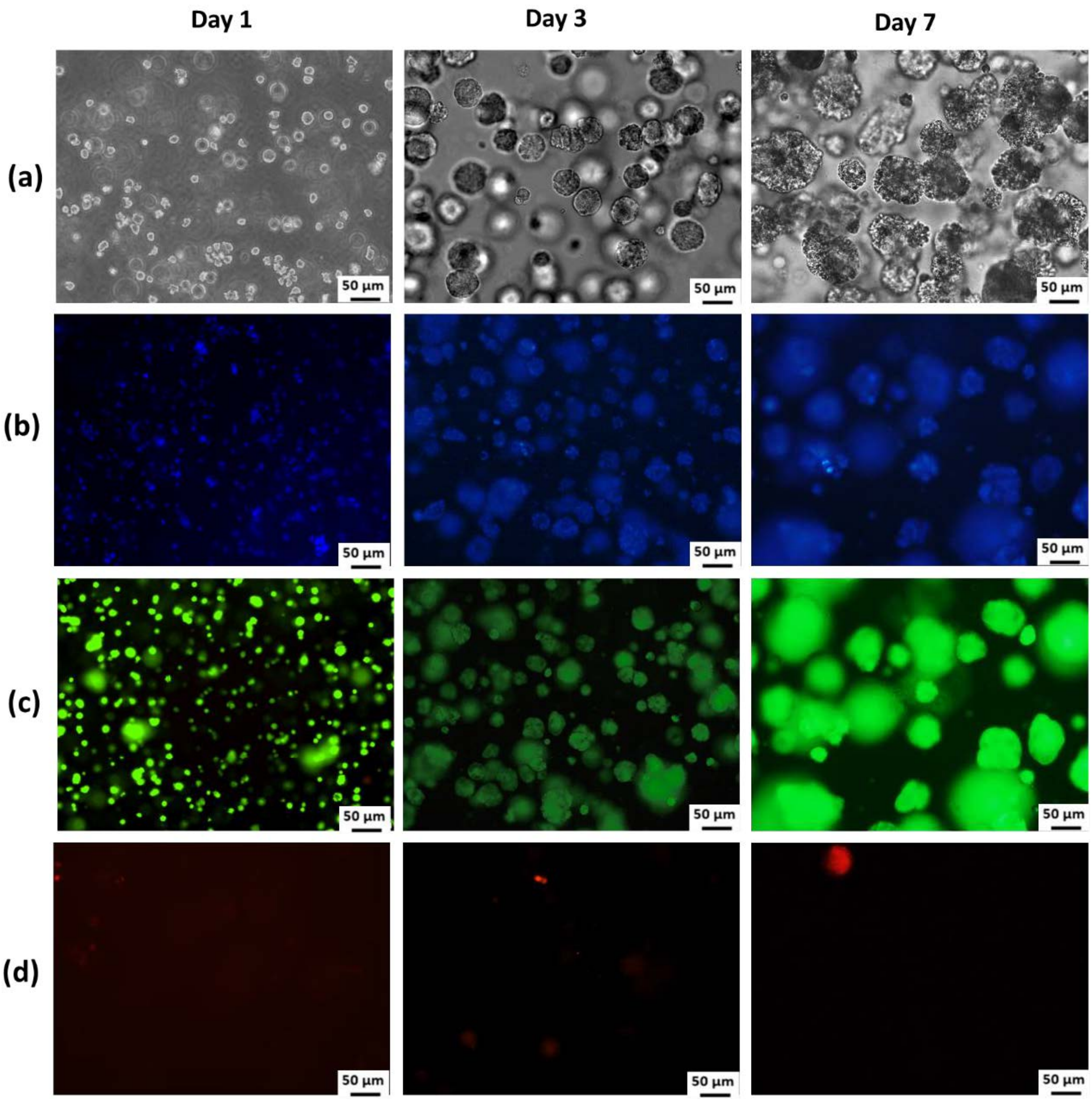

Figure 4.15. Representative bright-field (a) and fluorescence microscopy (b-d) images of NG108-15 neuronal cells at a concentration of 4 × 10^6 cells/mL embedded in a GelMA hydrogel with concentrations of 2.5% (w/v) at days 1, 3 and 7 at 37 °C, 5% (v/v) CO_2 in the air. (b) The nuclei were stained with Hoechst and are shown in blue. (c) The cytoplasm of live cells was stained with Calcein AM and is shown in green. (d) Dead cells were stained with propidium iodide and are shown in red.

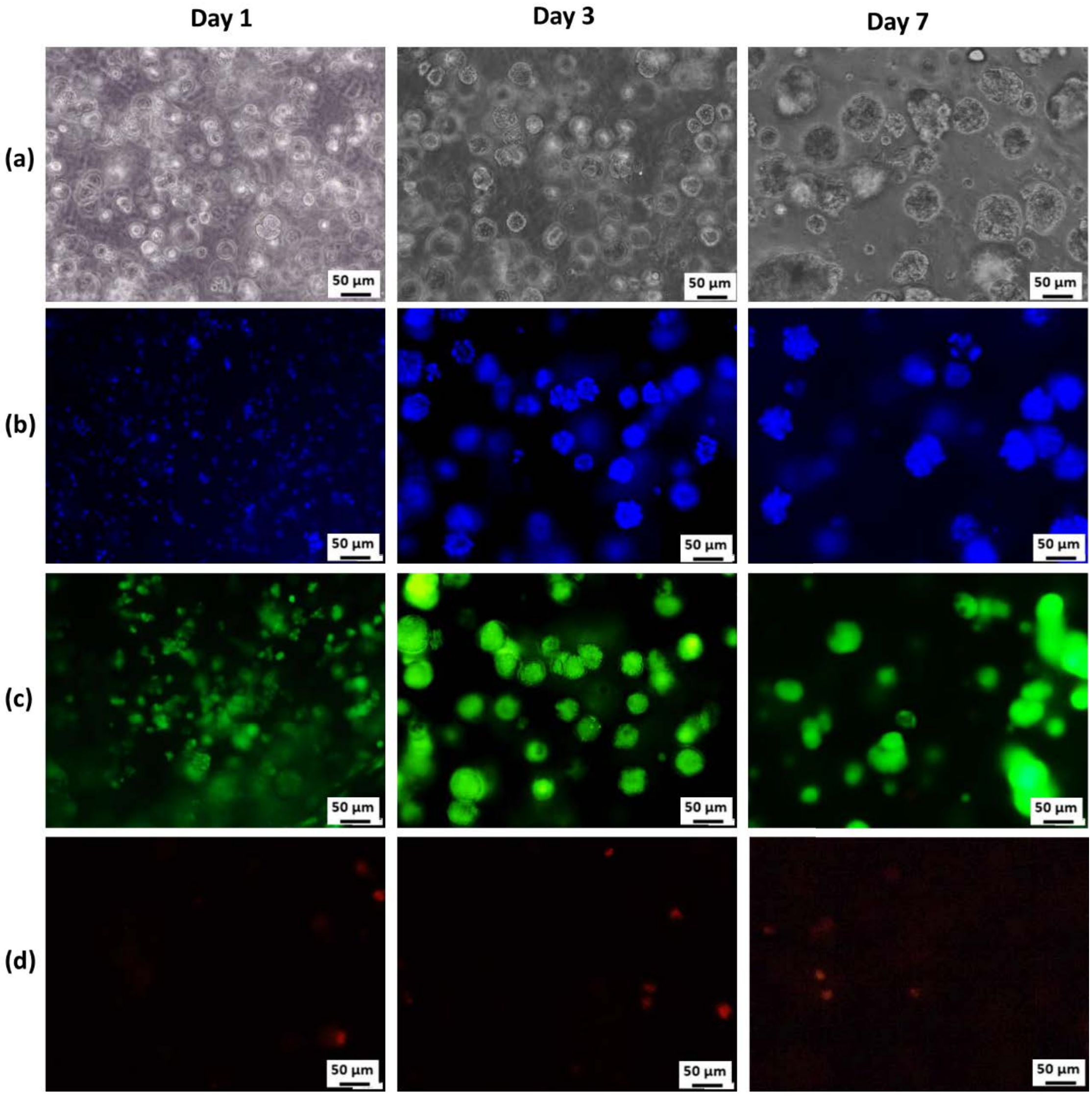

Figure 4.16. Representative bright-field (a) and fluorescence microscopy (b-d) images of NG108-15 neuronal cells at a concentration of 4 × 10^6 cells/mL embedded in a GelMA hydrogel with concentrations of 5% (w/v) at days 1, 3 and 7 at 37 °C, 5% (v/v) CO_2 in the air. (b) The nuclei were stained with Hoechst and are shown in blue. (c) The cytoplasm of live cells was stained with Calcein AM and is shown in green. (d) Dead cells were stained with propidium iodide and are shown in red.

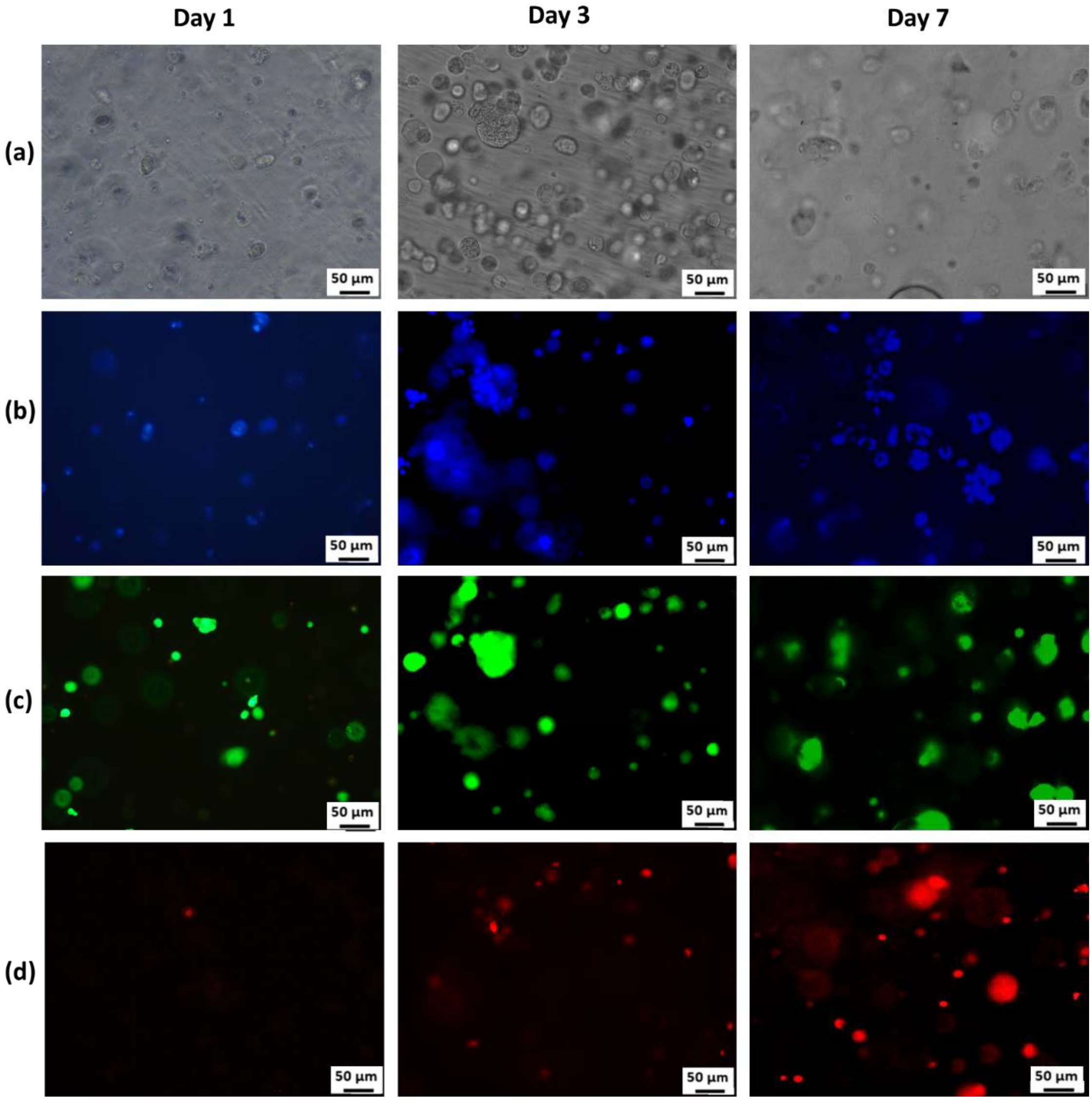

Figure 4.17. Representative bright-field (a) and fluorescence microscopy (b-d) images of NG108-15 neuronal cells at a concentration of 4 × 10^6 cells/mL embedded in a GelMA hydrogel with concentrations of 7.5% (w/v) at days 1, 3 and 7 at 37 °C, 5% (v/v) CO_2 in the air. (b) The nuclei were stained with Hoechst and are shown in blue. (c) The cytoplasm of live cells was stained with Calcein AM and is shown in green. (d) Dead cells were stained with propidium iodide and are shown in red.

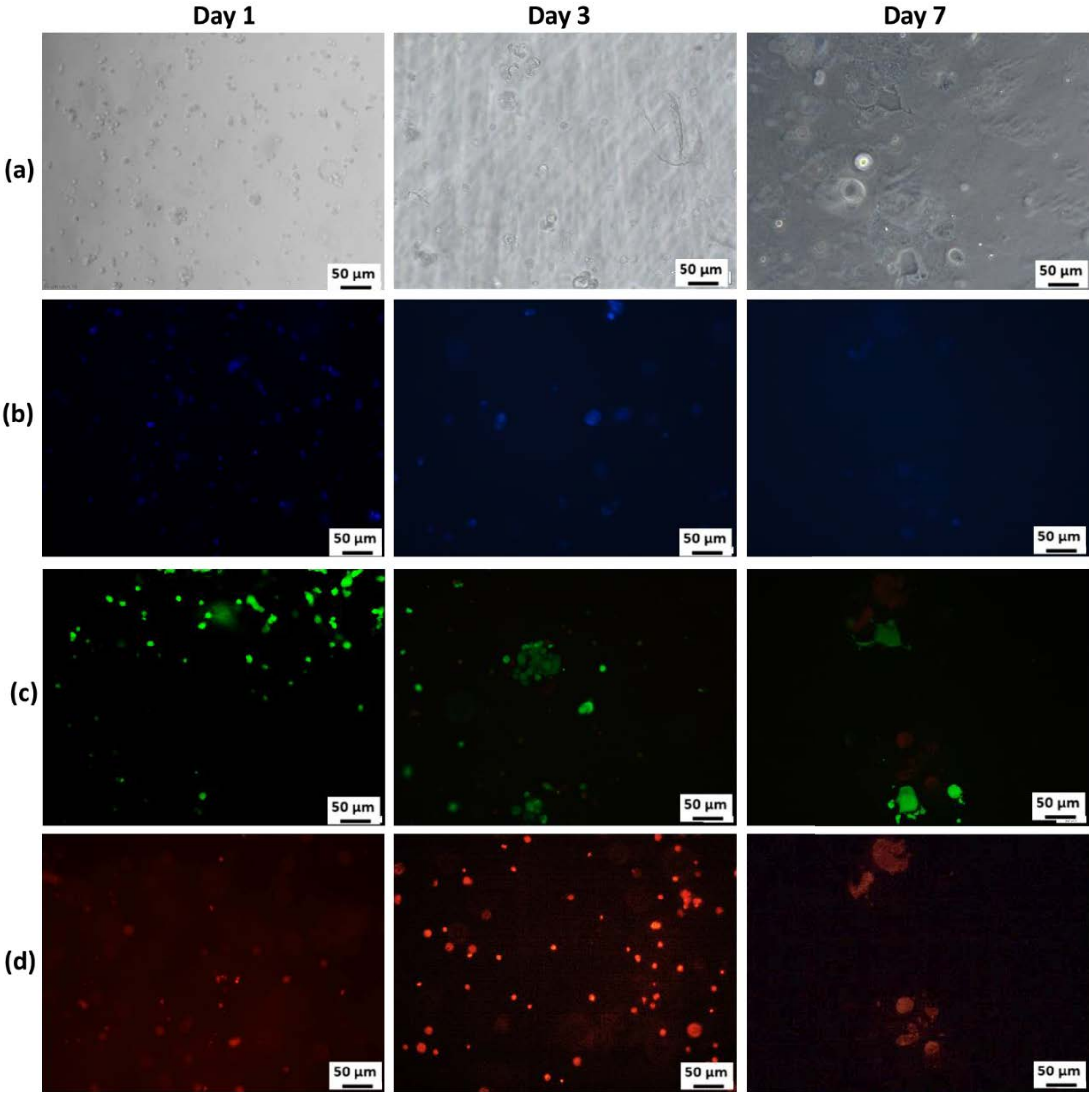

Figure 4.18. Representative bright-field (a) and fluorescence microscopy (b-d) images of NG108-15 neuronal cells at a concentration of 4 × 10^6 cells/mL embedded in a GelMA hydrogel with concentrations of 10% (w/v) at days 1, 3 and 7 at 37 °C, 5% (v/v) CO_2 in the air. (b) The nuclei were stained with Hoechst and are shown in blue. (c) The cytoplasm of live cells was stained with Calcein AM and is shown in green. (d) Dead cells were stained with propidium iodide and are shown in red.

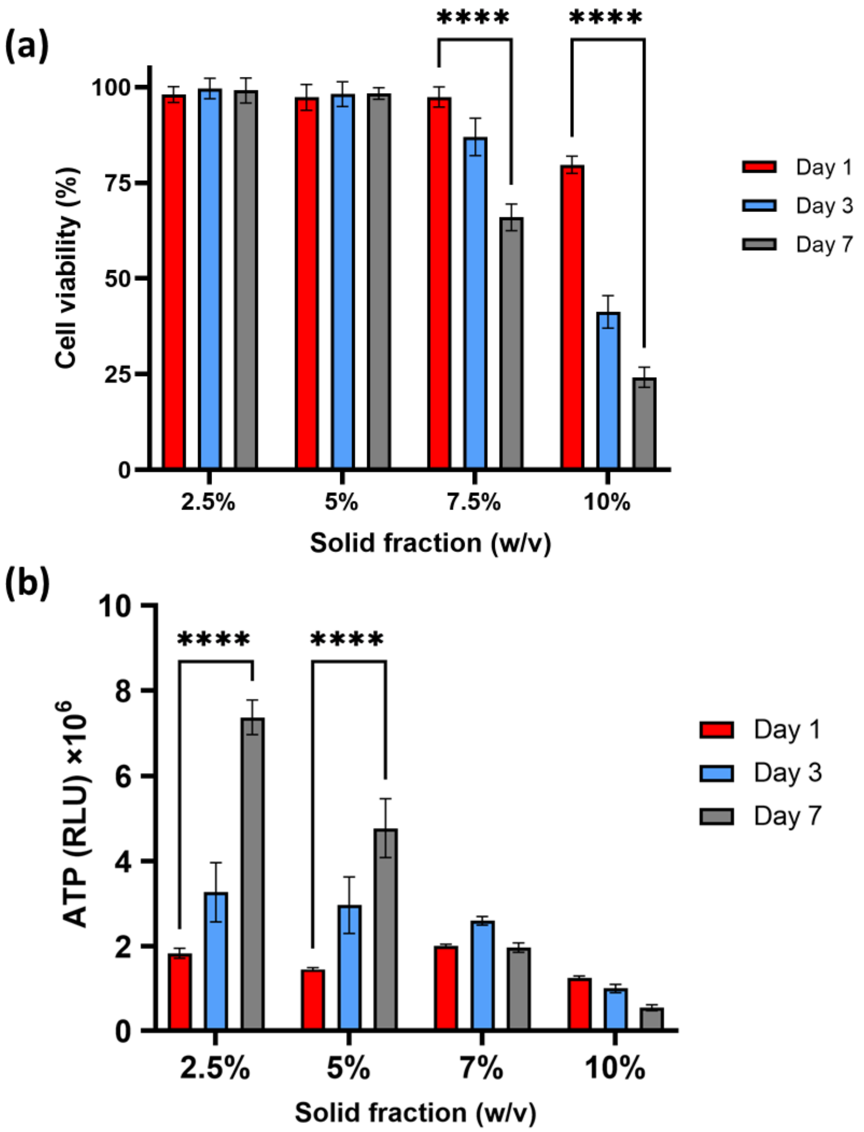

Figure 4.19. Quantification of (a) live/dead and (b) ATP cell viability assays results of NG 108-15 neuronal cells embedded at a concentration of 4 × 10^6 cells/mL in bioprinted GelMA hydrogels with various volume concentrations of 2.5, 5, 7.5 and 10 % (w/v). The bioprinted GelMA hydrogel samples were immersed with a culture medium and evaluated over 7 days of incubation at 37 °C, with 5% (v/v) CO_2 in air. Error bars indicate 95% confidence intervals; lines indicate statistical differences determined by two-way ANOVA, N = 3. Significance level: ****P<0.0001.

4.4.3 Determination of shape stability of bioprinted GelMA hydrogel scaffolds over time

The aim of this part of the study was to evaluate the stability of bioprinted GelMA hydrogel scaffolds over one week of culture. For this purpose, only GelMA hydrogel with volume concentrations of 2.5 and 5 % (w/v) that had good bicompatibility with C6 astrocyte-like and NG 108-15 neuronal cells were prepared and printed, as described in sections 4.3.2 and 4.3.3. Three printed samples of each volume concentration of 2.5 and 5 % (w/v) GelMA hydrogels were immersed in DMEM cell culture media containing 10 % (v/v) FBS and incubated at 37°C, 5% (v/v) CO_2 in air.

Light microscopy images of bioprinted GelMA hydrogel scaffolds embedded with C6 astrocyte-like cells at a concentration of 4×10^6 cells/mL over 7 days of incubation at 37 °C, 5% (v/v) CO_2 in air, are shown in Figure 4.20. 3D bioprinted cellular GelMA hydrogel scaffolds with a 5% (w/v) volume concentration retained structural stability over the 7 days, as shown in Figure 4.20 (a-c). As the images for 7.5% (w/v) and 10% (w/v) concentrations of GelMA were similar to that of 5% (w/v) GelMA, they were not included in the results. However, there was a lack of shape stability over 7 days of culture for GelMA hydrogels with 2.5% (w/v) volume concentration, as observed in Figures 4.20 (d-f). After 7 days of incubation, just a few areas of the scaffold with the 2.5 % (w/v) concentration remained, and the majority of the scaffold floated in the media (Figure 4.20 (f)). The bioprinted GelMA hydrogel scaffolds embedded with NG 108-15 neuronal cells at a concentration of 4×10^6 cells/mL over 7 days of culture are not shown, as similar results to C6 astrocyte-like cells were obtained.

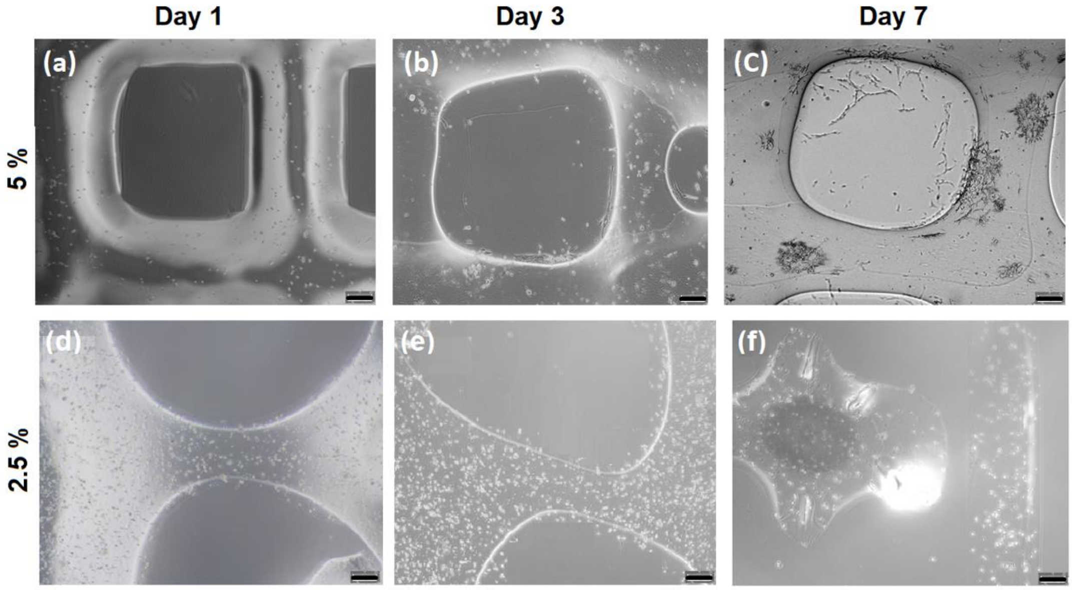

Figure 4.20. Light microscopy images of bioprinted GelMA hydrogel scaffolds with a volume concentration of (a-c) 5% (w/v) and (d-f) 2.5% (w/v) embedded with C6 astrocyte-like cells at a concentration of 4 × 10^6 cells/mL. The printed GelMA hydrogel scaffolds were immersed in DMEM cell culture media containing 10 % (v/v) FBS and incubated at 37 °C, 5% (v/v) CO_2 in the air over 7 days period. The scale bar is 200 μm.

4.5 Discussion

The aim of this chapter of the thesis was to optimise the 3D bioprinting process of GelMA hydrogels to form a basis for an in vitro spinal cord injury model. For this purpose, parameters like; printability to form reproducible 3D scaffolds, neuronal cell biocompatibility to allow attachment and proliferation of neural cells, structural stability to maintain the structure over extended incubation times, transparency to enable the observation of cell behaviour in a 3D system to allow analysis by fluorescent microscopy, were investigated.

4.5.1 Assessment of printability of GelMA hydrogels

The effect of printing parameters such as printhead temperature, printing pressure and printing speed on the printability of GelMA hydrogels with various volume concentrations of 2.5, 5, 7.5,10 and 15 % (w/v) were investigated. The results illustrated that the optimal printhead temperature was directly proportional to the volume concentrations of GelMA hydrogels. For instance, excessive printhead temperature (~ 32 °C) were required to extrude the bio-inks with very high viscosity (e.g. volume concentrations of 15 % (w/v)). Otherwise, a very low temperature (e.g. 22 °C) was needed to extrude the bio-inks with very low viscosity (e.g. volume concentrations of 2.5 % (w/v)). When the temperature deviated slightly from optimal temperature, the GelMA hydrogels barely formed regular filaments, so the printability became relatively poor. This is due to the shear-thinning properties of GelMA hydrogels [247]. When the temperature is higher than the sol-gel (gelation) temperature, GelMA becomes liquid, and when temperatures are lower than the sol-gel temperature, it becomes too solid [248]. However, GelMA hydrogels printed in a the solid gel phase offered structural integrity to grid patterns before crosslinking [249].

The bioprinting pressure and speed also played a decisive role in printability which has been extensively investigated in other studies [250, 251]. As described in this chapter, the linewidth of bioprinted GelMA hydrogels was directly proportional to the printing pressure, while it was inversely proportional to printing speed. The optimal printing pressure and speed for each volume concentration of GelMA hydrogel were obtained to fabricate grid patterns with high resolution. However, higher printing pressures than optimal pressure caused an overflow, spreading and filling the gaps in the grid pattern. On the other hand, printing pressures lower than optimal pressure did not provide enough force to extrude the bioink for the formation of the desired pattern, and it caused intermittent printing. Alternatively, when the printing speed was too high, the extruded filament did not stay with the perimeter as the nozzle was moving too quickly for the filament to form a bond which led to discontinuous filaments.

In addition, an issue with printed soft GelMA scaffolds (2.5% (w/v)) was instability in culture media over time. The GelMA hydrogels with a volume concentration of 5 % (w/v) provided better shape fidelity after printing and maintained shape post-printing over 7 days of incubation time. This was attributed to the higher stiffness of 5% (w/v) GelMA hydrogels compared to 2.5% (w/v), which will be discussed in terms of their mechanical properties in the next chapter.

The findings of this part of study are consistent with other research in the field that has investigated the effect of printing parameters on the printability of hydrogels. For instance, a study by Janmaleki et al. (2020) investigated the effect of printing parameters on the printability of GelMA hydrogels and showed that the optimal printing temperature was dependent on the GelMA concentration [252]. Similarly, other studies have reported that bioprinting pressure and speed affect the printability of hydrogels, and their optimization is crucial for achieving high-resolution structures. In a study by Noh et al.

(2019), the researchers investigated the effect of printing pressure and speed on the printability of a hyaluronic acid-based hydrogel [253]. They found that an optimal printing pressure and speed were necessary to achieve high-resolution structures, and that deviations from these parameters resulted in decreased print quality. Similarly, in a study by Naghieh et al. (2020), the researchers investigated the effect of various printing parameters on the printability of alginate hydrogels [254]. They found that the optimal printing speed and pressure were dependent on the alginate concentration, and that deviations from these parameters resulted in decreased print quality and structure resolution.

Overall, these studies highlight the importance of optimizing printing parameters for hydrogels in order to achieve high-quality structures with good resolution and mechanical stability. The findings of this study on GelMA hydrogels are consistent with these previous studies, further emphasizing the importance of carefully selecting and optimizing printing parameters for successful bioprinting of hydrogels.

4.5.2 Assessment of NG 108-15 Neuronal and C6 astrocyte-like cell viability within bioprinted GelMA hydrogels

Cell viability is another important issue to be considered for the fabrication of 3D bioprinted constructs. The potential of bioprinted GelMA hydrogels in terms of biocompatibility to support both NG108-15 neuronal and C6 astrocyte-like cell viability and attachment was assessed. Over seven days of *in vitro* culture, the viability of the GelMA-encapsulated with both cells at different concentrations was evaluated. The viability, morphology, and proliferation rate of cells exhibited dependence on the solid fraction of the GelMA hydrogel. The quantitative and qualitative cell viability results presented in this study indicated that both cell lines in the stiffer hydrogels (7.5 % and 10 % (w/v)) were minimally proliferative compared to cells in the softer hydrogels (2.5 % and 5 % (w/v)).

Other studies also demonstrated that the stiffness of a cross-linked bioprinted constructs is an essential property in deciding the cellular activity, which can influence cell migration and proliferation [255, 256]. Banerjee and co-workers showed that the proliferation of neuronal stem cells decreased as alginate hydrogel stiffness increased [93]. In this study, they prepared GelMA hydrogels at three concentrations of 5, 10, and 15% (w/v) by adjusting the ratio of methacrylate. They observed the most significant enhancement in the neuronal marker β-tubulin III expression within hydrogels with elastic modulus comparable to brain tissues (100-1000 Pa). In another study, Celikkin et al. [257] explored the effect of polymer concentration of GelMA scaffold on osteogenic differentiation. The authors demonstrated that a 5% (w/v) GelMA concentration elicited higher and more homogenous ECM calcification than the 10% GelMA concentration, as the softer substrates promoted mesenchymal stem cell (MSC) attachment on the scaffolds [257]. Possible reasons for low cell proliferation are low hydrophilicity and the wettability of stiff GelMA hydrogels (high volume concentrations) [258]. Further increasing the GelMA concentration to 10 % (w/v) caused a denser pore structure in the matrix, resulting in limited degradability and permeability characteristics for the hydrogels, impeding cellular migration and morphogenesis. Xu et al., demonstrated that 5% (w/v) GelMA hydrogels had the highest hydrophilicity and wettability compared to 10 and 15 % (w/v), thereby facilitating the penetration of nutrients and oxygen [259].

In addition, the bright-field and fluorescence microscopy images of NG108-15 neuronal cells embedded within various concentrations of GelMA hydrogels showed that cells were rounded and had a spheroid shape in softer hydrogels (2.5% and 5% (w/v)), which may have been due to the decreased numbers of arginine-glycine-aspartic acid (RGD) sequences and matrix metalloproteinase (MMP) in the lower volume concentrations hydrogels. It has been demonstrated that the addition of RGD (an integrin ligand) into the hydrogel networks can lead to increased cell adhesion, proliferation, migration, and matrix production [260]. However, C6 astrocyte-like cells displayed flattened spindle-like morphology after seven days. Previous studies also demonstrated that astrocytes were elongated and proliferated in bioprinted GelMA hydrogels with low concentrations (2.5 and 3.0 wt %) [261]. Therefore, it seems that the morphology of cells in 3D depends on the cell type. For instance, it was shown that Human epithelial cancer cells (MCF-7) grow naturally into 3D aggregates/spheroids in a 3D hydrogel environment, and the natural shape is retained [262].

4.5.3 The relationship between printability, structural stability and cell viability

In this chapter of the thesis, printability, biocompatibility and structural stability 3D bioprinted GelMA hydrogels with volume concentrations of 2.5, 5, 7.5,10 and 15 % (w/v) were assessed to form the basis for an in vitro 3D spinal cord injury model. The relationship between these factors with different GelMA concentrations is shown in Table

4.3 Generally, the GelMA concentrations with 5, 7.5 and 10 % (w/v) resulted in higher printability and structural stability than 2.5 % (w/v) GelMA concentration. On the other hand, the 2.5 % (w/v) GelMA concentration resulted in excellent biocompatibility and transparency. As shown in Table 4.3, only GelMA hydrogels with 5 % (w/v) concentration met all eligibility criteria for this research. However, the mechanical properties of 3D bioprinted GelMA hydrogel matrices are another critical factor that needs to be investigated to determine whether the bioprinted GelMA hydrogel is similar to native tissue. The mechanical assessment of 3D bioprinted GelMA hydrogels using Brillouin microspectroscopy, which is a non-invasive and label-free method, will be presented in the next chapter.

Table 4.3. Relationship between printability, cell viability and structural stability of scaffolds with different GelMA concentrations.

GelMA Concentration (W/V %)	**Printability**	**Cell viability**	**Structural stability**
Section	**4.4.1**	**4.4.2.**	**4.4.3**
2.5 %	x	✓	x
5 %	a	✓	✓
7.5 %	✓	x	✓
10 %	✓	x	✓

4.6 Key findings

- Printability was inversely related to the volume concentration of GelMA hydrogels. GelMA hydrogels with 2.5 % (w/v) volume concentration showed minimal printability and stability of 3D constructs over 7 days of incubation at 37 °C, 5% (v/v) CO_2 in air.

- The quantitative and qualitative cell viability results presented in this study indicated that both C6 astrocyte-like and NG 108-15 neuronal cells were minimally proliferative in the stiffer printed GelMA hydrogels (7.5 % and 10 % (w/v)) compared to softer printed GelMA hydrogels (2.5 % and 5 % (w/v)).

- The bioprinted GelMA hydrogel with 5% (w/v) concentration was the most appropriate matrix for a 3D in vitro spinal cord injury model due to optimal printability and structural stability over time, in addition to high cell viability, and adequate transparency.

CHAPTER 5 MECHANICAL ASSESSMENT OF 3D BIOPRINTED GELMA HYDROGELS USING RHEOLOGY AND BRILLOUIN MICROSPECTROSCOPY

5.1 Introduction

One of the major factors that needs to be considered in designing a 3D *in vitro* spinal cord injury model (SCI) is that the mechanical properties of the construct should be similar to the native neural extracellular matrix (ECM). Neural ECM has distinctive mechanical properties, such as low elastic modulus neural tissue (~ 0.1 - 4.8 kPa) [263-265] and larger porosity than other tissues, such as the heart, cartilage, and bones. Therefore, characterising the micromechanical properties of 3D constructs is valuable for dictating the success of modelling outcomes in relation to the accurate reproduction of the biological processes in native tissues. However, characterising the micromechanical properties of such models non-destructively and over a prolonged span of time are key challenges.

5.2 Aim and objectives

5.2.1 Aim

The aim of this chapter was to assess the micromechanical properties of 3D bioprinted acellular and cellular GelMA hydrogels encapsulating NG 108-15 neuronal cells using a non-destructive method such as Brillouin microspectroscopy (BM). The overall aim of the previous and the current chapter (chapters 4 and 5) was to design a 3D GelMA matrix for future investigations into the effect of mechanical injury on cells (neuronal and astrocytes) within a 3D matrix.

5.2.2 Objectives

The specific objectives of this chapter of the thesis were to:

1) Investigate the mechanical properties of acellular GelMA hydrogels using BM.
2) Investigate the mechanical properties of cellular GelMA hydrogel environment consisting of NG 108-15 neuronal cells using BM at bulk scale.
3) Investigate the mechanical properties of cellular GelMA hydrogel environment consisting of NG 108-15 neuronal cells using BM at local micro-scale.
4) Compare mechanical properties obtained from BM with unconfined compression and rheology.

Four critical criteria were used to guide the development of an *in vitro* spinal cord injury model:

- There was a requirement to measure the mechanical properties of bioprinted acellular GelMA hydrogels using a non-destructive method to understand which volume concentration of hydrogels can mimic a similar stiffness to neural tissue for use within a 3D injury model.

- There was a requirement to assess the mechanical integrity of printed cellular GelMA hydrogels constructs over 7 days in culture. Long-term stable structures cause hydrogels to be more predictable and reliable as a matrix component for a 3D spinal cord injury model.

- There was a requirement to assess the local stiffness changes of bioprinted cellular GelMA hydrogels to resolve individual cells and the surrounding hydrogel. Measuring the stiffness of the matrix around cells can help us interpret biological results, such as the effect of matrix stiffness on GFAP expression after injury.

- There was a requirement to use a conventional method like rheology to understand the reliability of the BM data. Acellular GelMA hydrogels were measured by rheology to eliminate the effect of cells on hydrogels.

5.3 Materials and Methods

5.3.1 Brillouin microspectroscopy system

The GHz frequency viscoelastic properties of cellular and acellular GelMA hydrogel samples were assessed using Brillouin microspectroscopy (BM). This system was used to collect the spontaneous Brillouin scattering spectra and comprised of a single-frequency solid-state laser (Torus, 660 nm), a confocal microscope (CM1, JRS Instruments), a 3D scanning microscopy stage (SmarAct), and a tandem Fabry-Perot interferometer (TFP1, JRS Instruments) (Figure 5.1(a)). A schematic of the BM is illustrated in Figure 5.1(b), which shows the Brillouin spectrometer, laser, objective lens, PBS-polarisation beam splitter and $\lambda/4$quarter-wave plate. The spectrometer resolution was approximately 360 MHz, and the spectral extinction ratio was above 10^{10}.

Objective lenses of 20X (Mitutoyo, Numerical Aperture (NA) = 0.42, WD = 20 mm) and 60X (Nikon, WD = 2.8 mm, NA = 1) were utilized for bulk (volume large-VA) and local micromechanical characterisation of hydrogels, respectively. The term local micro-scale imaging set-up refers to the measurements with sufficient resolution (focal volume of approx. 3 μm^3) to resolve individual cells and the surrounding hydrogel. The term bulk mechanical characterisation refers to the measurements with a low NA microscope objective lens that leads to averaging of the information of the microscopic nature of the material across a relatively large volume (approx. 200 μm^3). In addition, the axial resolution of the Brillouin system was approximately 120 µm and 12 µm for the objective lens of 20X and 60X, respectively. The lateral resolution (XY plane) for the BM system was estimated to be below 2 µm for both objective lenses. The laser power for acellular hydrogel samples was 100 mW, and for cellular hydrogel samples, this was kept at less than 20 mW to avoid sample damage by incident radiation.

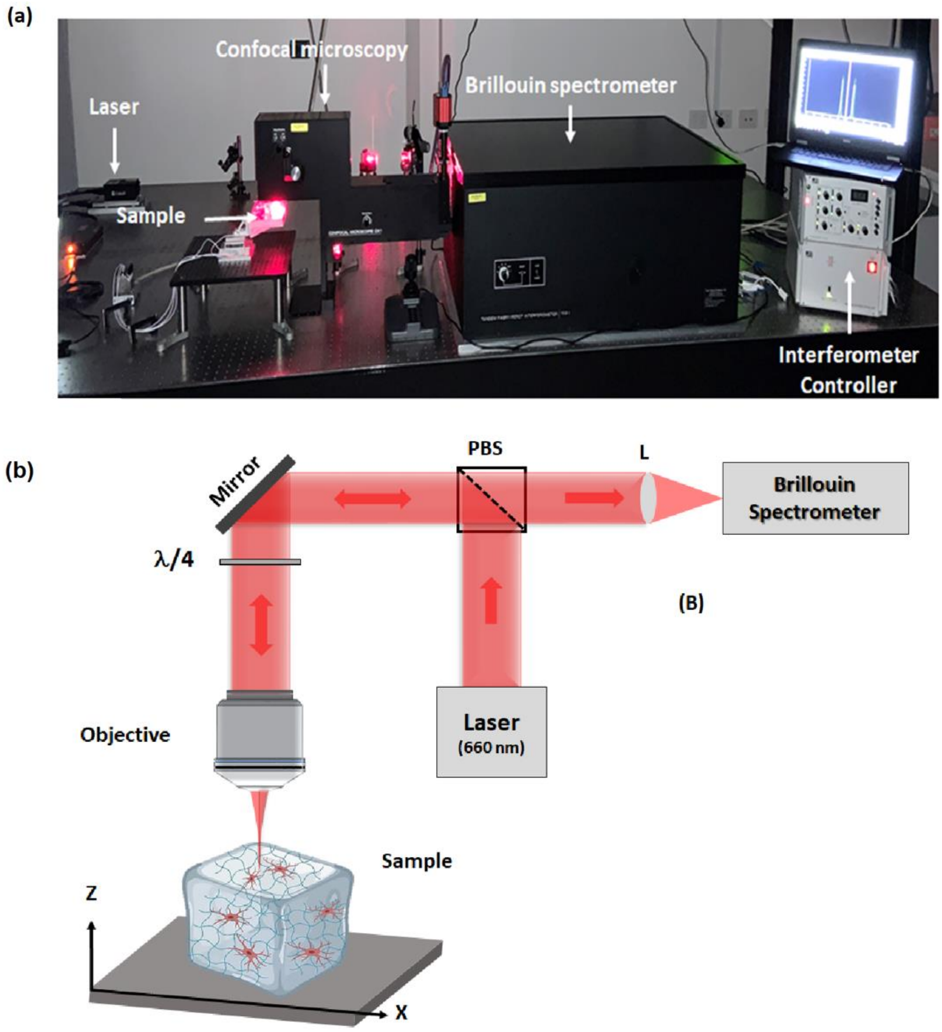

Figure 5.1. (a) The Brillouin microspectroscopy (BM) system. (b) Schematic of Brillouin microspectroscopy. Notations used: L-lens, PBS-polarisation beam splitter, λ/4 - quarter-wave plate.

A spontaneous Brillouin light scattering spectrum consists of two signals located at lower (Stokes, -Ω) and upper (Anti-Stokes, Ω) Brillouin frequency with respect to the incident light frequency (for simplicity, adjusted to be at 0 GHz) as shown in Figure 5.2. Two independent parameters can be extracted from the Brillouin spectrum: Brillouin frequency shift (BFS) and Brillouin linewidth (Γ), which are determined from the exact position and linewidth of Stokes and Anti-Stokes peaks, respectively. The frequency shift of Brillouin peaks can be presented as [266]:

$$\Omega = \pm Vq \qquad \text{Eq. (5.1)}$$

where V is the longitudinal acoustic velocity and q is the exchanged wavevector given by

$$q = \frac{4\pi n}{\lambda} \sin(\frac{\theta}{2}) \qquad \text{Eq. (5.2)}$$

Here n is the refraction index, λ is the incident wavelength, and θ is the scattering angle, which is equal to θ=180° (backscattering) in the utilised optical set-up, so that $\sin\left(\frac{\theta}{2}\right) = 1$. The complex longitudinal viscoelastic modulus (M^*) is composed of elastic storage (M') and loss (M'') moduli. In addition, V is related to the material density ρ and M':

$$V = \sqrt{\frac{M¢}{\rho}} \qquad \text{Eq. (5.3)}$$

Therefore,

$$\Omega = \pm\sqrt{\frac{M'}{\rho}}(\frac{4\pi n}{\lambda}) \qquad \text{Eq. (5.4)}$$

where ρ is the mass density. Moreover, the Brillouin linewidth is expressed by

$$\Gamma = \frac{\eta}{2\rho}(\frac{4\pi n}{\lambda})^2 \qquad \text{Eq. (5.5)}$$

where η is the material dynamic viscosity. Based on the above equations, M' and M'' are given by:

$$M'(\Omega) = \rho V^2 = \rho\frac{\Omega^2}{q^2} = \rho\Omega^2\left(\frac{\lambda}{2n}\right)^2 \qquad \text{Eq. (5.6)}$$

$$M'' = \rho\,\Omega\left(\frac{\lambda}{2n}\right)^2\Gamma \qquad \text{Eq. (5.7)}$$

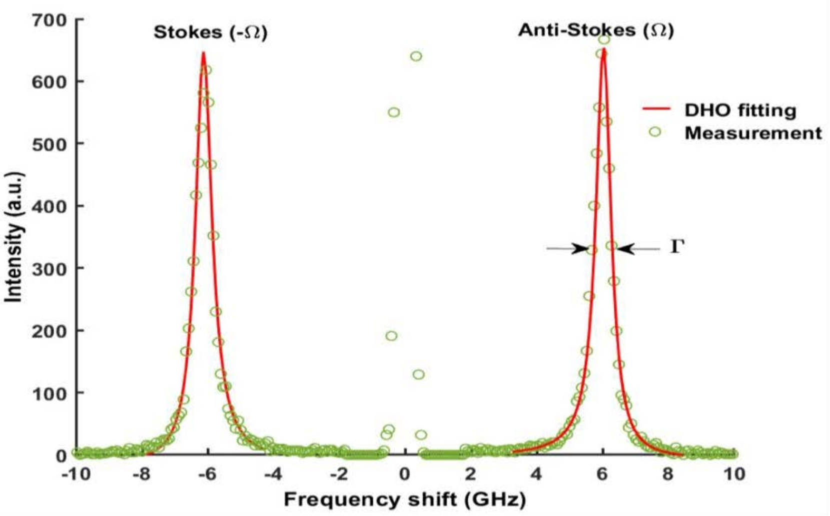

Figure 5.2. A typical Brillouin spectrum shows the Stokes and Anti-Stokes peaks fitting with the DHO model.

5.3.1.1 Sample preparation for BM

The acellular and cellular GelMA hydrogel samples with various volume concentrations from 2.5 to 15% (w/v) were bioprinted, as described in chapter 4, sections 4.3.2 and 4.3.3. Three samples for each volume concentration of GelMA hydrogel were printed to assess their mechanical properties using BM. For bulk measurements, hydrogels were printed in a 48-well plate, and a 20X objective lens was positioned at the top and outside of the well. In contrast, hydrogels were printed in a 6-well plate for microscale measurements to allow immersing the 60X objective lens into cell culture media and approaching the hydrogels.

5.3.1.2 Brillouin data collection modes

The BM data was acquired from single point and lateral line scan measurements using commercial Ghost (JRS Instruments) and custom-built software, respectively. Point measurement was used to measure the Brillouin frequency shift and the linewidth of the hydrogels at the bottom, middle and top of the samples while keeping both the microscope stage and optical system fixed. (Figure 5.3(a)). In contrast, the lateral line scan measurement was conducted along either x-axis of the microscope stage, which for a certain distance generates results for the Brillouin frequency shift and linewidth along with this distance. For the cellular hydrogel samples, the lateral scan was used to measure the cells and the surrounding hydrogel (Figure 5.3(b)).

The scan length of the cellular samples was determined by capturing the cell images through a CCD camera attached to the confocal microscope of the Brillouin system. The parameters of scan step size and acquisition time were required for the Brillouin line scans. The step size in the line scan was the distance between 2 steps within 1 scan and was selected based on the required resolution. For the scans with fine resolution, higher numbers of points were scanned, resulting in more information about the sample under study. For instance, a small step size (1 µm) was selected for cellular sample scans, in which the spheroid cell size was about 30 µm. The acquisition time of the scan is the time interval required to attain the Brillouin doublet signal, which was used to optimise the signal-to-noise ratio (SNR, >20) to improve the fitting precision and extract the measurable outputs of BM. The acquisition time for each scan was dependent on the strength of signals, and thus, stronger Brillouin signals were collected in a shorter acquisition time. In addition, it was clear that for a high number of sample points (1D and 2D scans), a relatively long scanning time was required. For instance, line scans could be time-consuming as an acquisition of 60 s along a distance of 30 µm took 30 minutes.

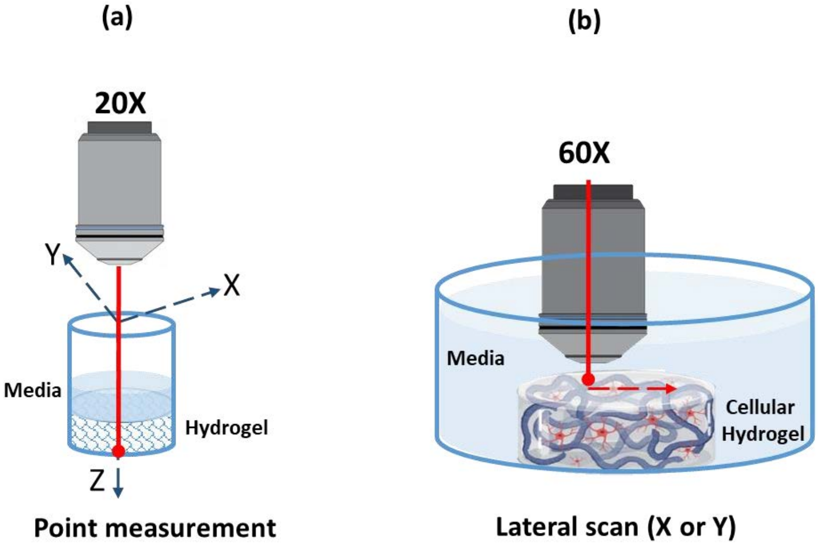

Figure 5.3. Schematic of Brillouin (a) Point measurement, (b) Lateral line scanning of the bioprinted cellular GelMA hydrogel samples.

5.3.1.3 Brillouin data processing

The collected Brillouin spectra data from point measurements were computationally processed using Ghost software (Figure 5.4). The frequency windows of Stokes and Anti-Stokes Brillouin peaks were selected on the spectrum (red marks), as shown in Figure 5.4(a). Then, the peak position and the linewidths were determined by curve fitting (Figure 5.4(b)) with a damped harmonic oscillator (DHO) model used for every Stokes and Anti-Stokes Brillouin peak. The curve fitting gives the half-width at half maximum (HWHM), which is defined as half of the linewidth, as shown in Figure 5.4(c). The longitudinal moduli M of the GelMA hydrogel samples was achieved using the Brillouin spectral shift and linewidth based on equations 5.6 and 5.7. For the Brillouin line scans, the data processing was performed using custom-built software, which in the BFS and LW were extracted during the scan and stored in the output file.

The measured Brillouin linewidths from the full-width at half-maximum (FWHM) of the raw data were broadened by the finite resolution of the instrument. This value was subtracted after the spectrometer linewidth was removed by deconvolution. Deconvolution is the process of filtering a signal to compensate for an undesired convolution. The goal of deconvolution is to recreate the signal as it existed before the convolution took place. Therefore, average linewidth parameters from Stokes and Anti-Stokes peaks were obtained after deconvolution of the instrumental response function, as shown in Figure 5.5. The spectrometer response has a Gaussian shape and a full width at half maximum of 0.37 GHz and was used to obtain natural Brillouin linewidth of samples (water, PBS, hydrogels). This was performed by deconvolution of the measured Brillouin linewidth with the spectral response function of the instrument.

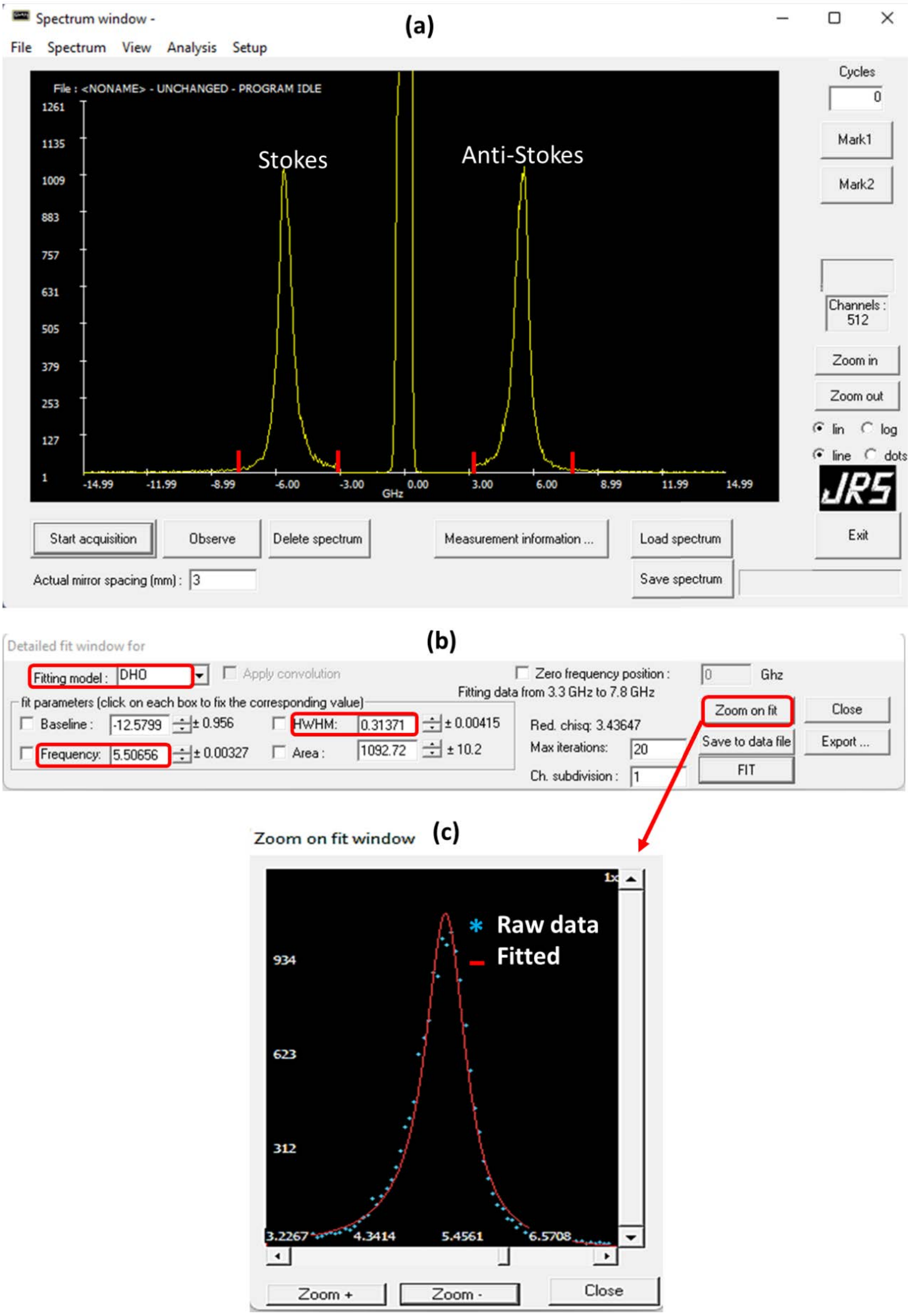

File : <NONAME> - UNCHANGED - PROGRAM IDLE

Cycles: 0

Channels : 512

● lin ○ log

● line ○ dots

Actual mirror spacing (mm) : 3

Fitting model : DHO

☐ Zero frequency position : 0 Ghz

Fitting data from 3.3 GHz to 7.8 GHz

fit parameters (click on each box to fix the corresponding value)

☐ Baseline : -12.5799 ± 0.956

☐ HWHM: 0.31371 ± 0.00415

☐ Frequency: 5.50656 ± 0.00327

☐ Area : 1092.72 ± 10.2

Red. chisq: 3.43647

Max iterations: 20

Ch. subdivision : 1

Figure 5.4. (a) Ghost software showing Stokes and Anti-Stokes peaks with Rayleigh peak. (b) Brillouin signal fitting to find the Brillouin shift and linewidth. (c) The fitting window shows the frequency shift and half-width at half maximum (HWHM) of the peak.

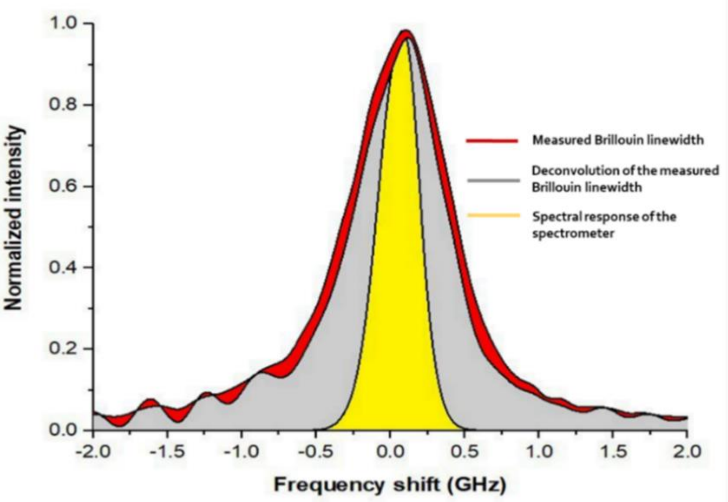

Figure 5.5. The spectral response of the spectrometer and measured and deconvoluted Brillouin signal.

5.3.2 Mechanical characterisation of GelMA hydrogels using conventional techniques

5.3.2.1 Sample preparation for compression and rheology tests

In this work, TA Instruments Dynamic Hybrid Rheometer (DHR-3, TA Instruments) (Figure 5.6) was used to perform the unconfined compression and rheology tests. A Rheometer contains a motor to rotate a cone or plate above the sample. For this analysis, disk-shaped GelMA hydrogels (~8 mm in diameter) with a height of approximately 1 mm were bioprinted (Figure 5.7(a)), as described in chapter 4, section 4.3.3. The gels were trimmed to the correct size using an 8 mm biopsy punch. The hydrogel sample was placed between the top and bottom plates, and the TA computer software was used to move the top plate so that it was just in contact with the surface of the sample, as shown in Figures 5.7(b) and (c). Finally, an axial force was applied to the hydrogel until reaching a stable force of 0.03 N (Figure 5.7(d)). On the same day, samples were also analysed using Brillouin microspectroscopy so that hydrogels had the same swelling conditions.

Figure 5.6. The Discovery Hybrid Rheometer HR-3. The inset shows the main components of the rheometer and a GelMA hydrogel sample under investigation.

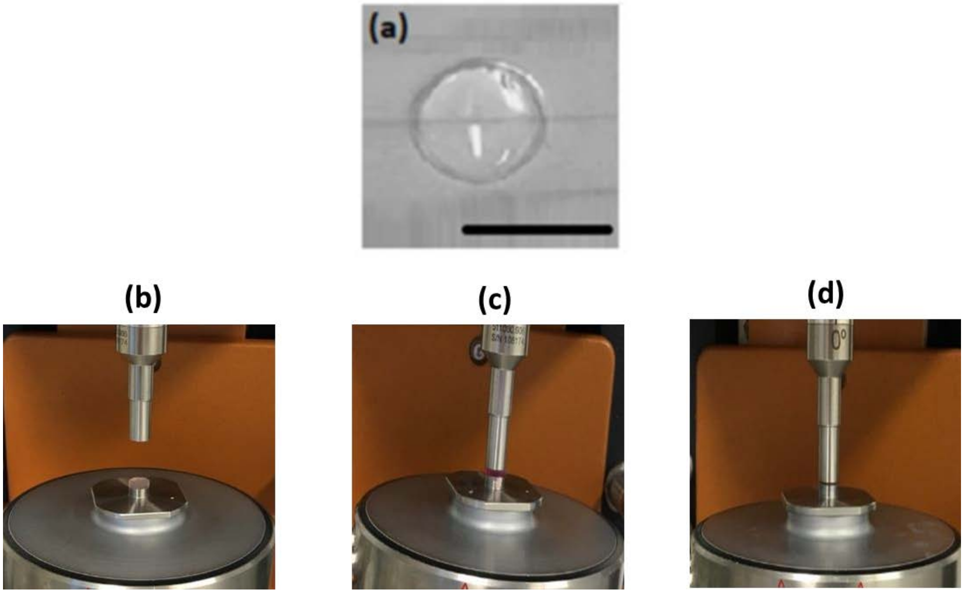

Figure 5.7. Rheology set-up. (a) A bioprinted disc-shaped hydrogel sample was trimmed using an 8 mm biopsy punch. (b) The sample was placed between the top and bottom plates. (c) Lowering of the upper geometry to touch the surface of the sample. (d) The axial force was applied to the hydrogel.

5.3.2.2 Characterisation of GelMA hydrogels using unconfined compression

An unconfined compression test (Figure 5.8(a)) was utilised to obtain Young's modulus (kPa) of acellular hydrogel samples, which is a measure of the stiffness of an elastic material. Young's modulus (or Elastic modulus) is equal to the longitudinal stress divided by the strain (relative deformation). This elastic deformation is a change due to the application of an external force, even very small forces. Stress (σ) is the ratio of applied force (F_V, Vertical force) to a cross-section area (A),

$$\sigma = \frac{F_V}{A} \tag{5.8}$$

and strain (ε) is defined as the ratio between the deformation (ΔL) along the length (L) of applied stress to the original dimension (L_0),

$$\varepsilon = \frac{\Delta L}{L_0} \tag{5.9}$$

The relationship between stress and strain for material is given by a stress-strain curve. For small values of strain (elastic region), the curve is linear, and the gradient of the line expresses Young's elastic modulus (E), as shown in Figure 5.8(b). Elastic materials maintain constant stress, and the relationship between stress and strain is expressed by Hooke's law,

$$\sigma = E\,\varepsilon \tag{5.10}$$

In this work, Young's modulus (kPa) of acellular GelMA hydrogel samples (N = 3) was obtained by measuring the stress-strain curves of a hydrogel and then finding the slope from the linear region of the stress-strain curve. The compression rate was 10 mm/min, and data output was in the form of axial force (N) and gap (the distance between the top and bottom plate geometries, mm). All samples were measured at 25° C and on the same day. The data was analysed, and a stress/strain curve for each replicate hydrogel was obtained.

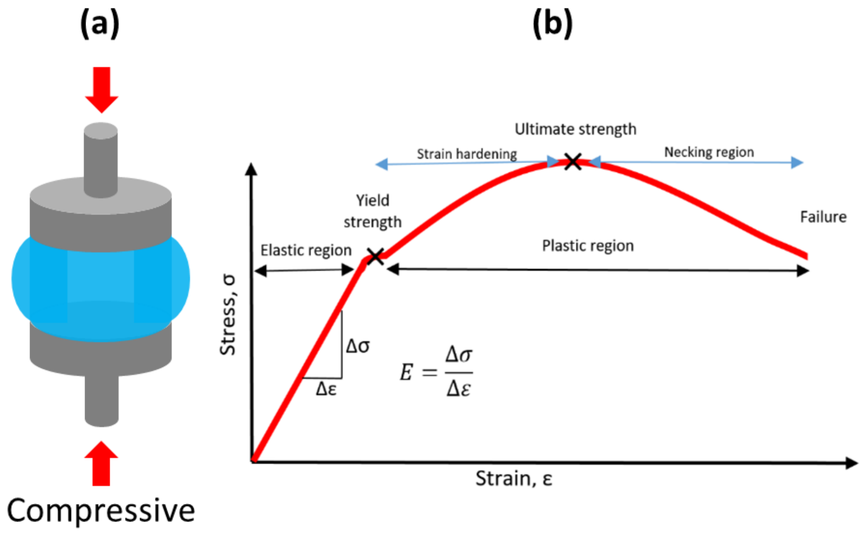

Figure 5.8. (a) Schematic of the sample under compression test. (b) A typical strain-stress curve for the compressive test.

5.3.2.3 Characterisation of GelMA hydrogels using rheology

Hydrogels are viscoelastic materials that exhibit both properties of elastic solids and viscous liquids. Viscous materials exhibit time-dependent strain, and shear flow occurs due to the application of a shear force on the fluid. The shear force (F_L, Lateral force) that is applied over a unit area (A) of the fluid is described as shear stress (τ) (Equation 5.11). Since both the bottom and top fluid layers do not respond to this force simultaneously, a displacement gradient (x/h) is formed through the sample, which is known as shear strain (γ). The shear rate ($\dot{\gamma}$) is a velocity gradient that is given as a differential of strain with respect to time based on equation (5.6).

$$Shear\ stress \quad \tau = \frac{F_L}{A} \tag{5.11}$$

$$Shear\ strain \quad \gamma = \frac{X}{h} \tag{5.12}$$

$$Shear\ rate \quad \dot{\gamma} = \frac{d\gamma}{dt} \tag{5.13}$$

Hence, the shear modulus is defined as the ratio of shear stress to shear strain:

$$Modulus = \frac{shear\ stress}{shear\ strain} \tag{5.14}$$

and the viscoelastic properties of the material are expressed using the complex modulus (G^*):

$$G^* = G' + G'' \tag{5.15}$$

where G' is the shear storage modulus, and a measure of the stored energy (elastic portion), and G'' is the shear loss modulus and is the dissipated heat energy (viscous portion).

In order to investigate the mechanical properties of the GelMA hydrogel matrices using rheology, it was necessary to determine the Linear Viscoelastic Region (LVER) for each hydrogel sample. The LVER is determined from an experiment by performing a stress or strain sweep test and observing the plateau portion of the graph before the material deformation (Figure 5.9). The limit of the linear viscoelastic region corresponds to the point at which G' becomes stress or strain-dependent. Amplitude sweeps were performed at a fixed oscillation frequency of 0.159 Hz for strain amplitudes ranging from 0.2 % to 2%. This determined the shear strain range which was within the LVER before the deformation of the material occurred.

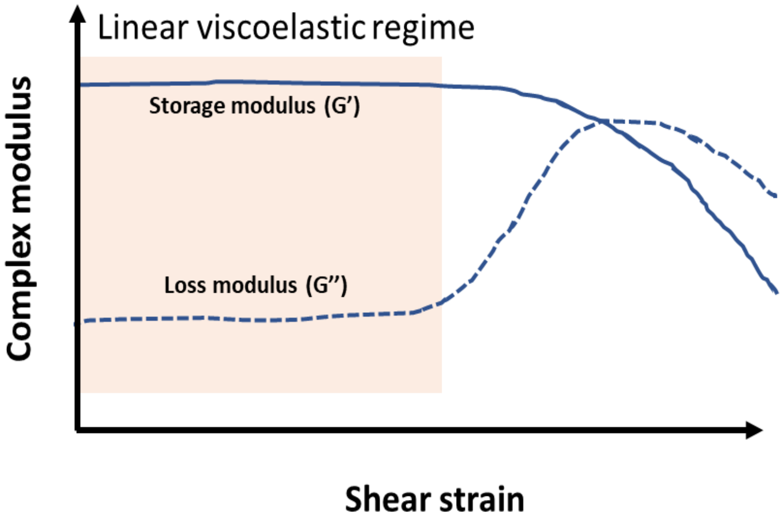

Figure 5.9. The Linear Viscoelastic Region (LVER).

5.4 Results

5.4.1 Micromechanical assessment of bioprinted acellular GelMA hydrogels using Brillouin microspectroscopy

One of the experimental questions considered in this part of the study was whether the mechanical properties of the GelMA hydrogels were similar to the stiffness of neural tissue for use within a 3D injury model. To answer this question, the effect of UV cross-linking exposure time, GelMA volume concentration, and incubation time on the mechanical properties of bioprinted acellular GelMA hydrogels were investigated using BM. For this purpose, three samples for each volume concentration of acellular GelMA hydrogels were printed, as described in section 4.3.3.

5.4.1.1 Effect of UV cross-linking duration on micromechanical properties of bioprinted acellular GelMA hydrogels using Brillouin microspectroscopy

The effect of UV cross-linking exposure time on the micromechanical properties of bioprinted acellular GelMA hydrogels with various volume concentrations of 2.5-15 % (w/v) was investigated using BM. The bioprinted hydrogels were cross-linked using UV light at a wavelength of 365 nm and an intensity of 19.42 mW.cm^{-2} for between 30 s to 300 s. As shown in Figure 5.10, a significant difference was observed in the Brillouin frequency shift (BFS) values between the samples which were cross-linked with UV for 120 s and those not exposed to UV light for gels of all solid fraction concentrations. However, this difference in BFS was found to be more significant for volume concentrations equal to or above 5% (w/v) ($P< 0.0001$) compared to 2.5% (w/v) ($P< 0.05$). The results presented in Figure 5.10 demonstrated the minimum time for cross-linking the bioprinted GelMA hydrogels with volume concentrations of 2.5, 5, 7.5, 10, and 15 % (w/v) was 120 s, 120 s, 90 s, 90 s and 30 s, respectively. It is concluded that significant crosslinking can be induced for all gel concentrations with a 120 s exposure time, which is the shortest time. Since the shortest exposure is also the safest for the cells as this induces minimal photodamage, we have chosen 120 s exposure as optimal condition for gel cross-linking.

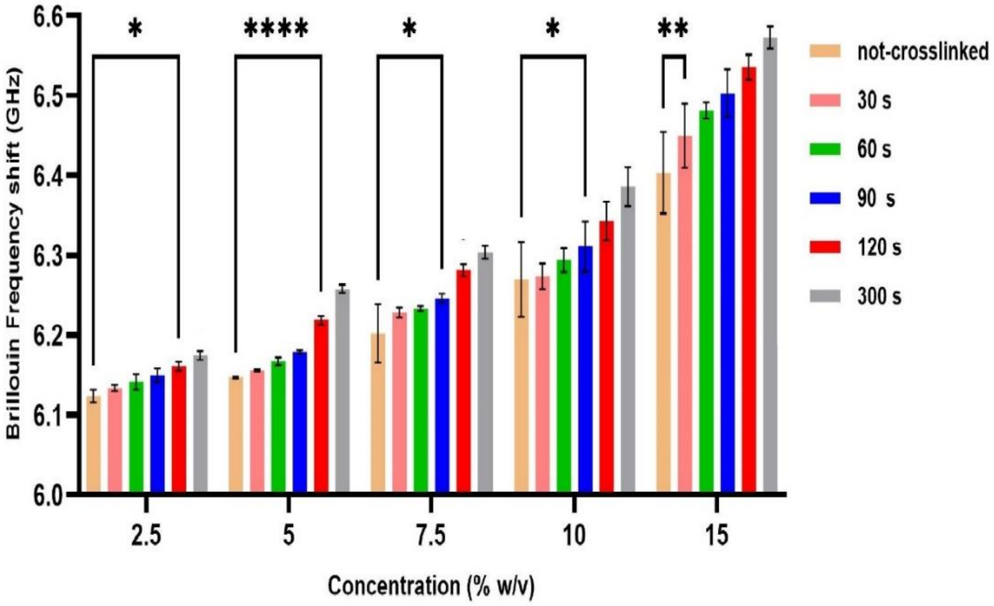

Figure 5.10. Brillouin frequency shift (BFS) of bioprinted acellular GelMA hydrogels with different volume concentrations of 2.5, 5, 7.5, 10 and 15% (w/v) and LAP concentration of 0.25% (w/v). The printed hydrogels were cross-linked using UV light at a wavelength of 365 nm and an intensity of 19.42 mW.cm^{-2} for between 30s to 300s. Error bars indicate 95% confidence interval; (n = 9). Two-way ANOVA followed by Tukey post-hoc correction tests, significance levels: *P < 0.05, **P<0.001, ****P <0.0001.

5.4.1.2 Effect of volume concentration and incubation time on micromechanical properties of bioprinted acellular GelMA hydrogels using Brillouin microspectroscopy

The stiffness changes of the bioprinted acellular GelMA hydrogels over 7 days in culture were investigated using BM. All bioprinted GelMA hydrogels were cross-linked using UV light at a wavelength of 365 nm, an optimised exposure time of 120 s and an intensity of 19.42 mW.cm^{-2}. Then, the bioprinted GelMA hydrogel samples were immersed with a culture medium and evaluated over 7 days of incubation at 37 °C, with 5% (v/v) CO_2 in air.

The BFS measurements of various volume concentrations of bioprinted acellular GelMA hydrogels with individual measurements taking place on days 1, 3, and 7 are shown in Figure 5.11. The BFS values of bioprinted GelMA hydrogels with volume concentrations of 2.5, 5, 7.5 and 10 % (w/v) were 6.192±0.014, 6.256±0.009, 6.309±0.009 and 6.390±0.018 GHz on day 1, respectively. The BFS values of all samples were decreased over 3 days of incubation at 37 °C, with 5% (v/v) CO_2 in the air. However, BFS reduction was more significant for GelMA hydrogel with volume concentration of 2.5 % (w/v) ($P < 0.0001$) compared to 5% (w/v) ($P < 0.005$), 7.5% (w/v) ($P < 0.005$) and 10% (w/v) ($P < 0.05$) from the days 1 to 3. In addition, no significant changes in the mechanical properties of the samples with volume concentrations of 5, 7.5 and 10% (w/v) were observed from the third day onwards. Overall, bioprinted acellular GelMA hydrogels with volume concentrations of 2.5 and 10 % (w/v) had the lowest (6.06±0.009 GHz) and highest (6.343±0.011 GHz) BFS values over seven days of incubation at 37 °C, with 5% (v/v) CO_2 in the air.

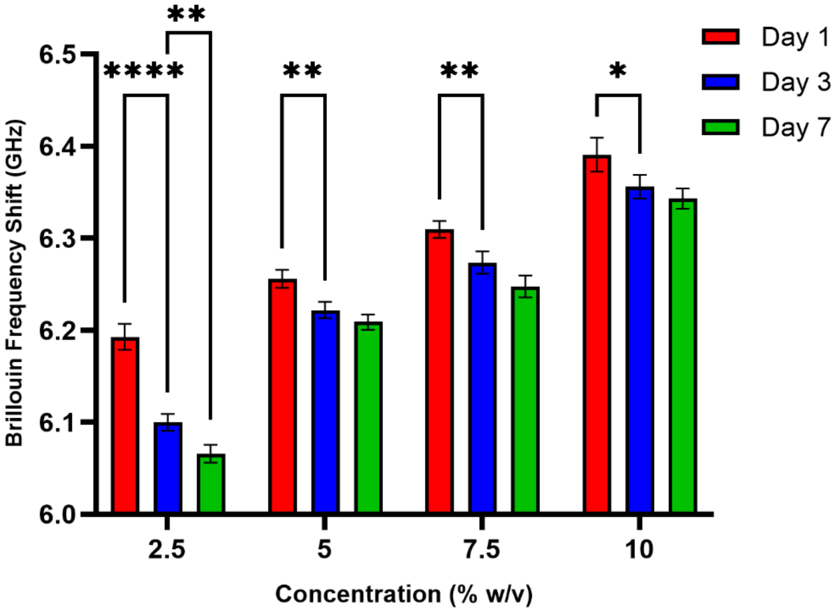

Figure 5.11. Brillouin frequency shift (BFS) of bioprinted acellular GelMA hydrogels with different volume concentrations of 2.5, 5, 7.5, 10 and 15% (w/v) and LAP concentrations of 0.25% (w/v). All bioprinted GelMA hydrogels were cross-linked using UV light at a wavelength of 365 nm, an optimised exposure time of 120 s and intensity of 19.42 $mW.cm^{-2}$. The bioprinted GelMA hydrogel samples were immersed with a culture medium and evaluated over 7 days of incubation at 37 °C, with 5% (v/v) CO_2 in air. Error bars indicate a 95% confidence interval; Two-way ANOVA followed by Tukey post-hoc correction tests, significance levels: Significance levels: *$p < 0.05$, **$P < 0.005$, ****$P < 0.0001$, n = 9.

5.4.2 Bulk and local micromechanical assessment of bioprinted cellular GelMA hydrogels using Brillouin microspectroscopy

This part of the study aimed to assess the mechanical properties of the bioprinted cellular GelMA hydrogels embedded with NG 108-15 neuronal cells using BM. For this purpose, GelMA hydrogels with various volume concentrations of 2.5-10% (w/v) were mixed with NG 108-15 neuronal cells and bioprinted according to the protocol outlined in sections 4.3.2 and 4.3.3. All bioprinted GelMA hydrogels were cross-linked using UV light at a wavelength of 365 nm, an optimised exposure time of 120 s and intensity of 19.42 mW.cm^{-2}. An optimized exposure time of 120 s was chosen for gels of all solid fraction concentrations, as it was observed that there was a significant difference in the BFS values between the samples that were cross-linked with UV and those that were not exposed to UV light, as described in section 5.4.1.1. Then, the bioprinted cellular GelMA hydrogel samples were immersed in a culture medium and their bulk and local micromechanical property were evaluated using Brillouin microspectroscopy over 7 days of incubation at 37 °C, with 5% (v/v) CO_2 in the air, as described in section 5.3.1.2. The 'Bulk' and 'Local' measurements were carried out using different objective lenses, as described in section 5.3.1 and shown in Figure 5.3. The BM measurements of three samples for each volume concentration of bioprinted cellular GelMA hydrogels were conducted, with the same samples being evaluated repeatedly over time for each assessment.

5.4.2.1 Bulk micromechanical assessment of bioprinted cellular GelMA hydrogels embedded with NG 108-15 neuronal cells using Brillouin microspectroscopy

The BFS of bioprinted cellular GelMA hydrogels embedded with NG 108-15 neuronal cells within various volume concentrations of 2.5-10 % (w/v) was evaluated with individual measurements on days 1, 3, and 7 of incubation at 37 °C, with 5% (v/v) CO_2 in the air, as illustrated in Figure 5.12. The BFS was obtained based on averaging 9 measurements for each type of hydrogel sample (three independent measurements on each of the three sample repeats). There was a significant decrease in BFS values of bioprinted cellular GelMA hydrogels with volume concentrations of 2.5% (w/v) ($P<0.0001$) and 5% (w/v) ($P<0.05$) from day 1 to day 3. However, the BFS of the bioprinted cellular GelMA hydrogels with 5 % (w/v) volume concentration wasn't changed significantly in culture at 37 °C from the third day onwards. In addition, the mechanical properties of the bioprinted GelMA hydrogels with volume concentrations of 7.5 and 10 % (w/v) remained constant, as no significant change in BFS values was observed over seven days of incubation at 37 °C, with 5% (v/v) CO_2 in air.

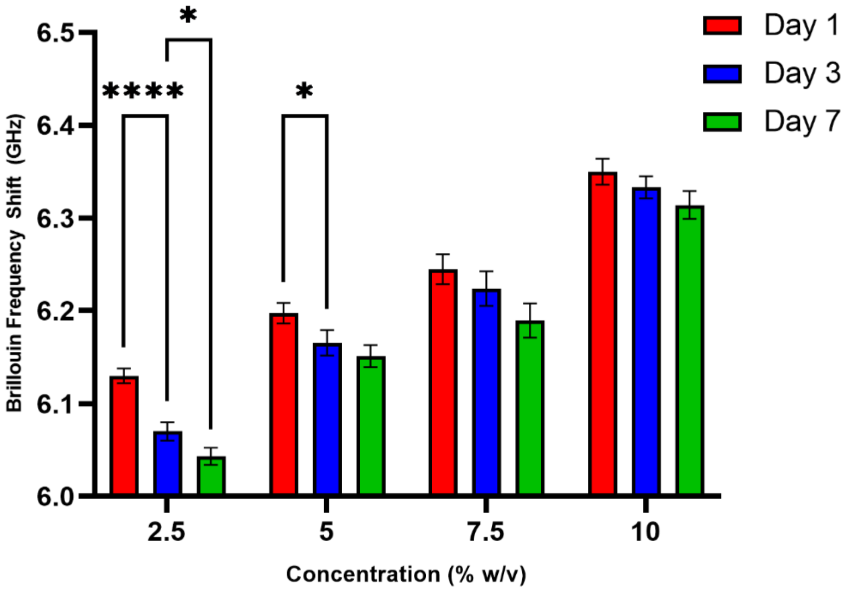

Figure 5.12. Brillouin frequency shift (BFS) of bioprinted cellular GelMA hydrogels embedded with NG 108-15 neuronal with different volume concentrations of 2.5, 5, 7.5, and 10 and LAP concentrations of 0.25% (w/v). All bioprinted GelMA hydrogels were cross-linked using UV light at a wavelength of 365 nm, an optimised exposure time of 120 s and intensity of 19.42 mW.cm^{-2}. The bioprinted GelMA hydrogel samples were immersed in a culture medium and evaluated over 7 days of incubation at 37 °C, with 5% (v/v) CO_2 in air. Error bars indicate a 95% confidence interval; lines indicate statistical difference determined by two-way ANOVA. Significance levels: *$P < 0.05$, ****$P < 0.0001$, $n = 9$.

5.4.2.2 Local micromechanical assessment of bioprinted cellular GelMA hydrogel embedded with NG 108-15 neuronal cells using Brillouin microspectroscopy

After the bulk measurements, the local micro-scale set-up was utilised to understand how the BFS of the hydrogels and NG 108-15 neuronal cells individually changed on days 1, 3, and 7 of incubation at 37 °C, with 5% (v/v) CO_2 in air. For this purpose, only the bioprinted cellular GelMA hydrogels with a volume concentration of 2.5% (w/v), which had given the optimal cell viability results using the quantitative cell viability assay (See section 4.4.2.2 in chapter 4), were analysed. The lateral scanning of bioprinted cellular GelMA hydrogels using BM is described in section 5.3.1.2.

The average and standard deviation (SD) BFS were calculated based on averaging three measurement repeats for each sample. The red line in the top panel of Figure 5.13 shows the laser scanning path across an NG 108-15 cell spheroid. As shown in Figure 5.13 (middle panel), the high and low-frequency shift values are attributed to the NG 108-15 neuronal cell spheroid and hydrogel, respectively. The BFS value of the NG 108-15 neuronal cell spheroid was 6.25 ± 0.03, 6.30 ± 0.03, and 6.43 ± 0.04 GHz on days 1, 3 and 7 days, respectively (Figure 5.13 (a-c)). The BFS values of GelMA hydrogels around the cells (not including the cells) were 6.13 ± 0.02, 6.09 ± 0.02, and 6.05 ± 0.02 GHz on the 1, 3 and 7 days, respectively. An apparent increase in BFS of spheroids was observed over seven days, possibly due to the increasing spheroid size and the number of cells, as is illustrated in the bottom panel of Figure 5.13.

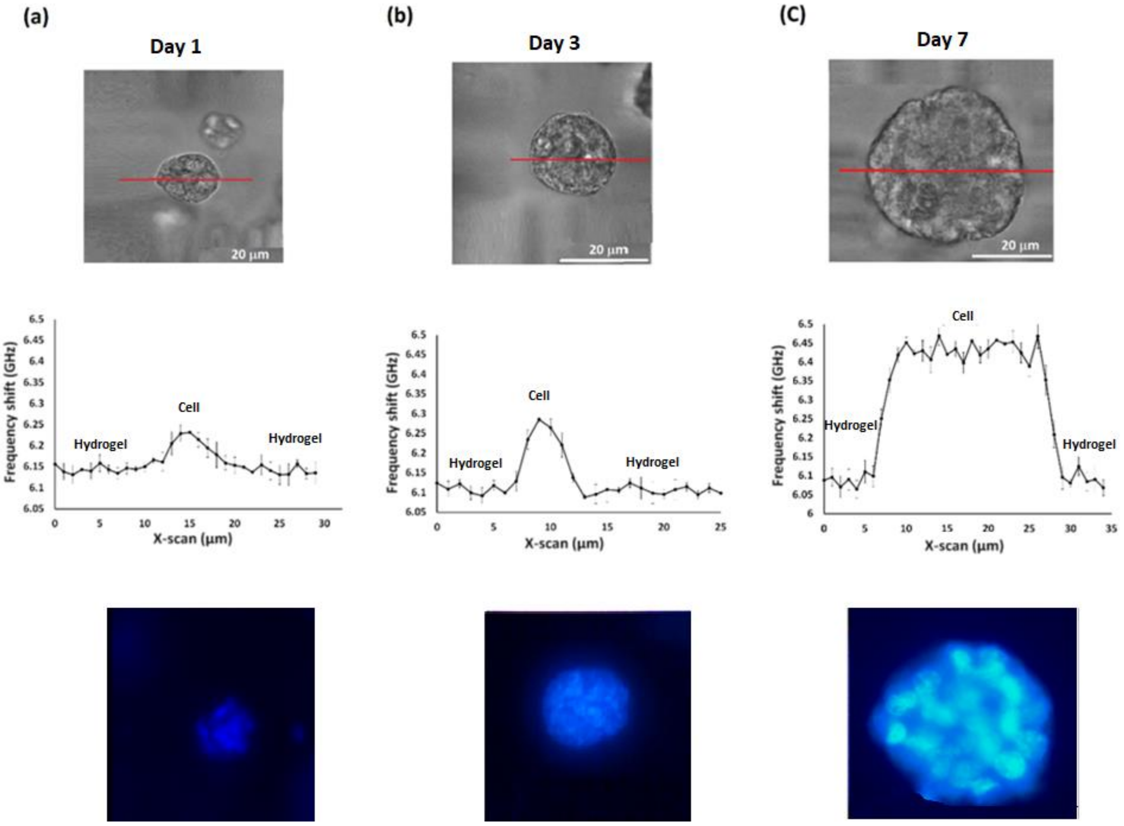

Figure 5.13. Local micro-scale BFS measurement across the bioprinted cellular GelMA hydrogels with 2.5 % (w/v) and embedded with NG 108-15 neuronal cells at a concentration of 4×10^6 cells/mL. The bioprinted GelMA hydrogels were immersed in DMEM cell culture media containing 10 % (v/v) FBS and incubated at 37 °C, 5% (v/v) CO_2 in the air over 7 days period. The top, middle and bottom panels are phase-contrast, Brillouin line scanning, and fluorescent microscopy images of cells on days (a) 1, (b) 3 and (c) 7. The average and SD are obtained based on averaging three measurement repeats for each hydrogel sample.

5.4.3 Comparison between micromechanical properties of bioprinted acellular and cellular GelMA hydrogels on the bulk scale using Brillouin microspectroscopy

Micromechanical properties of bioprinted acellular and cellular GelMA hydrogels were measured on the bulk scale using BM, as described in Sections 5.4.1.2 and 5.4.2.1. This section compares BFS of the acellular and cellular bioprinted GelMA hydrogels using a two-way ANOVA with Tukey’s un-paired multiple comparisons test. The bioprinted acellular GelMA hydrogels with volume concentrations of 2.5, 5 and 7.5% (w/v) generated a significantly higher BFS than the cellular GelMA hydrogels at all three time points, as shown in Figure 5.14(a-d). Interestingly, there was more significant difference between the acellular and cellular GelMA hydrogels with 2.5 and 5 % (w/v)

(P <0.0001) volume concentrations compared to 7.5 and 10% (w/v) (P <0.005), on day 1. In addition, the significance (P <0.05) between the BFS of acellular and cellular GelMA hydrogels with a volume concentration of 7.5 % (w/v) was decreased from the third day onwards. However, no significant difference in BFS was observed between cellular and acellular GelMA hydrogels with a volume concentration of 10 % (w/v) from the third day onwards, as shown in Figure 5.14 (d).

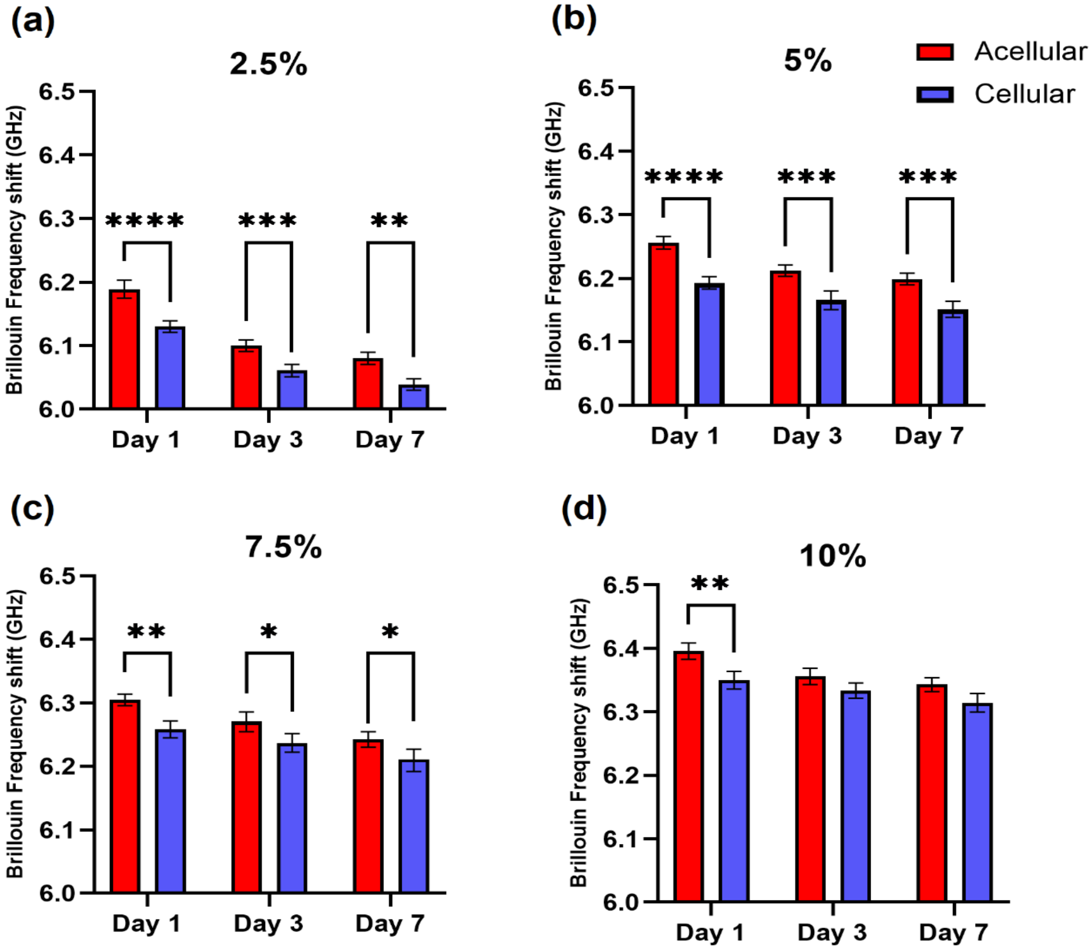

Figure 5.14. BFS measurements for the bioprinted acellular and cellular GelMA hydrogels embedded with NG 108-15 neuronal cells at a concentration of 4×10^6 cells/mL and GelMA volume concentrations of (a) 2.5%, (b) 5%, (c) 7.5% and (d) 10% (w/v). Error bars indicate 95% confidence interval; Two-way ANOVA followed by Tukey post-hoc correction tests, significance levels: Significance levels: *p < 0.05, **P <0.005, ***P <0.0005, ****P <0.0001, n = 9.

5.4.4 Mechanical assessment of bioprinted acellular GelMA hydrogels using unconfined compression testing and rheology

The micromechanical properties of bioprinted acellular GelMA hydrogels were investigated using unconfined compression and rheology to verify the accuracy of data achieved using Brillouin microspectroscopy. Three samples for each volume concentration (2.5-15% (w/v)) were prepared for unconfined compression and rheology tests, as described in section 5.3.2.1.

5.4.4.1 Mechanical assessment of bioprinted acellular GelMA hydrogels using unconfined compression testing

The unconfined compressive mechanical properties of the bioprinted acellular GelMA hydrogel samples were evaluated using a stress-strain curve. The Young's (E) modulus was obtained from the linear range of the elastic region, which is marked in a red dot line as illustrated in Figure 5.15(a). The initial portion of the stress-strain curve, referred to as the linear range of the elastic region, was determined by fitting a straight line to the data points using regression analysis. To ensure consistency in the selection of this region across different volume concentration curves, the same criteria applied consistently. Therefore, the range for each measurement was separately selected using the same criteria. The measurement was repeated three times for each GelMA hydrogel volume concentration. A one-way ANOVA was used to determine whether the increase in volume concentration was significant between all samples, as illustrated in Figure 5.15(b). The results showed that the increase of Young's modulus had been accompanied by an increase in the GelMA volume concentration ranging from 2.5 to 15% (w/v). The gradient of stress-strain curve showed that Young's modulus of bioprinted acellular GelMA hydrogels with volume concentrations of 2.5, 5, 7.5, 10 and 15% (w/v) were 2.075 ± 0.38 kPa, 4.3 ± 0.21 kPa, 13.7± 0.98 kPa, 25.65± 0.48 kPa and 45.14 ± 4.0 kPa, respectively. Additionally, the mean difference in Young's modulus between 2.5% and 5% (w/v) GelMA hydrogel concentrations was 3.18 kPa, while the mean difference between 10% and 15% (w/v) concentrations was 19.67 kPa. Overall, increasing the volume concentration of GelMA in the hydrogels from 2.5% to 15% (w/v) increased the compressive modulus by almost 14-fold.

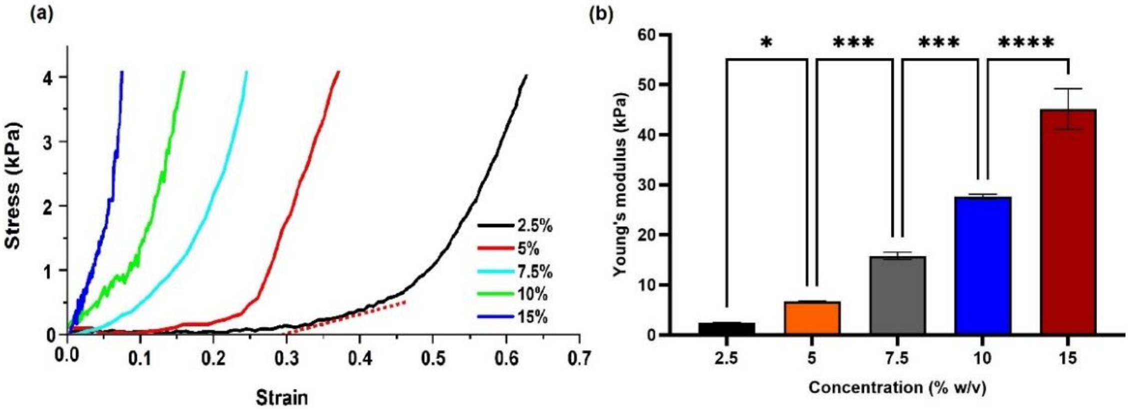

Figure 5.15. Unconfined compression measurements of bioprinted acellular GelMA hydrogels with 2.5-15% (w/v) volume concentrations. (a) Compressive stress vs strain curves, (b) Relationship between Young's modulus and hydrogel concentration, where Young's modulus was obtained from the linear range of the elastic region of the stress-strain curves (red dot line). Statistical analysis, one-way ANOVA was carried out to evaluate the significance of these variations of the compression measurements for three repeat samples for each hydrogel concentration. Significance levels: *P <0.05, ***P <0.005, ****P <0.0001.

5.4.4.2 Mechanical assessment of bioprinted acellular GelMA hydrogels using rheology

In addition to the unconfined compression tests, the viscoelastic properties of bioprinted acellular GelMA hydrogels were evaluated using rheology. The measurement was repeated three times for each volume concentration of bioprinted GelMA hydrogels to ensure reliable data. From the rheology results, the linear viscoelastic region of shear storage (elastic, *G′*) and loss (viscous, *G″*) moduli were determined, as described in section 5.3.2.3.

The variation of storage (G') and loss moduli (G″) versus shear strain values for the examined concentrations are shown in Figure 5.16. As evident, increasing the GelMA hydrogel volume concentration led to an increase in shear storage and loss moduli. The G' for strain amplitudes ranging from 0.2 % to 2 %, was approximately 0.219 ± 0.003 kPa for 2.5 % (w/v), 1.061 ± 0.01 kPa for 5% (w/v), 2.544 ± 0.040 kPa for 7.5% (w/v), 4.954 ± 0.17 kPa for 10 % (w/v) and 6.943 ± 0.07 kPa for 15% (w/v) bioprinted acellular GelMA hydrogels, as shown in Figure 5.16 (a). In addition, the G" for strain amplitudes ranging from 0.2 % to 2 %, was approximately 0.006 ± 0.002 kPa for 2.5% (w/v), 0.0106 ± 0.005 kPa for 5% (w/v), 0.04 ± 0.012 kPa for 7.5% (w/v), 0.143 ± 0.033 kPa for 10% (w/v) and 0.204±0.047 kPa for 15% (w/v) bioprinted acellular GelMA hydrogels, as shown in Figure 5.16 (b). Overall, the observed values for the G' were higher than that of the G″ for each volume concentration of GelMA hydrogels.

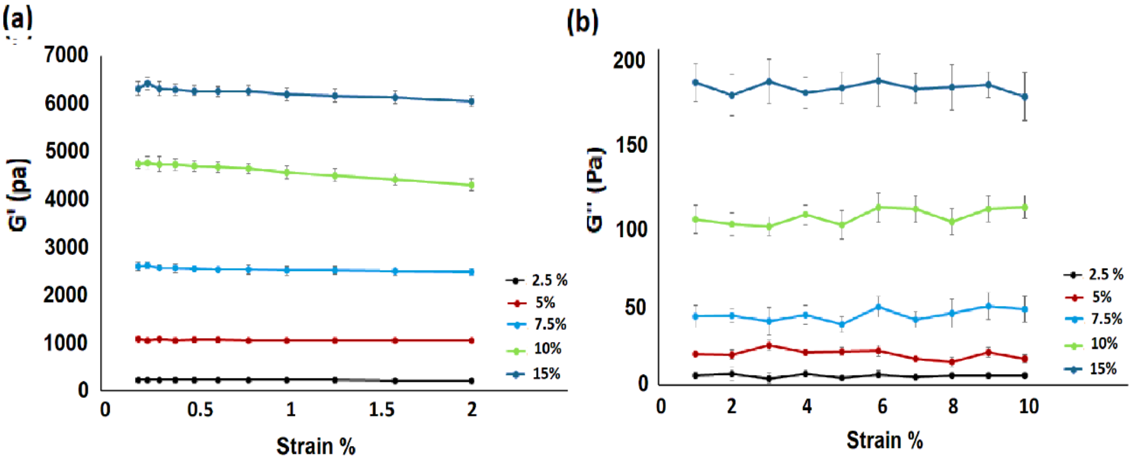

Figure 5.16. The linear viscoelastic region of amplitude sweeps of bioprinted acellular GelMA hydrogels with different volume concentrations (5%, 7.5%, 10%, 12.5% and 15% (w/v)). (a) Shear storage modulus (G') and (b) Shear loss modulus (viscous, G″) plotted against strain over a decade of oscillation strain ranging from 0.2% to 2%. Results are given as mean ±SD (n = 9).

5.4.5 The correlation between BM and rheology measurements for bioprinted acellular GelMA hydrogels

The longitudinal storage (*M′*) and loss (*M″*) moduli were calculated using equations 5.14 and 5.15 to obtain the relationship between BM and rheology measurements. All shear and longitudinal moduli were plotted against the volume concentration of GelMA hydrogels (2-15 % (w/v)), as illustrated in Figure 5.17. The *G′* and *M′* exhibited a highly significant difference between all volume concentrations, while significant changes in the *G″* and *M″* were observed at volume concentrations of 7.5% (w/v) and above, as shown in Figures 5.17 (a-d). By increasing the volume concentration from 2.5 to 15 % (w/v), the G′ was increased from 0.219±0.003 to 6.943±0.079 kPa, where M′ was increased from 2.335±0.004 to 2.638±0.030 GPa. In addition, by increasing the volume concentration from 2.5 to 15 % (w/v), *G″* were increased from 0.006±0.002 to 0.2048±0.047 kPa, where *M″* was increased from 0.189±0.015 to 0.367±0.053 (GPa).

The *M′* against *G'* (Figure 5.18 (a)) and *M″* against *G″* (Figure 5.18 (a)) were plotted for all GelMA hydrogel concentrations. A six-fold increase in solid fraction resulted in a thirty-five-fold increase in *G'*, whereas *M′* was increased by 14%, with a linear correlation coefficient of 0.97, as shown in Figure 5.18 (a). In addition, the increase in hydrogel solid fraction resulted in a thirty-three and two-fold increase in *G″* and *M″*, respectively, with a linear correlation coefficient of 0.90, as shown in Figure 5.18 (b).

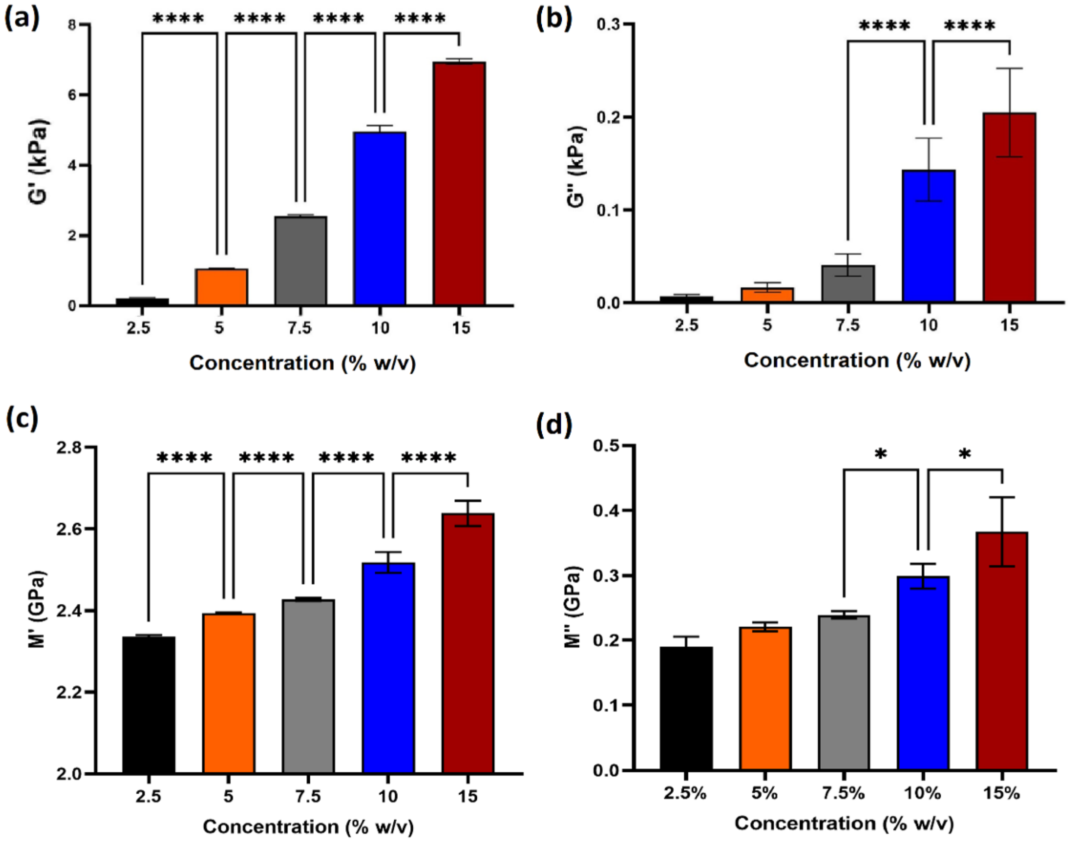

Figure 5.17. Relationship between (a) Shear storage (G′), (b) Shear loss (G″), (c) Longitudinal storage (M′), (d) Longitudinal loss (M″) moduli and bioprinted acellular GelMA hydrogel concentration (2.5-15 % (w/v)) measured using BM and rheology. One-way ANOVA, significance levels: Error bars indicate 95% confidence interval; *P <0.05, ****P <0.0001, n=9.

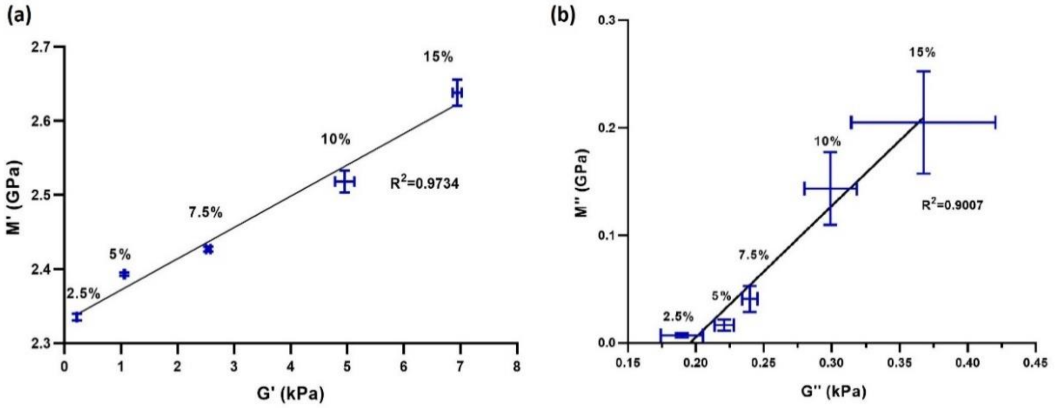

Figure 5.18. Relationship between (a) longitudinal storage (M′) and shear storage moduli (G′), and (b) longitudinal loss (M″) and shear loss moduli (G″) and bioprinted acellular GelMA hydrogel concentration (2.5-15 % (w/v)) measured using BM and rheology. Results are expressed as mean ± SD (n = 9). The solid lines show a linear regression across the measured data with (a) $R^2 = 0.9734$ and (b) $R^2 = 0.9007$, respectively.

5.5 Discussion

5.5.1 Mechanical properties of bioprinted acellular GelMA hydrogels

The first step in developing a 3D *in vitro* spinal cord injury model was to assess the mechanical properties of the matrix to determine if they were similar in stiffness to the native neural extracellular matrix. BM was chosen as a non-destructive method and successfully utilised to investigate the mechanical properties of bioprinted acellular GelMA hydrogel constructs in 3D. In this thesis, while the experiments were performed at room temperature, it's worth noting that the acellular and cellular samples were incubated at 37 °C prior to measurements in order to approximate the conditions of in vivo condition. Micromechanical properties of acellular GelMA hydrogel were shown to alter due to UV cross-linking time and solid fraction variation in the hydrogel composition. In addition, the BFS values of bioprinted acellular GelMA hydrogels changed from 6.192±0.014 GHz (~ 2.075 kPa) to 6.390±0.018 GHz (~ 25.65 kPa) by increasing the volume concentration from 2.5 to 10 % (w/v). In contrast, the BFS value was increased from 6.133±0.007 GHz to 6.174±0.008 GHz by changing UV duration from 30 to 300 s. Therefore, the BFS of GelMA hydrogels was more sensitive to polymer concentration than to the effects of UV exposure time. This was expected as the increase in GelMA hydrogel volume concentration caused an increase in polymer wall thickness, resulting in enhanced cross-linking and contributing to elevated stiffness [224]. By increasing the solid fraction of the GelMA hydrogels, the UV exposure time required to effectively cross-link the samples was decreased and significantly higher than non-crosslinked samples. The lowest BFS of non cross-linked hydrogels was due to the liquid form and the lack of polymerised network. These results fully agree with a previous study that reported increasing BFS with increasing polymer concentrations of GelMA hydrogel from 3 to 15% (w/v) [224].

Numerous studies have demonstrated that neurons tend to exhibit a preference for soft matrices, which can have significant effects on neuron regeneration [264]. Tissue stiffness of normal brain is approximately between 0.1-3 kPa [264, 265], whereas glioblastoma tumors have been shown to be markedly more stiff at 12 kPa [267]. Despite significant efforts to design three-dimensional (3D) systems for improving recovery after spinal cord injury, few 3D models exist for studying the immediate cellular response to injury. However, Quiroz et al. [268] developed a collagen matrix that can be molded into a 3D tubular shape with a lumen, allowing for cell interactions in a similar architecture and stiffness to that of the spinal cord. They demonstrated the critical importance of substrate stiffness when designing biomimetic engineered substrates for the spinal cord at the microscale level. In terms of selecting a matrix of a similar stiffness to neural tissue for use within a 3D injury model, both bioprinted acellular GelMA hydrogels with volume concentrations of 2.5 and 5 % (w/v) would seem appropriate, as neither were stiffer than neural tissue [269]. Although both concentrations (2.5 and 5 % (w/v)) fell within the range of mechanical stiffness values, the 5 % (w/v) gels were less variable over incubation time. Over one week, the BFS value of 2.5 % (w/v) gels decreased by 2.15 %, while 5% gels decreased by 0.75%. This difference was possibly due to the different swelling and degradation rates of 2.5 and 5% (w/v) of GelMA hydrogels, which can affect stiffness reduction rate. It should be mentioned that GelMA swelling occurred only in the first 24 h, and after that, the swelling ratio had no significant change as reported in [270].

5.5.2 Mechanical properties of bioprinted cellular GelMA hydrogels using BM on a bulk scale

Bulk measurements of cellular GelMA hydrogels, which expressed the BFS values from aggregate material (cells and gel), were used to assess the mechanical integrity of 3D printed GelMA hydrogel constructs over 7 days of incubation at 37 °C. This was performed to investigate the suitability of the matrix environments to form the basis of a spinal cord injury model. The results demonstrated that the stiffness of bioprinted cellular GelMA hydrogels with a volume concentration of 2.5% and 5% (w/v) decreased by 1.5% and 0.74% over one day, respectively. On the other hand, the stiffness of cellular GelMA hydrogels with volume concentrations of 7.5% and 10% (w/v) was not changed over 24 h of incubation. These results indicated that the cellular GelMA matrix with 2.5 % (w/v) concentration was less predictable and less reliable as a matrix component for the 3D model due to rapid mechanical degeneration which reduced the stiffness significantly. These results agree with the previous results in chapter 4 in section 4.4.3, which demonstrated that the bioprinted GelMA hydrogels with a volume concentration of 2.5 % (w/v) were unstable and dissolved in culture medium over seven days incubation time.

This observation was in agreement with a previous study performed at the University of Leeds led by Smith [9] to select a matrix for use within a 3D injury model. This author assessed fully stabilized (FS) collagen gels and reported their stiffness properties remained stable over the five days in culture, thus selecting it for use as a matrix component in a 3D SCI model. In our study, we also used a stable 5% GelMA hydrogel as a matrix component and observed instability and dissolution of the 2.5% volume concentration hydrogel in the culture medium.

One of the experimental questions considered in this study was whether neuronal cells affected the mechanical properties of GelMA hydrogels over time. The results in section 5.4.3 indicated that the BFS values were significantly different for all concentrations of hydrogel on day one of the culture period. However, the BFS of cellular GelMA hydrogels with 7.5 and 10% (w/v) volume concentration did not change significantly after day 1. A possible explanation for this finding was that the cellular remodelling of the hydrogel matrix was influenced by the volume concentration of hydrogel and cell viability [271]. As determined in chapter 4 in section 4.4.2, NG 108-15 neuronal cell viability within soft (2.5% and 5% (w/v)) and stiff (7.5% and 10% (w/v)) GelMA hydrogels were high and low, respectively, over the seven days of incubation at 37 ℃. The low cell survival rates in the stiffer hydrogels limited the opportunity for cell-matrix interaction, and therefore matrix remodelling was likely to be minimal.

These results are consistent with previous studies that have demonstrated the influence of cell viability on the mechanical properties of hydrogels. For example, in our study, we observed low cell survival rates in the stiffer GelMA hydrogels, which limited the opportunity for cell-matrix interaction and therefore matrix remodeling was likely minimal. This finding is similar to the results reported by Brown et al. [272], who found that the modulus of collagen gels seeded with fibroblasts was reduced by a third compared to the same gels without cells. Although the experimental conditions of Brown et al.'s study differ from ours, their results suggest that the presence of cells can lead to significant changes in the mechanical properties of hydrogels. Also, in Ahearne et al. [273], the authors demonstrated that the elastic modulus of collagen hydrogels seeded with human corneal fibroblasts was affected by viable cells and decreased over a 4-week culture period due to the strain applied by these cells. Together with our findings, these results highlight the importance of considering cell viability and the potential for matrix remodeling when assessing the mechanical properties of hydrogels in the presence of cells.

5.5.3 Mechanical properties of bioprinted cellular GelMA hydrogels using BM on a micro-scale

In addition to monitoring the hydrogels mechanical behaviour in bulk, it has been demonstrated that this technique can be used to examine how cells alter the mechanical properties of their surroundings by using local micromechanical assessment of hydrogels. Since changes in ECM stiffness have been correlated with glial scar formation post-injury [274, 275], it is therefore essential to better understand the response of the neural cells to a microenvironment stiffness. The local micro-scale mechanical measurements demonstrated that neuronal cells grew, multiplied and formed spheroid-type structures, with BFSs significantly higher (5.5%) than that of the surrounding hydrogel over the 7 days of the experiment. BM measurement of cellular spheroids was achieved using line-scanning rather than 2D/3D mapping due to the limited speed of the TFP interferometer (10-20 s per single spectrum). In future studies, the acquisition time per point could be reduced down to 20-100 ms, with different instrument designs, such as incorporating a virtually imaged phased array (VIPA) spectrometer [276] or by stimulated Brillouin scattering (SBS) microscopy [277]. Overall, the time required to obtain a 3D image using a Brillouin microscope is a major challenge for this technology. Several improvements have been suggested, e.g. line-scanning microscopy [278], that in the future will help to achieve speeds compatible with live cell imaging.

In a similar study, the mechanical properties of breast cancer cell spheroids of MCF-7, MDA-MB-231 and PC3 embedded in hydrogels were measured using BM [235]. A microscale technique was used, which measured line profiles over the spheroid width and showed an increase in BFS towards the spheroid cancer cell centre. In addition, they quantitatively mapped the mechanical properties of these spheroids in situ using BM to reveal spatial variations of the mechanical properties across the spheroids' cross-sections. By segmenting the obtained BM maps for the PEG-Heparin hydrogel area, they found higher BFS for stiff (15-20 kPa) compared to soft (1-2 kPa) hydrogels [235], resulting in a better understanding of cancer progression.

By measuring the mechanical properties of the 3D bioprinted models over time, we can better understand the time-dependent changes in the microenvironment of the injured spinal cord. Indeed, the resulting spinal cord injury (SCI) comprises two injury processes, namely primary and secondary, that are intrinsically linked to time. [279]. The primary cause is the initial mechanical impact, compression, and contusion resulting in damage to nerve cells, myelin and blood vessels. The secondary injury process involves swelling and hemorrhage, which causes even greater cell membrane dysfunction and cell death over the first few days to weeks post-injury. Due to the time-dependent changes in the microenvironment of the injured spinal cord, it is essential to investigate mechanical properties over time rather than at a single time point. Additionally, it is important to investigate the mechanical stiffness of hydrogels after the injury process to better comprehend the relationship between mechanical stiffness and GFAP expression. Indeed, these findings can provide valuable insights into the relationship between mechanical stiffness and GFAP expression, which may aid in interpreting the results of the next chapter and contribute to a better understanding of the biological response to injury in neural cells.

5.5.4 Comparison between micromechanical properties of bioprinted cellular GelMA hydrogels on bulk and microscale using Brillouin microspectroscopy

The results of the bulk (Macro-scale) and local (Micro-scale) BM measurements within acellular and cellular hydrogels with a volume concentration of 2.5 % (w/v) embedded with NG 108-15 neuronal cells are shown in Figure 5.19. The BFS average value of cellular GelMA hydrogel was 6.043 ± 0.009 GHz on day 7 of incubation time. The local micro-scale measurements exhibited higher BFSs on average for the cells (6.43 ± 0.041 GHz) and the surrounding hydrogel (6.09 ± 0.023 GHz) on day 7 of incubation time. This was expected since the macro-scale measurements were taken using a low NA objective lens and thus present information on the mechanical properties averaged across a relatively large volume (approx. 200 μm^3) of the aggregate material (cells and gel). Our local micro-scale imaging set-up has sufficient resolution (focal volume of approx. 3 μm^3) to resolve individual cells.

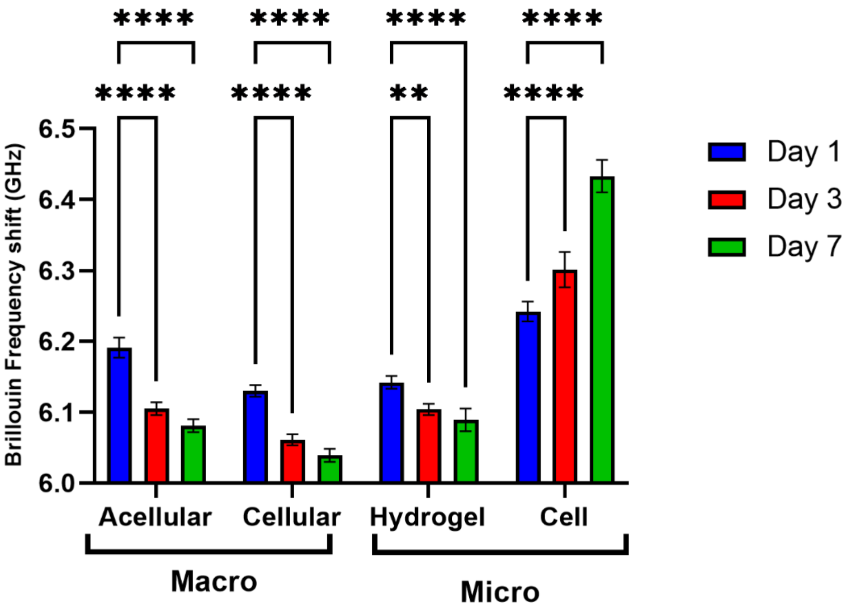

Figure 5.19. BFS measurements of the bioprinted acellular and cellular GelMA hydrogels with volume concentrations of 2.5% (w/v) and embedded with NG 108-15 neuronal cells on both the volume average (VA) and local micro-scale. Error bars indicate 95% confidence interval; Two-way ANOVA followed by Tukey post-hoc correction tests, significance levels: **P <0.005, ****P <0.0001, n = 9.

5.5.5 The relationship between BM and rheology measurements

The unconfined and rheology analysis of acellular GelMA hydrogels also was carried out to verify the accuracy of the data achieved from BM measurements. The relationship between the storage longitudinal modulus (M′) (from BM) and storage shear modulus (G′) (from rheology) showed a positive trend with respect to the solid fraction of hydrogels. A six-fold increase in solid fraction resulted in a thirty-five-fold increase in storage shear modulus, where longitudinal storage modulus was increased by 14%. This difference between the two measurements originated from the different physical meanings of these moduli, which assess different types of deformation. BM probes the materials longitudinal modulus, which measures stiffness under constrained deformation [280]. On the other hand, rheology probes the material deformation under shear stress, with the material being unconfined in the measurement chamber. For the hydrogels with low solid fractions (<10%), the gel compressibility was shown to be influenced by the liquid phase of the aggregate material and showed significantly less variation [280].

In addition, the relationship between loss longitudinal (M″) and loss shear moduli (G″) showed a positive trend with respect to the solid fraction of hydrogels, which resulted in a thirty-three and two-fold increase in shear and longitudinal loss moduli, respectively. The results showed less significance than storage moduli. As mentioned in section 5.3.1, M″ was calculated from Brillouin linewidth, and due to the Brillouin spectral resolution limit, the linewidth of acellular GelMA hydrogels was determined with lower precision than the BFS (Storage measurement standard deviation is approximately 3.5 times smaller than that of the loss). Consequently, the statistical analysis for longitudinal storage modulus data presented higher significance than it is found for the longitudinal loss modulus [233]. As the Brillouin linewidth was associated with the microscopic viscosity of the hydrogel, its variation could be attributed to the restricted mobility of water in hydrogels with high solid fractions and, consequently, dense polymer networks [233]. This phenomenon resulted from the high degree of cross-linking in the hydrogels with high solid fractions, which played a significant role in the mechanical properties of the hydrogel.

In addition, it should be mentioned that the refractive index (n) and mass density (ρ) are two parameters required to calculate the longitudinal storage and loss moduli. Since the acellular bioprinted GelMA hydrogel constructs tested in this study were homogeneous, it was expected that the ratio of index-density factor (n^2/ρ) would not make a considerable difference to the BFS. This assumption is supported by past direct investigation of the interplay between the Brillouin frequency shift, the refractive index and the density of hydrogels, with a maximum deviation of <1% over the broad range of polymer solid fraction (0-18%) [233].

Overall, the observation of a positive trend in the relationships between the storage longitudinal/shear and loss longitudinal/shear moduli verified the achieved results from BM, which confirmed that Brillouin microscopy could be seen as a characterisation technology complementary to 3D bioprinting.

5.6 Key Findings

- Brillouin microspectroscopy, as a non-invasive and label-free method, was utilised to characterise the micromechanical properties of 3D bioprinted acellular and cellular GelMA hydrogels to design a valid SCI model.

- By assessing bioprinted acellular GelMA hydrogels, it was found that the softer hydrogels with a volume concentration of 2.5 and 5% (w/v) had similar mechanical properties to native spinal cord tissue.

- By assessing the bioprinted cellular GelMA hydrogels on the bulk scale, it was found that the stiffness of the 2.5 % (w/v) GelMA volume concentration had significantly reduced from the third day onwards, which indicated this concentration of hydrogel was not appropriate for use in a 3D spinal cord injury model.

- By assessing bioprinted cellular GelMA hydrogels on the local micro-scale, the mechanical properties of the surrounding matrix of the NG 108-15 neuronal spheroids were measured successfully. This non damaging in situ mechanical characterisation method may be valuable for interpreting biological responses of cells after impaction in a 3D SCI model.

CHAPTER 6 DEVELOPMENT OF AN *IN VITRO* 3D SPINAL CORD INJURY MODEL USING BIOPRINTED GELMA HYDROGELS

6.1 Introduction

There are a variety of causes of spinal cord injury, including traumatic events such as falls that cause a contusion SCI. To model 3D *in vitro* contusion SCI, there was a requirement for the mechanical impaction system to be controllable and measurable to simulate a mechanical injury. There are several impaction systems that have been used to simulate SCI *in vitro*, such as an Infinite Horizons (IH-0400) impactor. The simulation of spinal cord injury on tethered and aligned collagen hydrogels has been carried out using this instrument at the University of Leeds in cooperation with Phillips group at the University College London (UCL) [9]. Similar impactors to the IH have been used to simulate traumatic central nervous system (CNS) injury for *in vivo* models [244, 281-283]. However, since it is impossible to control the IH impactor's displacement and velocity parameters using the impactor software, the hydrogels were often pierced by the impactor tip. The displacement could be controlled manually; however, this was not accurate or measurable, and it was extremely challenging to produce reproducible injuries using this system [9]. In contrast, the TA Instruments ElectroForce BioDynamic 5110 provides axial compressive load onto hydrogel models in a closed sterile system with the software provides precise control over different parameters [10, 11, 284].

6.2 Aim and Objectives

6.2.1 Aim

This chapter aimed to simulate a clinically relevant 3D *in vitro* SCI model in terms of the mechanical forces and the biological responses using the TA Instruments Electroforce BioDynamic 5110 system.

6.2.2 Objectives

The specific objectives of this chapter were as follows:

1. To optimise the working parameters of the TA Instruments 5110 Electroforce BioDynamic to simulate a spinal cord contusion injury using 3D bioprinted GelMA hydrogels.

2. To define a set of velocity (100, 1000 and 3000 mm.s^{-1}) and displacement parameters (1, 2 and 4 mm) to be simulated experimentally to represent a range of injury severities *in vitro*.

3. To determine the effects of injury simulation parameters (velocity and displacement) on C6 astrocyte-like and NG 108-15 neuronal cell responses in an *in vitro* spinal cord contusion injury model.

6.3 Materials and Methods

6.3.1 Bioprinting of 3D GelMA constructs

A cylinder shape (4 mm in height and 8 mm in diameter) was created in CAD software and stored in STL format and used to print constructs to model spinal cord injury (Figure 6.1). The diameter of 8 mm was selected based on the platen fixture in the Electroforce system, ensuring that the whole gel was in contact with the load platen during compression. In addition, a height of 4 mm was large enough to prevent the complete destruction of the gel during compression. The selection of these dimensions was based on the optimisation during preliminary experiments (Data not shown). The manufacturing and testing processes are simplified with a cylindrical shape, making it a practical choice. From a cell culture standpoint, the cylindrical shape allows for a more uniform distribution of cells and nutrients, providing consistent experimental conditions. The cylindrical shape serves as a simplified model for studying the basic cellular responses to mechanical stress, while reducing the complexity of the in vivo environment. While it may be relevant to discuss the potential differences in cell response between a cylinder and a spinal cord impacted transversely, it is important to note that the purpose of the study was not to precisely replicate spinal cord injury but rather to investigate the behavior of cells in response to mechanical stimulation.

The bioprinting parameters for GelMA hydrogels with a volume concentration of 5% (w/v) were selected based on the optimal parameters determined previously in chapter 4 and shown in Table 4.2. The parameters included using a print bed temperature of 10 °C, printhead temperature of 24 °C, printing pressure of 12 kPa and printing speed of 11 mm.s^{-1}. The cellular GelMA hydrogels were prepared and printed based on the protocols described in Chapter 4, sections 4.3.2 and 4.3.3. Subsequently, cellular GelMA hydrogels were cross-linked using UV light at a wavelength of 365 nm, an exposure time of 120 s and an intensity of 19.42 mW.cm^{-2}, as optimised and presented in chapter 5, section 5.4.1.1. Finally, the bioprinted GelMA hydrogel samples were immersed in a culture medium and incubated at 37 °C in 5% (v/v) CO_2 in air for 2 h before the compression tests. Keeping hydrogels in an incubator caused them to hydrate fully, which helps to maintain C6 astrocyte-like cells in a non-reactive state before injury [9].

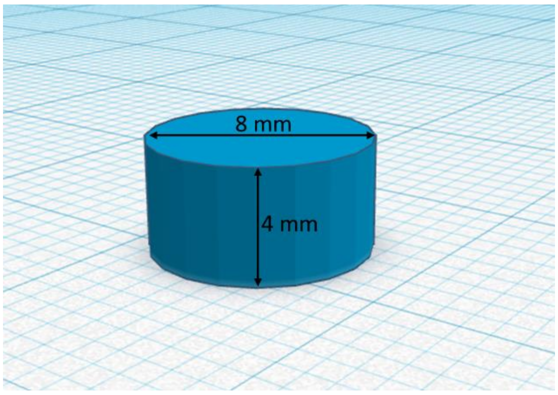

Figure 6.1. A 3D-CAD model of a cylinder shape (4 mm in height and 8 mm in diameter) was chosen as the most appropriate shape for bioprinted constructs.

6.3.2 Use of the TA Instruments ElectroForce BioDynamic 5110 system to create an injury

This study used the TA Instruments Electroforce BioDynamic Impaction system to simulate a spinal cord contusion injury model within 3D bioprinted GelMA hydrogels. This instrument is comprised of a load cell, sterile culture chamber and motor unit**,** as shown in Figure 6.2. Before commencing the experiment, all BioDynamic chamber components, including the manifold components, were sterilised using moist heat autoclaving at 120 °C, 15 psi for 20 minutes. The sterilised chamber parts and the entire frame were assembled and placed in a Class II biosafety cabinet to operate the system under sterile conditions. The chamber contains load and motor platens. The sample was placed on the motor platen and was moved up to reach the desired displacement. The upper load platen was connected to a load cell of 22N. The system was controlled by the WinTest® Control System software. After measuring gel height (section 6.3.3), the chamber was sealed and filled with preheated culture medium at 37 °C from a reservoir bottle using a peristaltic pump set to a speed of 80 mL.min^{-1}. After the compression process, the chamber was drained of culture medium before the hydrogel construct was removed. Gels were placed into a 48 well plate and immersed in a culture medium before incubation at 37 °C in 5% (v/v) CO_2 in air.

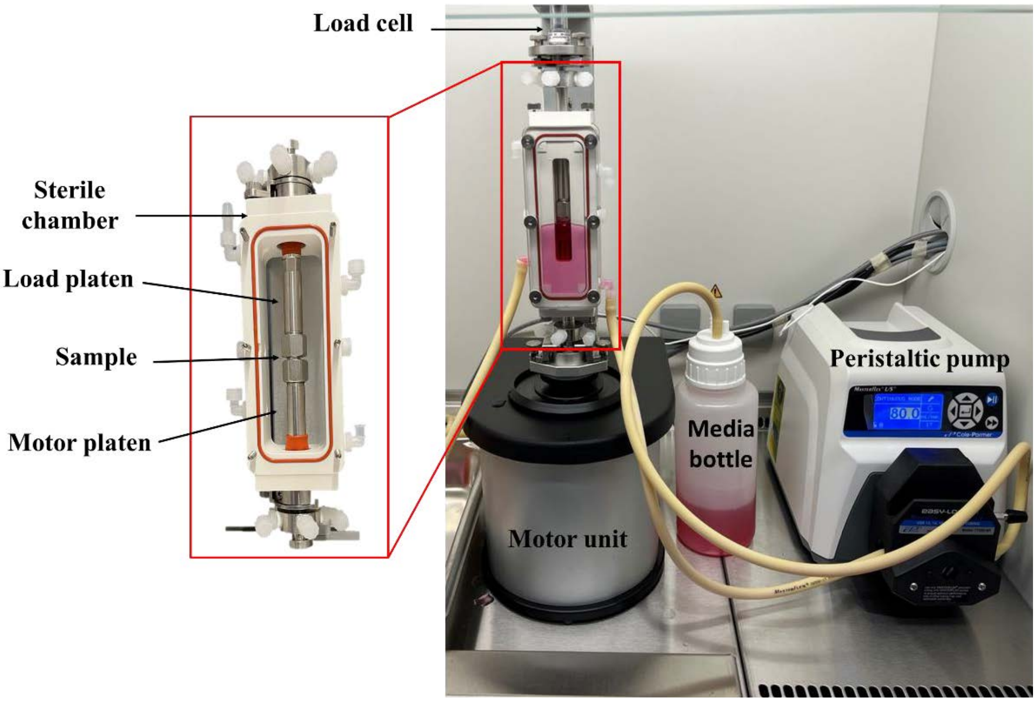

Figure 6.2. Setup of the TA Instruments 5110 Electroforce BioDynamic with compression platens.

6.3.2.1 Design of a Compression Platen Fixture for the TA Instruments ElectroForce system

The original motor and load platens that were supplied by the manufacturer of the TA Instruments ElectroForce BioDynamic 5110 were not appropriate for use in our work (Figure 6.3 (a)). The original platen fixture prevented compression of the gel because the gel was located in the middle of the indentation well. Therefore, a new platen for the TA Instruments ElectroForce BioDynamic 5110 was designed and fabricated at the University of Technology Sydney, as illustrated in Figure 6.3 (b). The addition of the new platen created a surface flush with the surround. The bioprinted GelMA hydrogel placement sat on the shaft, as shown in Figure 6.3 (c). The motor platen used was entirely flat, and the load platen had an 8 mm diameter.

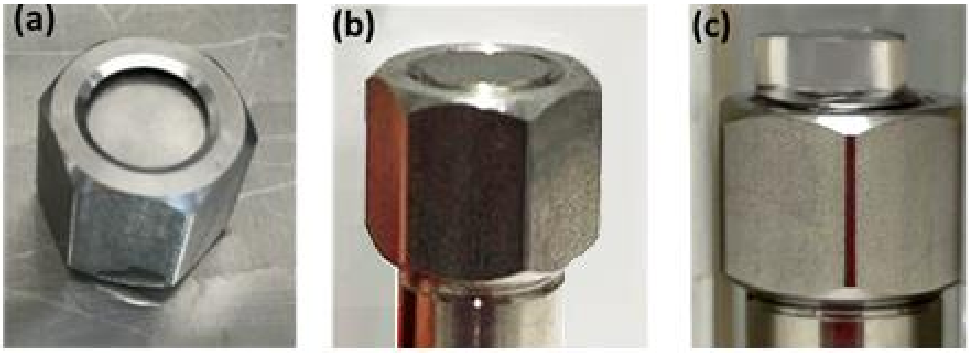

Figure 6.3. (a) The original and (b) new design of platen of TA instrument Electroforce system. (c) A bioprinted GelMA hydrogel on the newly designed platen.

6.3.3 Measurement of Gel Height using the TA Instruments ElectroForce BioDynamic 5110

The TA Instruments ElectroForce BioDynamic 5110 was connected to a desktop computer (Figure 6.4). In order to set the parameters of the injury stimulus and record the results during the impaction process, WinTest software was used to control the displacement, load and axis commands. The height of each bioprinted GelMA hydrogel sample was calculated after loading on the motor platen. In the initial setup of the apparatus, the motor platen was moved upwards to an absolute displacement value of -5 mm using the WinTest software (Figure 6.4 (a)). Then, the load platen was manually lowered until it came into contact with the motor platen, as indicated by a change in the load of at least 0.1 N, which represented 100% compression (Figure 6.4 (b)). Afterwards, the motor platen was moved down to a displacement value of +5 mm, and the GelMA hydrogel was loaded onto the motor platen (Figure 6.4 (c)). Afterwards, the motor platen was moved upwards until the sample top surface touched the load platen (Figure 6.4 (d)). Then, contact with the top surface of the sample was registered by load and the absolute displacement value at this point, y mm, was recorded (Figure 6.4 (e)). The GelMA hydrogel height was measured by calculating the difference between y and the displacement value of -5 mm, where the two platens were in contact.

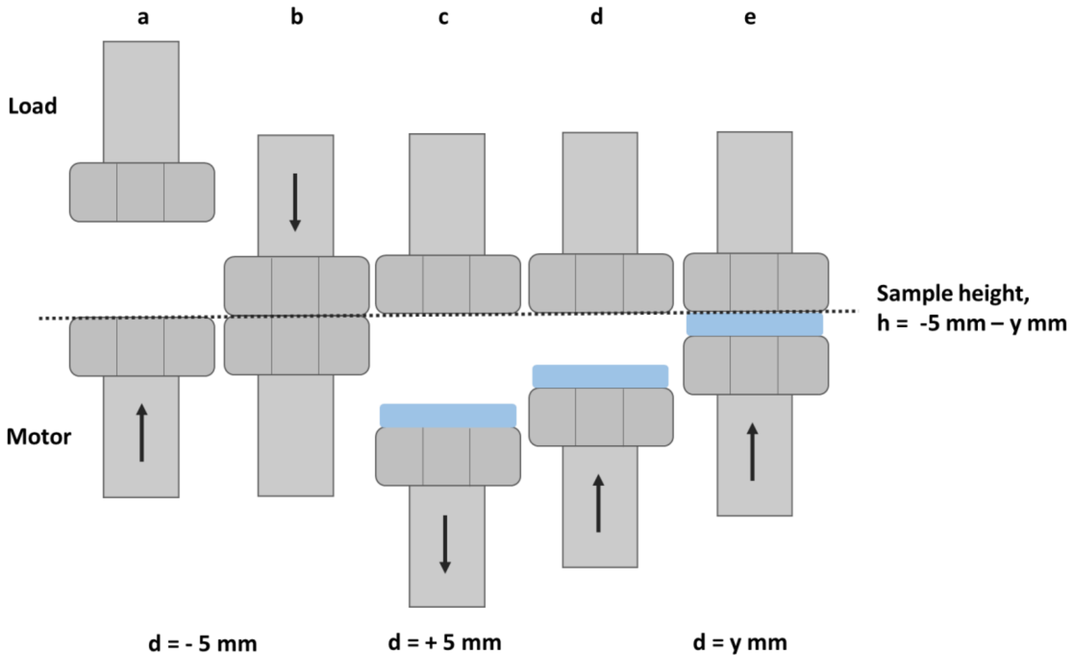

Figure 6.4. A method of calculating the thickness of individual bioprinted GelMA hydrogel samples using the TA Instruments. (a) Moving the motor platen upwards (b) Manually lowering the load platen to contact the motor platen was then undertaken, (c) After moving the motor platen downwards to +5 mm absolute displacement, the sample was loaded onto the motor platen. (d) Moving the motor platen upwards until the top surface of the sample touched the load platen. (e) The absolute displacement was recorded at the point of contact with the top surface of the sample.

6.3.4 Optimisation process of the mechanical parameters

A waveform regime was developed to represent a contusion spinal cord injury model. As mentioned previously, the control of the system was achieved by using WinTest® Control System software on the attached computer, which provides data acquisition, waveform generation and instrument control in one comprehensive package. In the block waveform, the impaction parameters were set, allowing ramps (changes in displacement depth) and dwells (delays) in the movement of the motor platen. The displacement was negative as the lower motor platen moved upwards towards the load platen. The input impaction parameters were set in a block waveform, defined in several dwells and ramps. Three scenarios were considered to represent a contusion injury, as shown in Figure 6.5. The waveform included a ramp to a displacement depth of 1, 2, and 4 mm of their initial GelMA heights.

In the first scenario, the simulated waveform was started with an initial dwell (10 ms) and then ramped at the velocity of 100, 1000 and 3000 mm.s^{-1} to the target displacement depth of 1, 2 and 4 mm, and then ramped to 0 mm, as shown in Figure 6.5 (a). In the second scenario, one excess dwell time of 200 ms was added between the two ramp steps, as shown in Figure 6.5 (b). In the third scenario, another ramp step at the velocity of 1 mm.s^{-1} was added at 0.1 mm before target displacement of 1, 2 and 4 mm, as shown in Figure 6.5 (c). All scenarios were ended with a dwell time (10 ms). The input parameters for building continuation injury models are shown in Tables 6.1-6.3.

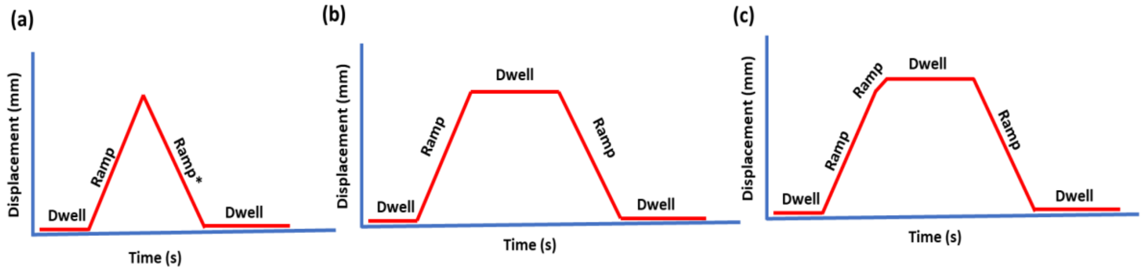

Figure 6.5. A visual representation of the input displacement profile of the waveform (a) without, (b) with a dwell step (200 ms) and two ramps, (c) with a dwell step (200 ms) and three ramps at the impaction time.

Table 6.1. Input parameters for building waveform without dwell time for the displacement of 1, 2, and 4 mm.

	Waveform	Waveform definition	Displacement
Step 1	Dwell	10 ms	0 mm
Step 2	Ramp	Velocity 100, 1000, 3000 mm.s^{-1}	1, 2 and 4 mm
Step 3	Ramp*	Velocity 100, 1000, 3000 mm. s^{-1}	-1, -2 and -4 mm

* Return to starting displacement

Table 6.2. Input parameters for building waveform with a dwell time (200 ms) and two ramp steps for the displacement of 1, 2, and 4 mm.

	Waveform	**Waveform definition**	**Displacement**
Step 1	Dwell	10 ms	0 mm
Step 2	Ramp	Velocity 1000 and 3000 mm.s^{-1}	1, 2 and 4 mm
Step 4	Dwell	200 ms	0 mm
Step 5	Ramp	Velocity 1000 and 3000 mm.s^{-1}	-1, -2 and -4 mm

Table 6.3. Input parameters for building waveform with a dwell time (200 ms) and three ramps for the displacement of 1, 2, and 4 mm.

	Waveform	**Waveform definition**	**Displacement**
Step 1	Dwell	10 ms	0 mm
Step 2	Ramp	Velocity 1000 and 3000 mm.s^{-1}	0.9, 1.9 and 3.9 mm
Step 3	Ramp	1 mm.s^{-1}	0.1 mm
Step 4	Dwell	200 ms	0 mm
Step 5	Ramp	Velocity 1000 and 3000 mm.s^{-1}	-1, -2 and -4 mm

In addition, a percentage error was calculated to verify the output measurement of displacement and velocity against the input. The following equation was used to calculate the percentage error:

$$Error\ (\%) = \frac{experimental - theoretical}{theoritecal} \times 100 \tag{6.1}$$

6.4 Results

6.4.1 Process parameter optimisation of the mechanical impact model using the TA Instruments Electroforce BioDynamic 5110

This chapter started with optimising the mechanical parameters of the TA Instruments Electroforce BioDynamic 5110, an apparatus for inducing a contusion injury to a 3D bioprinted construct containing either astrocytes or neurons. For this purpose, the compression waveforms were simulated to represent a contusion injury, as described in section 6.3.4. The samples used in this part of the study were cylinder-shaped bioprinted GelMA hydrogels embedded with either C6 astrocyte-like or NG 108-15 neuronal cells, as described in section 6.3.1. Three samples were bioprinted for each test as described in chapter 4 in section 4.3.3.

6.4.1.1 Comparison of input and output displacement profiles of a simulated contusion injury model without the presence of a dwell period

This section of the study investigated the resulting displacement output without a dwell time between the two ramp steps in the waveform displayed in Figure 6.5 (a). The waveform input parameters without dwell time were shown previously in table 6.1. The input (dashed line) and output (solid line) displacement values were plotted against time, and the resultant profiles were compared, as shown in Figure 6.6.

A lag period before the first ramping step was observed, which shifted the output profile peaks compared to input profile peaks, as shown in Figures 6.6 (a-c). The mean lag times at peak displacement were calculated and compared with the input peak displacement, as shown in Table 6.4. For instance, for the input displacement of 1 mm and velocity of 100 $mm.s^{-1}$, it was determined that the input peak displacement was at 20 ms, while it was actually observed to occur at 26.25 ± 0.05 ms, resulting in a lag time of 6.25 ± 0.05 ms. The grouped mean lag time was 6.53 ± 0.05 ms at 100 $mm.s^{-1}$, 6.15 ± 0.1 ms at 1000 $mm.s^{-1}$, and 6.01 ± 0.04 ms at 3000 $mm.s^{-1}$. Three samples were used for each test.

The percentage error between the input and output displacement profiles was calculated and is given in Table 6.5. The percentage error between the input and output displacement profiles was increased with an increasing velocity at a given input displacement. Although at 100 $mm.s^{-1}$, the displacement almost reached the input values for 1, 2 and 4 mm, the desired displacement was not achieved at any displacement depth at velocities of 1000 and 3000 mm.s^{-1}. In fact, at faster speeds, the mean displacement fell far below the desired displacement. For instance, for the working displacement of 4 mm at the velocity of 3000 mm.s^{-1}, the mean displacement was only approaching 1 mm, not to the desired displacement of 4 mm, which indicated only 25% of the desired displacement was reached.

Furthermore, increasing displacement at a given input velocity reduced the percentage error between input and output displacement profiles. For instance, at 100 mm.s^{-1}, the mean percentage error of the output peak displacement value decreased from 20.4 % to 9.5%, as input displacement was increased from 1 mm to 4 mm. Similarly, at input velocities of 1000 and 3000 mm.s^{-1}, the mean displacement percentage error decreased from 83.61% to 49.67% and 89.81% to 77.52%, respectively.

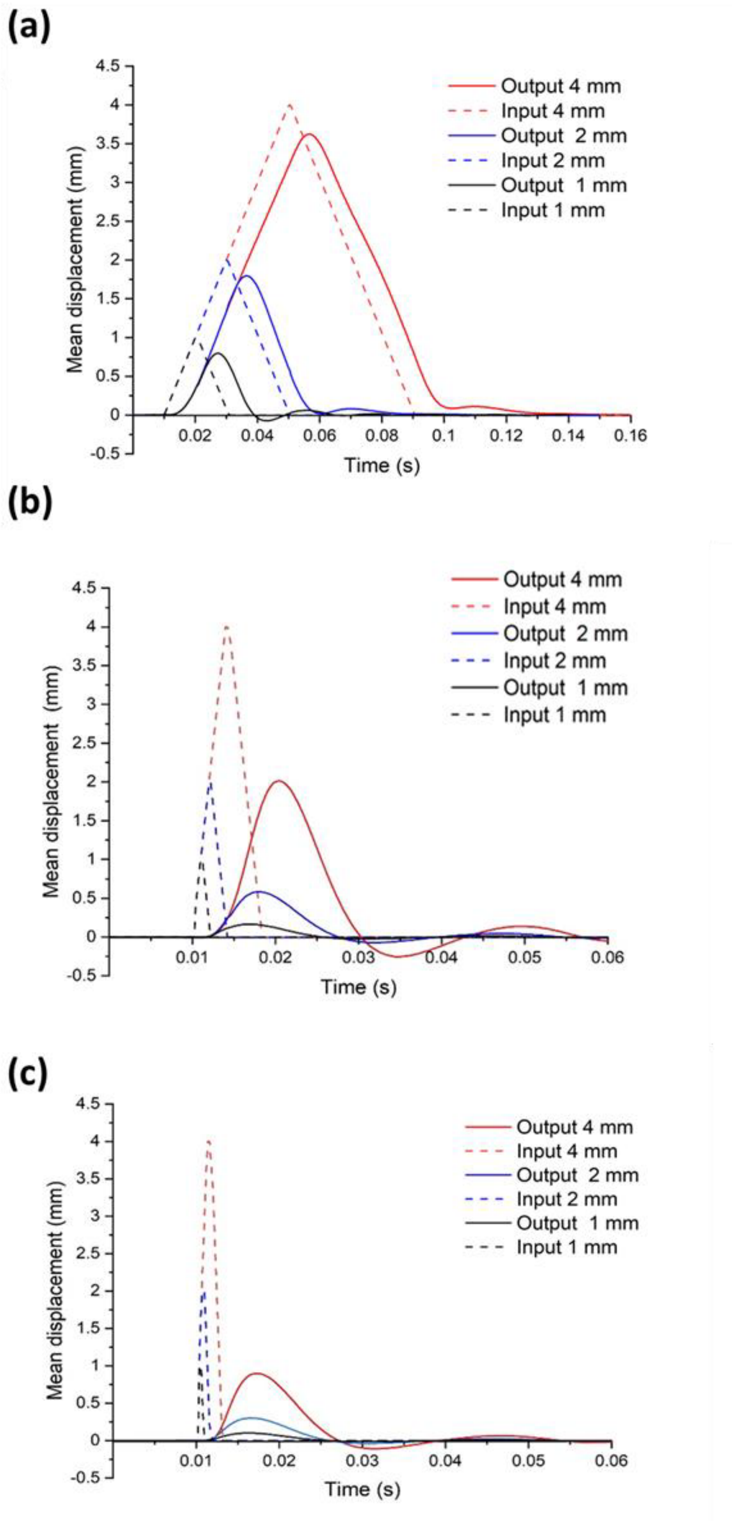

Figure 6.6. Comparison of input and output displacement profiles of a simulated compression regime with two ramp steps and without a dwell period. Solid lines represent the output profiles; dashed lines represent the input command. The simulated waveform was programmed as follows: dwell (10 ms), ramp at the velocity of (a) 100, (b) 1000 and (c) 3000 mm.s^{-1} to the defined displacement depth (1,2, 4 mm) relative to 0 mm in compression, then ramp at 100, 1000, or 3000 mm.s^{-1} back to 0 mm. N = 3.

Table 6.4. Mean lag time at output peak displacement compared to the input peak displacement under waveforms of various displacement and velocity parameters combinations. The time at peak output displacement was selected and compared to the time at peak input displacement. Data is shown as the mean ± SEM. N=3.

Input Displacement (mm)	**Mean Lag time (ms)**		
	100 mm.s^{-1}	**1000 mm.s^{-1}**	**3000 mm.s^{-1}**
1.00	6.61 ±0.04	6.03 ±0.09	6.20 ±0.13
2.00	6.60 ±0.08	6.02 ±0.11	6.01 ±0.06
4.00	6.60 ±0.05	6.40 ±0.08	5.80 ±0.04

Table 6.5. Mean peak output displacement values under compression waveforms without the addition of a 200 ms dwell step. Comparing peak output displacement values to input displacement values was performed under waveforms of various input displacement and velocity parameters. Data is shown as the mean ± SEM (% error). N=3.

Input Displacement (mm)	**Mean Output Peak Displacement (mm)**		
	100 mm.s^{-1}	**1000 mm.s^{-1}**	**3000 mm.s^{-1}**
1.000	$0.796 \pm 8.9 \times 10^{-4}$ (20.4)	$0.164 \pm 5.3 \times 10^{-4}$ (83.61)	$0.102 \pm 4.7 \times 10^{-4}$ (89.81)
2.000	$1.796 \pm 6.8 \times 10^{-4}$ (10.2)	$0.583 \pm 7.1 \times 10^{-4}$ (70.85)	$0.302 \pm 6.3 \times 10^{-4}$ (84.90)
4.000	$3.623 \pm 9.4 \times 10^{-4}$ (9.5)	$2.013 \pm 9.5 \times 10^{-4}$ (49.67)	$0.899 \pm 8.3 \times 10^{-4}$ (77.52)

6.4.1.2 Comparison of input and output displacement profiles of a simulated contusion injury model with a dwell time and two ramp steps

This section of the study investigated the resulting displacement output with the presence of a 200 ms dwell time between the two ramp steps in the waveform displayed in Figure 6.5 (b). The waveform input parameters were given previously in Table 6.2.

The input and output displacement profiles at the velocity of 100 mm.s^{-1} and different displacements were graphed and compared in Figure 6.7. The observed mean displacements were much lower than the input. For instance, the output displacements for the desired displacement of 1, 2 and 4 mm at the velocities of 100 mm.s^{-1} were 0.1, 0.7 and 1.2 mm, respectively. Furthermore, the displacement profiles didn't show any output displacement profile for higher velocities of 1000 of 3000 mm.s^{-1}. Therefore, this model wasn’t suitable for contusion injury scenarios.

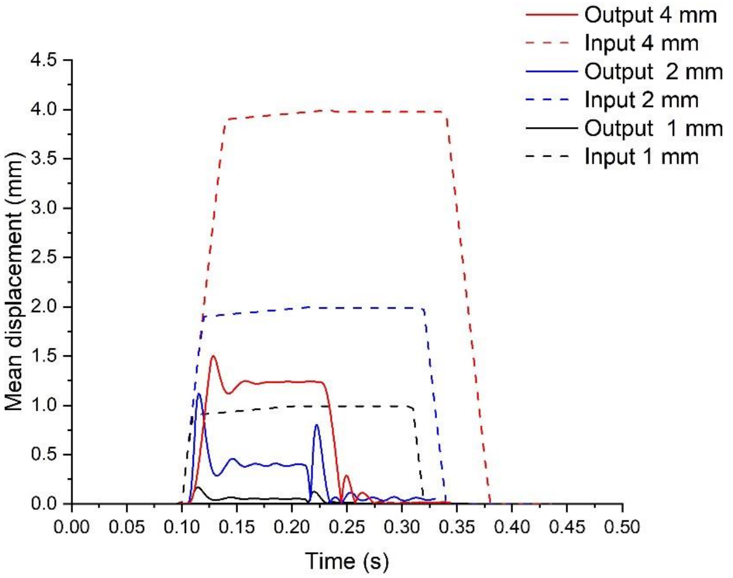

Figure 6.7. Comparison of input and output displacement profiles of a simulated compression regime with the presence of two ramp steps and a 200 ms dwell period. Solid lines represent the output profiles; dashed lines represent the input command. The simulated waveform was programmed as follows: a dwell time (10 ms), ramp at the velocity of 100 mm.s^{-1} to the defined displacement depth (1, 2 and 4 mm) relative to 0 mm in compression, a dwell time (200 ms), then ramp at 100 mm.s^{-1} back to 0 mm. N = 3.

6.4.1.3 Comparison of input and output displacement profiles of a simulated contusion injury model with a dwell time and three ramp steps

This section of the study investigated the resulting displacement output with three ramp steps in the waveform (Figure 6.5 (c)). The waveform input parameters were given previously in Table 6.3.

The input and output displacement profiles at different velocities and displacements were graphed and compared, as shown in Figure 6.8. The close alignment of the input and output displacement profile is clear in Figure 6.8 (a-c). The percentage error between the input and output displacement profiles with the presence of a 200 ms dwell time was calculated and is given in Table 6.6. The accuracy of the output displacement for all velocities was increased as the percentage error at each input displacement depth was decreased. For instance, the output displacements for the desired displacement of 1 mm at the velocities of 100, 1000 and 3000 $mm.s^{-1}$ were $0.994 \pm 3.1 \times 10^{-4}$, $0.996 \pm 7.0 \times 10^{-4}$ and $0.991 \pm 7.3 \times 10^{-4}$ mm, corresponding with 0.1, 0.1 and 0.4 % error, respectively. Therefore, for the input displacement of 1 mm with velocities of 1000 and 3000 $mm.s^{-1}$, a significant decrease in percentage error was observed with the presence of three ramp steps, and a 200 ms dwell time, as shown in Table 6.6. Although the desired displacement depth was achieved in all tests, there was a time delay of approximately 0.1 seconds in the peak displacement. Furthermore, the displacement profiles showed a recoil event in the output displacement profile in contrast to the input displacement profile, which was more pronounced at input velocities of 1000 of 3000 $mm.s^{-1}$ compared to 100 $mm.s^{-1}$ (Figure 6.8).

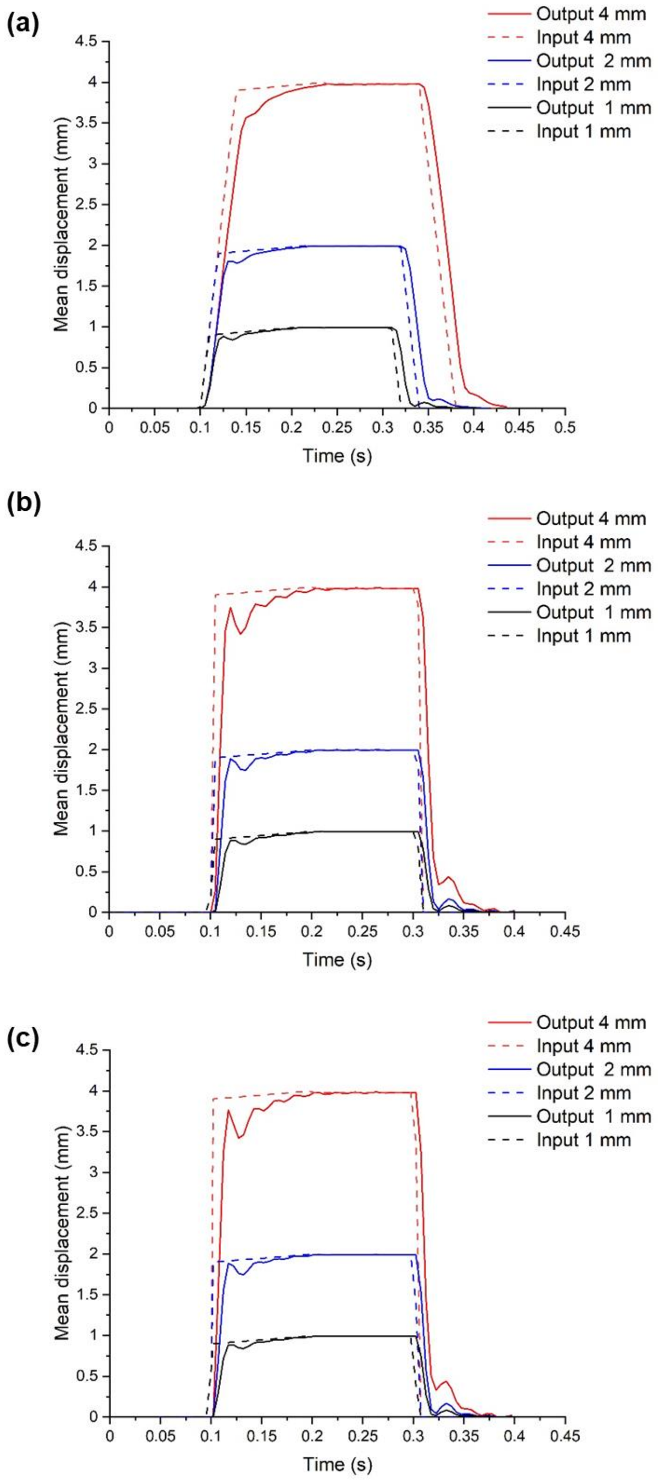

Figure 6.8. Comparison of input and output displacement profiles of a simulated compression regime with the presence of a dwell period and three ramp steps. Solid lines represent the output profiles; dashed lines represent the input command. The simulated waveform was programmed as follows: a dwell time (10 ms), a ramp at the velocity of (a) 100, (b) 1000 and (c) 3000 mm.s^{-1} to the defined displacement depth (0.9, 1.9 and 3.9 mm) relative to 0 mm, a ramp at the velocity of 0.1 mm.s^{-1} to the defined displacement depth (1, 2 and 4 mm) relative to 0 mm, a dwell (200 ms), then ramp at 100, 1000, or 3000 mm.s^{-1} back to 0 mm. N = 3.

Table 6.6. Mean peak output displacement values under compression waveforms with a 200 ms dwell time and three ramp steps. Comparing peak output displacement values to input displacement values was performed under waveforms of various input displacement and velocity parameters. Data are presented as the mean ± SEM (% error). N=3.

Input Displacement (mm)	**Mean Output Peak Displacement (mm)**		
	100 mm.s^{-1}	1000 mm.s^{-1}	3000 mm.s^{-1}
1.00	$0.994\pm3.1\times10^{-4}$ (0.1)	$0.996\pm7.0\times10^{-4}$ (0.1)	$0.991\pm7.3\times10^{-4}$ (0.4)
2.00	$1.991\pm3.7\times10^{-4}$ (0.25)	$1.998\pm4.1\times10^{-4}$ (0.15)	$1.994\pm6.1\times10^{-4}$ (0.05)
4.00	$3.975\pm4.3\times10^{-4}$ (0.5)	$3.986\pm6.1\times10^{-4}$ (0.22)	$3.983\pm6.3\times10^{-4}$ (0.3)

The input and output displacement values were recorded and compared to their respective output values with and without dwell time. The outcome of comparing input and output displacement profiles of a simulated compression regime with and without the dwell step is summarised in Figure 6.9. It was observed that there were significant differences in the mean output peak displacement between the waveform with and without the dwell step at each velocity. Furthermore, it was observed that the accuracy of the output displacement profile was significantly increased by adding additional a ramp step and a 200 ms dwell time for all input displacement depths and velocities.

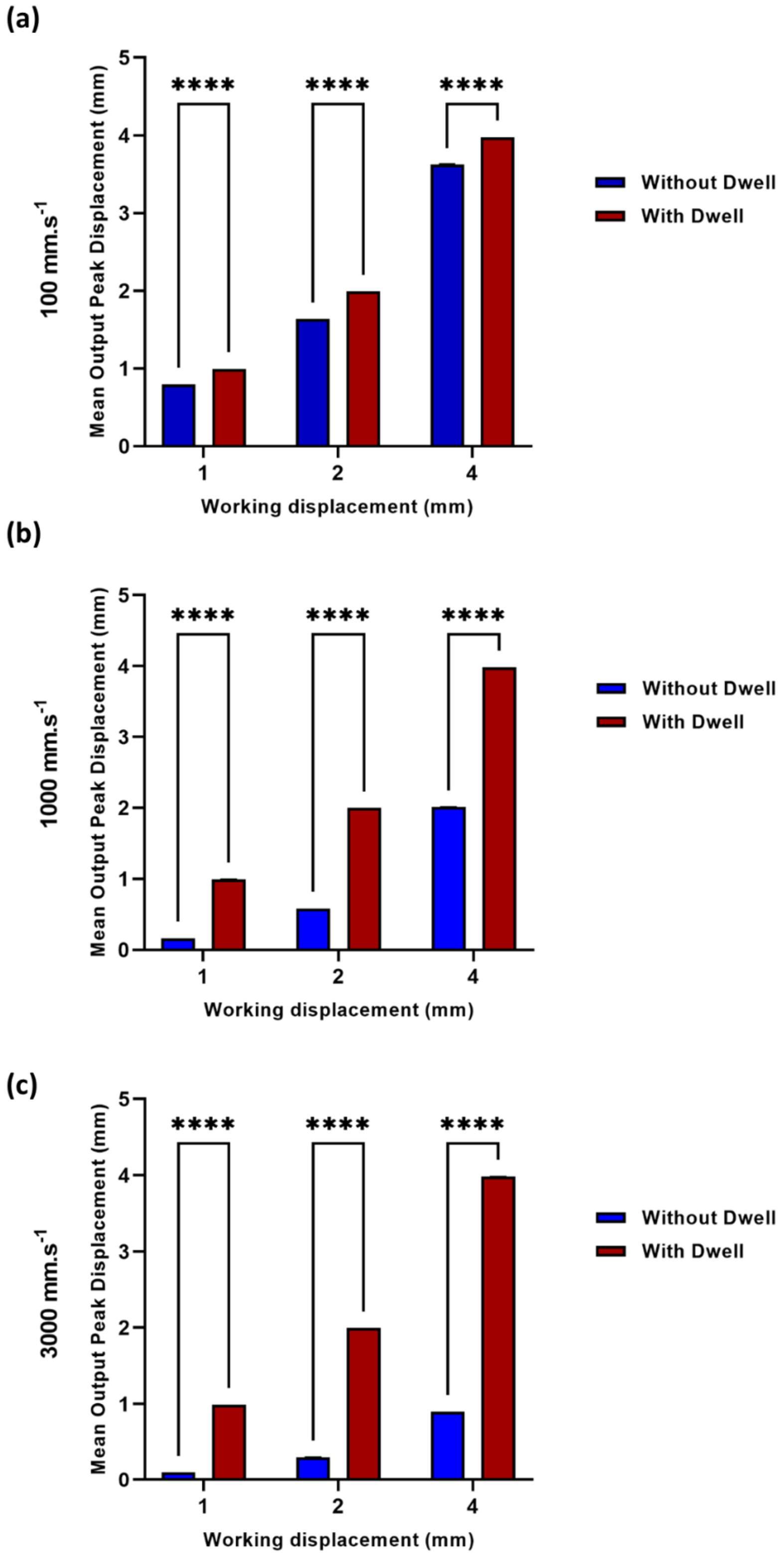

Figure 6.9. Summary of the effects of the incorporation of a ramp step and a 200 ms dwell time on output peak displacement measurements at the input velocity of (a) 100, (b) 1000 and (c) 3000 mm.s^{-1} of the TA Instruments. Two-way ANOVA with Tukey's post-hoc test was performed for each displacement group. Statistical significance levels ****p<0.0001. N = 3.

6.4.2 C6 astrocyte-like and NG 108-15 neuronal cell behaviour in 2D culture

Two-dimensional (2D) immunocytochemistry staining of C6 astrocyte-like and NG 108-15 neuronal cells in isolation and co-culture at a concentration of 5 × 10^6 cells/mL was performed in this research before carrying out 3D experiments in bioprinted GelMA hydrogels. The cells were fixed after three days of cultured on glass chamber slides at 37 °C, with 5% (v/v) CO_2 in air. The protocol for immunostaining cells in 2D was similar to that for staining cells in 3D GelMA hydrogels, described in section 3.6, but with shorter incubation steps, since antibody solutions did not have to penetrate a 3D environment. The C6 astrocyte-like and NG 108-15 neuronal cells were immunopositive for the astrocyte marker GFAP (green) and neuronal marker β-III tubulin (red), respectively, in the 2D environment, as shown in Figure 6.10 (a) and (b). However, NG 108-15 neuronal cells were double-stained with both the GFAP antibody and the β-III tubulin antibody in co-culture with C6 astrocyte-like cells, which resulted in the observation of yellow colour in the merged images (Figure 6.10 (c)).

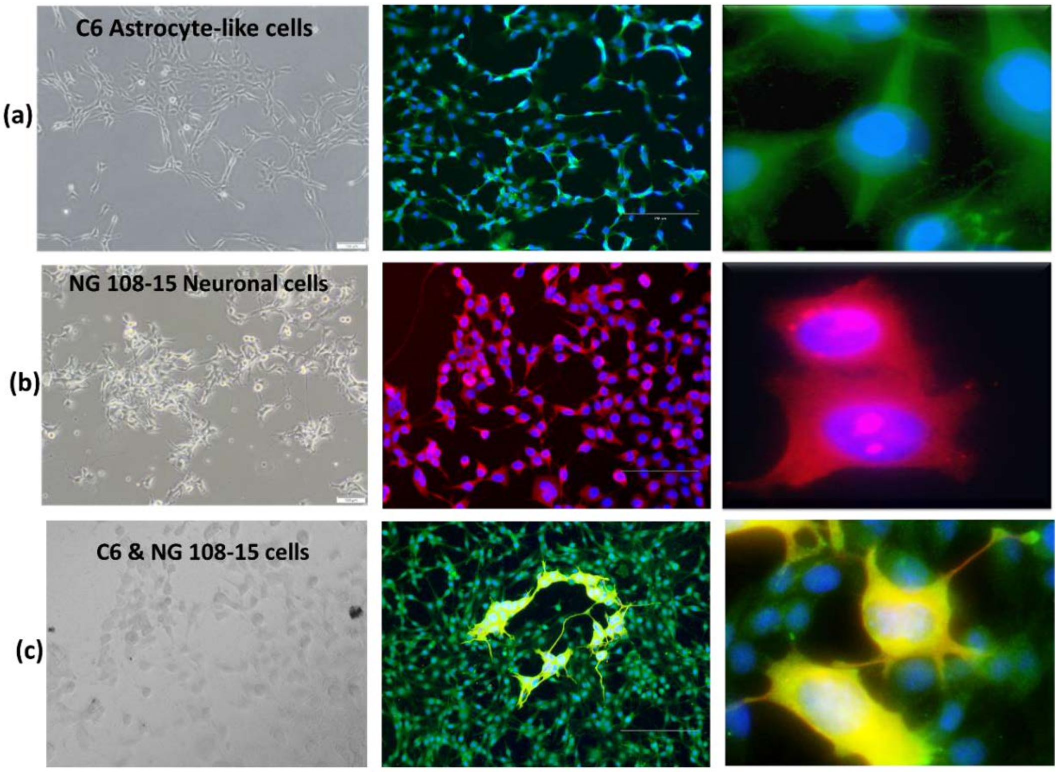

Figure 6.10. Representative bright-field and Immunofluorescence images of (a) C6 astrocyte-like and (b) NG 108-15 neuronal cells in isolation and (c) co-culture at a concentration of 5 × 10^6 cells/mL. The cells were fixed after three days of culture on glass chamber slides at 37 °C, 5% (v/v) CO_2 in air. The cells were then stained with anti-GFAP antibody (green), anti-β-III tubulin (red) and DAPI (blue).

6.4.3 C6 astrocyte-like and NG 108-15 neuronal cell behaviour following a contusion Injury

In this section, the effect of impaction displacement and velocity on C6 astrocyte-like cells and NG 108-15 neuronal cells following injury were studied. For this purpose, the 3D cylinder-shaped GelMA hydrogels embedded with either C6 astrocyte-like or NG 108-15 neuronal cells were bioprinted, as described in section 6.3.1. Each bioprinted cellular GelMA hydrogel was cultured for 2 hours at 37 °C, 5% CO_2 in air to allow hydrating of the hydrogel with an appropriate culture medium before the impaction process was initiated. The contusion SCI was modelled *in vitro* using a TA Instruments ElectroForce BioDynamic 5110 at input velocities of 1000 and 3000 $mm.s^{-1}$. The compression protocol with a 200 ms dwell time was selected as described in section 6.3.4. Three samples for each experiment were tested. The hydrogel height was measured before the impaction (as described in section 6.3.3), and the impaction protocol was set to either compressive displacements of 1, 2, and 4 mm.

The impacted gels were overlapped with a 2 mL cell culture medium and placed in a humidified incubator at 37 °C, 5% CO_2 in air. The control sample was a bioprinted cellular GelMA hydrogel that was not impacted; however, it was incubated under the same conditions, e.g. 37 °C, 5% CO_2 in air. On days 1 and 10 after compression, cellular GelMA hydrogels were fixed, and C6 astrocyte-like and NG 108-15 neuronal cells were stained with GFAP and III β-tubulin antibodies, respectively, using immunocytochemistry, as described in section 3.6.

6.4.3.1 The effect of impaction displacement and velocity on GFAP expression of C6 astrocyte-like cells following injury

The morphology of C6 astrocyte-like cells embedded in bioprinted GelMA hydrogels was observed using confocal microscopy and analysed using ImageJ software. Following a contusion injury using the approach described in sections 3.6 and 3.8, respectively. The cellular hydrogels were also stained with DAPI nuclear stain to locate C6 astrocyte-like cells, which did not express GFAP. Under control conditions (no injury), a relatively small number of cells were GFAP-positive, as shown by most nuclei not being co-stained with GFAP antibody over 10 days of incubation in a culture medium (Figure 6.11).

At the input velocity of 1000 mm.s^{-1}, upon applying a mechanical injury with 1 mm displacement, a slight change in GFAP expression in C6 astrocyte-like cells was observed at days 10 post-injury, and cells became ramified. Their morphology was changed from rounded to one with many projections, as indicated in the in Figure 6.11. When the displacement was increased to 2 and 4, the majority of the GFAP-positive cells were small and had a rounded morphology on day 1 after injury. However, over time GFAP expression progressively changed so that by day 10 post-impaction with a compression displacement at 2 and 4 mm, the majority of the cells expressed GFAP and had a ramified "spikey" appearance.

At the input velocity of 3000 mm.s^{-1}, when hydrogels were compressed at 1 mm, C6 astrocyte-like cells showed similar behaviour to that described above for the 1000 mm.s^{-1} velocity, as shown in Figure 6.12. The GFAP-positive C6 astrocyte-like cells appeared rounded in shape on day 1 post-impact, and ramification of cells increased over time. The only difference was for cells on day 1 post-injury with 2 and 4 mm compression, there were more GFAP positive cells with a rounded morphology compared to the 1000 mm.s^{-1} velocity.

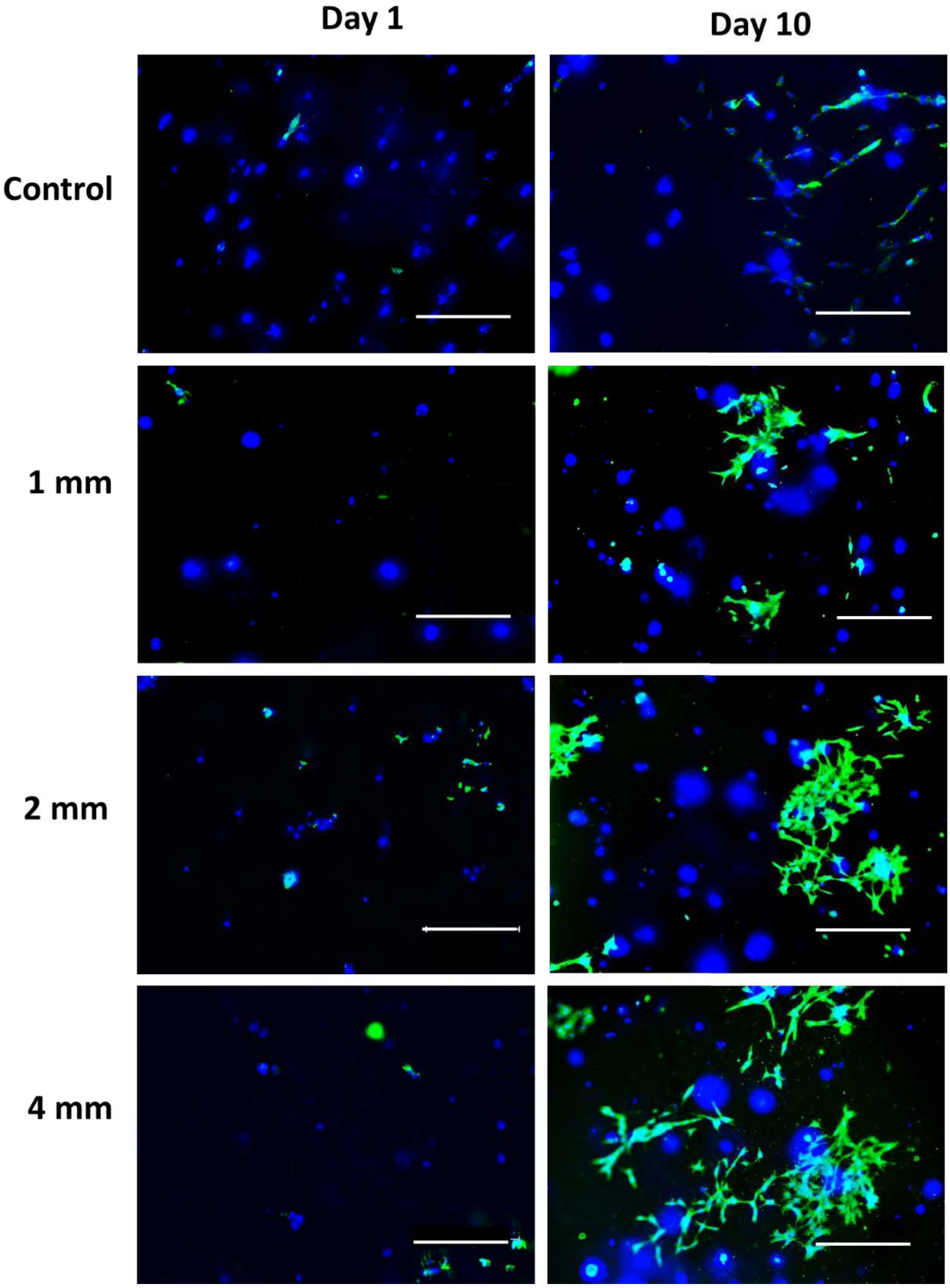

Figure 6.11. Representative immunofluorescence maximum intensity projection images of C6 astrocyte-like cells embedded within bioprinted GelMA hydrogels with a volume concentration of 5 % (w/v) and cultured for 10 days post impaction (compressive displacements of 1, 2, and 4 mm) at 37 °C, 5% CO_2 in air. Mechanical compression injury at 1000 mm. s^{-1} induces an astrogliosis response by Day 10 post-injury. Cells were labelled with a polyclonal antibody against GFAP (astrocytes, green) and counterstained with DAPI (nuclei, blue). 200 µm depth. The scale bar represents 300 µm in the image. N=3.

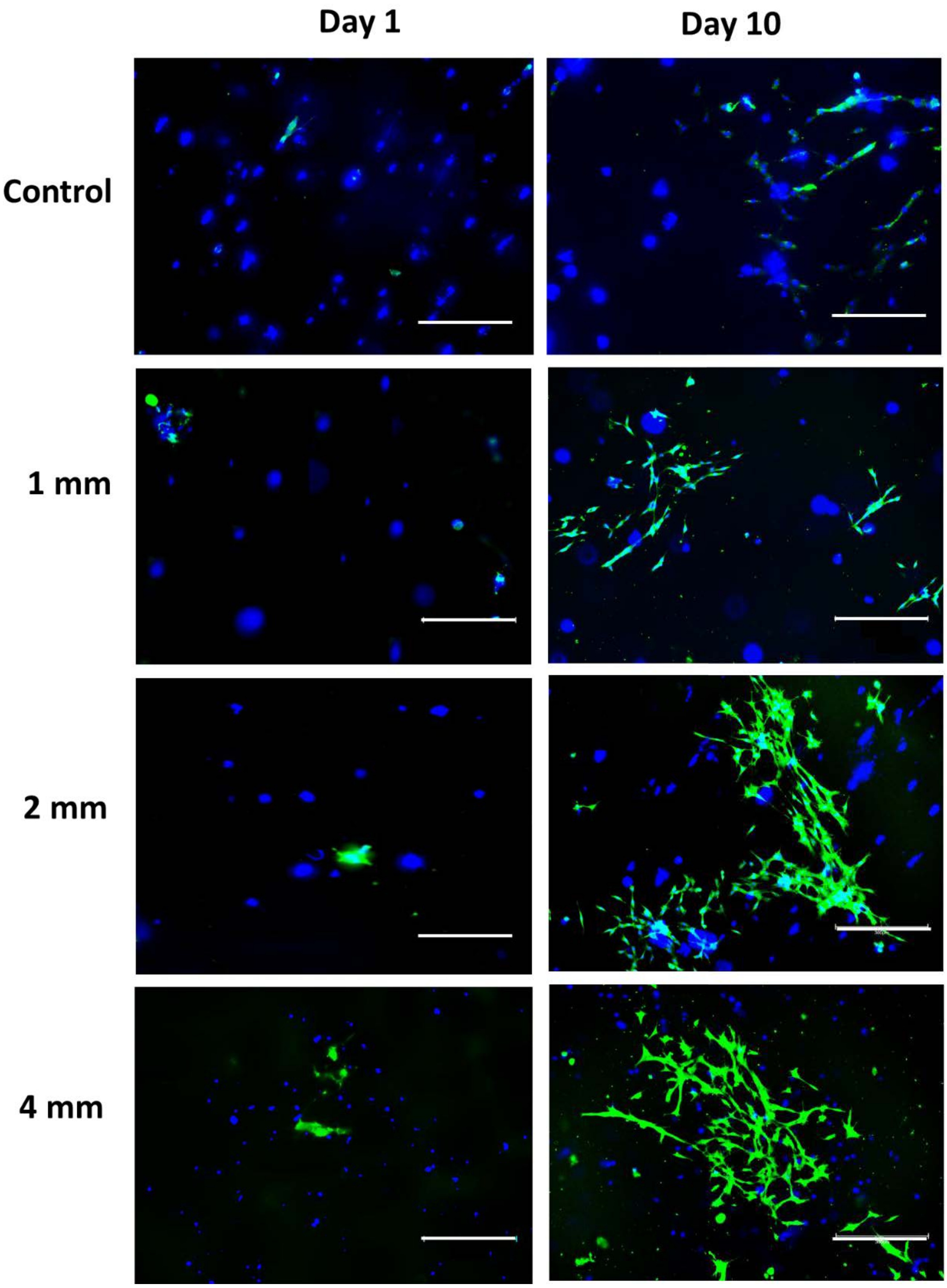

Figure 6.12. Representative immunofluorescence maximum intensity projection images of C6 astrocyte-like cells embedded within bioprinted GelMA hydrogels with a volume concentration of 5 % (w/v) and cultured for 10 days post impaction (compressive displacements of 1, 2, and 4 mm) at 37 °C, 5% CO_2 in air. Mechanical compression injury at 3000 mm. s^{-1} induces an astrogliosis response at Day 10 post-injury. Cells were labelled with a polyclonal antibody against GFAP (astrocytes, green) and counterstained with DAPI (nuclei, blue). 200 μm depth. The scale bar represents 300 μm in the image. N=3.

Quantitative data was also generated by measuring the area of GFAP expression using FIJI as described in section 3.9. The percentage of the total area of GFAP expression in C6 astrocytes-like cells following a simulated compression injury at input velocities of 1000 mm.s^{-1} and 3000 mm.s^{-1} on day 1 and day 10 post impaction is shown in Figure 6.13. C6 astrocyte-like cells in the control group represented the lowest percentage of the total area of GFAP expression (~5.31 %) on day 1 post-injury (Figure 6.13 (a)), which did not change significantly (~10.73 %) after 10 days post-injury after incubation at 37 °C, 5% CO_2 in air (Figure 6.13 (b)).

At 1 mm displacement, there was no statistical difference in GFAP expression between the experimental and control groups at both velocities of 1000 and 3000 mm.s^{-1} on day 1 post-injury (Figure 6.13 (a)). However, the total percentage area of GFAP expression was significantly increased compared to the control group on day 10 post-injury, which was ~37% at 1000 mm.s^{-1} and ~ 40% at 3000 mm.s^{-1} velocity, respectively. Although GFAP expression was higher than the control sample, it was in the same between 1000 and 3000 mm.s^{-1} velocity groups, and no significant difference was observed over 10 days post-injury.

At 2 mm displacement, the total percentage area of GFAP expression was significantly greater than the control group at both velocities of 1000 and 3000 mm.s^{-1} on day 1 post-injury. In addition, at 10 days post-injury, the cells expressed significantly more GFAP, so the percentage value increased from 20% to 51% and from 24.5% to 61% at the input velocities of 1000 and 3000 mm.s^{-1}, respectively. It is notable to mention that the GFAP percentage value in the experimental group subjected to 3000 mm.s^{-1} velocity injury was significantly higher than the 1000 mm.s^{-1} velocity on both days 1 ($P < 0.05$) and 10 ($P < 0.0001$) post-injury.

At 4 mm displacement, there was a significant difference between experimental groups with input velocities of 1000 and 3000 mm.s^{-1} on day 1 post-injury. However, few cells expressed GFAP in both experimental groups of 1000 (~21%) and 3000 (~30%) mm.s^{-1} on day 1 post-injury. Ten days after injury, many reactive C6 astrocyte-like cells expressed large amounts of GFAP, where the mean value of the total area in experimental groups was increased to ~57% and ~79% at input velocity of 1000 and 3000 mm.s^{-1}, respectively. Overall, at day 10 post-injury, the percentage of the total area of GFAP expression was significantly higher than the control in both of the experimental groups. Further, there was a significant difference between the experimental groups.

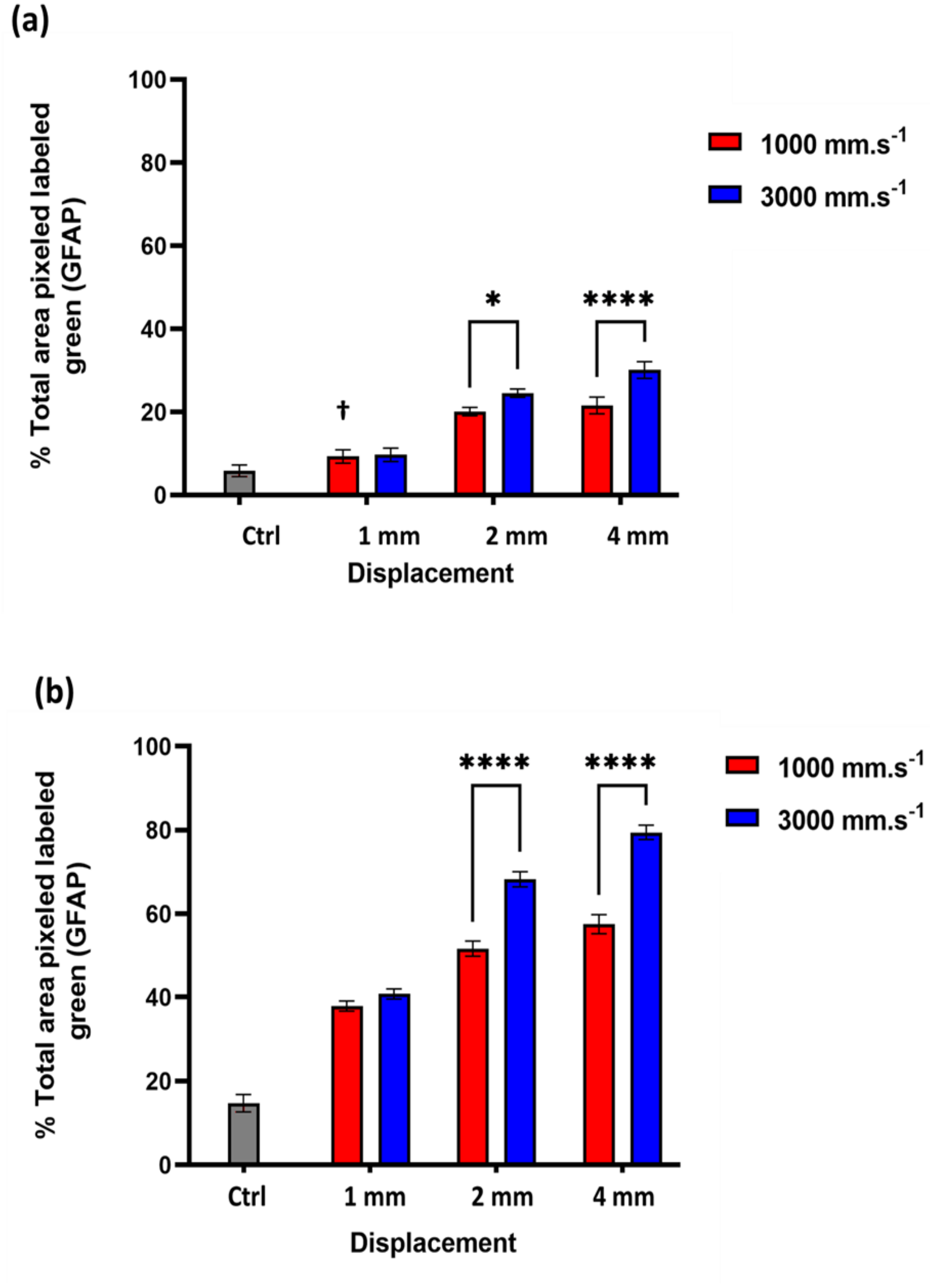

Figure 6.13. The percentage of the total area of GFAP expression in C6 astrocytes-like cells following simulated compression injury at input velocity of 1000 mm.s^{-1} and 3000 mm.s^{-1} at (a) day 1 and (b) day 10 post impaction. The impaction displacement depth was 1, 2 and 4 mm. Error bars indicate 95% confidence intervals; Two-way ANOVA followed by Tukey post-hoc correction tests, significance levels: Significance levels *P <0.05: **P <0.005, ****P <0.0001, n = 9. All experimental groups were significant (****P <0.0001) with the control group except 1 mm displacement on day 1 post-injury (denoted by †).

6.4.3.2 The effect of impaction displacement and velocity on the metabolic activity of C6 astrocyte-like cells following injury

An ATP assay was performed to monitor the metabolic activity of C6 astrocytes-like cells per sample over the 10 days post-injury, as detailed in section 3.5. Compression injury inflicted at 1000 mm.s^{-1} did not cause in any significant changes to the metabolic activity of the C6 cells on day 1. In addition, there were no differences between the test groups (Figure 6.14 (a)). On day 3, all test groups showed significantly increased metabolic activity compared to the control conditions (no injury), in which injury to 1, 2 and 4 mm displacement resulted in mean RLU ±95 CIs of $6.14 \pm 0.48 \times 10^6$, $9.04 \pm 0.37 \times 10^6$ and $9.09 \pm 0.23 \times 10^6$ RLU, respectively (Figure 6.14 (a)). Metabolic activity for all test groups was significantly increased ($P < 0.0001$) compared to the control group on day 10, where it was $11.14 \pm 0.48 \times 10^6$, $16.05 \pm 0.38 \times 10^6$ and $17.5 \pm 0.59 \times 10^6$ RLU after injury with 1, 2 and 4 mm displacements, respectively (Figure 6.14 (a)).

Compression injury imposed at 3000 mm.s^{-1} and 4 mm displacement induced significant changes in metabolic activity of C6 astrocyte-like cells compared to the control group on day 1 (Figure 6.14 (b)). On day 3, all experimental groups showed considerably increased metabolic activity compared to the control, where injury to 1, 2 and 4 mm displacement resulted in RLU ± 95% CIs of $6.21 \pm 0.48 \times 10^6$, $7.03 \pm 0.30 \times 10^6$ and $8.47 \pm 0.20 \times 10^6$ RLU, respectively. In addition, similar to the velocity of 1000 mm.s^{-1}, metabolic activity for all test groups significantly increased on day 10, where the 4 mm displacement depth resulted in the most significant metabolic activity (mean $21.51 \pm 0.51 \times 10^6$ RLU).

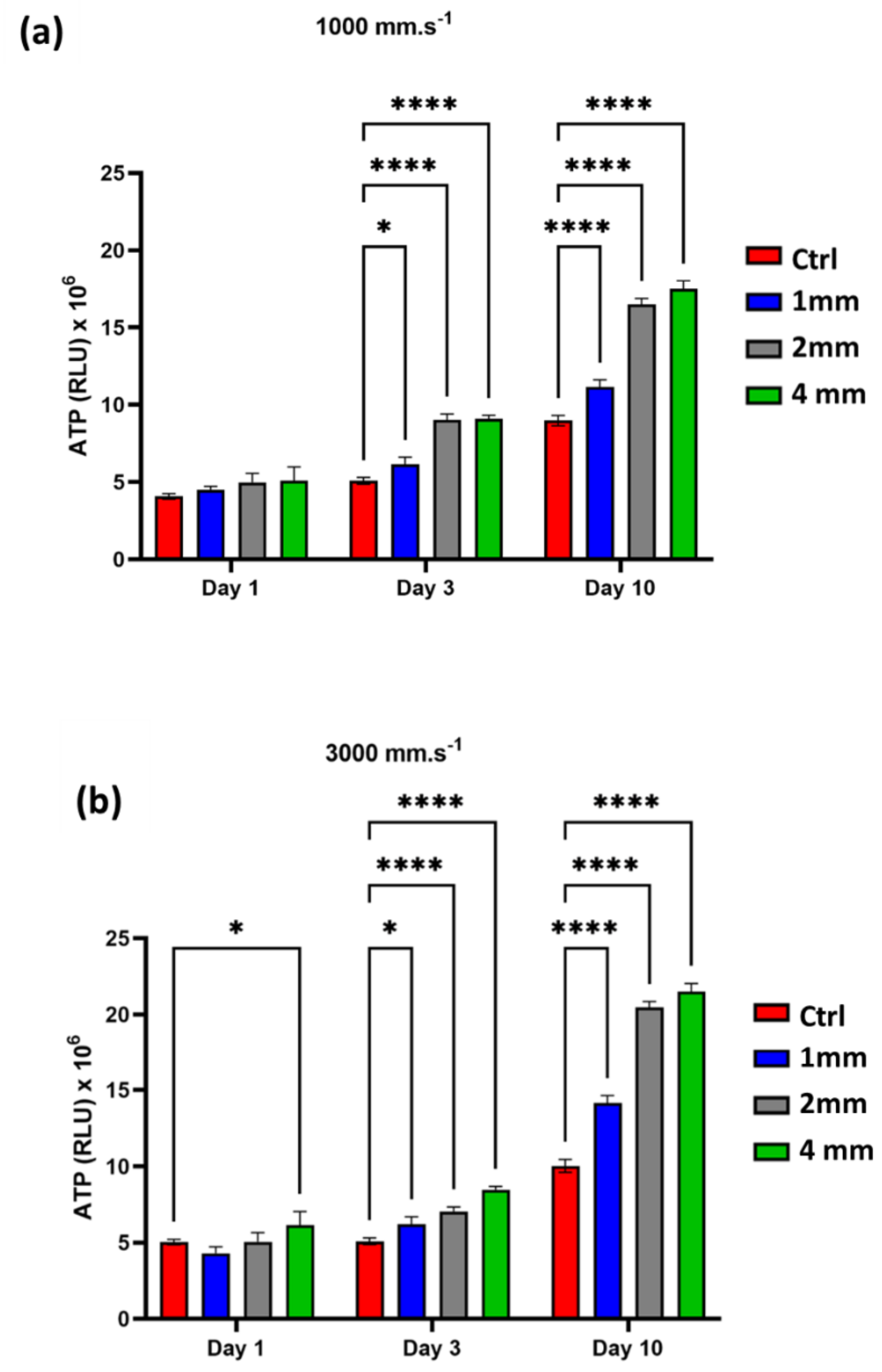

Figure 6.14. Metabolic activity of C6 astrocyte-like cells embedded in bioprinted GelMA hydrogels following simulated compression injury inflicted at (a) 1000 mm.s^{-1} and (b) 3000 mm.s^{-1}. The impaction displacement depth was 1, 2 and 4 mm. All test and control group (no injury) samples were immersed in a culture medium and incubated at 37 °C in 5% (v/v) CO_2 in air for 10 days post-injury. Error bars indicate a 95% confidence intervals; Two-way ANOVA followed by Tukey post-hoc correction tests, significance levels: Significance levels: *P <0.05, **P <0.005, ****P <0.0001, N = 3.

6.4.3.3 The effect of impaction displacement and velocity on the morphology of NG 108-15 neuronal cells following injury

The Immunofluorescence microscopy images of NG 108-15 neuronal cells embedded in bioprinted GelMA hydrogels and compressed to 1, 2 and 4 mm displacement depths at velocities of 1000 mm.s^{-1} and 3000 mm.s^{-1} are shown in Figures 6.15 and 6.16, respectively. Three samples for each group were tested.

At a velocity of 1000 mm.s^{-1}, immunocytochemistry labelling for βIII-tubulin (red) (a neuronal marker) and DAPI (blue) indicated round morphology of cells for all test groups and control samples on day 1 post-injury (Figure 6.15). After 10 days post-injury, encapsulated neurons projected branched neurites which stained positive for β-III tubulin at the bottom of hydrogels (near the plastic surface) for control and test samples subjected to displacement depths of 1 mm. However, the number of cells was decreased in the test groups that were subjected to displacement depths of 2 and 4 mm, compared to control and 1 mm displacement depth test samples. In addition, cells had a larger spheroid size in the control sample compared to other test group samples at 10 days post-injury.

At a velocity of 3000 mm.s^{-1}, cell morphology showed the same trend as observed at a velocity of 1000 mm.s^{-1}for all test group samples at 10 days post-injury (Figure 6.16). However, more cells were observed on day 1 post-injury for the samples impacted at 2 and 4 mm displacement depth at a velocity of 1000 mm.s^{-1} compared to 3000 mm.s^{-1}.

Overall, NG 108-15 neuronal cells appeared to be in a healthy state, as evidenced by the increased number of projections and neurites in the control samples. However, following the introduction of the injury, the number of projections significantly decreased, indicating that the neurons were not able to successfully regenerate across the injury site.

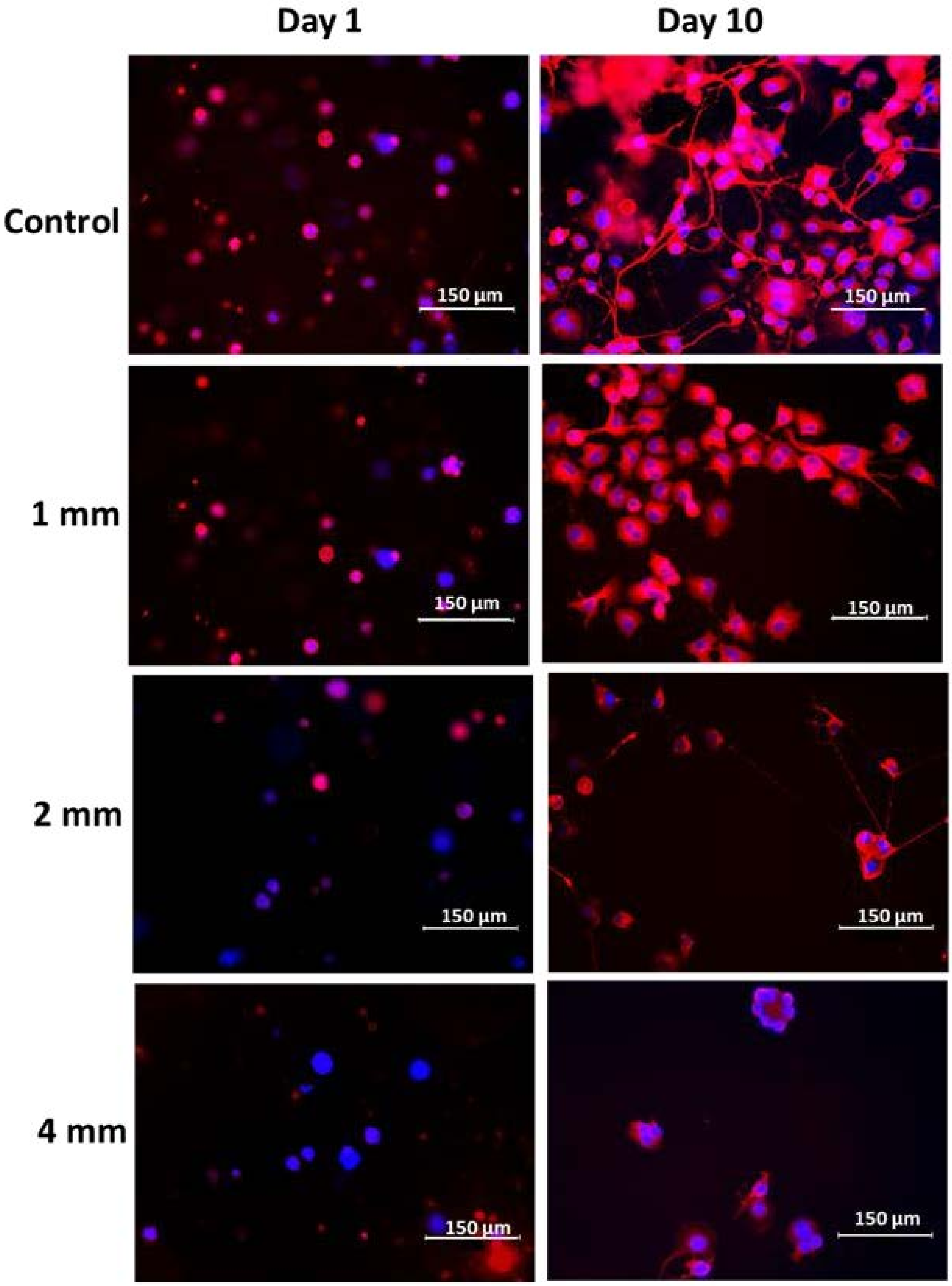

Figure 6.15. Immunofluorescence microscopy images of NG 108-15 neuronal cells embedded in bioprinted GelMA hydrogels following simulated compression injury inflicted at 1000 mm.s^{-1} on days 1 and 10. The cellular GelMA hydrogels were compressed at 1, 2 and 4 mm displacement. βIII-tubulin is shown in red and DAPI in blue. N=3.

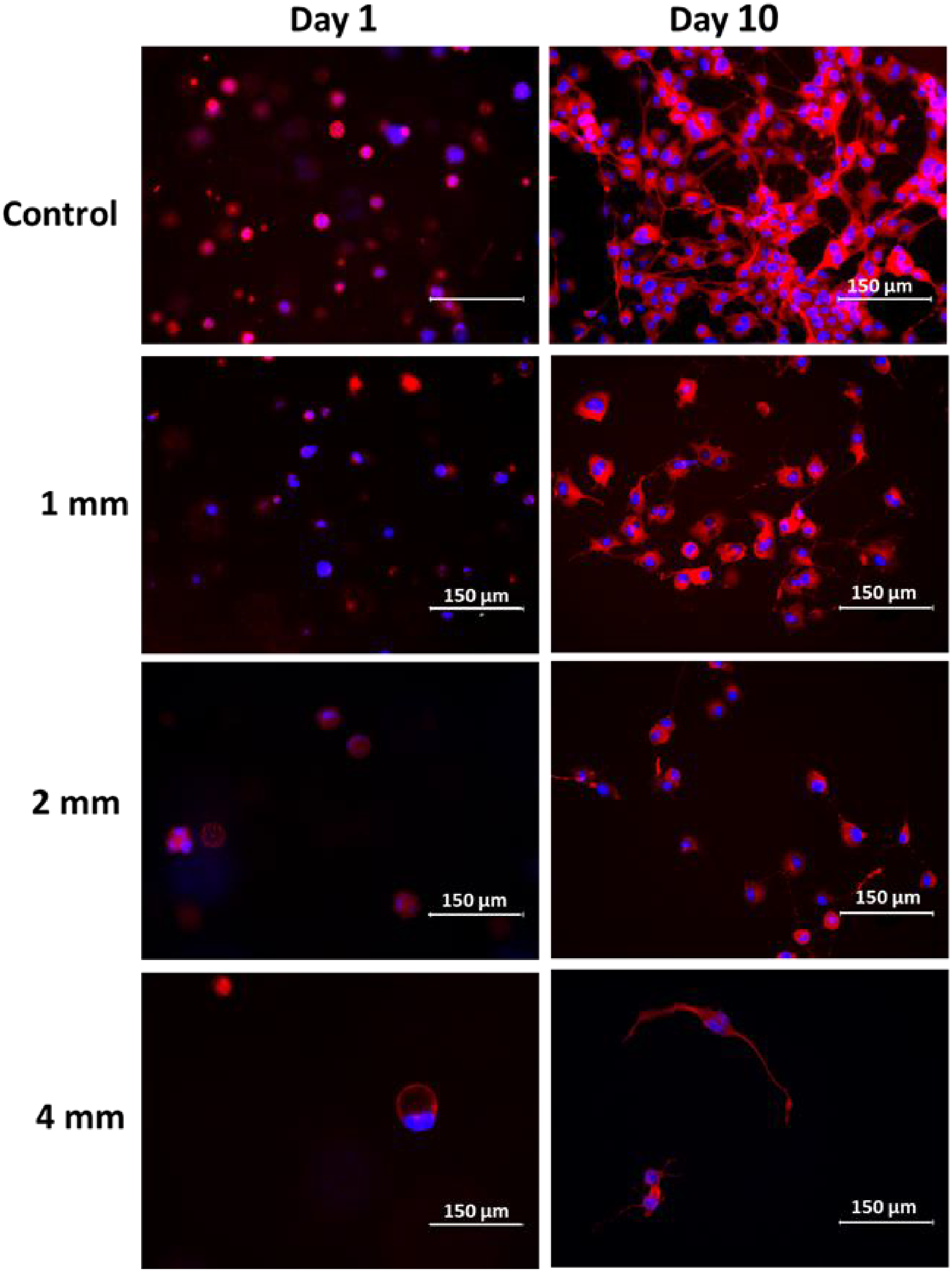

Figure 6.16. Immunofluorescence microscopy images of NG 108-15 neuronal cells embedded in bioprinted GelMA hydrogels following simulated compression injury inflicted at 3000 mm.s^{-1} on days 1 and 10. The cellular GelMA hydrogels were compressed at 1, 2 and 4 mm displacement. βIII-tubulin is shown in red and DAPI in blue. N=3.

6.4.3.4 The effect of impaction displacement and velocity on the viability of NG 108-15 neuronal cells following injury

The viability of NG 108-15 neuronal cells embedded in bioprinted GelMA hydrogels was determined by quantifying the ATP content of cells on days 1, 3 and 10 post-injury, as detailed in section 6.3.9.

Compression injury at a velocity of 1000 $mm.s^{-1}$ resulted in a significant reduction in cell viability in all test groups compared to control conditions (no injury), as shown in Figure 6.17 (a). On day 3, the cell viability was increased to $2.59 \pm 0.10 \times 10^6$, $2.40 \pm 0.21 \times 10^6$ and $2.26 \pm 0.10 \times 10^6$ RLU for samples impacted at 1, 2 and 4 mm displacement, respectively. However, the viability of cells in all test groups was still significantly lower than in the control group ($3.29 \pm 0.10 \times 10^6$ RLU). On day 10, the cell viability in control and 1 mm displacement test samples was increased to $6.8 \pm 0.13 \times 10^6$ and $4.79 \pm 0.3 \times 10^6$ RLU. However, the cell viability at 2 mm displacement depths ($2.72 \pm 0.10 \times 10^6$ RLU) and 4 mm displacement depths ($2.87 \pm 0.10 \times 10^6$ RLU) test samples slightly increased on day 10 compared to day 3 post-injury.

Compression injury at a velocity of 3000 $mm.s^{-1}$ caused a significant reduction in NG 108-15 neuronal cell viability to $1.1 \pm 0.095 \times 10^6$, $0.94 \pm 0.10 \times 10^6$ and $0.96 \pm 0.10 \times 10^6$ RLU for test samples subjected to 1, 2 and 4 mm displacement depths on day 1 post-injury, respectively, which was significantly lower than the control samples ($1.83 \pm 0.07 \times 10^6$ RLU), as shown in Figure 6.17 (b). On day 3, the cell viability of all test and control group samples increased to $2.90 \pm 0.40 \times 10^6$, $2.73 \pm 0.25 \times 10^6$ and $2.69 \pm 0.10 \times 10^6$ RLU, the control group was significantly higher ($3.72 \pm 0.10 \times 10^6$ RLU). In addition, at 10 days post-injury, the same trend with test samples that were compressed at 1000 $mm.s^{-1}$ velocity was observed for all test groups. However, the viability of cells was lower in the samples at injury speeds of 3000 $mm.s^{-1}$ than in the 1000 $mm.s^{-1}$ velocity samples.

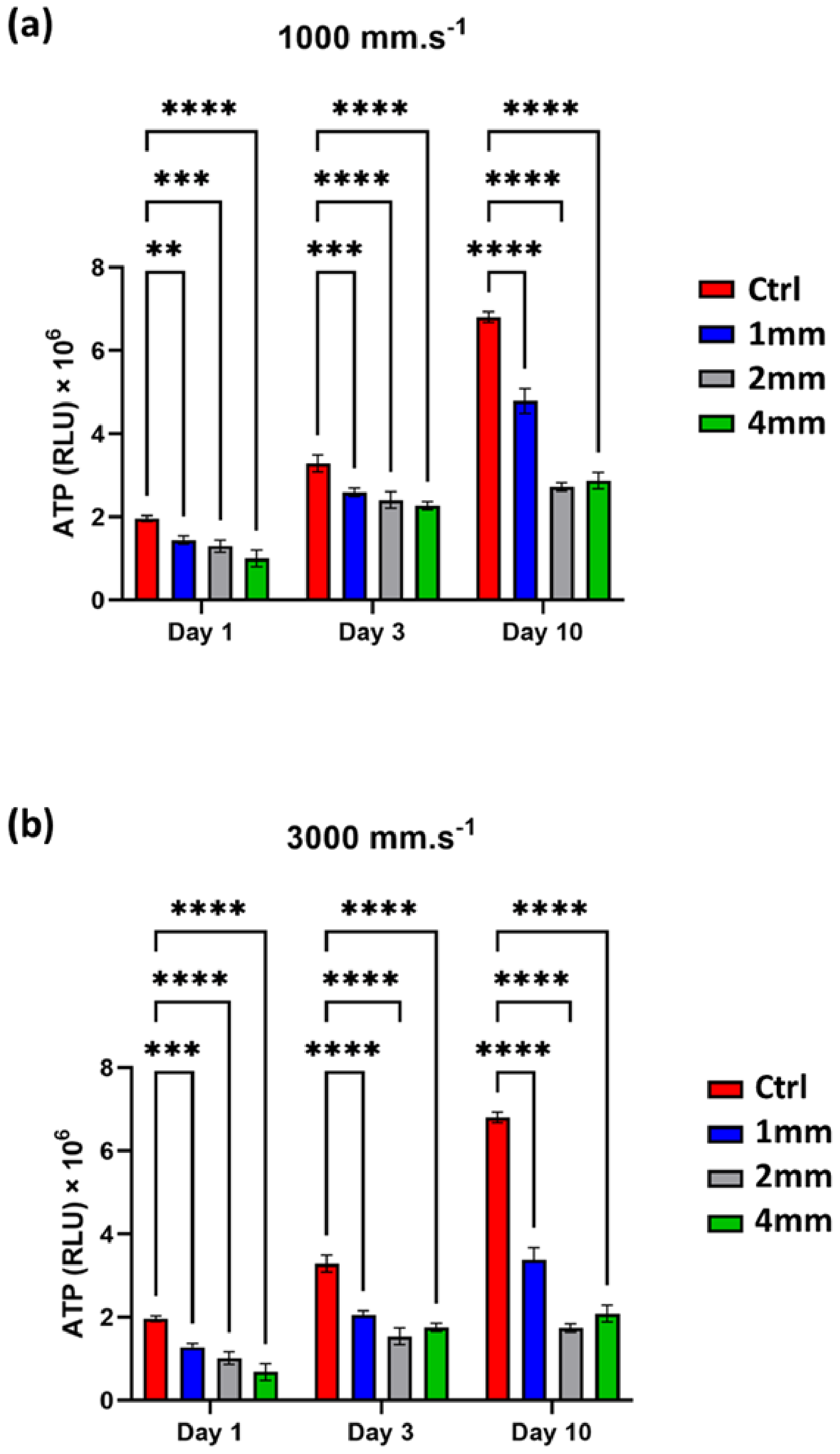

Figure 6.17. Viability of NG 108-15 cells embedded in bioprinted GelMA hydrogels following simulated compression injury inflicted at (a) 1000 and (b) 3000 mm.s^{-1}. The impaction displacement depth was 1, 2 and 4mm. All test and control group (no injury) samples were immersed with a culture medium and incubated at 37 °C in 5% (v/v) CO$_2$ in the air over 10 days post-injury. Error bars indicate a 95% confidence interval; Two-way ANOVA followed by Tukey post-hoc correction tests, significance levels: Significance levels: **P <0.005, ***P <0.0005, ****P <0.0001, N = 3.

6.5. Discussion

This chapter aimed to develop a clinically relevant 3D *in vitro* spinal cord injury model in terms of the mechanical forces and the biological responses. Protocols were defined with a range of input displacement and velocity parameters to represent contusion. Since the SCI occurs at high velocity and impact, the maximum possible velocity of the TA Instruments 5051 (3000 mm.s^{-1}) was also considered in our research. In addition, the hydrogel displacement depths of 1, 2, and 4 mm were selected based on clinical studies showing symptoms can occur above 15 to 50% compression of the spinal cord [285, 286]. The study successfully enabled precise and accurate axial compressive loads to be applied to cellular bioprinted GelMA hydrogel. The effect of impaction displacement and velocity on C6 astrocyte-like cells and NG 108-15 neuronal cells following injury were studied.

6.5.1 A 3D *in vitro* spinal cord contusion injury model

The first aim of this chapter was to optimise the mechanical outputs of TA Instruments Electroforce BioDynamic 5110 to simulate a spinal cord contusion injury model *in vitro,* using a 3D bioprinted GelMA hydrogel. The TA Instruments was used due to independent control of input velocity and displacement depth. Three scenarios were considered to represent a contusion injury, including a waveform with two ramp steps without a dwell time, two ramp steps with a 200 ms dwell time, and three ramp steps with a 200 ms dwell, as explained in section 6.3.4. The first two scenarios in this project were adapted from previous research (unpublished) at The University of Leeds to simulate a clinically relevant contusion injury event on 3D collagen hydrogels Nguyen [11].

In the first scenario, in a waveform with two ramps without dwell time, the percentage error between the input and output displacement profiles was increased with an increasing velocity at a given input displacement. The error percentage between input and output displacements was 20.4 %, 83.61 and 89.81 % at the velocity of 100, 1000 and 3000 mm.s^{-1}, respectively. The previous research by Nguyen [11] demonstrated that incorporating a dwell step between two ramps reduced the error between input and output profiles at the velocities of 100 and 1000 mm.s^{-1}. However, we didn't get the same results by adding just a dwell time between two ramp steps, and the percentage error between input and output profiles was still significant. The differences may be attributed to the different mechanical properties and height between collagen hydrogels, and 3D printed

GelMA hydrogels. The height of 3D bioprinted GelMA hydrogels in this thesis was approximately 4 mm, while the mean height of collagen hydrogels in the research by Nguyen [11] was 1.276 ± 0.1 mm.

In addition, in the model that Nguyen introduced, a contusion injury at a high velocity of 3000 mm.s^{-1} wasn't possible. In this thesis, by introducing an excess ramp step, satisfactory output profiles were observed at velocities 100, 1000 and 3000 mm.s^{-1} for all displacements of 1, 2 and 4 mm. In our contusion injury mode, the velocity was reduced to 1 mm.s^{-1} at 0.1 mm below the target displacement (1, 2 and 4 mm) to allow the apparatus to stop at the desired position. Although the recoil event was still observed in overshooting displacement, output displacements in our work closely matched input values with an additional ramp and a 200 ms dwell time.

It should be mentioned that a recoil event in the output displacements was observed for the waveforms with velocities of 1000 and 3000 mm.s^{-1}. Kirk [10] also observed the same results in the TA instrument Electroforce 5110 system and hypothesised that the recoil event was due to the elastic properties of the hydrogels. However, subsequently, Nguyen demonstrated that the appearance of the recoil was due to the working of the apparatus, regardless of the material presented [11]. Recoil can be explained by the abrupt change in momentum of the apparatus at high speeds. The apparatus cannot immediately change from high velocities to stationary; instead, recoil occurs. In this thesis, the results demonstrated that incorporating a dwell step and additional ramp step reduced the error between the input and output peak displacement value from 89% to less than 0.5%.

Although Kirk modelled a contusion injury at a high velocity of 3000 mm.s^{-1} using a TA Instrument 5110 Electroforce system [9, 10], the accuracy of displacements was undetermined since the input and output parameters weren't compared. In addition, the 3D collagen constructs used in previous studies had some challenges, such as meniscus formation in cast hydrogels, which created a non-uniform surface with inconsistent displacement depths. Another challenge in using collagen hydrogels was their batch-to-batch variability of them, which makes it challenging to tune their mechanical properties of them. The 3D printed GelMA hydrogels which was used in this thesis eliminated the problems experienced in previous works.

6.5.2 C6 Astrocyte-like responses to contusion injury *in vitro*

In this part of the study, GFAP expression of C6 astrocyte-like cells embedded within bioprinted GelMA hydrogels following simulated compression injury was evaluated one and ten days after impaction. The ten-day period was chosen based on clinical findings because the glial scar typically matures within two weeks post-injury [287-289]. Therefore, it was hypothesized that ten days would be sufficient to monitor a range of phenotypic changes in cells. Under control conditions (no injury), many of the intact cells with stained nuclei notably did not express GFAP, while an applied mechanical injury resulted in an increase in GFAP expression severity 10 days post impaction due to the increased energy applied to the cells [11]. In addition, the maximum branching and overlapping of astrocyte processes were observed at 4 mm displacement depths 10 days post impaction. Other research also showed that astrocytes respond to a range of CNS insults such as infection, trauma and neurodegenerative disease by becoming hypertrophic, increasing GFAP expression and undergoing molecular and morphological changes [184, 290].

An increase in input velocity from 1000 to 3000 $mm.s^{-1}$ resulted in a significant increase in astrocyte reactivity at the higher displacement depths (2 and 4 mm), as measured via the total area of GFAP expression. In part, this is a result of the viscoelastic nature of GelMA hydrogels which increases stiffness at higher speeds. It is well established that at high strain rates, the elastic response dominates, and the hydrogel exhibits an increased elastic modulus [291, 292]. Astrogliosis alterations may be triggered by direct strain transfer to astrocytes via mechanosensation or mechanotransduction, which is the process by which cells convert mechanical signals into biochemical signals. A very small number of studies have evaluated the effects of changing velocity (shear strain rate) on astrocyte outcomes in the context of spinal cord injury [293]. According to their findings [293], both cell death and degree of astrogliosis depend significantly on strain rate, thus implicating this biomechanical parameter in astrocytic mechanotransduction. Some *in vivo* studies also established that viscoelastic materials have an increased stiffness at high velocities or strain rates [294].

An ATP assay also was used to characterise cell viability and metabolic activity. A significant difference between the control and test samples (4 mm displacement, 3000 $mm.s^{-1}$ velocity) was observed on day 1 post-injury. The increase in ATP with exposure to injury may be due to the activation of astrocytes, which caused an increase in the metabolic activity of cells, thereby increasing the production of ATP. In a similar *in vitro* model also using the TA Instruments 5110 Electroforce apparatus to inflict injury, Kirk [10] observed a significant increase in ATP content on day 1 post-injury, at focal contusion displacement depths of 80% and 100% gel height (input velocity of 3000 mm.s^{-1}). In addition, the current study demonstrated that the GFAP expression progressed over time (10 days post-impaction) in terms of metabolic activity. This is comparable with a previous work, in which contusion injury was simulated at 1000 mm.s^{-1} for primary astrocytes within 3D collagen hydrogels [11].

6.5.3 NG 108-15 neuronal cells responses to contusion injury *in vitro*

The bioprinted GelMA hydrogels embedded with NG 108-15 neuronal cells, which were subjected to an injury, were investigated using immunocytochemistry and an ATP assay. An increased number of cells expressing β-III tubulin neuronal marker in NG 108-15 neuronal cells in a control sample (no injury) was observed. Neurite outgrowth was dependent on displacement depth, where cells in the control sample exhibited maximum numbers of projections.

A reduction in cell viability was observed for all experimental groups compared with the control group, which were impacted with input velocities of 1000 and 3000 mm.s^{-1} and cultured for 1, 3 and 10 days. Neuronal cell viability was decreased by increasing the velocity and displacement depth over 10 days post-injury. Samples impacted at 3000 mm/s with 4 mm displacement depth showed a maximum reduction of 71.5%, compared to a reduction of 57.7% for those impacted at 1000 mm/s with 4 mm displacement depth. Several *in vivo* studies have also reported the effect of biomechanical parameters on the severity of the injury. Pearse *et al.* [295] observed an increase in axon demyelination and decreased motor function with increasing impact depth from 0.80 to 1.1 mm, at a fixed velocity (100 mm.s^{-1}). In addition, there is evidence to suggest that the impactor speed can affect the pathology outcomes in spinal cord injury (SCI) models in vivo. For example, a study by Sparrey *et al.* [296] reported that the velocity of the contusion injury model at a 1 mm displacement depth affected the magnitude of white matter and neuronal damage in the rat spinal cord. They found that increasing the impactor speed led to more severe injuries, greater tissue damage, and increased cell death.

Generally, we have described the in vitro studies that were conducted to validate our 3D in vitro spinal cord injury model in terms of its mechanical and biological responses.

While these studies were essential for establishing the feasibility and initial validation of our model, we recognize the need for further validation using in vivo models.

6.6 Key findings

- The use of bioprinting created a 3D environment in that cells had fewer variations than a cast natural collagen hydrogel. Therefore, before presenting the injury scenario to the sample, a response to the injury was truly recorded rather than the inherent variability of the system.

- The TA Instruments Electroforce BioDynamic Impaction system successfully simulated a spinal cord contusion injury at high velocities of 1000 and 3000 mm.s^{-1} by incorporating a dwell step and three ram steps in a compression waveform

- The contusion injury simulation increased GFAP expression and metabolic activity of C6 astrocyte-like cells in impacted samples, which were not observed in the control group (non-injury).

- Astrocytic expression of the glial fibrillary acidic protein (GFAP), ramification and metabolic activity of C6 astrocyte-like cells increased with increasing displacement depth and velocity over 10 days post impaction.

- Neuronal cells showed the opposite behaviour, where βIII-tubulin (a neuronal marker) highlighted significantly higher neurite outgrowth and cell viability in control samples (no injury) compared to post-injury samples over 10 days.

CHAPTER 7 GENERAL DISCUSSION AND FUTURE WORK

7.1 General Discussions

The underpinning aim of this thesis was to simulate a clinically relevant 3D *in vitro* spinal cord contusion injury model in terms of mechanical forces and biological responses. There are three general categories of injury frequently used in animals to model spinal cord injury (SCI) *in vivo*; transection, compression and contusion [297]. SCI by transection is rare in humans; therefore, many researchers prefer to use compression or contusion injury to model human SCI [298]. Compression models injury to the spinal cord at low energy impact and progress over a while to years in length. Throughout the literature, contusion models of SCI have been developed to simulate an acute and transient SCI. A limitation of *in vivo* SCI models that isn't clinically relevant to human SCI is that most contusion SCI animal models require vertebral stabilization to produce a reproducible SCI [299]. The speed and injury mechanisms aren't similar to human injury, and errors of up to 73% in the velocity were measured for the *in vivo* SCI study [300]. In addition, the *in vivo* SCI model doesn't allow individual cell population responses or the effects of one cell type on another to be investigated.

In vitro models have greater control over the matrix environment, cells, and surrounding environment than *in vivo* models. Until now, the gold standard for 3D *in vitro* SCI model has been introduced by Philips and co-workers [73]. They used tethered self-aligned collagen hydrogels to simulate the alignment of the tracts within the naturally occurring nervous system. They demonstrated that neurite growth in the aligned regions of the astrocyte-seeded gels was more significant than in the unaligned areas. Afterwards, these models were utilised by Smith [9] to model contusion injury, using an Infinite Horizons Impactor to apply mechanical force. However, this model has some limitations, such as using a very large volume of collagen gel and a high number of cells, high cost and the inability to position cells. In other studies at the University of Leeds by [11], cast collagen hydrogels in a well plate were used in lower volumes to make a 3D environment for forming a basis for spinal cord injury models. However, this model also has some limitations, such as a lack of accuracy in casting the gels and meniscus formation. Due to a lack of precision in casting the gels into wells, cells couldn't be uniformly distributed, and the areas of the hydrogel with higher cell densities tend to cause faster contraction and a non-uniform surface.

Batch-to-batch variability of collagen hydrogels is another limitation of previous research. Due to the concentration of collagen varies from batch to batch so challenging to maintain consistency with natural materials. It should be mentioned that due to the high viscosity of properties of hydrogels, a large number of air bubbles are often formed when using a pipette to transfer hydrogels, which can influence the viability of cells. Limiting the consistency and reproducibility of the final product can affect the cells in a 3D environment, leading to cellular reactivity within 3D cast hydrogels before the injury has been applied. This makes it difficult to differentiate cellular responses that result from the injury and those that result from artefacts caused by the experimental set-up. So, in the case of presenting the injury scenario to the sample, a response to the injury couldn't be truly recorded.

The first part of the thesis aimed to fabricate 3D cellular environment constructs by 3D bioprinting techniques. A 3D printed structure with a high level of precise control of the structure and shape of the construct was achieved and eliminated the variations caused by natural cast hydrogels. A printed cylinder-shaped GelMA hydrogel had a consistent shape and a uniform surface. Cells were distributed uniformly through the gels, which supported the non-reactive state of C6- astrocyte cells in this environment. In addition, the mechanical properties of GelMA hydrogels were easily changed by changing the concentration of GelMA hydrogels. C6 astrocyte-like and NG 108-15 neuron cells were mechanosensitive, and hydrogel stiffness affected cell viability, as mentioned previously. The role of matrix stiffness in regulating CNS cells (neuronal and astrocyte) behaviour was discussed in the literature review chapter of this thesis.

The second part of this study aimed to assess the micromechanical properties of the 3D bioprinted hydrogels using Brillouin microspectroscopy (BM) to determine whether the bioprinted constructs were similar in stiffness to the native neural extracellular matrix to design a valid SCI model. The results in this thesis exhibited that the softer GelMA hydrogels with a volume concentration of 2.5 and 5% (w/v) had similar mechanical properties to native spinal cord tissue (~ 0.1-4.8 kPa) [269]. In addition, an evaluation of the mechanical properties of the GelMA hydrogels was done over incubation time and demonstrated that the stiffness of the 5 % (w/v) GelMA volume concentration was stable from the third day onwards. This indicates that this hydrogel concentration (5 % (w/v)) is appropriate for use in a 3D spinal cord injury model. The previous study performed by Smith [9] showed that stiffness properties of both fully hydrated (FH) and fully stabilised

(FS) collagen gels which were stable over the five days in culture, were selected for use as a matrix component in a 3D SCI model. They demonstrated that mechanical stability hydrogel help to keep astrocyte cells in were in a non-reactive state before the injury. However, they used the rheology technique, which caused damage to the gel after measurement. In this thesis, the micromechanical properties of such models were characterised non-destructively and over a prolonged span of time using BM. BM allowed the monitoring of the micromechanical properties of cellular hydrogels over time with repeated measurements on the same sample.

By assessing bioprinted cellular GelMA hydrogels on the local micro-scale, the mechanical properties of the surrounding matrix of the NG 108-15 neuronal spheroids were measured successfully. This result may be valuable for investigating the mechanical properties of the matrix after injury. It is not clear what the full effects of the mechanical properties of tissue after injury mechanism have on GFAP expression, and answering this question could help to understand neuron regeneration in the glial scar area.

After a 3D environment was successfully fabricated, the TA Instruments Electroforce BioDynamic Impaction system simulated a spinal cord contusion injury. The capabilities of the TA Instruments Electroforce BioDynamic 5110 system to simulate *in vitro* SCI models have already been verified in previous PhD studies by Nguyen [11], Timms [284] and Kirk [10] at the University of Leeds. In all previous research, cast collagen hydrogels were used as a 3D environment to model traumatic and non-traumatic spinal cord injury *in vitro*. Although the research carried out in the last chapter of this thesis builds on the previous study at the University of Leeds by Nguyen [11], the effects of different injury mechanisms and injury severity on neurite outgrowth were not assessed in the last contusion injury model. In the research carried out by Nguyen [11], astrocytes embedded in a collagen hydrogel were used to simulate the conditions in the CNS in a 3D culture model. They modelled a contusion injury using the TA Instrument 5110 Electroforce BioDynamic 5110 at 100 and 1000 mm.s^{-1} to depths of 25, 50, and 75% gel thickness. Our research improved the previous model and considered the maximum velocity possible of the TA Instruments (3000 mm.s^{-1}) since SCI occurs at high speeds and impact.

The results in chapter 6 of this thesis showed that more GFAP was expressed by increasing velocity from 1000 to 3000 mm.s^{-1}. The contusion injury simulation induced GFAP expression of C6 astrocyte-like cells that was not observed in the control groups.

In addition, the metabolic activity of C6 astrocyte-like cells increased with increasing displacement depth and velocity over 10 days post impaction. However, NG 108-15 Neuronal cells showed the opposite behaviour, where the number of projections was significantly reduced after injury.

Overall, the in vitro model developed in this thesis provides a valuable tool for investigating the complex cellular and molecular events involved in SCI. By controlling injury parameters, this model enables the interrogation of the response of individual cell types to injury mechanics, which is difficult to achieve using animal models. Several *in vivo* models also demonstrated the same cellular behaviour after the injury mechanism [295, 296]. Pearse *et al.* [295] and Sparrey *et al.* [296] simulated contusion injury models. They showed that the variation of velocity and impact depth affected neuronal damage and axon demyelination in the rat spinal cord. In addition, in [301], Yan and co-authors used an impactor to establish a contusion SCI model in rats. These authors [301] demonstrated that an increase in GFAP expression and proliferation occurred in the region of injury. However, in their model, some parameters like velocity, strike force and cord displacement during injury were not identified. The accurate measurement of these injury parameters improves the consistency and reproducibility of SCI models. The contusion injury which was modelled in this thesis used a TA Instruments Electroforce, which allowed injury parameters to be controlled in this system.

The novel aspects of this thesis include the 3D printing of GelMA hydrogels and the mechanical assessment of these hydrogels using the non-contact and non-destructive method of BM. In a recent study by Alakpa et al. [302], bioprinted Schwann and mesenchymal stem cells encapsulated in GelMA and hyaluronic acid (HA) were used to promote neurite outgrowth in a spatially controlled manner for potential use in spinal cord injury repair. Such models hold promise for improving tissue repair and regeneration by providing a more biologically relevant environment that can guide and support cell behavior. However, the mechanical properties of a hydrogel play a crucial role in investigating neuron regeneration, which was not investigated in their study. In this thesis, an in vitro model was developed by understanding the mechanisms involved in cell-hydrogel interactions at the microscale level. The results presented in Chapters 4 and 5 may aid in modeling spinal cord injury more accurately, resembling the in vivo conditions. However, further modifications to the in vitro model may be necessary to mimic the in vivo environment more closely. For example, the incorporation of additional cell types or extracellular matrix proteins may enhance the biological relevance of the model.

The use of in vitro co-culture models has been increasingly explored in SCI research to investigate the complex interplay between various cell types in the spinal cord microenvironment. One such study by Jones and colleagues utilized a co-culture system consisting of spinal cord neurons and astrocytes to investigate the role of astrocytes in axonal regeneration after injury [303]. The authors found that the presence of astrocytes inhibited axonal regeneration and that this effect was mediated by the secretion of inhibitory molecules such as chondroitin sulfate proteoglycans (CSPGs). Similarly, another study by Scott and colleagues utilized a co-culture system consisting of neurons, astrocytes, and oligodendrocyte precursor cells (OPCs) to investigate the effects of CSPGs on OPC differentiation and myelination. The authors found that the presence of CSPGs inhibited OPC differentiation and myelination and that this effect was mediated by the upregulation of the bone morphogenetic protein (BMP) signaling pathway [304]. While these co-culture models have provided valuable insights into the cellular and molecular mechanisms underlying SCI, it is important to note that they are still limited in their ability to fully replicate the complex in vivo microenvironment of the spinal cord. In particular, the absence of mechanical forces and other cell types such as immune cells and endothelial cells may limit the relevance of these models to the in vivo setting.

Overall, the focus of this study was to investigate the passive effects of mechanical forces on biological responses in an in vitro model of SCI. The aim was to better understand the intricate relationship between mechanical forces and biological responses in spinal cord injury, which can inform future therapeutic approaches. Using non-destructive biophysical measurements, such as characterizing the mechanical properties of in vitro models, the study was able to provide insightful knowledge into how mechanical forces can impact the response of neuronal and glial cells to varying impact parameters. The results of this study provide a foundation for future investigations into the development of more clinically relevant in vivo models and the potential for improved therapeutic strategies.

7.2 Future Investigation

A 3D *in vitro* model of SCI used in this study demonstrated the potential to be a clinically relevant model in the future. However, the functionality of the model could be improved with several future research directions, which are recommended as follows:

7.2.1 Cell combinations and types

In this thesis, only the response of astrocytes and neuron cells to impaction injury in isolation was investigated. However, astrocyte cells can affect the survival of neuron cells by regulating synaptic function and supporting neurite outgrowth. Increasing the cellular complexity of the model by incorporating astrocytes and neuron cells into co-cultures needs to be examined in future. It would be interesting to compare the results of *in vitro* co-culture model with *in vivo* models regarding mechanical forces and biological responses.

7.2.2 Geometry complexity of the model

As mentioned previously, the aligned nature of collagen hydrogels has been utilised as a matrix material to model neuronal cell types. Therefore, it would be interesting to fabricate bioprinted aligned structures in GelMA hydrogels for 3D culturing of neuronal cells and compare them with those observed within 3D collagen hydrogel models. Additionally, aligned scaffold structures could provide better oxygen diffusion within a three-dimensional structure and improvement of cell viability and proliferation.

7.2.3 Further Assays

It would be useful to investigate other methods of analysis and assays to extract as much information as possible from our 3D *in vitro* model. It would be interesting to characterise the cytokine release of C6 astrocytes-like and NG 108-18 neuronal cells by an enzyme-linked immunoabsorbant assay (ELISA) in isolation and co-culture. In addition, gene expression can be measured by PCR to investigate whether there are any differences in gene expression profiles (GEPs) between non-activated and activated astrocytes.

7.2.4 Oxygen concentration effects

The difference in oxygen concentration between in vitro and in vivo conditions could have a significant impact on the outcomes of the spinal cord injury (SCI) model. In vivo, the oxygen concentration in tissues can decrease significantly after injury, leading to hypoxia and oxidative stress. These factors can contribute to secondary injury and cell death, which can have significant implications for recovery outcomes.

By incubating cell cultures in air containing 20% oxygen, the SCI model may not accurately reflect the oxygen levels present in the in vivo situation. Varying the oxygen concentration in cell cultures could provide important insights into the impact of hypoxia on cellular and molecular mechanisms involved in SCI.

For instance, it has been shown that decreasing oxygen levels can influence the expression of genes involved in inflammation and cell death pathways. Moreover, the levels of reactive oxygen species (ROS) can also be affected by changes in oxygen concentration. ROS play a critical role in the secondary injury phase, and their levels are tightly regulated in vivo. Therefore, exploring the impact of varying oxygen concentrations on ROS levels in vitro could provide valuable information for designing future SCI models.

Overall, understanding how oxygen concentration affects outcomes in the SCI model could provide important insights into the molecular mechanisms underlying SCI and could help to improve the relevance of in vitro models to the in vivo situation.

7.2.5 BM measurements post-injury

Since, in this thesis, there were some differences in GFAP expression of C6 astrocyte-like cells between test samples (injured) and control samples (non-injury), it would be interesting to evaluate whether there are also mechanical differences. Bulk and local mechanical properties of the hydrogel environment can be evaluated using BM. Mechanical characterisation would be very valuable for investigating and controlling glial scar formation after the injury process.

7.3 Overall conclusion

In conclusion, a clinically relevant 3D *in vitro* contusion injury model using bioprinted GelMA hydrogels has been developed in this study. The main findings of the study were as follows:

- Printability was inversely related to the volume concentration of GelMA hydrogels. GelMA hydrogels with 2.5 % (w/v) volume concentration showed minimal printability and stability of 3D constructs over 7 days of incubation at 37 °C, 5% (v/v) CO_2 in air.

- The quantitative and qualitative cell viability results presented in this study indicated that both C6 astrocyte-like and NG 108-15 neuronal cells were minimally proliferative in the stiffer printed GelMA hydrogels (7.5 % and 10 % (w/v)) compared to softer printed GelMA hydrogels (2.5 % and 5 % (w/v)).

- The bioprinted GelMA hydrogel with 5% (w/v) concentration was the most appropriate matrix for a 3D *in vitro* spinal cord injury model due to optimal printability and structural stability over time, in addition to high cell viability, and adequate transparency.

- Brillouin microspectroscopy, as a non-invasive and label-free method, was utilised to characterise the micromechanical properties of 3D bioprinted acellular and cellular GelMA hydrogels to design a valid SCI model.

- By assessing bioprinted acellular GelMA hydrogels, it was found that the softer hydrogels with a volume concentration of 2.5 and 5% (w/v) had similar mechanical properties to native neural tissue.

- By assessing the bioprinted cellular GelMA hydrogels on the bulk scale, it was found that the stiffness of the 2.5 % (w/v) GelMA volume concentration had significantly reduced from the third day onwards, which indicated this concentration of hydrogel was not appropriate for use in a 3D spinal cord injury model.

- By assessing bioprinted cellular GelMA hydrogels on the local micro-scale, the mechanical properties of the surrounding matrix of the NG 108-15 neuronal spheroids were measured successfully. This non damaging in situ mechanical characterisation method may be valuable for interpreting biological responses of cells after impaction in a 3D *in vitro* SCI model.

- The TA Instruments Electroforce BioDynamic Impaction system successfully simulated a spinal cord contusion injury at different velocities of 100, 1000 and 3000 mm.s^{-1} by incorporating a dwell step and three ram steps in a compression waveform.

- The use of bioprinting created a 3D environment in that cells had fewer variations than a cast natural collagen hydrogel. Therefore, before presenting the injury scenario to the sample, a response to the injury was truly recorded rather than the inherent variability of the system.

- The contusion injury simulation increased GFAP expression and metabolic activity of C6 astrocyte-like cells in impacted samples, which were not observed in the control group (non-injury).

- Astrocytic expression of the glial fibrillary acidic protein (GFAP), ramification and metabolic activity of C6 astrocyte-like cells increased with increasing displacement depth and velocity over 10 days post impaction.

- Neuronal cells showed the opposite behaviour, where βIII-tubulin (a neuronal marker) highlighted significantly higher neurite outgrowth and cell viability in control samples (no injury) compared to post-injury samples over 10 days.

References

1. Bican, O., A. Minagar, and A.A. Pruitt, *The spinal cord: a review of functional neuroanatomy.* Neurologic clinics, 2013. **31**(1): p. 1-18.
2. Carlson, G.D., et al., *Sustained spinal cord compression: part II: effect of methylprednisolone on regional blood flow and recovery of somatosensory evoked potentials.* JBJS, 2003. **85**(1): p. 95-101.
3. AIHW. *Spinal cord injury, Australia 2017–18*. 2021; Available from: https://www.aihw.gov.au/reports/injury/spinal-cord-injury-australia-2017-18/summary.
4. *Spinal cord injury key facts*. 2022 [cited 2023; Available from: https://www.spinalcure.org.au/media-releases/media-release-tommy-little-hands-over-103520-cheque-for-world-leading-experimental-therapy-for-spinal-cord-injury/#:~:text=Spinal%20cord%20injury%20key%20facts&text=There%20are%20over%2020%2C000%20people,2020%20estimated%20at%20%2475%20billion.
5. Moshayedi, P., et al., *The relationship between glial cell mechanosensitivity and foreign body reactions in the central nervous system.* Biomaterials, 2014. **35**(13): p. 3919-3925.
6. Vitale, A.M., et al., *Variability in the generation of induced pluripotent stem cells: importance for disease modeling.* Stem cells translational medicine, 2012. **1**(9): p. 641-650.
7. Azari, H. and B.A. Reynolds, *In vitro models for neurogenesis.* Cold Spring Harbor perspectives in biology, 2016. **8**(6): p. a021279.
8. Joung, D., et al., *3D printed neural regeneration devices.* Advanced functional materials, 2020. **30**(1): p. 1906237.
9. Smith, J.T., *A 3D Culture Model to Investigate Cellular Responses to Mechanical Loading in Spinal Cord Injury*. 2016, University of Leeds.
10. Kirk, J.S.L., *Development of a 3D in vitro spinal cord injury model to investigate how the mechanical properties of the matrix affect CNS cell behaviour*. 2018, University of Leeds.
11. Nguyen, T.K., *Modelling of Traumatic Spinal Cord Injury In Vitro*. 2020, University of Leeds.
12. Holloway, J.L., *Three-dimensional bioprinting to bridge the gap in spinal cord injuries.* Science Translational Medicine, 2018. **10**(455): p. eaau8874.
13. Rea, P., *Essential clinical anatomy of the nervous system*. 2015: Academic Press.
14. Laurencin, C.T. and Y. Khan, *Regenerative engineering*. 2013: CRC Press.
15. Purves, D.E., et al., *Neuroscience.* 2008.
16. Jacobson, S., E.M. Marcus, and S. Pugsley, *Neuroanatomy for the Neuroscientist*. 2011: Springer.
17. *SPINAL CORD & COLUMN*. 2022; Available from: https://www.sci-info-pages.com/spinal-cord-and-column/.
18. Krames, E., P.H. Peckham, and A.R. Rezai, *Neuromodulation: comprehensive textbook of principles, technologies, and therapies*. 2018: Academic Press.
19. Chédotal, A., *Roles of axon guidance molecules in neuronal wiring in the developing spinal cord.* Nature Reviews Neuroscience, 2019. **20**(7): p. 380-396.
20. Rehfeld, A., M. Nylander, and K. Karnov, *Nerve Tissue*, in *Compendium of Histology*. 2017, Springer. p. 247-266.

21. Jäkel, S. and L. Dimou, *Glial cells and their function in the adult brain: a journey through the history of their ablation.* Frontiers in cellular neuroscience, 2017. **11**: p. 24.
22. Sofroniew, M.V. and H.V. Vinters, *Astrocytes: biology and pathology.* Acta neuropathologica, 2010. **119**(1): p. 7-35.
23. Del Bigio, M.R., *Ependymal cells: biology and pathology.* Acta neuropathologica, 2010. **119**(1): p. 55-73.
24. Singh, V., *Textbook of clinical neuroanatomy*. 2014: Elsevier Health Sciences.
25. Ding, Y., et al., *Reticulocalbin-1 facilitates microglial phagocytosis.* PloS one, 2015. **10**(5): p. e0126993.
26. Ones, K., et al., *Comparison of functional results in non-traumatic and traumatic spinal cord injury.* Disability and rehabilitation, 2007. **29**(15): p. 1185-1191.
27. Gedde, M.H., et al., *Traumatic vs non-traumatic spinal cord injury: A comparison of primary rehabilitation outcomes and complications during hospitalization.* The journal of spinal cord medicine, 2019: p. 1-7.
28. Karunakaran, K.D., *A multimodal approach to investigate brain reorganization after spinal cord injury using functional magnetic resonance imaging and functional near-infrared spectroscopy*. 2019, New Jersey Institute of Technology.
29. Rowland, J.W., et al., *Current status of acute spinal cord injury pathophysiology and emerging therapies: promise on the horizon.* Neurosurgical focus, 2008. **25**(5): p. E2.
30. Dumont, R.J., et al., *Acute spinal cord injury, part I: pathophysiologic mechanisms.* Clinical neuropharmacology, 2001. **24**(5): p. 254-264.
31. Ahuja, C.S., et al., *Traumatic spinal cord injury—repair and regeneration.* Neurosurgery, 2017. **80**(3S): p. S9-S22.
32. Ahuja, C.S., et al., *Traumatic spinal cord injury.* Nature reviews Disease primers, 2017. **3**(1): p. 1-21.
33. Li, N. and G.K. Leung, *Oligodendrocyte precursor cells in spinal cord injury: a review and update.* BioMed research international, 2015. **2015**.
34. Gruner, J.A., *A monitored contusion model of spinal cord injury in the rat.* Journal of neurotrauma, 1992. **9**(2): p. 123-128.
35. Rivlin, A. and C. Tator, *Effect of duration of acute spinal cord compression in a new acute cord injury model in the rat.* Surgical neurology, 1978. **10**(1): p. 38-43.
36. Dabney, K.W., et al., *A model of experimental spinal cord trauma based on computer-controlled intervertebral distraction: characterization of graded injury.* Spine, 2004. **29**(21): p. 2357-2364.
37. STOKES, B.T., *Experimental spinal cord injury: a dynamic and verifiable injury device.* Journal of neurotrauma, 1992. **9**(2): p. 129-134.
38. Bottai, D., et al., *Embryonic stem cells promote motor recovery and affect inflammatory cell infiltration in spinal cord injured mice.* Experimental Neurology, 2010. **223**(2): p. 452-463.
39. Marcol, W., et al., *Air gun impactor—a novel model of graded white matter spinal cord injury in rodents.* Journal of reconstructive microsurgery, 2012. **28**(08): p. 561-568.
40. Agrawal, G., et al., *Characterization of graded MASCIS contusion spinal cord injury using somatosensory evoked potentials.* Spine, 2010. **35**(11): p. 1122.
41. Blight, A.R., *Morphometric analysis of a model of spinal cord injury in guinea pigs, with behavioral evidence of delayed secondary pathology.* Journal of the neurological sciences, 1991. **103**(2): p. 156-171.

42. Jazayeri, S.B., et al., *The effect of timing of decompression on neurologic recovery and histopathologic findings after spinal cord compression in a rat model.* Acta Medica Iranica, 2013: p. 431-437.
43. Tarlov, I., H. Klinger, and S. Vitale, *Spinal cord compression studies: I. experimental techniques to produce acute and gradual compression.* AMA Archives of Neurology & Psychiatry, 1953. **70**(6): p. 813-819.
44. da Costa, E.S.A., et al., *Strapping the spinal cord: an innovative experimental model of CNS injury in rats.* Journal of neuroscience methods, 2008. **170**(1): p. 130-139.
45. Min-Te Choo, A., et al., *Modeling spinal cord contusion, dislocation, and distraction: characterization of vertebral clamps, injury severities, and node of Ranvier deformations.* Journal of neuroscience methods, 2009. **181**(1): p. 6-17.
46. Seifert, J., et al., *Characterization of a novel bidirectional distraction spinal cord injury animal model.* Journal of neuroscience methods, 2011. **197**(1): p. 97-103.
47. Lukovic, D., et al., *Complete rat spinal cord transection as a faithful model of spinal cord injury for translational cell transplantation.* Scientific reports, 2015. **5**: p. 9640.
48. Cheriyan, T., et al., *Spinal cord injury models: a review.* Spinal cord, 2014. **52**(8): p. 588-595.
49. Watson, B.D., et al., *Photochemically induced spinal cord injury in the rat.* Brain research, 1986. **367**(1-2): p. 296-300.
50. Teo, L., J. Rosenfeld, and J. Bourne, *Models of CNS injury in the nonhuman primate: a new era for treatment strategies.* Translational Neuroscience, 2012. **3**(2): p. 181-195.
51. Fiford, R., et al., *A vertebral dislocation model of spinal cord injury in rats.* Journal of neurotrauma, 2004. **21**(4): p. 451-458.
52. Petteys, R.J., et al., *Design and testing of a controlled electromagnetic spinal cord impactor for use in large animal models of acute traumatic spinal cord injury.* Journal of Clinical Neuroscience, 2017. **43**: p. 229-234.
53. Cavaliere, F., E. San Vicente, and C. Matute, *An organotypic culture model to study nigro-striatal degeneration.* Journal of neuroscience methods, 2010. **188**(2): p. 205-212.
54. Ravikumar, M., et al., *An organotypic spinal cord slice culture model to quantify neurodegeneration.* Journal of neuroscience methods, 2012. **211**(2): p. 280-288.
55. Sypecka, J., et al., *The organotypic longitudinal spinal cord slice culture for stem cell study.* Stem cells international, 2015. **2015**.
56. Mazuchowski, E.L. and L.E. Thibault. *Biomechanical properties of the human spinal cord and pia mater.* in *Summer Bioengineering Conference, Sonesta Beach Resort, Key Biscayne, FL, USA*. 2003.
57. Oakland, R., et al., *The biomechanical response of spinal cord tissue to uniaxial loading.* Proceedings of the Institution of Mechanical Engineers, Part H: Journal of Engineering in Medicine, 2006. **220**(4): p. 489-492.
58. Carter, J.W., et al., *Canal geometry changes associated with axial compressive cervical spine fracture.* Spine, 2000. **25**(1): p. 46.
59. Bilston, L.E., *Neural tissue biomechanics*. Vol. 3. 2011: Springer Science & Business Media.
60. Yu, A.C., Y. Lee, and L. Eng, *Astrogliosis in culture: I. The model and the effect of antisense oligonucleotides on glial fibrillary acidic protein synthesis.* Journal of neuroscience research, 1993. **34**(3): p. 295-303.

61. Polikov, V.S., et al., *In vitro model of glial scarring around neuroelectrodes chronically implanted in the CNS.* Biomaterials, 2006. **27**(31): p. 5368-5376.
62. Slovinska, L., et al., *In Vitro Models of Spinal Cord Injury*, in *Recovery of Motor Function Following Spinal Cord Injury*. 2016, IntechOpen.
63. Alexander, J.K., B. Fuss, and R.J. Colello, *Electric field-induced astrocyte alignment directs neurite outgrowth.* Neuron glia biology, 2006. **2**(2): p. 93-103.
64. Wu, V.W. and J.P. Schwartz, *Cell culture models for reactive gliosis: new perspectives.* Journal of neuroscience research, 1998. **51**(6): p. 675-681.
65. Fornasari, B.E., et al., *Natural-based biomaterials for peripheral nerve injury repair.* Frontiers in bioengineering and biotechnology, 2020. **8**: p. 554257.
66. Wang, Y., H. Tan, and X. Hui, *Biomaterial scaffolds in regenerative therapy of the central nervous system.* BioMed research international, 2018. **2018**.
67. Perale, G., et al., *Hydrogels in spinal cord injury repair strategies.* ACS chemical neuroscience, 2011. **2**(7): p. 336-345.
68. Raghavan, S., et al., *Decoupling diffusional from dimensional control of signaling in 3D culture reveals a role for myosin in tubulogenesis.* Journal of cell science, 2010. **123**(17): p. 2877-2883.
69. Leung, B.M., et al., *Microscale 3D collagen cell culture assays in conventional flat-bottom 384-well plates.* Journal of laboratory automation, 2015. **20**(2): p. 138-145.
70. Lee, H., *Spinal cord cellular response to wear debris from metal-on-metal total disc replacements*. 2016, University of Leeds.
71. Glass-Brudzinski, J., D. Perizzolo, and D. Brunette, *Effects of substratum surface topography on the organization of cells and collagen fibers in collagen gel cultures.* Journal of Biomedical Materials Research: An Official Journal of The Society for Biomaterials, The Japanese Society for Biomaterials, and The Australian Society for Biomaterials and the Korean Society for Biomaterials, 2002. **61**(4): p. 608-618.
72. Lanfer, B., et al., *Directed growth of adult human white matter stem cell–derived neurons on aligned fibrillar collagen.* Tissue Engineering Part A, 2010. **16**(4): p. 1103-1113.
73. East, E., et al., *Alignment of astrocytes increases neuronal growth in three-dimensional collagen gels and is maintained following plastic compression to form a spinal cord repair conduit.* Tissue engineering Part A, 2010. **16**(10): p. 3173-3184.
74. Kahl, M., et al., *Ultra-low-cost 3D bioprinting: modification & application of an off-the-shelf desktop 3D-printer for biofabrication.* Frontiers in bioengineering and biotechnology, 2019. **7**: p. 184.
75. Berg, J., et al., *Optimization of cell-laden bioinks for 3D bioprinting and efficient infection with influenza A virus.* Scientific reports, 2018. **8**(1): p. 1-13.
76. Heinrich, M.A., et al., *3D Bioprinting: from Benches to Translational Applications.* Small, 2019. **15**(23): p. 1805510.
77. Lee, S.-J., et al., *Fabrication of a highly aligned neural scaffold via a table top stereolithography 3D printing and electrospinning.* Tissue Engineering Part A, 2017. **23**(11-12): p. 491-502.
78. Chen, C., et al., *Collagen/heparin sulfate scaffolds fabricated by a 3D bioprinter improved mechanical properties and neurological function after spinal cord injury in rats.* Journal of Biomedical Materials Research Part A, 2017. **105**(5): p. 1324-1332.

79. Yuan, T.-Y., et al., *3D Bioprinting for Spinal Cord Injury Repair.* Frontiers in Bioengineering and Biotechnology, 2022. **10**.
80. Garg, S. and A. Garg, *Hydrogel: Classification, Properties, Preparation and Technical Features.* Asian J. Biomat. Res, 2016. **2**: p. 163-170.
81. Prang, P., et al., *The promotion of oriented axonal regrowth in the injured spinal cord by alginate-based anisotropic capillary hydrogels.* Biomaterials, 2006. **27**(19): p. 3560-3569.
82. Stokols, S., et al., *Templated agarose scaffolds support linear axonal regeneration.* Tissue engineering, 2006. **12**(10): p. 2777-2787.
83. Aurand, E.R., K.J. Lampe, and K.B. Bjugstad, *Defining and designing polymers and hydrogels for neural tissue engineering.* Neuroscience research, 2012. **72**(3): p. 199-213.
84. Samadikuchaksaraei, A., *An overview of tissue engineering approaches for management of spinal cord injuries.* Journal of neuroengineering and rehabilitation, 2007. **4**(1): p. 15.
85. Chvatal, S.A., et al., *Spatial distribution and acute anti-inflammatory effects of methylprednisolone after sustained local delivery to the contused spinal cord.* Biomaterials, 2008. **29**(12): p. 1967-1975.
86. Kim, Y.-t., J.-M. Caldwell, and R.V. Bellamkonda, *Nanoparticle-mediated local delivery of methylprednisolone after spinal cord injury.* Biomaterials, 2009. **30**(13): p. 2582-2590.
87. Lee, H., R.J. McKeon, and R.V. Bellamkonda, *Sustained delivery of thermostabilized chABC enhances axonal sprouting and functional recovery after spinal cord injury.* Proceedings of the National Academy of Sciences, 2010. **107**(8): p. 3340-3345.
88. Jain, A., et al., *Sustained delivery of activated Rho GTPases and BDNF promotes axon growth in CSPG-rich regions following spinal cord injury.* PloS one, 2011. **6**(1).
89. Jain, A., et al., *In situ gelling hydrogels for conformal repair of spinal cord defects, and local delivery of BDNF after spinal cord injury.* Biomaterials, 2006. **27**(3): p. 497-504.
90. Stokols, S. and M.H. Tuszynski, *Freeze-dried agarose scaffolds with uniaxial channels stimulate and guide linear axonal growth following spinal cord injury.* Biomaterials, 2006. **27**(3): p. 443-451.
91. Luo, Y. and M.S. Shoichet, *A photolabile hydrogel for guided three-dimensional cell growth and migration.* Nature materials, 2004. **3**(4): p. 249-253.
92. Zuidema, J.M., et al., *Fabrication and characterization of tunable polysaccharide hydrogel blends for neural repair.* Acta biomaterialia, 2011. **7**(4): p. 1634-1643.
93. Banerjee, A., et al., *The influence of hydrogel modulus on the proliferation and differentiation of encapsulated neural stem cells.* Biomaterials, 2009. **30**(27): p. 4695-4699.
94. Novikova, L.N., et al., *Alginate hydrogel and matrigel as potential cell carriers for neurotransplantation.* Journal of Biomedical Materials Research Part A: An Official Journal of The Society for Biomaterials, The Japanese Society for Biomaterials, and The Australian Society for Biomaterials and the Korean Society for Biomaterials, 2006. **77**(2): p. 242-252.
95. Ashton, R.S., et al., *Scaffolds based on degradable alginate hydrogels and poly (lactide-co-glycolide) microspheres for stem cell culture.* Biomaterials, 2007. **28**(36): p. 5518-5525.

96. Shanbhag, M.S., et al., *Neural progenitor cells grown on hydrogel surfaces respond to the product of the transgene of encapsulated genetically engineered fibroblasts.* Biomacromolecules, 2010. **11**(11): p. 2936-2943.
97. Gu, H., et al., *Control of in vitro neural differentiation of mesenchymal stem cells in 3D macroporous, cellulosic hydrogels.* Regenerative medicine, 2010. **5**(2): p. 245-253.
98. Crompton, K.E., et al., *Polylysine-functionalised thermoresponsive chitosan hydrogel for neural tissue engineering.* Biomaterials, 2007. **28**(3): p. 441-449.
99. Horn, E.M., et al., *Influence of cross-linked hyaluronic acid hydrogels on neurite outgrowth and recovery from spinal cord injury.* Journal of Neurosurgery: Spine, 2007. **6**(2): p. 133-140.
100. Iwata, A., et al., *Long-term survival and outgrowth of mechanically engineered nervous tissue constructs implanted into spinal cord lesions.* Tissue engineering, 2006. **12**(1): p. 101-110.
101. Pfister, B.J., et al., *Development of transplantable nervous tissue constructs comprised of stretch-grown axons.* Journal of neuroscience methods, 2006. **153**(1): p. 95-103.
102. Hiraoka, M., et al., *Enhanced survival of neural cells embedded in hydrogels composed of collagen and laminin-derived cell adhesive peptide.* Bioconjugate chemistry, 2009. **20**(5): p. 976-983.
103. Semino, C.E., et al., *Entrapment of migrating hippocampal neural cells in three-dimensional peptide nanofiber scaffold.* Tissue engineering, 2004. **10**(3-4): p. 643-655.
104. Willerth, S.M., et al., *The effects of soluble growth factors on embryonic stem cell differentiation inside of fibrin scaffolds.* Stem cells, 2007. **25**(9): p. 2235-2244.
105. Wang, L.-S., et al., *Injectable biodegradable hydrogels with tunable mechanical properties for the stimulation of neurogenesic differentiation of human mesenchymal stem cells in 3D culture.* Biomaterials, 2010. **31**(6): p. 1148-1157.
106. Silva, N.A., et al., *Development and characterization of a novel hybrid tissue engineering–based scaffold for spinal cord injury repair.* Tissue Engineering Part A, 2010. **16**(1): p. 45-54.
107. Park, J., et al., *Nerve regeneration following spinal cord injury using matrix metalloproteinase-sensitive, hyaluronic acid-based biomimetic hydrogel scaffold containing brain-derived neurotrophic factor.* Journal of Biomedical Materials Research Part A: An Official Journal of The Society for Biomaterials, The Japanese Society for Biomaterials, and The Australian Society for Biomaterials and the Korean Society for Biomaterials, 2010. **93**(3): p. 1091-1099.
108. Pan, L., et al., *Viability and differentiation of neural precursors on hyaluronic acid hydrogel scaffold.* Journal of Neuroscience Research, 2009. **87**(14): p. 3207-3220.
109. Varghese, O.P., et al., *In Situ Cross-Linkable High Molecular Weight Hyaluronan− Bisphosphonate Conjugate for Localized Delivery and Cell-Specific Targeting: A Hydrogel Linked Prodrug Approach.* Journal of the American Chemical Society, 2009. **131**(25): p. 8781-8783.
110. Wei, Y.T., et al., *Hyaluronic acid hydrogel modified with nogo-66 receptor antibody and poly-l-lysine to promote axon regrowth after spinal cord injury.* Journal of Biomedical Materials Research Part B: Applied Biomaterials, 2010. **95**(1): p. 110-117.

111. Wei, Y., et al., *Hyaluronic acid hydrogels with IKVAV peptides for tissue repair and axonal regeneration in an injured rat brain.* Biomedical Materials, 2007. **2**(3): p. S142.
112. Tian, W., et al., *Hyaluronic acid hydrogel as Nogo-66 receptor antibody delivery system for the repairing of injured rat brain: in vitro.* Journal of Controlled Release, 2005. **102**(1): p. 13-22.
113. Hou, S., et al., *The enhancement of cell adherence and inducement of neurite outgrowth of dorsal root ganglia co-cultured with hyaluronic acid hydrogels modified with Nogo-66 receptor antagonist in vitro.* Neuroscience, 2006. **137**(2): p. 519-529.
114. Baumann, M.D., et al., *Intrathecal delivery of a polymeric nanocomposite hydrogel after spinal cord injury.* Biomaterials, 2010. **31**(30): p. 7631-7639.
115. Wang, Y., et al., *Accelerated release of a sparingly soluble drug from an injectable hyaluronan–methylcellulose hydrogel.* Journal of Controlled Release, 2009. **140**(3): p. 218-223.
116. Baumann, M.D., et al., *An injectable drug delivery platform for sustained combination therapy.* Journal of Controlled Release, 2009. **138**(3): p. 205-213.
117. Reynolds, L.F., et al., *Transplantation of porous tubes following spinal cord transection improves hindlimb function in the rat.* Spinal Cord, 2008. **46**(1): p. 58-64.
118. Shoichet, M.S., et al., *Intrathecal drug delivery strategy is safe and efficacious for localized delivery to the spinal cord.* Progress in brain research, 2007. **161**: p. 385-392.
119. Kang, C.E., et al., *A new paradigm for local and sustained release of therapeutic molecules to the injured spinal cord for neuroprotection and tissue repair.* Tissue Engineering Part A, 2009. **15**(3): p. 595-604.
120. Hsieh, A., et al., *Hydrogel/electrospun fiber composites influence neural stem/progenitor cell fate.* Soft Matter, 2010. **6**(10): p. 2227-2237.
121. Brännvall, K., et al., *Enhanced neuronal differentiation in a three-dimensional collagen-hyaluronan matrix.* Journal of neuroscience research, 2007. **85**(10): p. 2138-2146.
122. Thonhoff, J.R., et al., *Compatibility of human fetal neural stem cells with hydrogel biomaterials in vitro.* Brain Research, 2008. **1187**: p. 42-51.
123. Coviello, T., et al., *A new scleroglucan/borax hydrogel: swelling and drug release studies.* International Journal of Pharmaceutics, 2005. **289**(1-2): p. 97-107.
124. *Implantation of Functionalized Thermally Gelling Xyloglucan Hydrogel Within the Brain: Associated Neurite Infiltration and Inflammatory Response.* Tissue Engineering Part A, 2010. **16**(9): p. 2833-2842.
125. Nisbet, D.R., et al., *Enhancing neurite outgrowth from primary neurones and neural stem cells using thermoresponsive hydrogel scaffolds for the repair of spinal cord injury.* Journal of Biomedical Materials Research Part A, 2009. **89A**(1): p. 24-35.
126. Rodriguez-Tenreiro, C., et al., *Estradiol sustained release from high affinity cyclodextrin hydrogels.* European Journal of Pharmaceutics and Biopharmaceutics, 2007. **66**(1): p. 55-62.
127. Rodriguez-Tenreiro, C., et al., *Cyclodextrin/carbopol micro-scale interpenetrating networks (ms-IPNs) for drug delivery.* Journal of Controlled Release, 2007. **123**(1): p. 56-66.

128. Yang, C.-Y., et al., *Biocompatibility of amphiphilic diblock copolypeptide hydrogels in the central nervous system.* Biomaterials, 2009. **30**(15): p. 2881-2898.
129. Jiang, F.X., et al., *Neurite Outgrowth on a DNA Crosslinked Hydrogel with Tunable Stiffnesses.* Annals of Biomedical Engineering, 2008. **36**(9): p. 1565.
130. Ramires, P.A., et al., *In vitro and in vivo biocompatibility evaluation of a polyalkylimide hydrogel for soft tissue augmentation.* Journal of Biomedical Materials Research Part B: Applied Biomaterials, 2005. **72B**(2): p. 230-238.
131. *Three-Dimensional Nanofibrous Scaffolds Incorporating Immobilized BDNF Promote Proliferation and Differentiation of Cortical Neural Stem Cells.* Stem Cells and Development, 2010. **19**(6): p. 843-852.
132. Hu, B.-H., J. Su, and P.B. Messersmith, *Hydrogels Cross-Linked by Native Chemical Ligation.* Biomacromolecules, 2009. **10**(8): p. 2194-2200.
133. Lampe, K.J., et al., *Effect of macromer weight percent on neural cell growth in 2D and 3D nondegradable PEG hydrogel culture.* Journal of Biomedical Materials Research Part A, 2010. **94A**(4): p. 1162-1171.
134. Skornia, S.L., et al., *Mechanical Properties of Layered Poly (Ethylene Glycol) Gels.* Journal of Applied Biomaterials and Biomechanics, 2007. **5**(3): p. 176-183.
135. Mahoney, M.J. and K.S. Anseth, *Three-dimensional growth and function of neural tissue in degradable polyethylene glycol hydrogels.* Biomaterials, 2006. **27**(10): p. 2265-2274.
136. Krsko, P., et al., *Length-scale mediated adhesion and directed growth of neural cells by surface-patterned poly(ethylene glycol) hydrogels.* Biomaterials, 2009. **30**(5): p. 721-729.
137. Koh, W.-G., A. Revzin, and M.V. Pishko, *Poly(ethylene glycol) Hydrogel Microstructures Encapsulating Living Cells.* Langmuir, 2002. **18**(7): p. 2459-2462.
138. Salmaso, S., et al., *Cyclodextrin/PEG based hydrogels for multi-drug delivery.* International Journal of Pharmaceutics, 2007. **345**(1): p. 42-50.
139. Ali, O.A., et al., *Infection-mimicking materials to program dendritic cells in situ.* Nature Materials, 2009. **8**(2): p. 151-158.
140. Rauch, M.F., et al., *Engineering angiogenesis following spinal cord injury: a coculture of neural progenitor and endothelial cells in a degradable polymer implant leads to an increase in vessel density and formation of the blood–spinal cord barrier.* European Journal of Neuroscience, 2009. **29**(1): p. 132-145.
141. Rauch, M.F., et al., *Co-culture of primary neural progenitor and endothelial cells in a macroporous gel promotes stable vascular networks in vivo.* Journal of Biomaterials Science, Polymer Edition, 2008. **19**(11): p. 1469-1485.
142. Pritchard, C.D., et al., *An injectable thiol-acrylate poly(ethylene glycol) hydrogel for sustained release of methylprednisolone sodium succinate.* Biomaterials, 2011. **32**(2): p. 587-597.
143. Burdick, J.A., et al., *Stimulation of neurite outgrowth by neurotrophins delivered from degradable hydrogels.* Biomaterials, 2006. **27**(3): p. 452-459.
144. Piantino, J., et al., *An injectable, biodegradable hydrogel for trophic factor delivery enhances axonal rewiring and improves performance after spinal cord injury.* Experimental Neurology, 2006. **201**(2): p. 359-367.
145. Metters, A.T., K.S. Anseth, and C.N. Bowman, *Fundamental studies of a novel, biodegradable PEG-b-PLA hydrogel.* Polymer, 2000. **41**(11): p. 3993-4004.

146. Metters, A.T., C.N. Bowman, and K.S. Anseth, *Verification of scaling laws for degrading PLA-b-PEG-b-PLA hydrogels.* AIChE Journal, 2001. **47**(6): p. 1432-1437.
147. Comolli, N., et al., *In vitro analysis of PNIPAAm–PEG, a novel, injectable scaffold for spinal cord repair.* Acta Biomaterialia, 2009. **5**(4): p. 1046-1055.
148. Li, J., X. Ni, and K.W. Leong, *Injectable drug-delivery systems based on supramolecular hydrogels formed by poly(ethylene oxide)s and α-cyclodextrin.* Journal of Biomedical Materials Research Part A, 2003. **65A**(2): p. 196-202.
149. Hejčl, A., et al., *Macroporous hydrogels based on 2-hydroxyethyl methacrylate. Part 6: 3D hydrogels with positive and negative surface charges and polyelectrolyte complexes in spinal cord injury repair.* Journal of Materials Science: Materials in Medicine, 2009. **20**(7): p. 1571.
150. Ales, H., et al., *Acute and delayed implantation of positively charged 2-hydroxyethyl methacrylate scaffolds in spinal cord injury in the rat.* Journal of Neurosurgery: Spine SPI, 2008. **8**(1): p. 67-73.
151. Bakshi, A., et al., *Mechanically engineered hydrogel scaffolds for axonal growth and angiogenesis after transplantation in spinal cord injury.* 2004. **1**(3): p. 322.
152. Carone, T.W. and J.M. Hasenwinkel, *Mechanical and morphological characterization of homogeneous and bilayered poly(2-hydroxyethyl methacrylate) scaffolds for use in CNS nerve regeneration.* Journal of Biomedical Materials Research Part B: Applied Biomaterials, 2006. **78B**(2): p. 274-282.
153. Syková, E., et al., *Bone Marrow Stem Cells and Polymer Hydrogels—Two Strategies for Spinal Cord Injury Repair.* Cellular and Molecular Neurobiology, 2006. **26**(7): p. 1111-1127.
154. Katayama, Y., et al., *Coil-reinforced hydrogel tubes promote nerve regeneration equivalent to that of nerve autografts.* Biomaterials, 2006. **27**(3): p. 505-518.
155. Nomura, H., et al., *COMPLETE SPINAL CORD TRANSECTION TREATED BY IMPLANTATION OF A REINFORCED SYNTHETIC HYDROGEL CHANNEL RESULTS IN SYRINGOMYELIA AND CAUDAL MIGRATION OF THE ROSTRAL STUMP.* Neurosurgery, 2006. **59**(1): p. 183-192.
156. Tsai, E.C., et al., *Matrix inclusion within synthetic hydrogel guidance channels improves specific supraspinal and local axonal regeneration after complete spinal cord transection.* Biomaterials, 2006. **27**(3): p. 519-533.
157. Piotrowicz, A. and M.S. Shoichet, *Nerve guidance channels as drug delivery vehicles.* Biomaterials, 2006. **27**(9): p. 2018-2027.
158. Hejčl, A., et al., *HPMA-RGD Hydrogels Seeded with Mesenchymal Stem Cells Improve Functional Outcome in Chronic Spinal Cord Injury.* Stem cells and development, 2010. **19**: p. 1535-46.
159. Geever, L.M., et al., *Characterisation and controlled drug release from novel drug-loaded hydrogels.* European Journal of Pharmaceutics and Biopharmaceutics, 2008. **69**(3): p. 1147-1159.
160. Strappe, P.M., et al., *Delivery of a lentiviral vector in a Pluronic F127 gel to cells of the central nervous system.* European Journal of Pharmaceutics and Biopharmaceutics, 2005. **61**(3): p. 126-133.
161. Gander, B., et al., *Effect of Polymeric Network Structure on Drug Release from Cross-Linked Poly(Vinyl Alcohol) Micromatrices.* Pharmaceutical Research, 1989. **6**(7): p. 578-584.
162. Tsai, E.C., et al., *Synthetic hydrogel guidance channels facilitate regeneration of adult rat brainstem motor axons after complete spinal cord transection.* Journal of neurotrauma, 2004. **21**(6): p. 789-804.

163. Piao, Y., et al., *Biomedical applications of gelatin methacryloyl hydrogels.* Engineered Regeneration, 2021. **2**: p. 47-56.
164. Yue, K., et al., *Synthesis, properties, and biomedical applications of gelatin methacryloyl (GelMA) hydrogels.* Biomaterials, 2015. **73**: p. 254-271.
165. Van Den Bulcke, A.I., et al., *Structural and rheological properties of methacrylamide modified gelatin hydrogels.* Biomacromolecules, 2000. **1**(1): p. 31-38.
166. Perale, G., et al., *Hydrogel for Cell Housing in the Brain and in the Spinal Cord.* The International Journal of Artificial Organs, 2011. **34**(3): p. 295-303.
167. Perale, G., et al., *In situ agar–carbomer hydrogel polycondensation: A chemical approach to regenerative medicine.* Materials Letters, 2011. **65**(11): p. 1688-1692.
168. Park, S.-H., M.-K. Chun, and H.-K. Choi, *Preparation of an extended-release matrix tablet using chitosan/Carbopol interpolymer complex.* International Journal of Pharmaceutics, 2008. **347**(1): p. 39-44.
169. Leipzig, N.D., et al., *Differentiation of neural stem cells in three-dimensional growth factor-immobilized chitosan hydrogel scaffolds.* Biomaterials, 2011. **32**(1): p. 57-64.
170. Yu, L.M.Y., K. Kazazian, and M.S. Shoichet, *Peptide surface modification of methacrylamide chitosan for neural tissue engineering applications.* Journal of Biomedical Materials Research Part A, 2007. **82A**(1): p. 243-255.
171. Leipzig, N.D. and M.S. Shoichet, *The effect of substrate stiffness on adult neural stem cell behavior.* Biomaterials, 2009. **30**(36): p. 6867-6878.
172. Wang, X., et al., *Dog sciatic nerve regeneration across a 30-mm defect bridged by a chitosan/PGA artificial nerve graft.* Brain, 2005. **128**(8): p. 1897-1910.
173. Zheng Shu, X., et al., *In situ crosslinkable hyaluronan hydrogels for tissue engineering.* Biomaterials, 2004. **25**(7): p. 1339-1348.
174. Mehrotra, S., et al., *Time Controlled Protein Release from Layer-by-Layer Assembled Multilayer Functionalized Agarose Hydrogels.* Advanced Functional Materials, 2010. **20**(2): p. 247-258.
175. Royce Hynes, S., et al., *Photopolymerized poly(ethylene glycol)/poly(L-lysine) hydrogels for the delivery of neural progenitor cells.* Journal of Biomaterials Science, Polymer Edition, 2007. **18**(8): p. 1017-1030.
176. DeForest, C.A., E.A. Sims, and K.S. Anseth, *Peptide-Functionalized Click Hydrogels with Independently Tunable Mechanics and Chemical Functionality for 3D Cell Culture.* Chemistry of Materials, 2010. **22**(16): p. 4783-4790.
177. de Jong, S.J., et al., *Physically crosslinked dextran hydrogels by stereocomplex formation of lactic acid oligomers: degradation and protein release behavior.* Journal of Controlled Release, 2001. **71**(3): p. 261-275.
178. Kang, Y.M., et al., *Thermosensitive polymer-based hydrogel mixed with the anti-inflammatory agent minocycline induces axonal regeneration in hemisected spinal cord.* Macromolecular Research, 2010. **18**(4): p. 399-403.
179. Fan, L., et al., *Directing induced pluripotent stem cell derived neural stem cell fate with a three-dimensional biomimetic hydrogel for spinal cord injury repair.* ACS applied materials & interfaces, 2018. **10**(21): p. 17742-17755.
180. Koffler, J., et al., *Biomimetic 3D-printed scaffolds for spinal cord injury repair.* Nature medicine, 2019. **25**(2): p. 263-269.
181. Chen, Z., et al., *NSC-derived extracellular matrix-modified GelMA hydrogel fibrous scaffolds for spinal cord injury repair.* NPG Asia Materials, 2022. **14**(1): p. 1-11.

182. Chen, C., et al., *Bioinspired hydrogel electrospun fibers for spinal cord regeneration.* Advanced Functional Materials, 2019. **29**(4): p. 1806899.

183. Royce Hynes, S., et al., *Photopolymerized poly (ethylene glycol)/poly (L-lysine) hydrogels for the delivery of neural progenitor cells.* Journal of Biomaterials Science, Polymer Edition, 2007. **18**(8): p. 1017-1030.

184. Sofroniew, M.V., *Molecular dissection of reactive astrogliosis and glial scar formation.* Trends in neurosciences, 2009. **32**(12): p. 638-647.

185. Mucke, L., et al., *Rapid activation of astrocyte-specific expression of GFAP-lacZ transgene by focal injury.* The New biologist, 1991. **3**(5): p. 465-474.

186. Wilson, C.L., S.L. Hayward, and S. Kidambi, *Astrogliosis in a dish: Substrate stiffness induces astrogliosis in primary rat astrocytes.* RSC advances, 2016. **6**(41): p. 34447-34457.

187. Min, S.K., et al., *Regulation of astrocyte activity via control over stiffness of cellulose acetate electrospun nanofiber.* In Vitro Cellular & Developmental Biology-Animal, 2015. **51**(9): p. 933-940.

188. Placone, A.L., et al., *Human astrocytes develop physiological morphology and remain quiescent in a novel 3D matrix.* Biomaterials, 2015. **42**: p. 134-143.

189. Georges, X.J.P.C., et al., *Cell growth in response to mechanical stiffness is affected by neuron-astroglia interactions.* The Open Neuroscience Journal, 2007. **1**(1).

190. Seidlits, S.K., et al., *The effects of hyaluronic acid hydrogels with tunable mechanical properties on neural progenitor cell differentiation.* Biomaterials, 2010. **31**(14): p. 3930-3940.

191. Mahmoud, S., et al., *Astrocytes maintain glutamate homeostasis in the CNS by controlling the balance between glutamate uptake and release.* Cells, 2019. **8**(2): p. 184.

192. Wen, Y.-Q., et al., *Substrate stiffness affects neural network activity in an extracellular matrix proteins dependent manner.* Colloids and Surfaces B: Biointerfaces, 2018. **170**: p. 729-735.

193. Willits, R.K. and S.L. Skornia, *Effect of collagen gel stiffness on neurite extension.* Journal of Biomaterials Science, Polymer Edition, 2004. **15**(12): p. 1521-1531.

194. Flanagan, L.A., et al., *Neurite branching on deformable substrates.* Neuroreport, 2002. **13**(18): p. 2411.

195. Wu, Y., et al., *The influence of the stiffness of GelMA substrate on the outgrowth of PC12 cells.* Bioscience reports, 2019. **39**(1).

196. Koch, D., et al., *Strength in the periphery: growth cone biomechanics and substrate rigidity response in peripheral and central nervous system neurons.* Biophysical journal, 2012. **102**(3): p. 452-460.

197. Lowery, L.A. and D. Van Vactor, *The trip of the tip: understanding the growth cone machinery.* Nature reviews Molecular cell biology, 2009. **10**(5): p. 332-343.

198. Franze, K., et al., *Neurite branch retraction is caused by a threshold-dependent mechanical impact.* Biophysical journal, 2009. **97**(7): p. 1883-1890.

199. Zhou, W., et al., *Comparison of neurite growth in three dimensional natural and synthetic hydrogels.* Journal of Biomaterials Science, Polymer Edition, 2013. **24**(3): p. 301-314.

200. Her, G.J., et al., *Control of three-dimensional substrate stiffness to manipulate mesenchymal stem cell fate toward neuronal or glial lineages.* Acta Biomaterialia, 2013. **9**(2): p. 5170-5180.

201. Man, A.J., et al., *Neurite outgrowth in fibrin gels is regulated by substrate stiffness.* Tissue Engineering Part A, 2011. **17**(23-24): p. 2931-2942.
202. Ju, Y.-E., et al., *Enhanced neurite growth from mammalian neurons in three-dimensional salmon fibrin gels.* Biomaterials, 2007. **28**(12): p. 2097-2108.
203. Matyash, M., et al., *Novel soft alginate hydrogel strongly supports neurite growth and protects neurons against oxidative stress.* Tissue Engineering Part A, 2012. **18**(1-2): p. 55-66.
204. Balgude, A., et al., *Agarose gel stiffness determines rate of DRG neurite extension in 3D cultures.* Biomaterials, 2001. **22**(10): p. 1077-1084.
205. Gunn, J.W., S.D. Turner, and B.K. Mann, *Adhesive and mechanical properties of hydrogels influence neurite extension.* Journal of Biomedical Materials Research Part A: An Official Journal of The Society for Biomaterials, The Japanese Society for Biomaterials, and The Australian Society for Biomaterials and the Korean Society for Biomaterials, 2005. **72**(1): p. 91-97.
206. Urbanski, M.M., et al., *Myelinating glia differentiation is regulated by extracellular matrix elasticity.* Scientific reports, 2016. **6**(1): p. 1-12.
207. Leach, J.B., et al., *Neurite outgrowth and branching of PC12 cells on very soft substrates sharply decreases below a threshold of substrate rigidity.* Journal of neural engineering, 2007. **4**(2): p. 26.
208. Lantoine, J., et al., *Matrix stiffness modulates formation and activity of neuronal networks of controlled architectures.* Biomaterials, 2016. **89**: p. 14-24.
209. Franze, K., *Atomic force microscopy and its contribution to understanding the development of the nervous system.* Current Opinion in Genetics & Development, 2011. **21**(5): p. 530-537.
210. Zemła, J., et al., *Atomic force microscopy as a tool for assessing the cellular elasticity and adhesiveness to identify cancer cells and tissues.* Seminars in Cell & Developmental Biology, 2018. **73**: p. 115-124.
211. Esteban-Manzanares, G., et al., *Improved Measurement of Elastic Properties of Cells by Micropipette Aspiration and Its Application to Lymphocytes.* Annals of Biomedical Engineering, 2017. **45**(5): p. 1375-1385.
212. Wang, N. and D.E. Ingber, *Probing transmembrane mechanical coupling and cytomechanics using magnetic twisting cytometry.* Biochemistry and Cell Biology, 1995. **73**(7-8): p. 327-335.
213. Guck, J., et al., *The Optical Stretcher: A Novel Laser Tool to Micromanipulate Cells.* Biophysical Journal, 2001. **81**(2): p. 767-784.
214. Mierke, C.T., *The Role of the Optical Stretcher Is Crucial in the Investigation of Cell Mechanics Regulating Cell Adhesion and Motility.* Frontiers in Cell and Developmental Biology, 2019. **7**(184).
215. Gossett, D.R., et al., *Hydrodynamic stretching of single cells for large population mechanical phenotyping.* Proceedings of the National Academy of Sciences, 2012. **109**(20): p. 7630-7635.
216. Otto, O., et al., *Real-time deformability cytometry: on-the-fly cell mechanical phenotyping.* Nature Methods, 2015. **12**(3): p. 199-202.
217. Nyberg, K.D., et al., *Quantitative Deformability Cytometry: Rapid, Calibrated Measurements of Cell Mechanical Properties.* Biophysical Journal, 2017. **113**(7): p. 1574-1584.
218. Wirtz, D., *Particle-Tracking Microrheology of Living Cells: Principles and Applications.* Annual Review of Biophysics, 2009. **38**(1): p. 301-326.
219. Guck, J., et al., *Critical review: cellular mechanobiology and amoeboid migration.* Integrative Biology, 2010. **2**(11-12): p. 575-583.

220. Narasimhan, B., M. Ting, and T. Kollmetz, *Mechanical characterization for cellular mechanobiology: current trends and future prospects. Front Bioeng Biotechnol 8: 595978*. 2020.
221. Meng, Z., et al., *Seeing cells in a new light: a renaissance of Brillouin spectroscopy.* Advances in Optics and Photonics, 2016. **8**(2): p. 300-327.
222. Scarcelli, G. and S.H. Yun, *Confocal Brillouin microscopy for three-dimensional mechanical imaging.* Nature photonics, 2008. **2**(1): p. 39-43.
223. Poon, C., et al., *Brillouin imaging for studies of micromechanics in biology and biomedicine: from current state-of-the-art to future clinical translation.* Journal of Physics: Photonics, 2020. **3**(1): p. 012002.
224. Meng, Z., et al., *Assessment of local heterogeneity in mechanical properties of nanostructured hydrogel networks.* Acs Nano, 2017. **11**(8): p. 7690-7696.
225. Vaughan, J. and J. Randall, *Brillouin scattering, density and elastic properties of the lens and cornea of the eye.* Nature, 1980. **284**(5755): p. 489-491.
226. Margueritat, J., et al., *High-frequency mechanical properties of tumors measured by Brillouin light scattering.* Physical review letters, 2019. **122**(1): p. 018101.
227. Palombo, F., et al., *Biomechanics of fibrous proteins of the extracellular matrix studied by Brillouin scattering.* Journal of The Royal Society Interface, 2014. **11**(101): p. 20140739.
228. Edginton, R.S., et al., *Preparation of extracellular matrix protein fibers for Brillouin spectroscopy.* JoVE (Journal of Visualized Experiments), 2016(115): p. e54648.
229. Antonacci, G. and S. Braakman, *Biomechanics of subcellular structures by non-invasive Brillouin microscopy.* Scientific Reports, 2016. **6**(1): p. 1-6.
230. Elsayad, K., et al., *Mapping the subcellular mechanical properties of live cells in tissues with fluorescence emission–Brillouin imaging.* Science signaling, 2016. **9**(435): p. rs5-rs5.
231. Raghunathan, R., et al., *Evaluating biomechanical properties of murine embryos using Brillouin microscopy and optical coherence tomography.* Journal of biomedical optics, 2017. **22**(8): p. 086013.
232. Zhang, J., et al., *Tissue biomechanics during cranial neural tube closure measured by Brillouin microscopy and optical coherence tomography.* Birth defects research, 2019. **111**(14): p. 991-998.
233. Bailey, M., et al., *Viscoelastic properties of biopolymer hydrogels determined by Brillouin spectroscopy: A probe of tissue micromechanics.* Science advances, 2020. **6**(44): p. eabc1937.
234. Mahmodi, H., et al., *Mechanical mapping of bioprinted hydrogel models by brillouin microscopy.* Bioprinting, 2021. **23**: p. e00151.
235. Mahajan, V., et al., *Mapping tumor spheroid mechanics in dependence of 3D microenvironment stiffness and degradability by Brillouin microscopy.* Cancers, 2021. **13**(21): p. 5549.
236. Gao, X., et al., *An anti-inflammatory and neuroprotective biomimetic nanoplatform for repairing spinal cord injury.* Bioactive Materials, 2022. **18**: p. 569-582.
237. Alizadeh, A., S.M. Dyck, and S. Karimi-Abdolrezaee, *Traumatic spinal cord injury: an overview of pathophysiology, models and acute injury mechanisms.* Frontiers in neurology, 2019. **10**: p. 282.
238. Pinkernelle, J., et al., *Prolonged minocycline treatment impairs motor neuronal survival and glial function in organotypic rat spinal cord cultures.* PLoS One, 2013. **8**(8): p. e73422.

239. Huang, Y., et al., *Pannexin-1 contributes to the apoptosis of spinal neurocytes in spinal cord injury.* Frontiers in physiology, 2021: p. 555.
240. Wei, H., et al., *Systematic analysis of purified astrocytes after SCI unveils Zeb2os function during astrogliosis.* Cell reports, 2021. **34**(5): p. 108721.
241. Munteanu, C., et al., *Main cations and cellular biology of traumatic spinal cord injury.* Cells, 2022. **11**(16): p. 2503.
242. Potokar, M., et al., *The diversity of intermediate filaments in astrocytes.* Cells, 2020. **9**(7): p. 1604.
243. Frost, F., et al., *Inflammatory C-reactive protein and cytokine levels in asymptomatic people with chronic spinal cord injury.* Archives of physical medicine and rehabilitation, 2005. **86**(2): p. 312-317.
244. Visavadiya, N.P., et al., *Cellular and subcellular oxidative stress parameters following severe spinal cord injury.* Redox biology, 2016. **8**: p. 59-67.
245. Hassan, W., Y. Dong, and W. Wang, *Encapsulation and 3D culture of human adipose-derived stem cells in an in-situ crosslinked hybrid hydrogel composed of PEG-based hyperbranched copolymer and hyaluronic acid.* Stem cell research & therapy, 2013. **4**(2): p. 1-11.
246. Mao, H., et al., *Recent advances and challenges in materials for 3D bioprinting.* Progress in Natural Science: Materials International, 2020. **30**(5): p. 618-634.
247. Gu, Z., et al., *Development of 3D bioprinting: From printing methods to biomedical applications.* Asian Journal of Pharmaceutical Sciences, 2020. **15**(5): p. 529-557.
248. Shie, M.-Y., et al., *Effects of gelatin methacrylate bio-ink concentration on mechano-physical properties and human dermal fibroblast behavior.* Polymers, 2020. **12**(9): p. 1930.
249. Liu, W., et al., *Extrusion bioprinting of shear-thinning gelatin methacryloyl bioinks.* Advanced healthcare materials, 2017. **6**(12): p. 1601451.
250. He, Y., et al., *Research on the printability of hydrogels in 3D bioprinting.* Scientific reports, 2016. **6**(1): p. 1-13.
251. Kyle, S., et al., *'Printability'of candidate biomaterials for extrusion based 3D printing: state-of-the-art.* Advanced healthcare materials, 2017. **6**(16): p. 1700264.
252. Janmaleki, M., et al., *Role of temperature on bio-printability of gelatin methacryloyl bioink in two-step cross-linking strategy for tissue engineering applications.* Biomedical Materials, 2020. **16**(1): p. 015021.
253. Noh, I., et al., *3D printable hyaluronic acid-based hydrogel for its potential application as a bioink in tissue engineering.* Biomaterials research, 2019. **23**(1): p. 1-9.
254. Naghieh, S., et al., *Printability of 3D printed hydrogel scaffolds: Influence of hydrogel composition and printing parameters.* Applied Sciences, 2019. **10**(1): p. 292.
255. Fazal, F., et al., *Recent advancements in the bioprinting of vascular grafts.* Biofabrication, 2021.
256. Liu, Y., et al., *Stiffness-mediated mesenchymal stem cell fate decision in 3D-bioprinted hydrogels.* Burns & Trauma, 2020. **8**.
257. Celikkin, N., et al., *Gelatin methacrylate scaffold for bone tissue engineering: the influence of polymer concentration.* Journal of Biomedical Materials Research Part A, 2018. **106**(1): p. 201-209.

258. Xu, P., et al., *Stiffness of photocrosslinkable gelatin hydrogel influences nucleus pulposus cell propertiesin vitro.* Journal of Cellular and Molecular Medicine, 2021. **25**(2): p. 880-891.
259. Xu, P., et al., *Stiffness of photocrosslinkable gelatin hydrogel influences nucleus pulposus cell propertiesin vitro.* Journal of Cellular and Molecular Medicine, 2020.
260. Mann, B.K. and J.L. West, *Cell adhesion peptides alter smooth muscle cell adhesion, proliferation, migration, and matrix protein synthesis on modified surfaces and in polymer scaffolds.* Journal of biomedical materials research, 2002. **60**(1): p. 86-93.
261. Ouyang, L., et al., *Expanding and optimizing 3D bioprinting capabilities using complementary network bioinks.* Science advances, 2020. **6**(38): p. eabc5529.
262. Huang, H., et al., *Peptide hydrogelation and cell encapsulation for 3D culture of MCF-7 breast cancer cells.* PloS one, 2013. **8**(3): p. e59482.
263. Evans, E.B., et al., *Schwann cell durotaxis can be guided by physiologically relevant stiffness gradients.* Biomaterials research, 2018. **22**(1): p. 1-13.
264. Yi, B., Q. Xu, and W. Liu, *An overview of substrate stiffness guided cellular response and its applications in tissue regeneration.* Bioactive materials, 2022. **15**: p. 82-102.
265. Taylor, Z. and K. Miller, *Reassessment of brain elasticity for analysis of biomechanisms of hydrocephalus.* Journal of biomechanics, 2004. **37**(8): p. 1263-1269.
266. Palombo, F. and D. Fioretto, *Brillouin light scattering: applications in biomedical sciences.* Chemical reviews, 2019. **119**(13): p. 7833-7847.
267. Niu, C.J., et al., *Polyacrylamide gel substrates that simulate the mechanical stiffness of normal and malignant neuronal tissues increase protoporphyin IX synthesis in glioma cells.* Journal of biomedical optics, 2015. **20**(9): p. 098002-098002.
268. Quiroz, J.F.D., et al., *Development of a 3D matrix for modeling mammalian spinal cord injury in vitro.* Neural Regeneration Research, 2016. **11**(11): p. 1810.
269. Mijailovic, A.S., et al., *Localized characterization of brain tissue mechanical properties by needle induced cavitation rheology and volume controlled cavity expansion.* Journal of the Mechanical Behavior of Biomedical Materials, 2021. **114**: p. 104168.
270. Krishnamoorthy, S., B. Noorani, and C. Xu, *Effects of encapsulated cells on the physical–mechanical properties and microstructure of gelatin methacrylate hydrogels.* International journal of molecular sciences, 2019. **20**(20): p. 5061.
271. Ahearne, M., *Introduction to cell–hydrogel mechanosensing.* Interface focus, 2014. **4**(2): p. 20130038.
272. Brown, R.A., et al., *Ultrarapid engineering of biomimetic materials and tissues: Fabrication of nano-and microstructures by plastic compression.* Advanced functional materials, 2005. **15**(11): p. 1762-1770.
273. Ahearne, M., et al., *Online monitoring of the mechanical behavior of collagen hydrogels: influence of corneal fibroblasts on elastic modulus.* Tissue Engineering Part C: Methods, 2010. **16**(2): p. 319-327.
274. Hu, Y., et al., *Matrix stiffness changes affect astrocyte phenotype in an in vitro injury model.* NPG Asia Materials, 2021. **13**(1): p. 1-15.
275. Bradbury, E.J. and E.R. Burnside, *Moving beyond the glial scar for spinal cord repair.* Nature Communications, 2019. **10**(1): p. 1-15.

276. Scarcelli, G., et al., *In vivo biomechanical mapping of normal and keratoconus corneas.* JAMA ophthalmology, 2015. **133**(4): p. 480-482.
277. Remer, I., et al., *High-sensitivity and high-specificity biomechanical imaging by stimulated Brillouin scattering microscopy.* Nature Methods, 2020. **17**(9): p. 913-916.
278. Zhang, J., et al., *Line-scanning Brillouin microscopy for rapid non-invasive mechanical imaging.* Scientific reports, 2016. **6**(1): p. 1-8.
279. Ahuja, C.S., et al., *Traumatic spinal cord injury.* Nature reviews Disease primers, 2017. **3**(1): p. 1-21.
280. Wu, P.-J., et al., *Water content, not stiffness, dominates Brillouin spectroscopy measurements in hydrated materials.* Nature methods, 2018. **15**(8): p. 561-562.
281. Hooshmand, M.J., et al., *Characterization of recovery, repair, and inflammatory processes following contusion spinal cord injury in old female rats: is age a limitation?* Immunity & Ageing, 2014. **11**(1): p. 1-13.
282. Carter, M.W., et al., *Comparison of mechanical allodynia and recovery of locomotion and bladder function by different parameters of low thoracic spinal contusion injury in rats.* The Korean Journal of Pain, 2016. **29**(2): p. 86.
283. Gattlen, C., et al., *Spinal cord T-cell infiltration in the rat spared nerve injury model: a time course study.* International journal of molecular sciences, 2016. **17**(3): p. 352.
284. Timms, K.V., *Developing Experimental Models of Non-traumatic Spinal Cord Injury*. 2020, University of Leeds.
285. Matsunaga, S., et al., *Radiographic predictors for the development of myelopathy in patients with ossification of the posterior longitudinal ligament: a multicenter cohort study.* Spine, 2008. **33**(24): p. 2648-2650.
286. Lim, Y.S., et al., *Dural sac area is a more sensitive parameter for evaluating lumbar spinal stenosis than spinal canal area: a retrospective study.* Medicine, 2017. **96**(49).
287. Yang, T., et al., *Dissecting the dual role of the glial scar and scar-forming astrocytes in spinal cord injury.* Frontiers in cellular neuroscience, 2020. **14**: p. 78.
288. Cregg, J.M., et al., *Functional regeneration beyond the glial scar.* Experimental neurology, 2014. **253**: p. 197-207.
289. Tran, A.P., P.M. Warren, and J. Silver, *New insights into glial scar formation after spinal cord injury.* Cell and tissue research, 2021: p. 1-18.
290. Soung, A. and S. Klein, *Astrocytes: initiators of and responders to inflammation.* Glia in Health and Disease, 2020. **89760**(10.5772).
291. Motte, S. and L.J. Kaufman, *Strain stiffening in collagen I networks.* Biopolymers, 2013. **99**(1): p. 35-46.
292. Fratzl, P., *Collagen: structure and mechanics, an introduction*, in *Collagen*. 2008, Springer. p. 1-13.
293. Cullen, D.K., C.M. Simon, and M.C. LaPlaca, *Strain rate-dependent induction of reactive astrogliosis and cell death in three-dimensional neuronal–astrocytic co-cultures.* Brain research, 2007. **1158**: p. 103-115.
294. Kim, J.H., et al., *Impact speed does not determine severity of spinal cord injury in mice with fixed impact displacement.* Journal of neurotrauma, 2009. **26**(8): p. 1395-1404.
295. Pearse, D.D., et al., *Histopathological and behavioral characterization of a novel cervical spinal cord displacement contusion injury in the rat.* Journal of neurotrauma, 2005. **22**(6): p. 680-702.

296. Sparrey, C.J., et al., *The distribution of tissue damage in the spinal cord is influenced by the contusion velocity.* Spine, 2008. **33**(22): p. E812-E819.
297. Sharif-Alhoseini, M., et al., *Animal models of spinal cord injury: a systematic review.* Spinal cord, 2017. **55**(8): p. 714-721.
298. Rosenzweig, E.S. and J.W. McDonald, *Rodent models for treatment of spinal cord injury: research trends and progress toward useful repair.* Current opinion in neurology, 2004. **17**(2): p. 121-131.
299. Bilgen, M., *A new device for experimental modeling of central nervous system injuries.* Neurorehabilitation and neural repair, 2005. **19**(3): p. 219-226.
300. Salegio, E.A., et al., *A unilateral cervical spinal cord contusion injury model in non-human primates (Macaca mulatta).* Journal of neurotrauma, 2016. **33**(5): p. 439-459.
301. Yan, R., et al., *A modified impactor for establishing a graded contusion spinal cord injury model in rats.* Annals of Translational Medicine, 2022. **10**(8).
302. Alakpa, E.V., et al., *Bioprinted Schwann and Mesenchymal Stem Cell Co-Cultures for Enhanced Spatial Control of Neurite Outgrowth.* Gels, 2023. **9**(3): p. 172.
303. Jones, L.L., D. Sajed, and M.H. Tuszynski, *Axonal Regeneration through Regions of Chondroitin Sulfate Proteoglycan Deposition after Spinal Cord Injury: A Balance of Permissiveness and Inhibition.* The Journal of Neuroscience, 2003. **23**(28): p. 9276-9288.
304. Dyck, S.M. and S. Karimi-Abdolrezaee, *Role of chondroitin sulfate proteoglycan signaling in regulating neuroinflammation following spinal cord injury.* Neural Regeneration Research, 2018. **13**(12).